DISSERTATION

INVESTIGATION OF VERTICAL MIXING IN RACEWAY POND SYSTEMS USING COMPUTATIONAL FLUID DYNAMICS

Submitted by

Chen Shen

Department of Chemical and Biological Engineering

In partial fulfillment of the requirements

For the Degree of Doctor of Philosophy

Colorado State University

Fort Collins, Colorado

Fall 2021

Doctoral Committee:

Advisor: David S. Dandy

Kenneth F. Reardon
Thomas Bradley
Ashok Prasad

ABSTRACT

INVESTIGATION OF VERTICAL MIXING IN RACEWAY POND SYSTEMS USING COMPUTATIONAL FLUID DYNAMICS

Raceway ponds are widely used as cost-efficient and easily set up outdoor algal cultivation systems. Growth rates strongly depend on cumulative light exposure, which can be predicted using accurate computational fluid dynamics simulations of the ponds' dynamics. Of particular importance in computing the three-dimensional velocity field is the vertical component that is responsible for transporting cells between light and dark regions. Numerous previous studies utilized one of the turbulence models derived from the Reynolds-averaged Navier–Stokes equations to predict the turbulent behaviors in raceway ponds. Because vertical fluid motion is secondary and the primary flow is in the horizontal plane, using one of the Reynolds-averaged Navier–Stokes turbulence equations has the potential to decrease the fidelity of information about vertical motion.

In Chapter 2, large eddy simulation (LES) and k-ε models are used to simulate fluid dynamics in a mesoscale (615 L) raceway pond system and compared with laboratory data. It is found that swirling motions present in the liquid phase play an essential role in the vertical mixing performance. LES is shown to have the capability to provide more realistic and highly time-dependent hydrodynamic predictions when compared with experimental data, while the k-ε model under-predicts the magnitude of the swirling behavior and over-predicts the volume of dead zones in the pond. The instantaneous spatial distribution of high vertical velocity regions and dead zones, as well as their time-accumulated volume fraction, are investigated. LES results suggest that swirling motion exists in the low-velocity regions predicted by the k-ε model to be

dead zones where the high-velocity flow takes place over more than 50% of the flow time, and the recirculating motion may be responsible for stratification and unwanted chemical accumulation. LES results indicate that strong vortex regions exist near the paddle wheel, and the first 180° bend, and the geometry of the divider will contribute to the generation of vortices, enhance the vertical motion, and increase the light/dark effect.

In Chapter 3, it will be demonstrated that the swirling motion appears to play a critical role in enhancing the vertical mixing and enhancing the light/dark effect. In Chapter 3, a dimensional analysis is performed to predict the persistence of the swirling motion generated at the hairpin bend by modeling 7 raceway pond geometries with shape ratios—defined as the ratio of the width of a straight section to the liquid depth—ranging from 0.5 to 7.05, and Dean numbers ranging from 16,140 to 242,120. The fluid dynamics were simulated using a transient multiphase solver with a large eddy simulation turbulence model in the open-source code openFoam framework. The results demonstrate that the number of instances of swirling motion strongly depends on the shape ratio of the ponds. When the shape ratio is close to 1, a single instance of swirling motion is most likely to be found downstream of the first 180° bend, while multiple occurrences of swirling motion are observed when the shape ratio is larger than 1. It was also found that the strength of the swirling motion has a linear dependence on the average velocity magnitude downstream of the first 180° bend after the paddle wheel. The strength and persistence of the swirling motion are fit with a rational function that can be used to predict the mixing performance of a raceway pond without the need for complicated and expensive simulations.

In Chapter 4, transient particle tracking is performed to predict microalgae cells' vertical motion for more than 800 s, which is subsequently converted to the cells' light intensity history.

The data of light intensity history, along with the velocity field, are compared to validate the hypothesis that the cells' trajectories and L/D transition are significantly dominated by vertical mixing in raceway ponds, mostly, the swirling motions generated by the secondary flow in the hairpin bends. It is found that the region where cells have a high probability to experience light/dark transitions coincides with the spatial prediction of swirling motion, suggesting that the swirling motion significantly contributes to reducing the light/dark frequency exposure by microalgae.

In Chapter 5, a novel use of vortex generators in a raceway pond is presented that passively generate swirling motion in the regions where the strength of vertical motion is predicted to otherwise be low. The flow field is quantitatively simulated using computational fluid dynamics using the large eddy simulation turbulence model. Persistence lengths of the swirling motion generated by the vortex generators indicate that significant vertical mixing can be achieved by placing vortex generators in the straight section opposite the paddle wheel, downstream of the first hairpin bend. Relatively simple vortex generators are capable of creating stronger swirling motions that persist for a longer distance than those caused by the paddle wheel. For optimal performance, vortex generators are positioned side by side but in opposite directions, and their diameters should be equal to or slightly less than the liquid depth, as suggested by the CFD model. The optimal length of a 0.18 m diameter vortex generator in a 0.2 m deep pond was determined to be 0.3 m. Furthermore, it has been demonstrated that a longer persistence length is achieved by inducing a swirling motion with its rotational axis parallel to the primary flow direction.

ACKNOWLEDGEMENTS

I would like to convey my heartfelt gratitude to Professor David S. Dandy, my adviser, for his advice, encouragement, and unwavering support during this research. Your enlightening remarks pushed me to refine my thinking and enhance my work. I am grateful to Professor A. Ted Watson for introducing me to fluid dynamics and Dr. Wolfgang Bangerth for his C++ guidance. Additionally, I would like to thank the members of my doctorate committee, Drs. Kenneth F. Reardon, Ashok Prasad, and Thomas Bradley, for their guidance and recommendations about this study. Many thanks to all of the EFRI project's principal investigators, collaborators as well as Alex Day for walking me through HPC commands and the Linux system. I would also like to thank to my family for their support and understanding throughout the program. A big thank you to all of my friends here and in China for their encouragement and support. I would also like to express my thanks to Mr. Tim Gonzales for assisting me in building a pygmy flowmeter, as well as Prof. Karan Venayagamoorthy and Mr. Matthew Klema for allowing me to use their tilting flume and LDA equipment. I am grateful to Jeff Penn and other staff of the engineering technology services and National Renewable Energy Laboratory high-performance computing services for their continuous assistance with software, licensing, and network services, as well as for providing access to high-performance computing resources. This research was made possible by a National Science Foundation grant number 1332404 and Department of Energy grant number DE-EE00-08514.

My heartfelt gratitude to my best friend, Yan Wang. For no reason, and for all reasons, I have to thank you for being in my life, and I owe more than thanks to you.

A special thank goes to my dog Papala for your silly antics, cheerful and adventurous

personality, and unconditional accompany. Thank you for chewing my cellphone, stealing and hiding food, and many other joys and surprises you have brought to me.

DEDICATION

I would like to dedicate this Dissertation to my fluffy dog Papala.

TABLE OF CONTENTS

LIST OF FIGURES

Chapter 1: Introduction

1.1 Background and Motivation

Due to the excessive use of fossil fuels, at least 50% to 75% of the carbon dioxide (CO_2) and other greenhouse gases emitted into the atmosphere are contributed by the use of these fuels [1-2]. These greenhouse gases released from the combustion of fossil fuels have been identified as the primary cause of climate change.

Increasing environmental temperatures are anticipated to raise hot season cooling demands and increase agricultural irrigation energy consumption during crop-growing seasons [3-5]. Simulations of earth system models predict that the global energy demand will increase at a rate of 1.7 to 2.8 times due to social and economic developments by 2050. Considering the effect of global warming, the energy demand could further be increased by 25-58% around 2050 [6]. A major obstacle to attaining sustainable global development is the continuing dependence of world economies on fossil fuel-derived energy. Reducing this reliance is therefore of critical importance to achieve sustainable global development environmentally, socially, and economically [7-8]. The rising demand for energy and the associated climate change concerns have spurred investigations into alternative energy sources that are renewable, sustainable, and environmentally friendly. Because of these driving forces, microalgae-based biofuels have drawn significant attention. Microalgae, the major producers of oxygen in the oceans, provide for around 40%–50% of the oxygen in the atmosphere, which has the potential to significantly reduce the rate of global warming [9]. Other benefits of microalgae-based biofuels include rapid growth, a high lipid carbohydrate content, land utilization that does not compete with food crops, can use wastewater as a nutrition source, and the generation of valuable by-product chemicals while using CO_2 from the atmosphere [10-18]. Microalgae cultivation can be accomplished using enclosed photobioreactors (PBR) or open, outdoor ponds.

Faster growth rate and higher biomass yield can be achieved in enclosed PBRs as they can employ customized, programmable light sources, cultivation conditions that are easier to monitor, and to be tightly controlled to reduce the risk of contamination. Microalgae growing in closed PBRs, on the other hand, has significant drawbacks since closed PBRs frequently require higher capital investments and operational and maintenance costs than outdoor ponds. Additionally, scaling up closed PBRs incurs a considerable increase in capital costs, rendering them economically uncompetitive with commercial mass manufacturing [19-23]. Commercial production and large-scale growth of microalgae are frequently accomplished with the use of outer door open PBRs.

Raceway ponds are the most frequently used and popular open cultivation method because they are easy to construct and scale up, need little initial investment, are easy to maintain, and have low operational energy requirements [13, 24-26]. A raceway pond consists of a closed-loop channel that is usually in an oval shape. In the center of the pond, a divider is placed along the length of the straight sections to direct the flow and aid in recirculation. One or more paddle wheels are placed in the straight sections to generate the driving force required for recirculation. For pilot-scale raceway ponds, sunlight is commonly utilized as the light source to save capital investment. When carried along by the fluid motion, the microalgae's vertical location and the resulting light intensity received by each cell change dynamically. To simplify characterization, the light intensity regimes to which microalgae cells are exposed are classified as light and dark zones [27]. Agitation is required to propel cells into and out of these zones.

Otherwise, microalgae will stratify, and they will either spend excessively long times in the light zone where photo-inhibition may occur or be trapped in the dark zone where the light intensity does not reach the compensation point and photosynthesis will not occur [28].

A number of studies have demonstrated that when microalgae are subjected to light/dark changes, a faster growth rate may be achieved by increasing the light/dark (L/D) frequency, referred to as the flashing-light effect [29]. For example, Kyong-Hee Park used the concept of critical cell density and reported that the specific oxygen production rate increased under flashing light. A more recent effort studied the effect of flashing light on the species *Dunaliella salina* [30]. The investigators found that flashing light with a frequency between 10 and 50 Hz can be used to enhance photosynthetic activity and growth rate of *D. salina*. In another study, the impact of flashing light on biomass production rate was measured [31]. In that study, a thin-layer PBR device equipped with an alternating L/D system was utilized to identify the photosynthetic properties of *Spirulina platensis* consistent and periodic irradiation with a range of light intensity levels. It was observed that the specific growth rate and the light utilization efficiency were increased with the increase of the L/D frequency from 0.01 Hz to 20 Hz, and a stronger enhancement was reported for a higher light intensity. Apart from biomass growth rate and photosynthesis, the flashing light effect also has an impact on lipid content. The study conducted by Combe et al. (2015) demonstrated that the growth rate of *D. salina* increased from 0.25 day^{-1} to 0.93 day^{-1} when the L/D frequency increased from 0.017 Hz to 5.0 Hz [32]. Abu-Ghosh et al. have pointed out that the optimal way to enhance the flashing light effect in outdoor open pond systems is to improve the mixing velocity in sunny locations [33]. A similar conclusion has been drawn by Grobbelaar (1991) [34]. The investigators suggested that the impact of the mixing and light effect should be investigated separately since the turbulence aids in the movement of the algae through an optically dense medium and influences the boundary layer. The study revealed that the primary benefit and purpose of mixing in PBRs would be to prevent cells from settling out and to reducing the boundary layer thickness around the cells, which would have an indirect and positive impact on improving the light utilization efficiency and therefore the production. Additionally, adequate agitation and mixing facilitate mass transmission, reduce heat stratification and oxygen accumulation, and minimize cell stacking [35-37].

The turbulent mixing in raceway ponds has been studied by investigators using computational fluid dynamics (CFD) methods [38-45]. Kurt et al. simulated raceway ponds with different bend configurations and reported that the energy loss due to the dead zones can be reduced up to 87% with a modified bend configuration relative to the conventional bend design [46]. In another effort, a variation of the k–ε model was used as the turbulence model to simulate the flow field and capture turbulence characteristics in raceway ponds at paddle wheel rotational speeds of 10, 15, and 20 RPM and length/width ratios of 6, 8, and 10 [47]. The CFD results were validated with particle image velocimetry (PIV), and the investigators concluded that increasing the length/width ratio from 6 to 10 could result in cell settling, and the clearance between the paddle wheel tip and the bottom surface should be within 0.05 m to 0.08 m. Rainier et al. conducted CFD simulations in meso-scale raceway ponds and pointed out that the configuration of the paddle wheel plays an important role in the mixing rate and that wind can have a significant impact on the hydrodynamics in a raceway even at a moderate paddle RPM [48]. Another technique commonly used in the CFD community to model turbulence is the LES model, where a filtering function is employed to remove small length scale eddies, and the remaining large-scale eddies are resolved numerically by solving the spatial-filtered Navier-Stokes equation.

Sub-grid scale (SGS) stress models are used to depict the motion of the filtered small-scale eddies. The advantage of using the LES model is that it has the capability to predict more detailed transient flow where the motion of turbulent eddies with a length scale larger than the cut-off length scale is well captured. LES model has been used extensively for transient incompressible flows [49-58]. Nevertheless, only a few works have used LES as the turbulence model to investigate mixing in raceway pond systems. Zeng et al. (2016) conducted an investigation of inclined paddle wheels using LES as the turbulence model and reported that the best mixing efficiency could be achieved with a 15° inclined angle of the blades [59]. There is no study focused on the vertical mixing in raceway ponds with LES as the turbulence model. The turbulence model used in other studies was selected from the RANS family, which is derived by time averaging the Navier-Stocks equations; these models have the potential to under-predict the extent of fluid motion in the vertical direction because of loss of fluctuating behavior due to time-averaging. To explore this further, in chapter 2, the LES and k–ε models are tested and validated for their capability to accurately resolve the vertical motion in raceway ponds. It will be shown that the k–ε model fails to resolve the vertical motion accurately and fails to identify a unique longitudinal rotational motion downstream of the hairpin-bends that is correctly predicted by the LES model, referred to as the swirling motion.

The swirling motion is hypothesized to be the result of secondary flow and flow instability due to boundary layer separation. Dean provided an analytical solution for the flow in curved pipes in which one pair of counter-rotating vortices can be observed [60]. Several studies have been conducted to investigate hydrodynamic characteristics in curved open channels. The shear stress distribution was investigated in a 180° sharp open channel bend [61]. In this research, a three-dimensional acoustic doppler velocimeter was used to measure the velocity field and determine the three-dimensional flow pattern in the bend. The investigators reported rotational motion present in the 40°, 80°, 90°, 130°, and 180° cross sections in the bend by visualizing the longitudinal velocity and path lines. In another study, the impact of sharp meander bends on the flow field was studied using an acoustic doppler velocity device [62]. In the study, swirling motions are observed starting from the 0° location of the outer bend and 55° of the inner bend. CFD simulations had been utilized with LES as the turbulence model in studying the flow characteristics in a curved open channel flow and the investigators observed recirculation in the inner bends and high velocity regions in the outer bends where strong rotational motion exists [63]. However, the bend investigated in those studies had a large inner bend radius, representing bends whose direction changes gradually. On the contrary, the radius of the inner bend used in conventional raceway ponds is comparable to the thickness of the divider, resulting in a large value of the second term in the definition of the Dean number: $D_h/2R$. Furthermore, those researchers focused on the curved open channels present in river topographies, which have irregular cross sections while the cross section in raceway ponds are commonly rectangular with a constant area. Finally, all these previous investigations were focused on the flow characteristics in the bends from a civil engineering perspective, and none of these focused on the spatial distribution of the swirling motions and how far they can travel before being dissipated, which is critical to be able to understand the impact of the hairpin bends on vertical mixing in raceway ponds. To address this research question regarding the formation of swirling motion in the bends and their downstream persistence, a set of raceway ponds with 7 shape ratios and 8 paddle wheel RPMs for each shape ratio is simulated in chapter 3, and an empirical equation is established to predict the strength and the persistence length of swirling motions.

The ability to measure or model the microalgae cells' movements and convert the trajectories into the light intensity histories is crucial to be able to understand the light environment that microalgae cells are exposed to under different operating conditions. Several efforts have been made on this topic [64-70]. However, the longest tracking time performed in those studies was around 120 s, and a more statistically confident conclusion could be drawn from the particle tracking data with a longer tracking time. Moreover, none of these studies used the LES model to predict the velocity coupled with a particle tracking method. Because it will be demonstrated that the k–ε model fails to fully resolve the swirling motion and significantly under-predicts the strength of the vertical mixing in raceway ponds in Chapter 2, the particle trajectories obtained by solving fluid equations of motion using the k–ε model will be smoothed out and under-estimate the light/dark frequency. Furthermore, none of the previous research attempted to identify the regions in raceway ponds where cells are more prone to experience light/dark transitions. It is hypothesized that the vertical liquid motion will contribute to the cell's vertical movements, and those regions with a greater likelihood of cells experiencing light/dark transitions will be coinciding with the high vertical velocity regions. To address this hypothesis, an investigation is conducted and summarized in Chapter 4, in which the cells' trajectories are predicted using a transient particle tracking method coupled with velocity field predicted by the LES model and converted to the light intensity history, which is then used to determine the spatial distribution of the regions with a high L/D transition probability.

It will be established in chapter 2 that the swirling motion plays a significant role in vertical mixing, and in chapter 3 that the generated swirling motion will persist for a deterministic distance before dissipating. In chapter 4 it will be shown that the vertical motion created by the paddle wheel and 180° bends enhances the L/D effect in a deterministic manner.

However, it is identified that the volume fraction of the pond experiencing the high vertical motion is low (in chapter 2), and the swirling motion can only persist for a specific distance (in chapter 3). A good way to induce vertical mixing in raceway ponds is to deploy passive vortex generating devices in the pond. Zhang et al. designed and tested flow deflectors and wing baffles in raceway ponds where it is reported that the volume of the dead zone is reduced by 60.42% and the L/D frequency is increased for more than 3 folders [71]. Several other designs are proposed and tested to improve the vertical mixing in open raceway ponds and enhance the L/D effect [59, 72-76]. However, the swirling motion generated by these designs has rotational axes that are perpendicular to the main flow direction, and it is hypothesized that the performance of the vortex generators can be improved if the induced swirling motion has the rotational axis parallel to the main flow direction. For this purpose, a novel vortex generator design is developed, and the performance is tested in chapter 5. The optimal diameter of the vortex generator is identified, and the optimal length for 0.18 m diameter vortex generators is determined.

1.2 Objectives of this dissertation

The main objective of this dissertation is to investigate the vertical mixing performance of raceway pond systems with a variety of shape ratios and operating conditions. Extensive research has been conducted on this topic using computational fluid dynamic tools, however, nearly all of those studies used one of the Reynolds Averaged Navier-Stokes turbulence models, which was later shown to under-estimate the vertical mixing in raceway ponds. In Chapter 2, the large eddy simulation turbulence model is utilized to accurately capture the vertical mixing in raceway ponds, and swirling motion due to the secondary flow as a consequence of the hairpin-bends are observed. This swirling motion is recognized to play critical roles in enhancing the vertical mixing in raceway ponds. Therefore, in Chapter 3, the spatial distribution and the persistence length of the swirling motion are predicted using dimensionless analysis. In Chapter 4, unsteady particle tracking is performed to predict the microalgae cells' motion and light intensity history. It is found that the spatial distribution of the high light/dark transition regions coincides with the strong swirling motion regions. To enhance the swirling motion without increasing energy requirement significantly, in Chapter 5, a novel design of a passive vortex generator is presented and tested. Lastly, the author was fortunate to be involved during his Ph.D. program in the research to investigate the effect of body wake and operator motion on a novel design and a traditional fume hood. The report is included in the appendix.

1.3 References

[1] T. A. Boden, R. J. Andres, and G. Marland, "Global, Regional, and National Fossil-Fuel CO2 Emissions (1751 - 2014) (V. 2017)," Environmental System Science Data Infrastructure for a Virtual Ecosystem (ESS-DIVE) (United States); Carbon Dioxide Information Analysis Center (CDIAC), Oak Ridge National Laboratory (ORNL), Oak Ridge, TN (United States), Jan. 2017. doi: 10.3334/CDIAC/00001_V2017.

[2] DECC, DEFRA. "Guidelines to Defra/DECC's GHG conversion factors for company reporting." London: Department for Environment, Food and Rural Affairs and Department for Energy and Climate Change (2011).

[3] Y. Petri and K. Caldeira, "Impacts of global warming on residential heating and cooling degree-days in the United States," *Sci. Rep.*, vol. 5, no. 1, p. 12427, Aug. 2015, doi: 10.1038/srep12427.

[4] A. Damm, J. Köberl, F. Prettenthaler, N. Rogler, and C. Töglhofer, "Impacts of +2°C global

warming on electricity demand in Europe," *Clim. Serv.*, vol. 7, pp. 12–30, Aug. 2017, doi: 10.1016/j.cliser.2016.07.001.

[5] M. Sylla, J. Pal, A. Faye, K. Dimobe, and H. Kunstmann, "Climate change to severely impact West African basin scale irrigation in 2 °C and 1.5 °C global warming scenarios," *Sci. Rep.*, vol. 8, Sep. 2018, doi: 10.1038/s41598-018-32736-0.

[6] B. J. van Ruijven, E. De Cian, and I. Sue Wing, "Amplification of future energy demand growth due to climate change," *Nat. Commun.*, vol. 10, no. 1, p. 2762, Jun. 2019, doi: 10.1038/s41467-019-10399-3.

[7] J. Scheffran, M. Felkers, and R. Froese, "Economic Growth and the Global Energy Demand," in *Green Energy to Sustainability*, John Wiley & Sons, Ltd, 2020, pp. 1–44. doi: 10.1002/9781119152057.ch1.

[8] A. Vertes, N. Qureshi, H. Blaschek, and H. Yukawa, *Green Energy to Sustainability: Strategies for Global Industries*. 2020.

[9] R. A. Andersen, Ed., *Algal culturing techniques*. Burlington, Mass: Elsevier/Academic Press, 2005.

[10] W. Zhou, Y. Li, M. Min, B. Hu, P. Chen, and R. Ruan, "Local bioprospecting for high-lipid producing microalgal strains to be grown on concentrated municipal wastewater for biofuel production," *Bioresour. Technol.*, vol. 102, no. 13, pp. 6909–6919, Jul. 2011, doi: 10.1016/j.biortech.2011.04.038.

[11] P. M. Slegers, M. B. Lösing, R. Wijffels, G. van Straten, and T. van Boxtel, "Scenario evaluation of open pond microalgae production," *Algal Res.*, vol. 2, Oct. 2013, doi: 10.1016/j.algal.2013.05.001.

[12] Z. Li, H. Yuan, J. Yang, and B. Li, "Optimization of the biomass production of oil algae

Chlorella minutissima UTEX2341," *Bioresour. Technol.*, vol. 102, no. 19, pp. 9128–9134, Oct. 2011, doi: 10.1016/j.biortech.2011.07.004.

[13] F. Javed *et al.*, "Microalgae-based biofuels, resource recovery and wastewater treatment: A pathway towards sustainable biorefinery," *Fuel*, vol. 255, p. 115826, Nov. 2019, doi: 10.1016/j.fuel.2019.115826.

[14] C.-Y. Chen *et al.*, "Microalgae-based carbohydrates for biofuel production," *Biochem. Eng. J.*, vol. 78, pp. 1–10, Sep. 2013, doi: 10.1016/j.bej.2013.03.006.

[15] C. E, Q. Arita, Christie, Peebles, T. H, and Bradley, "Scalability of combining microalgae-based biofuels with wastewater facilities: A review," *Algal Res.*, 2015, Accessed: Oct. 08, 2021. [Online]. Available: http://dx.doi.org/10.1016/j.algal.2015.03.001

[16] J. Weinberg, M. Kaltschmitt, and C. Wilhelm, "Analysis of greenhouse gas emissions from microalgae-based biofuels," *Biomass Convers. Biorefinery*, vol. 2, no. 2, pp. 179–194, Jun. 2012, doi: 10.1007/s13399-012-0044-4.

[17] H.-W. Yen, I.-C. Hu, C.-Y. Chen, S.-H. Ho, D.-J. Lee, and J.-S. Chang, "Microalgae-based biorefinery – From biofuels to natural products," *Bioresour. Technol.*, vol. 135, pp. 166–174, May 2013, doi: 10.1016/j.biortech.2012.10.099.

[18] V. Ananthi, R. Raja, I. S. Carvalho, K. Brindhadevi, A. Pugazhendhi, and A. Arun, "A realistic scenario on microalgae based biodiesel production: Third generation biofuel," *Fuel*, vol. 284, p. 118965, Jan. 2021, doi: 10.1016/j.fuel.2020.118965.

[19] Y. Chisti, "Biodiesel from microalgae," *Biotechnol. Adv.*, vol. 25, no. 3, pp. 294–306, May 2007, doi: 10.1016/j.biotechadv.2007.02.001.

[20] B. Singh, D. Sharma, R. Sahu, O. SAHINb, and A. WARRENc, "Towards algal biofuel production: a concept of green bio energy development," *Innov. Romanian Food*

Biotechnol., vol. 12, pp. 1–21, Mar. 2013.

[21] M. R. Tredici, "Mass Production of Microalgae: Photobioreactors," in *Handbook of Microalgal Culture*, John Wiley & Sons, Ltd, 2003, pp. 178–214. doi: 10.1002/9780470995280.ch9.

[22] J. Masojídek, M. Koblizek, and G. Torzillo, "Handbook of Microalgal Culture: Applied Phycology and Biotechnology, Second Edition," 2007, pp. 20–39. doi: 10.1002/9780470995280.ch2.

[23] D. Kamravamanesh, D. Kiesenhofer, S. Fluch, M. Lackner, and C. Herwig, "Scale-up challenges and requirement of technology-transfer for cyanobacterial poly (3-hydroxybutyrate) production in industrial scale," *Int. J. Biobased Plast.*, vol. 1, no. 1, pp. 60–71, Jan. 2019, doi: 10.1080/24759651.2019.1688604.

[24] C. Posten and C. Walter, *Microalgal Biotechnology: Potential and Production*. Walter de Gruyter, 2012.

[25] C. Jiménez, B. R. Cossío, D. Labella, and F. Xavier Niell, "The Feasibility of industrial production of Spirulina (Arthrospira) in Southern Spain," *Aquaculture*, vol. 217, no. 1, pp. 179–190, Mar. 2003, doi: 10.1016/S0044-8486(02)00118-7.

[26] L. Rodolfi *et al.*, "Microalgae for Oil: Strain Selection, Induction of Lipid Synthesis and Outdoor Mass Cultivation in a Low-Cost Photobioreactor," *Biotechnol. Bioeng.*, vol. 102, pp. 100–12, Jan. 2009, doi: 10.1002/bit.22033.

[27] Y. Chisti, "Microalgae as sustainable cell factories," *Env. Eng Manage J*, vol. 5, pp. 261–274, Sep. 2006.

[28] A. Richmond, "Principles for attaining maximal microalgal productivity in photobioreactors: an overview," p. 5.

[29] I. Martín-Girela, M. D. Curt, and J. Fernandez, “Flashing light effects on CO2 absorption by microalgae grown on a biofilm photobioreactor,” 2017, doi: 10.1016/J.ALGAL.2017.06.008.

[30] S. Abu-Ghosh *et al.*, “Flashing light enhancement of photosynthesis and growth occurs when photochemistry and photoprotection are balanced in Dunaliella salina,” *Eur. J. Phycol.*, vol. 50, Sep. 2015, doi: 10.1080/09670262.2015.1069404.

[31] S. Xue, Z. Su, and W. Cong, “Growth of Spirulina platensis enhanced under intermittent illumination,” *J. Biotechnol.*, vol. 151, no. 3, pp. 271–277, Feb. 2011, doi: 10.1016/j.jbiotec.2010.12.012.

[32] C. Combe, P. Hartmann, S. Rabouille, A. Talec, O. Bernard, and A. Sciandra, “Long-term adaptive response to high-frequency light signals in the unicellular photosynthetic eukaryote Dunaliella salina,” *Biotechnol. Bioeng.*, vol. 112, no. 6, pp. 1111–1121, Jun. 2015, doi: 10.1002/bit.25526.

[33] S. Abu-Ghosh, D. Fixler, Z. Dubinsky, and D. Iluz, “Flashing light in microalgae biotechnology,” *Bioresour. Technol.*, vol. 203, Dec. 2015, doi: 10.1016/j.biortech.2015.12.057.

[34] J. U. Grobbelaar, “The influence of light/dark cycles in mixed algal cultures on their productivity,” *Bioresour. Technol.*, vol. 38, no. 2, pp. 189–194, Jan. 1991, doi: 10.1016/0960-8524(91)90153-B.

[35] G. Persoone, J. Morales, H. Verlet, and N. De Pauw, “Air-lift pumps and the effect of mixing on algal growth,” 2000. Accessed: Oct. 04, 2021. [Online]. Available: http://www.vliz.be/imisdocs/publications/128033.pdf

[36] A. Richmond, “Biological Principles of Mass Cultivation of Photoautotrophic Microalgae,”

in *Handbook of Microalgal Culture*, John Wiley & Sons, Ltd, 2013, pp. 169–204. doi: 10.1002/9781118567166.ch11.

[37] Y. Chisti, “Large-Scale Production of Algal Biomass: Raceway Ponds,” in *Algae Biotechnology: Products and Processes*, F. Bux and Y. Chisti, Eds. Cham: Springer International Publishing, 2016, pp. 21–40. doi: 10.1007/978-3-319-12334-9_2.

[38] J. P. Bitog *et al.*, “Application of computational fluid dynamics for modeling and designing photobioreactors for microalgae production: A review,” *Comput. Electron. Agric.*, vol. 76, no. 2, pp. 131–147, May 2011, doi: 10.1016/j.compag.2011.01.015.

[39] C. Inostroza, A. Solimeno, J. García, J. M. Fernández-Sevilla, and F. G. Acién, “Improvement of real-scale raceway bioreactors for microalgae production using Computational Fluid Dynamics (CFD),” *Algal Res.*, vol. 54, p. 102207, Apr. 2021, doi: 10.1016/j.algal.2021.102207.

[40] A. Lima, B. Marinho, and T. Morais, “Hydrodynamic analysis of flow in raceway ponds for algae cultivation under versatile conditions,” *Aquac. Int.*, vol. 29, no. 1, pp. 19–35, Feb. 2021, doi: 10.1007/s10499-020-00606-0.

[41] R. Peralta Muniz Moreira, A. Cabrera Reina, P. Soriano Molina, J. A. Sánchez Pérez, and G. Li Puma, “Computational fluid dynamics (CFD) modeling of removal of contaminants of emerging concern in solar photo-Fenton raceway pond reactors,” *Chem. Eng. J.*, vol. 413, p. 127392, Jun. 2021, doi: 10.1016/j.cej.2020.127392.

[42] P. Fernández Del Olmo, F. G. Acién, and J. M. Fernández-Sevilla, “Analysis of productivity in raceway photobioreactor using computational fluid dynamics particle tracking coupled to a dynamic photosynthesis model,” *Bioresour. Technol.*, vol. 334, p. 125226, Apr. 2021, doi: 10.1016/j.biortech.2021.125226.

[43] J. Xu, J. Cheng, K. Xin, J. Xu, and W. Yang, "Strengthening flash light effect with a pond-tubular hybrid photobioreactor to improve microalgal biomass yield," *Bioresour. Technol.*, vol. 318, p. 124079, Dec. 2020, doi: 10.1016/j.biortech.2020.124079.

[44] W. Guo *et al.*, "Improving flashing light frequency and CO2 fixation rate with vortex movement of algal cells in raceway pond with conic baffles," *Chem. Eng. Sci.*, vol. 216, p. 115536, Apr. 2020, doi: 10.1016/j.ces.2020.115536.

[45] V. Belohlav, E. Uggetti, J. García, T. Jirout, L. Kratky, and R. Díez-Montero, "Assessment of hydrodynamics based on Computational Fluid Dynamics to optimize the operation of hybrid tubular photobioreactors," *J. Environ. Chem. Eng.*, vol. 9, no. 5, p. 105768, Oct. 2021, doi: 10.1016/j.jece.2021.105768.

[46] K. Liffman, D. A. Paterson, P. Liovic, and P. Bandopadhayay, "Comparing the energy efficiency of different high rate algal raceway pond designs using computational fluid dynamics," *Chem. Eng. Res. Des.*, vol. 91, no. 2, pp. 221–226, Feb. 2013, doi: 10.1016/j.cherd.2012.08.007.

[47] R. Pandey and M. Premalatha, "Design and analysis of flow velocity distribution inside a raceway pond using computational fluid dynamics," *Bioprocess Biosyst. Eng.*, vol. 40, pp. 1–12, Mar. 2017, doi: 10.1007/s00449-016-1712-8.

[48] R. Hreiz, B. Sialve, J. Morchain, R. Escudié, J.-P. Steyer, and P. Guiraud, "Experimental and numerical investigation of hydrodynamics in raceway reactors used for algaculture," *Chem. Eng. J.*, vol. 250, pp. 230–239, Aug. 2014, doi: 10.1016/j.cej.2014.03.027.

[49] X. Y. Luo, J. S. Hinton, T. T. Liew, and K. K. Tan, "LES modelling of flow in a simple airway model," *Med. Eng. Phys.*, vol. 26, no. 5, pp. 403–413, Jun. 2004, doi: 10.1016/j.medengphy.2004.02.008.

[50] G. Kristóf and B. Papp, “Application of GPU-Based Large Eddy Simulation in Urban Dispersion Studies,” *Atmosphere*, vol. 9, no. 11, Art. no. 11, Nov. 2018, doi: 10.3390/atmos9110442.

[51] A. Posa and E. Balaras, “Large-Eddy Simulations of a notional submarine in towed and self-propelled configurations,” *Comput. Fluids*, vol. 165, pp. 116–126, Mar. 2018, doi: 10.1016/j.compfluid.2018.01.013.

[52] A. Posa, R. Broglia, M. Felli, M. Falchi, and E. Balaras, “Characterization of the wake of a submarine propeller via Large-Eddy Simulation,” *Comput. Fluids*, vol. 184, Mar. 2019, doi: 10.1016/j.compfluid.2019.03.011.

[53] P. Ouro, C. A. M. E. Wilson, P. Evans, and A. Angeloudis, “Large-eddy simulation of shallow turbulent wakes behind a conical island,” *Phys. Fluids*, vol. 29, no. 12, p. 126601, Dec. 2017, doi: 10.1063/1.5004028.

[54] J. Ke, “RANS and hybrid LES/RANS simulations of flow over a square cylinder,” *Adv. Aerodyn.*, vol. 1, no. 1, p. 10, May 2019, doi: 10.1186/s42774-019-0012-9.

[55] Z.-T. Xie and I. Castro, “Large-eddy simulation for flow and dispersion in urban streets,” *Atmospheric Environ. - ATMOS Env.*, vol. 43, Apr. 2009, doi: 10.1016/j.atmosenv.2009.01.016.

[56] D. S. Henn and R. I. Sykes, “Large-eddy simulation of flow over wavy surfaces,” *J. Fluid Mech.*, vol. 383, pp. 75–112, Mar. 1999, doi: 10.1017/S0022112098003723.

[57] K. B. Shah and J. H. Ferziger, “A fluid mechanicians view of wind engineering: Large eddy simulation of flow past a cubic obstacle,” *J. Wind Eng. Ind. Aerodyn.*, vol. 67–68, pp. 211–224, Apr. 1997, doi: 10.1016/S0167-6105(97)00074-3.

[58] C.-H. Liu and M. C. Barth, “Large-Eddy Simulation of Flow and Scalar Transport in a

Modeled Street Canyon.," *J. Appl. Meteorol.*, vol. 41, pp. 660–673, Jun. 2002, doi: 10.1175/1520-0450(2002)041<0660:LESOFA>2.0.CO;2.

[59] F. Zeng, J. Huang, C. Meng, F. Zhu, J. Chen, and Y. Li, "Investigation on novel raceway pond with inclined paddle wheels through simulation and microalgae culture experiments," *Bioprocess Biosyst. Eng.*, vol. 39, no. 1, pp. 169–180, Jan. 2016, doi: 10.1007/s00449-015-1501-9.

[60] W. R. Dean, "XVI.Note on the motion of fluid in a curved pipe," *Lond. Edinb. Dublin Philos. Mag. J. Sci.*, vol. 4, no. 20, pp. 208–223, Jul. 1927, doi: 10.1080/14786440708564324.

[61] M. Vaghefi, M. Akbari, and A. R. Fiouz, "An experimental study of mean and turbulent flow in a 180 degree sharp open channel bend: Secondary flow and bed shear stress," *KSCE J. Civ. Eng.*, vol. 20, no. 4, pp. 1582–1593, May 2016, doi: 10.1007/s12205-015-1560-0.

[62] K. Blanckaert, "Hydrodynamic processes in sharp meander bends and their morphological implications," 2011, doi: 10.1029/2010JF001806.

[63] W. Balen, W. Uijttewaal, and K. Blanckaert, "Large-eddy simulation of a curved open-channel flow over topography," *Phys. Fluids 22 7 2010 Doi10106313459152*, vol. 22, Jul. 2010, doi: 10.1063/1.3459152.

[64] S. Ls, S. Aj, and A.-D. Mh, "Mapping of microalgae culturing via radioactive particle tracking," *Chem. Eng. Sci.*, vol. 192, pp. 739–758, 2018.

[65] H.-P. Luo *et al.*, "Analysis of photobioreactors for culturing high-value microalgae and cyanobacteria via an advanced diagnostic technique: CARPT," *Chem. Eng. Sci.*, vol. 58, pp. 2519–2527, Jun. 2003, doi: 10.1016/S0009-2509(03)00098-8.

[66] S. IlHwan *et al.*, "Evaluation of a photobioreactor performance grafting microalgal growth

model and particle tracking technique using CFD.," 2014, doi: 10.13031/TRANS.57.10339.

[67] A. Nikolaou, P. Booth, F. Gordon, J. Yang, O. Matar, and B. Chachuat, "Multi-Physics Modeling of Light-Limited Microalgae Growth in Raceway Ponds," *IFAC-Pap.*, vol. 49, no. 26, pp. 324–329, Jan. 2016, doi: 10.1016/j.ifacol.2016.12.147.

[68] I. Perner-Nochta and C. Posten, "Simulations of light intensity variation in photobioreactors," *J. Biotechnol.*, vol. 131, no. 3, pp. 276–285, Sep. 2007, doi: 10.1016/j.jbiotec.2007.05.024.

[69] Z. Chen, X. Zhang, Z. Jiang, X. Chen, H. He, and X. Zhang, "Light/dark Cycle of Microalgae Cells in Raceway Ponds: Effects of Paddlewheel Rotational Speeds and Baffles Installation," *Bioresour. Technol.*, vol. 219, Jul. 2016, doi: 10.1016/j.biortech.2016.07.108.

[70] Q. H. Zhang, X. Wu, S. Z. Xue, Z. H. Wang, C. H. Yan, and W. Cong, "Hydrodynamic characteristics and microalgae cultivation in a novel flat-plate photobioreactor," *Biotechnol. Prog.*, vol. 29, no. 1, pp. 127–134, Feb. 2013, doi: 10.1002/btpr.1641.

[71] Q. Zhang, S. Xue, C. Yan, X. Wu, S. Wen, and W. Cong, "Installation of flow deflectors and wing baffles to reduce dead zone and enhance flashing light effect in an open raceway pond," *Bioresour. Technol.*, vol. 198, pp. 150–156, Dec. 2015, doi: 10.1016/j.biortech.2015.08.144.

[72] B. Xu, P. Li, and P. Waller, "Study of the flow mixing in a novel ARID raceway for algae production," *Renew. Energy*, vol. 62, pp. 249–257, Feb. 2014, doi: 10.1016/j.renene.2013.06.049.

[73] J. Cheng, Z. Yang, Q. Ye, J. Zhou, and K. Cen, "Enhanced flashing light effect with up-down chute baffles to improve microalgal growth in a raceway pond," *Bioresour. Technol.*,

vol. 190, pp. 29–35, Aug. 2015, doi: 10.1016/j.biortech.2015.04.050.

[74] J. Cheng, W. Guo, Y. Song, S. Kumar, K. Ameer Ali, and J. Zhou, “Enhancing vorticity magnitude of turbulent flow to promote photochemical efficiency and trichome helix pitch of Arthrospira platensis in a raceway pond with conic baffles,” *Bioresour. Technol.*, vol. 269, pp. 1–8, Dec. 2018, doi: 10.1016/j.biortech.2018.08.058.

[75] J. Cheng, W. Guo, C. Cai, Q. Ye, and J. Zhou, “Alternatively permutated conic baffles generate vortex flow field to improve microalgal productivity in a raceway pond,” *Bioresour. Technol.*, vol. 249, Oct. 2017, doi: 10.1016/j.biortech.2017.10.031.

[76] Z. Yang, J. Cheng, Q. Ye, J. Liu, J. Zhou, and K. Cen, “Decrease in light/dark cycle of microalgal cells with computational fluid dynamics simulation to improve microalgal growth in a raceway pond,” *Bioresour. Technol.*, vol. 220, pp. 352–359, Nov. 2016, doi: 10.1016/j.biortech.2016.08.094.

Chapter 2: Mapping swirling motion in a mesoscale raceway pond predicted by three-dimensional computational fluid dynamics simulations using LES and k-ε models.

2.1 Introduction

Biofuels are a promising and renewable substitute for traditional fossil fuels and will help reduce the accumulation of carbon dioxide in the atmosphere [1]. Among different feedstocks for biofuel production, microalgae have been considered as one of the most promising because as a non-cellulosic carbon source, they do not require cultivation in forests or farmlands and have an order of magnitude higher yield of oil compared to traditional oilseeds [2]. Other benefits include a high photon conversion efficiency; in the right location, it can provide a year-round supply of biofuel feedstock; it can utilize nutrients in domestic wastewater, which can be used as a wastewater treatment method [3-4].

Raceway ponds are widely used for outdoor microalgae cultivation, given that they require less capital and operating costs than enclosed photobioreactor systems [1]. Raceway ponds typically consist of a closed-loop channel divided into two long, straight, parallel sections with two 180° hairpin-shaped bends. The liquid medium is driven by one or more paddle wheels [5]. A divider is placed at the center of ponds so that the pond is shaped like a raceway and the liquid is guided circularly, and the sunlight is commonly utilized as the light source. Rather than other cultivation factors such as temperature and nutritional requirements, light intensity appears to be the most important factor in operating a raceway pond [6]. Although light intensity varies continuously from the liquid interface to the bottom of the pond, the cells' exposure can be categorized as a light zone and a dark zone. When cells are in the light zone, the light source can provide adequate intensity for photosynthesis, while in the dark zone, the light intensity cannot reach the compensation point, and photosynthesis will not occur [7]. However, photo-inhibition may occur if cells remain near the surface for too long and light intensity is high enough that biomass growth rate is reduced. The extremes of too much light and insufficient light are mitigated by continuous horizontal and vertical motions of the cells induced by the paddlewheel and secondary flows resulting from the raceway pond geometry. These light/dark fluctuations can enhance the photosynthetic utilization with a light intensity higher than the saturation point, known as the flashing-light effect [8-9]. It has also been reported that an exponential increase in photosynthetic rate is observed with an increased light/dark frequency [10].

Despite the relatively low velocities present in raceway ponds, the flow field is fully turbulent, which is critical for mixing and inducing vertical liquid motion away from the paddle wheel. The turbulence and secondary flows move cells to cycle between light and dark regions, prevent cells from stacking (stratifying), enhance the inorganic carbon utilization through the gas-liquid interface, and homogenize nutrient distribution [11]. Therefore, the effect of turbulence on the system must be well characterized to investigate the effect of the liquid media on the cells' motions and the mixing behavior in the raceway pond. Furthermore, high vertical velocity regions exhibiting significant vertical motion need to be identified to characterize a raceway pond system because those regions contribute to enhancing the light/dark (L/D) frequency. Without those high vertical velocity regions, cells will remain at relatively constant vertical positions, causing photo-inhibition near the surface where light intensity is too strong or low photosynthetic rates near the bottom where light supply is insufficient. Understanding the spatial distribution of these locations will help engineers modify and design new raceway pond systems with higher production rates.

As will be discussed in more detail below, swirling motion, and consequently increased vertical velocity magnitude, is the direct result of the paddle wheel motion and causes a significant vertical redistribution of the cells immediately downstream of the wheel. Additionally, it is found that the liquid inertia coupled with the hairpin bends creates additional zones of high vorticity, and the strength of a vortex determines its persistence length and rate of vertical motion. Accurate characterization of these swirling motions is critical for developing a quantitative understanding of cellular light exposure histories and the strong linkage to growth. Vorticity strength is often used as the criterion to identify swirling motion or vortices. However, using vorticity to determine the vortex region is ambiguous as there is a lack of a threshold value, and it fails to identify a vortex region in some circumstances, as reported by Haller [12]. Other characterization methods that require spiraling path lines are also not objective as the shape of path lines is highly dependent on how the coordinate system is defined, in other words, they are not Galilean-invariant. The Q-criterion is a powerful tool and an objective and unambiguous criterion that can be used to detect vortices and generate high quality and high-resolution profiles to identify vortex regions of different scales and has been widely used in computational fluid dynamics (CFD) applications [13-15]. Q is defined as the second invariant of the velocity gradient tensor, and its mathematical definition will be given in the materials and methods section. A region with vortices is identified when the Q value is positive.

The liquid gains momentum from the rotational motion of the paddlewheel that induces turbulence. Generally, turbulent flows are disordered in time and space, making them challenging to simulate. Other than that, a wide range of spatial wavelengths is involved in turbulent flows [16]. In turbulent flow, eddies can be observed with a broad range of length and time scales, which are responsible for transferring momentum and energy in the fluid. The length scale of large eddies can be similar to the mean flow length scale, which is the hydraulic diameter in this case, and the scale of smallest eddies can be as small as the Kolmogorov length scale η, where η is defined as $(\nu^3/\varepsilon)^{1/4}$, where ε is the average rate of dissipation of turbulence kinetic energy per unit mass, and ν is the kinematic viscosity of the fluid [17]. Without requiring specific turbulence models, direct numerical simulation (DNS) has been used as a tool to simulate turbulent flow by solving the original governing equations, that is, the Navier–Stokes and continuity equations with the whole range of spatial and temporal scales of the turbulence. This method is used to capture all length and time scales of turbulent motion but usually in simple geometries [18]. DNS requires enormous computational resources and is not always practical, even with today's massive high-performance computers. For example, Hosseini et al. carried out a DNS of the flow around a portion of an airfoil with a chord Reynolds number of 400,000; it required around 3.2 billion grid points and 35 million core-hours [19]. Therefore, for the scale of a raceway pond different, more computationally tractable numerical models should be implemented to model turbulence.

One of the most widely used turbulence models is the k-ε model, which has been widely used to predict flow in engineering applications. As one of the Reynolds-averaged Navier-Stokes (RANS) methods, the k-ε model allows the time-averaged or ensemble-averaged solution of the velocity field to be directly obtained [20]. The k-ε model contains two equations, one for the turbulence kinetic energy (k) and the other is for turbulence dissipation rate (ε). The k-ε and other RANS models have been deployed by many researchers to design and modify raceway ponds so that productivity can be maximized, and the operating cost can be reduced. Those design issues included but were not limited to mixing performance, the geometry of the raceway ponds and paddlewheel, and light-dark cyclings [21-29].

However, Zijlema et al. reported that the k-ε model is not capable of accurately predicting the turbulence characteristics of liquids in some U-bends [30]. LES is another mathematical model widely used in CFD to simulate turbulent flow and was first proposed by Smagorinsky [31]. As the larger eddies break up, their energy is transferred to smaller eddies. This process continues until the smallest eddies break up, and the energy is transferred as heat. Unlike the k-ε model, large eddy simulation (LES) resolves large eddies directly by solving the full Navier-Stokes equation for large eddies, and small eddies are filtered using low-pass methods. The implantation of LES consists of three steps: (1) filtering the Navier-Stokes equations to remove small scale eddies, (2) replacing the sub-grid scale (SGS) by spatial and time averaging, and (3) calculating the large-scale field from 'closed' equations [32]. LES reduces the computational cost by filtering the small-scale eddies but directly solving for the large eddies, which should result in better fidelity than the k-ε model.

LES has been recently employed to simulate a raceway pond with inclined paddle wheels and is reported to be more accurate than the k-ε model in the prediction of the turbulence kinetic energy when compared with experimental observations [33]. However, their conclusion was drawn by comparing simulation results with a single frame of particle image velocimetry (PIV) data. As the velocity field inside a raceway pond is highly time-dependent, comparing the results against the PIV data over time would be a more rigorous demonstration of model accuracy. Moreover, the average mesh cell size for the LES model in the study was 0.001 m and for the k-ε model was 0.014 m. The mesh for the LES model was finer than the mesh used for the k-ε model, which might be the reason why LES predicts a more accurate result. It would be more convincing to compare the two models with the same mesh and use a finer resolution than 0.001 m.

Due to the presence of the paddle wheel and the geometry of a raceway pond, it is hypothesized that there will be eddies with different length scales in the fluid. Those eddies might be highly spatially and time dependent as they are transported by the flow field and are the primary source that induces vertical mixing in raceway pond systems that enhances the L/D effect. Therefore, one of the goals of this work is to test the numerical capability to accurately resolve the motion of the eddies by both models. LES is hypothesized to be more suitable for resolving the motion of those eddies as they might be got smoothed out because the k-ε model will time average the velocity components. In the present work, the simulations of a mesoscale raceway pond are carried out using both k-ε and LES turbulence models to explore the reason why the LES model predicts a more accurate velocity field than the k-ε model and the magnitude of the difference between them. The same meshes are used for both models to control for that parameter. The predictions of LES and k-ε are compared and validated as a function of time with the real flow field obtained by a custom-made pygmy flow meter. After the solution was validated and the results by LES model were analyzed, the temporal and spatial behavior of the swirling motion as well as other fluid dynamic characteristics such as the size and spatial distribution of dead zones, velocity field at a cross-section at the center of the liquid depth of the raceway pond, were predicted and determined. A transient particle tracking method is applied to predict the trajectories of microalgae, and the regions where cells will have a higher probability of L/D transitions are identified. This information is applied to get a better quantitative understanding of raceway pond dynamics by categorizing the pond into three regions, with suggestions provided for the locations to embed mixing enhancement devices.

2.2. Material and methods

2.2.1. The geometry of the mesoscale raceway pond

An image, schematics, and dimensions of the mesoscale raceway pond used in this study are shown in Figure. 2.1. The raceway pond was custom manufactured by Ace Composites. It is convenient to divide the raceway pond into four regions when discussing the simulation results and analyses: (1) the straight section where the paddle wheel is installed, (2) the first hairpin bend, (3) the second straight section, and (4) the second hairpin bend, as illustrated in Figure. 2.1a. The straight sections of the raceway pond are 1.98 m long and 0.56 m wide, and the radius of the bend region is 0.56 m. A central divider is located at the center of the raceway pond to guide the fluid so that the liquid is forced to flow circularly. The liquid in the pond is driven by an impeller situated in the middle of the first straight region and consists of four trapezoidal-shaped blades. The wall and the divider are slightly inclined (i.e., not perfectly vertical).

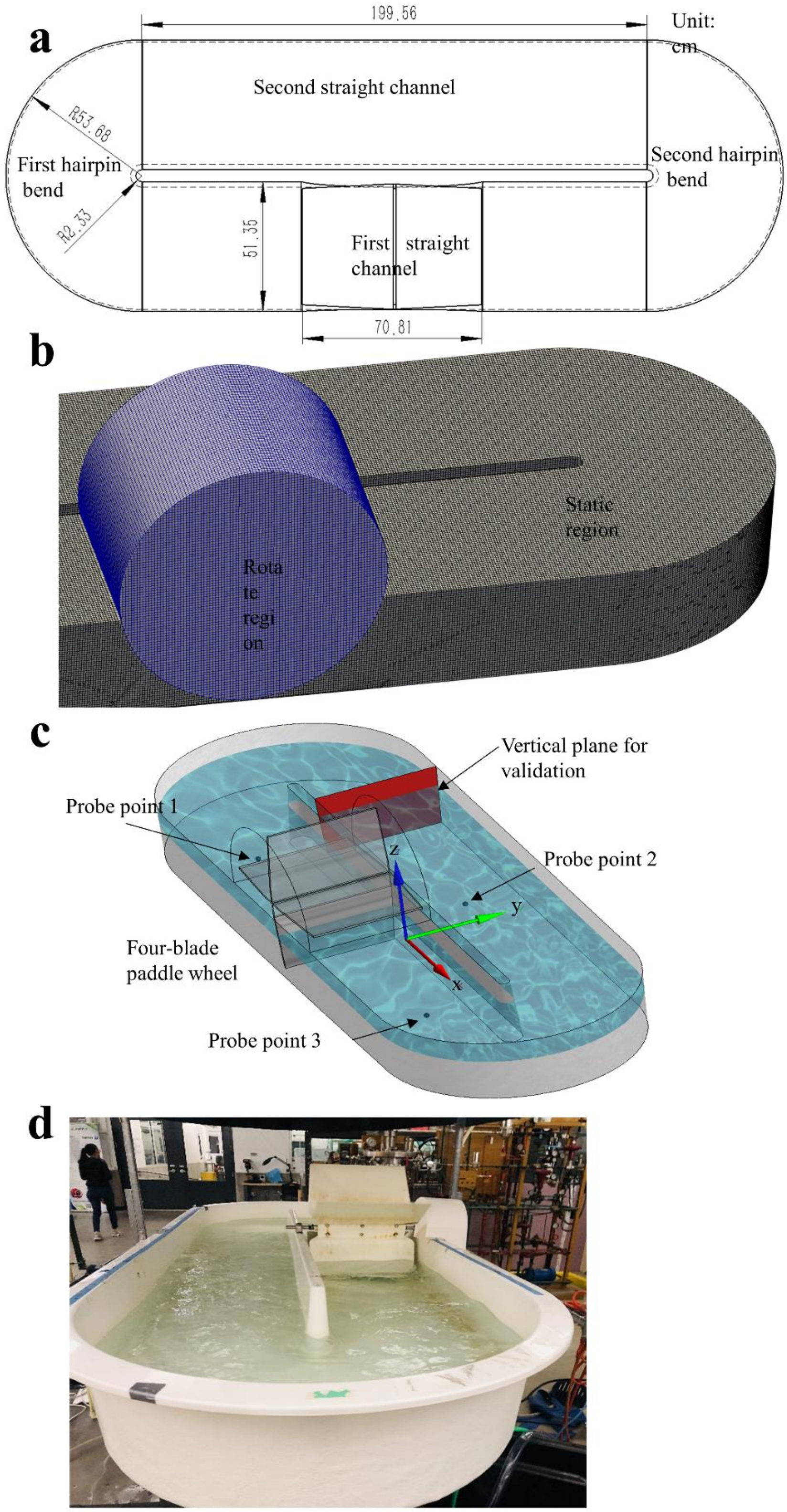

Figure. 2.1 Schematic diagram of the raceway pond. (a) The drawing with main dimensions and

the name applied to each region. (b) Mesh used in the simulations. (c) The simulated raceway pond showing the location of the validation plane and probe points. (d) Image of the mesoscale raceway pond.

More details about the dimension of the modeled raceway pond can be found in Figure. 2.1a, and the exact shape of the divider and the full dimension of the paddle can be found in Figure. 2.2. The coordinate system was chosen so that the x-axis was horizontal and parallel to the straight section and the z-axis was vertical (parallel to the gravity vector). The properties of the working fluid are assumed to be the same as water, incompressible Newtonian fluid with density ρ_l = 998.2 kg/m^3 and viscosity μ_l = 0.001003 kg/m-s. The initial condition of water depth is set to a uniform 0.2 m, which is typical for cyanobacteria cultivation, for example, Mendoza et al. reported that the lowest specific power consumption was achieved when the water depth was set to 20 cm [11, 34-35].

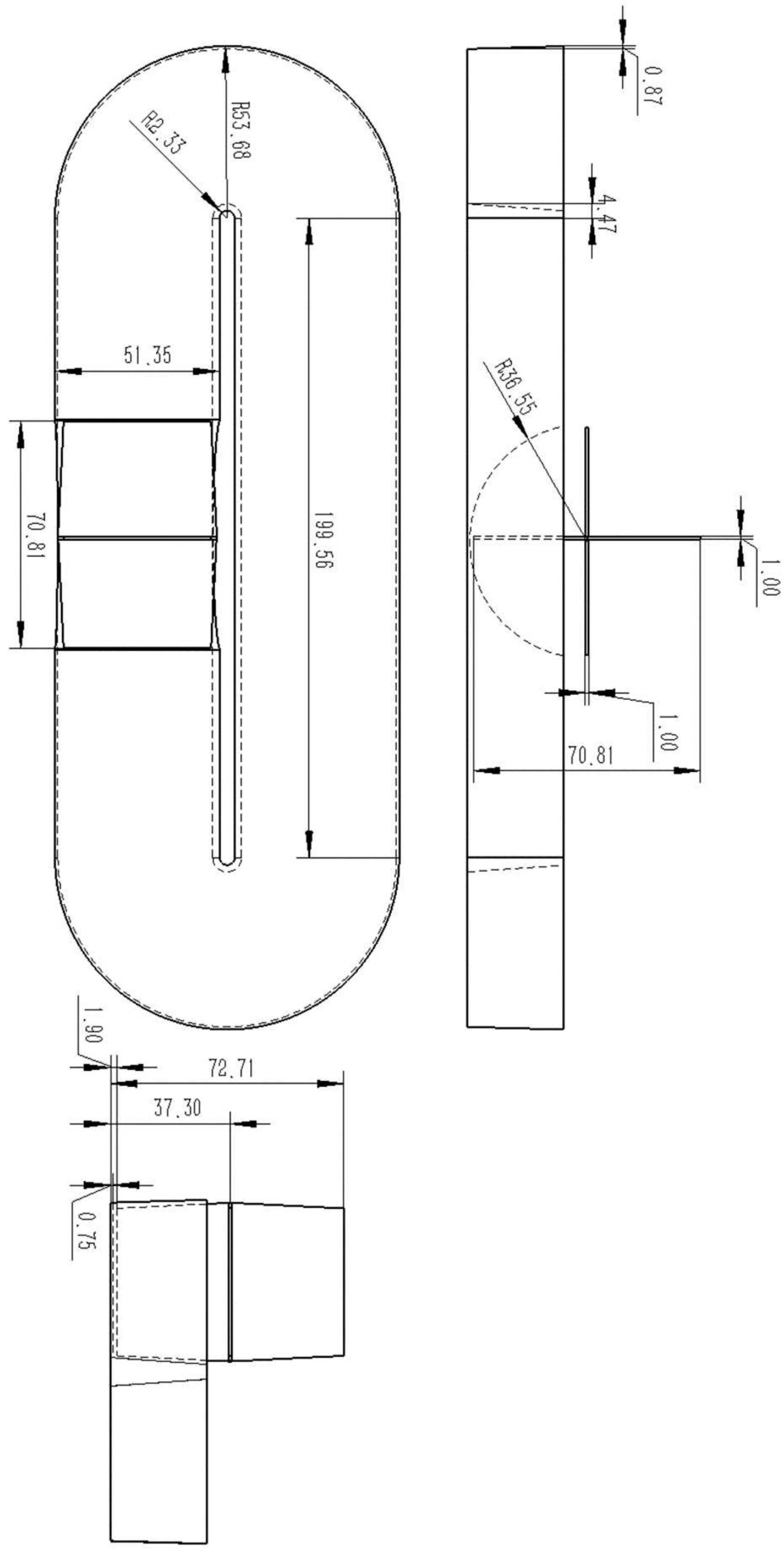

Figure. 2.2. Detailed schematic diagram of the raceway pond. Units (cm)

2.2.2. Numerical tools

2.2.2.1. Solver

The simulation is carried using a commercial CFD package ANSYS Fluent 16.2 on Sun Grid Engine (SGE) in a Linux high-performance computer with 120 Intel® Xeon® E5-2640 processors at 2.5 GHz. Convergence criteria required the absolute scaled residual of the continuity equation to converge to 10^{-4} and other equations to converge to 10^{-7}.

2.2.2.2. Discretization

A three-dimensional mesh of the raceway pond is generated by ANSYS meshing 16.2. To simulate the motion of the paddle wheel and its influence on the liquid, a sliding mesh technique is applied, and the computational domain is divided into a static region and a moving region. These two adjacent regions are linked across a non-conformal interface, which allows mass, momentum, and energy to pass through, even though the nodes at the interface are not coincident. A three-dimensional structured hexahedron mesh is generated for both the moving and static regions with 3,092,371 mesh elements and 0.00174m average cell mesh size, as shown in Figure. 2.1b. It was found in preliminary studies that this type of mesh can make the simulations more stable and faster than using a tetrahedron mesh. For the k-ε model, the standard wall functions are chosen for near-wall treatment. It is recommended by ANSYS Fluent, and there is no attempt to simulate the flow near the wall or in the boundary layer and therefore, the near-wall mesh is not refined further. The details about the discretization of each variable can be found in Table 2.1.

Table. 2.1. Algorithm, discretization scheme used in the simulations.

	LES	k-ε
Solver	SIMPLE	SIMPLE
Gradient	Least Squares Cell Based	Least Squares Cell Based
Pressure	PRESTO!	PRESTO!
Momentum	Bounded Central Differencing	Second Order Upwind
Volume Fraction	Compressive	Compressive
Turbulent Kinetic Energy	N/A	First Order Upwind
Turbulent Dissipation Rate	N/A	First Order Upwind
Transient Formulation	Bounded Second Order Implicit	Bounded Second Order Implicit

2.2.2.3. VOF

To accurately track the gas/liquid interface and solves the velocity field of the liquid phase, the fluid of the pond is modeled as a multiphase flow, and the influence of the cells on liquid motion is believed to be small and neglected. The volume of fluid (VOF) model is used to simulate the multiphase flow and the interaction between the gas and the liquid phases. The velocity field is calculated, and the two-phase interface region is reconstructed with the continuity equation and linear momentum equation.

$$\frac{\partial}{\partial t}\left(\alpha_g \rho_g\right) + \nabla \cdot \left(\alpha_g \rho_g \boldsymbol{u}_g\right) = 0 \tag{2.1}$$

$$\frac{\partial}{\partial t}\left(\alpha_l \rho_l\right) + \nabla \cdot \left(\alpha_l \rho_l \boldsymbol{u}_l\right) = 0 \tag{2.2}$$

where α is the volume fraction, $\boldsymbol{u}$ is the velocity vector, and the subscripts *g* and *l* denote the gas and liquid phases, respectively.

The momentum equation is

$$\frac{\partial}{\partial t}(\alpha_k \rho_k \boldsymbol{u}_k) = -\nabla \cdot \left((\alpha_k \rho_k \boldsymbol{u}_k \boldsymbol{u}_k)\right) - \alpha_k \nabla p - \nabla \cdot (\alpha_k \overline{\boldsymbol{\tau}_k}) + \alpha_k \rho_k \boldsymbol{g} + \boldsymbol{F} \tag{2.3}$$

where p is the pressure, $\overline{\boldsymbol{\tau}}$ is the stress tensor, $\boldsymbol{g}$ is the gravity vector, $\boldsymbol{F}$ is the source term, and subscript k denotes this equation is for the kth phase. Last,

$$\alpha_g + \alpha_l = 1 \tag{2.4}$$

The incompressible Navier-Stokes equation coupled with the VOF model is solved, and the gas-liquid phase interface is reconstructed. In this work, a transient implicit VOF model is applied so that a larger stable time-step size can be used to improve computational efficiency [36]. The implicit VOF model also requires that the volume fraction at the current time step is known in order to iteratively solve the secondary phase volume fraction. The compressive interface capturing scheme is chosen as the interface interpolation method to obtain better resolution of the gas-liquid phase interface position.

2.2.2.4. Turbulence model

Both the standard k-ε model and LES models are investigated as the turbulence model. The terms in the Navier-Stokes equations are decomposed into a time-averaged component and a fluctuating component and substituted back into the original equation. The resulted equations are called the Reynolds Averaged Navier-Stokes (RANS) equations. Since the RANS equations are not closed, several models have been proposed to solve the Reynolds stress components. The k-ε model is one of these, and it is a two-equation turbulence model. One equation is for turbulent kinetic energy k, and the other is for the specific dissipation rate ε.

The equation for kinetic energy k is

$$\frac{\partial}{\partial t}(\rho k) + \nabla \cdot (\rho k \boldsymbol{u}) = \nabla \cdot \left[\left(\mu + \frac{\mu_t}{\sigma_t} \nabla k\right)\right] + G_k - \rho \varepsilon \tag{2.5}$$

and the equation for specific dissipation rate ε is

$$\frac{\partial}{\partial t}(\rho \varepsilon) + \nabla \cdot (\rho \varepsilon \boldsymbol{u}) = \nabla \cdot \left[\left(\mu + \frac{\mu_t}{\sigma_\varepsilon}\right) \nabla \varepsilon\right] + C_{1\varepsilon} \frac{\varepsilon}{k}(G_k + G_{3\varepsilon} G_b) - C_{2\varepsilon} \rho \frac{\varepsilon^2}{k} \tag{2.6}$$

where $C_{1\varepsilon}$=1.44, $C_{2\varepsilon}$=1.92, σ_ε= 1.30, and G_k is the turbulence kinetic energy generation term due to mean velocity gradients.

In LES, the sub-grid scale size is modeled by the sub-grid scale tensor$\bar{\tau}_{ij}$, where $\bar{\tau}_{ij} = \overline{u_i u_j} - \bar{u}_i \bar{u}_j$ is the SGS tensor first proposed by Smagorinsky and $\bar{S}_{ij}$ is the strain rate tensor [31]:

$$\bar{\tau}_{ij} - \frac{1}{3}\bar{\tau}_{kk}\delta_{ij} = -2C\Delta^2 |\bar{S}| \bar{S}_{ij} \tag{2.7}$$

$$S_{ij} = \frac{1}{2}\left(\frac{\partial \overline{u_i}}{\partial x_j} + \frac{\partial \overline{u_j}}{\partial x_i}\right) \tag{2.8}$$

The wall-adapting local eddy-viscosity (WALE) model was first proposed by Nicoud and Ducros and can be written as [37]

$$\mu_t = \rho L_S^2 \frac{S_{ij}^d S_{ij}^{d\,3/2}}{\bar{S}_{ij}^d \bar{S}_{ij}^{d\,5/2} + S_{ij}^d S_{ij}^{d\,5/4}} \tag{2.9}$$

where $L_S = \min\,(\kappa d, C_w V^{1/3})$ (2.10)

$$S_{ij}^d = \frac{1}{2}\left(\bar{g}_{ij}^2 + \bar{g}_{ji}^2\right) - \frac{1}{3}\delta_{ij}\bar{g}_{kk}^2 \tag{2.11}$$

$$\bar{g}_{ji}^2 = \frac{\partial \bar{u}_i}{\partial \bar{x}_j} \tag{2.12}$$

and C_w = 0.325.

2.2.2.5. Particle tracking

The microalgae are modeled as the dispersed phase in the discrete phase model (DPM) in order to obtain their trajectories. A transient particle tracking method is performed where the motion of particles is guided by the flow, and the effect of the particles on the liquid is neglected. Then particles' position at each time step was predicted by solving the equation of motion for each particle:

$$\frac{d\boldsymbol{u}_p}{dt} = F_D\left(\boldsymbol{u} - \boldsymbol{u}_p\right) + \frac{\boldsymbol{g}(\rho_p - \rho)}{\rho_p} + \boldsymbol{F} \tag{2.13}$$

where $\boldsymbol{u}_p$ is the velocity vector for particles, F_D is the drag force coefficient, $\boldsymbol{u}$ is the fluid velocity vector, ρ_p is the particle density, ρ is the fluid density, and $\boldsymbol{F}$ is the acceleration term due to additional forces. The drag force coefficient F_D is defined as

$$F_D = \frac{18\mu}{\rho_p d_p^2}\frac{C_D Re}{24} \tag{2.14}$$

where μ is the molecular viscosity of the fluid, d_p is the particle diameter, and Re is the relative Reynolds number. The shape of microalgae is approximated as spherical and thus a spherical drag law can be applied to calculate C_D:

$$C_D = a_1 + \frac{a_2}{Re} + \frac{a_3}{Re^2} \tag{2.15}$$

where a_1, a_2, and a_3 are given by [38].

A total of 10216 particles with a diameter of 2 μm are uniformly injected at t = 118.14 s when the flow is known to be fully developed and are tracked for more than 1,111 s. It is found when a diameter of 2 μm is used, a small fraction of particles escape into the gas phase due to the way that the particle tracking algorithm is implemented within Fluent. It was necessary to incorporate a user-defined function (UDF) to prevent particles from escaping from the liquid phase. The UDF is executed when a particle is detected to be in the liquid-gas interface, and its diameter increased so that it will settle below the interface by gravity and is then changed back to 2 μm. Once acquired, the trajectories are visualized and analyzed with a Matlab code.

2.2.2.6. Boundary conditions and solution procedure

Simulating the motion of the paddle wheel is critically important for accurately modeling a raceway pond since it provides the driving force for the flow. To quantitatively predict the effect of the paddlewheel, the sliding mesh method has been implemented. To use the sliding mesh technique, the domain of the raceway pond is divided into two subdomains, a static region, and a moving region. For raceway pond systems, the moving region is a rotary cylindrical region that contains the paddle wheel, as shown in Figure. 2.1b. The gap between the tip of the paddle and the bottom of the pond is designed to be small in order to maximize the driving efficiency of the paddlewheel. Therefore, the gap between the tip of the paddle blade and the top of the rotating region is small as well, and this causes the gas phase above the pond to be rapidly moved in the reverse direction due to the strong pressure force created by the motion of the paddlewheel and the small gap when the upper boundary is set as no-slip wall. To overcome this artificial flow behavior, Amini et al. used three subdomains, where there is a second static region surrounding the rotating subdomain [39]. However, this approach reduces the mesh efficiency as it assigns additional mesh cells to the gas phase where the flow field is of minor importance, and the mesh points would be better used in the liquid phase to enhance resolution. At the same time, it has been reported that wind will have an impact on the velocity field and interface shape of the liquid in the pond [23]. To eliminate the wind effect and maximize the mesh efficiency, the top boundary of the static subdomain is set as a pressure outlet so that air can be exchanged, and the side and bottom boundary of the static subdomain are set as no-slip walls. The angular velocity of the paddle wheel is set to be 1.428 rad/s, or 13.64 RPM, as this was the mid-level RPM for the paddle wheel as provided by the manufacturer. With this RPM setting, the tip velocity of the paddle wheel was 0.492 m/s. Once the proper boundary conditions are chosen, 40 iterations per time step are used along with the time-dependent time step size procedure discussed below to obtain a converged solution. The total number of mesh cells is chosen as 3,092,371 as it provides a good trade-off between the resolution and the computational expense. The simulation took about 80 hours to simulate 160 s of flow time, and Fluent reported that the clock time per time step was 22 s.

The velocity fields of both gas and liquid phases in the pond are initialized to zero at t = 0 s. Due to the fact that the liquid is static at the beginning and the driving force is applied abruptly, the velocity field will have a larger change at the first several seconds where the simulation is intrinsically unstable, a much smaller time step size was used to enhance the stability and accuracy. A UDF is used to gradually increase the time step size. Although it should be pointed out the appropriate time step size changes with the mesh size and quality, a small time step size should be used for a fine mesh or low-quality mesh. The temporary time step size is given in Table 2.2 for the present simulation. When the final time step size is achieved, the simulation is carried out for another 100 s to let the flow field fully develop.

Table 2.2. Time variant time-step size used in the simulations to enhance the stability.

Time (seconds)	Time step size (seconds)
0-0.03	0.0005
0.03-0.5	0.001
0.5-3	0.005
3-10	0.01
10-20	0.02
>20	0.03

2.2.2.7. Q criterion

The gradient of velocity field can be written as:

$$\bar{A} = \begin{bmatrix} A_{11} & A_{12} & A_{13} \\ A_{21} & A_{22} & A_{23} \\ A_{31} & A_{32} & A_{33} \end{bmatrix} = \begin{bmatrix} \frac{\partial u_x}{\partial x} & \frac{\partial u_x}{\partial y} & \frac{\partial u_x}{\partial z} \\ \frac{\partial u_y}{\partial x} & \frac{\partial u_y}{\partial y} & \frac{\partial u_y}{\partial z} \\ \frac{\partial u_z}{\partial x} & \frac{\partial u_z}{\partial y} & \frac{\partial u_z}{\partial z} \end{bmatrix} \tag{2.16}$$

The eigenvalues of tensor A will satisfy:

$$\boldsymbol{\lambda}^3 + P\boldsymbol{\lambda}^2 + Q\boldsymbol{\lambda} + R = 0 \tag{2.17}$$

where:

$$Q = \frac{1}{2}[P^2 - tr(\overline{AA})] = (A_{22}A_{33} - A_{23}A_{32}) + (A_{11}A_{22} - A_{12}A_{21}) + (A_{33}A_{11} - A_{13}A_{31}) \tag{2.18}$$

2.2.2.8 Flow field validation

The simulation results are validated by comparing the experimental data, collected within the cross-section shown in Figure. 2.1c, against the CFD predictions. A custom-made pygmy flow meter is used to measure the average magnitude of the x-component of velocity. The flow meter consists of a magnetic encoder that transforms the rotational motion to pulse signals. A custom C++ code is implemented for the microprocessing chip (NODEMCU ESP-32S) to calculate the time period of high voltage to high voltage signals produced from the hall-effect sensor and then converted to the RPM of the pygmy flow meter. The flow meter was calibrated using FlowExplorer laser doppler anemometry (LDA) manufactured by DENMARK in the Armfield model S6MkII glass-sided tilting flume so that the velocity for a given RPM can be determined, as shown in Figure. 2.3a.

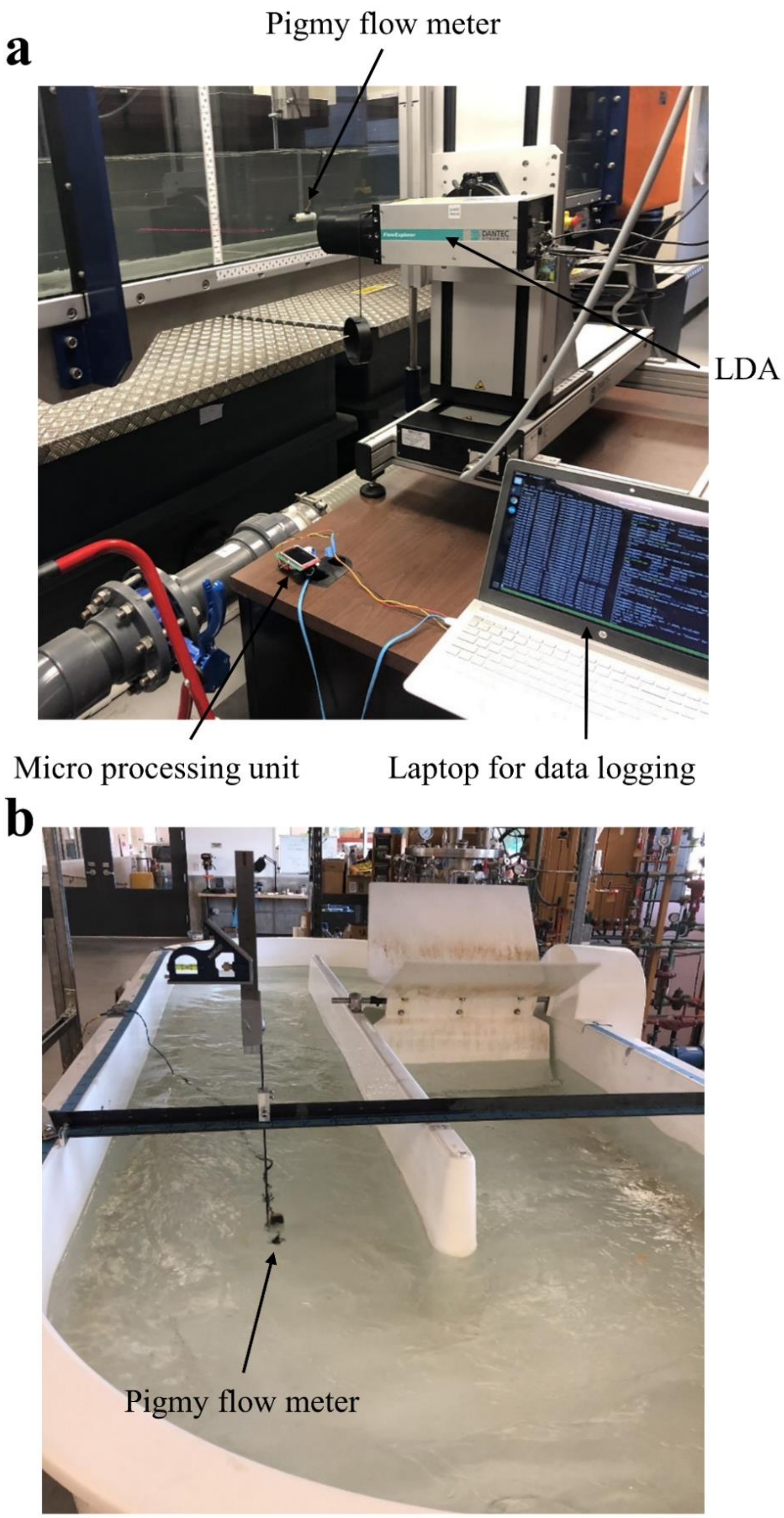

Figure. 2.3. Setup of the validation experiments. (a) Experimental setup for flow meter calibration. (b) Experimental setup for flow validation.

An 11 point by 10 point probe grid located in the plane shown in Figure. 2.1c is selected to take measurements during an averaged period of 137 s with an interval of 0.15 s when the averaged velocity is found to be converged, and the fluctuation is excluded. The horizontal component of the velocity along with the fluid direction is extracted from the simulation for 110 seconds.

2.3. Numerical Results and Discussion

2.3.1. Flow field validation

Qualitative comparisons between the CFD predictions and the experimental measurements are shown in Figure. 2.4, where the vertical cross-section used for validation is defined previously (Figure. 2.1 c). The contour plots are generated using pointwise interpolation within a Matlab framework. Because of the geometry of the hairpin bends, inertia pushes the liquid to the outer region downstream of the bend. Both CFD models and experimental data demonstrate that there is a high-velocity region near the bottom, outer region of the selected cross-section where the velocity magnitude reaches as high as 0.62 m/s. Furthermore, it can be seen that there is a low-velocity region in the inner part of the straight section, which is referred to as a dead zone. Comparison of the three contour plots indicates that the time-averaged velocity data using the LES and k-ε models are in agreement with the experimental measurements of the velocity field and high speed-low speed boundary, i.e., the general structure of the dead zone, suggesting that the time-averaged hydrodynamic characteristic and the mean velocity field of the flow are well captured by CFD simulations using both models.

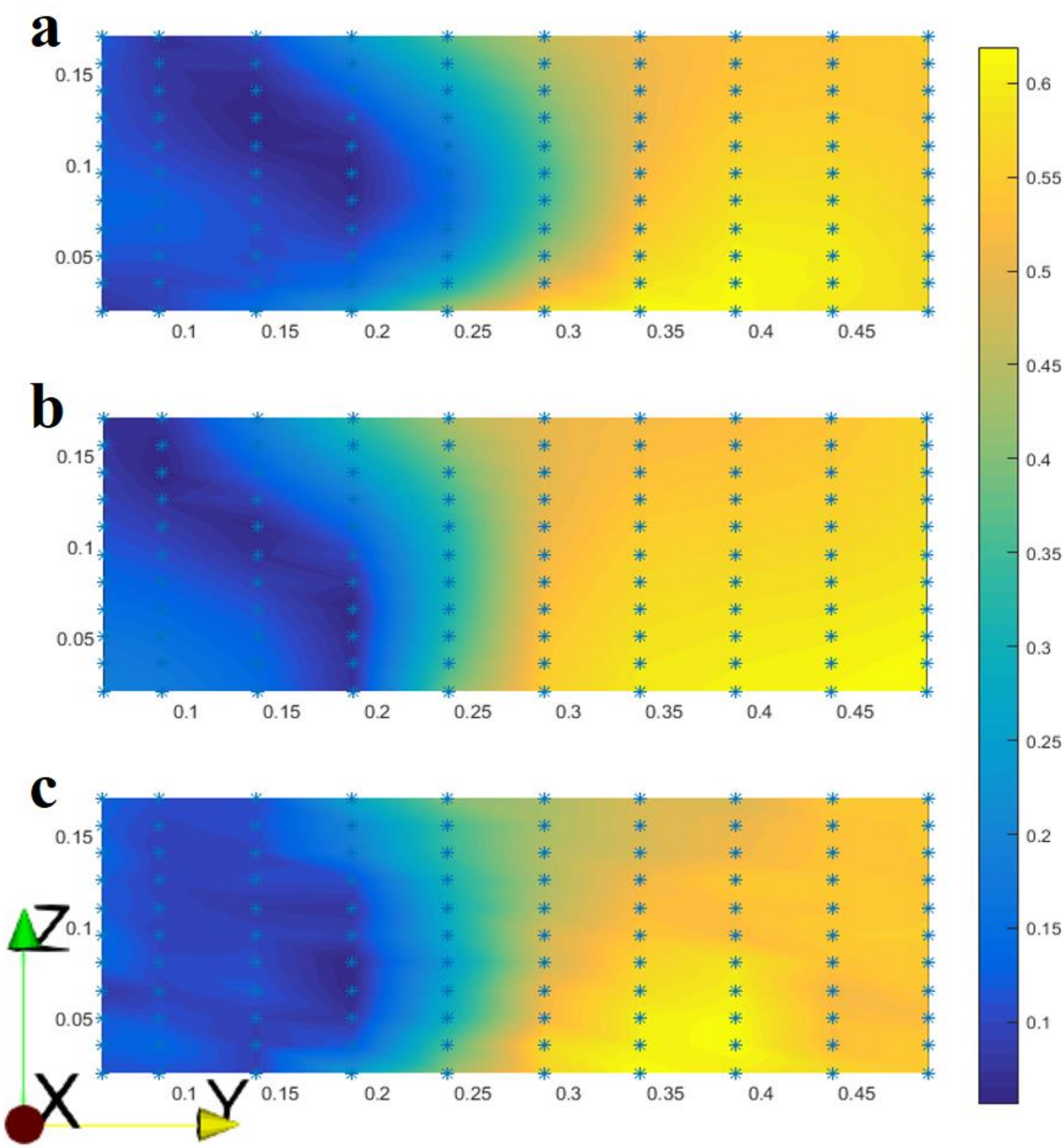

Figure. 2.4. Comparison of the time averaged x-component of the velocity in the vertical cross section shown in Figure. 2.1c. (a) prediction by the LES model. (b) prediction by the k-ε model. (c) experimental measurements.

2.3.2. Time to reach fully developed flow

To obtain a realistic hydrodynamic characterization of the tested raceway pond system under standard operating conditions and determine how long it took for flow to fully develop, three numerical probe points were utilized, with their locations shown in Figure. 2.1c, and the velocity data were recorded during the first 140 s of the simulations.

In the simulation, the system is quiescent at time t = 0 s and gradually speeds up over time as the paddle wheel is put in motion. Taking into account the turbulent fluctuations in the velocity field, particularly for the LES model predictions, an averaged velocity magnitude of a 10 s interval is used to determine the time required for the flow to be fully developed. From Figure. 2.5, it might be observed that the velocity magnitudes for all three points reached their long-time averaged magnitude within approximately 40 s for both the k-ε and LES models. The results of the LES model exhibit a considerably stronger oscillation where the amplitude reaches around 0.4 m/s (Figure. 2.5b) while the velocity magnitude at the probe points only oscillates at an amplitude of 0.03 m/s for the k-ε model. The reason why the LES model predicts a flow field for which the velocity magnitude had a strong oscillation is that it resolves the swirling motions and their propagation, which will be discussed in more detail. On the other hand, it is not surprising that k-ε does not predict a flow field with this strong oscillation behavior because of the fact that k-ε model time averages the velocity component to simulate turbulent stress. Although the velocity field predictions using LES yield strong oscillations, the 10 s averaged velocity magnitude still converges at around 40 s.

As a result of the start-up study, the flow could be treated as fully developed after 40 s for both turbulence models, and that time was used to study the flow characteristics of the raceway pond at the current paddle rotation rate (13.64 RPM). However, 100 s is chosen to ensure that the flow field is fully developed when being analyzed.

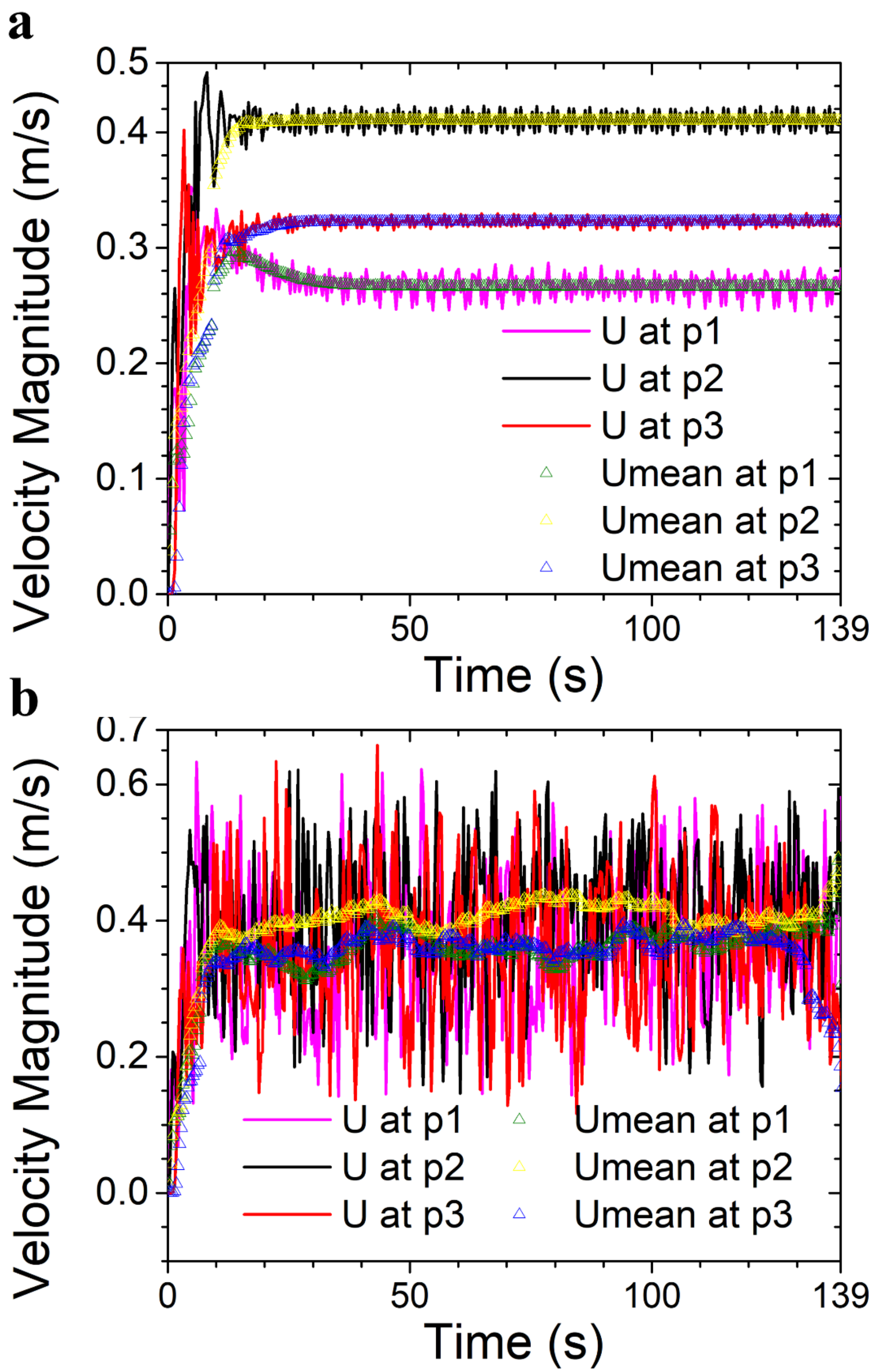

Figure. 2.5. mag(***u***) and averaged mag(***u***) at probe points to determine the mixing time for (a) k-ε model, and (b) LES model

2.3.3. Flow characteristics of the mesoscale raceway pond

To provide an accurate evaluation of flow pattern variation between the two models, velocity contours of the simulated flow using the two turbulence models are shown in Figure. 2.6 at a horizontal plane measured 0.1 m from the bottom of the pond at t = 100 s, where 0.1 m is chosen since it is half of the water depth.

Because of the geometry of the bends and centripetal force effect, the liquid is forced to the outer region of the straight section downstream of the bends, forming two high velocity regions. Both LES and k-ε models resolve these phenomena well, as high-velocity regions can be observed at the outer side of the straight section and dead zones (low-velocity regions where the velocity magnitude is less than 0.1 m/s) can be found after the divider and at the entrance of the bend (Figures. 2.6c and 2.6d). The threshold value 0.1 m/s was chosen as a lower value suggested by Weissman et al. will cause settling of microalgae cells, and it represents a microalgae cell transit time of 2 seconds from top to bottom in a raceway pond with 20 cm of water depth [11]. Although the velocity magnitude contours predicted by the LES and k-ε model show similar patterns, the velocity magnitude contours predicted by the LES model show that the instantaneous high velocity regions do not have a smooth boundary as suggested by the k-ε model. On the contrary, the LES model predicts that there is high velocity motion in the dead zone regions predicted by the k-ε model.

Figures. 2.6a and 2.6b display the vertical velocity magnitude contour at the 10 cm depth cross section. As expected, we observe a high vertical velocity region near the paddlewheel, but also near 90-180° of the first bend (Figure. 2.6a). The simulations also resolve the propagation of the vortices along the straight section, where their strength dissipates due to viscous effects. Given that the k-ε model time-averages the velocity field, the details of the vortex structures, as well as the vertical motion of the eddies, are not predicted with great accuracy and high resolution (Figures. 2.6b and 6d). This difference between the two predictions can be seen because the contours predicted by the LES model show a much more abundant detail in resolving the boundary of the high vertical velocity regions while the k-ε model predicts a smoother pattern. Moreover, the k-ε model under predicts the strength of the vertical motions as it predicts a maximum vertical velocity magnitude of approximately 0.24 m/s near the first bend, while it reaches up to 0.38 m/s as predicted by the LES model. Furthermore, most of the high vertical velocity regions predicted by the LES model could not be found in the contours predicted by the k-ε model, which could be explained by the swirling motion. This swirling motion, which will be discussed in the next section, was generated when fluid flows around a hairpin bend and is resolved by the LES model. Therefore, the high vertical velocity regions shown in Figure. 2.6a were contributed by swirling motions that propagate along with the channel over time. Because of this propagation of the swirling motion, a location that exhibits upward motion at a given time point could have downward motion at another time point. As the k-ε model time-averaged the velocity field, such vertical motions can cancel, with the result that the k-ε model under predicts the strength of the vertical motion.

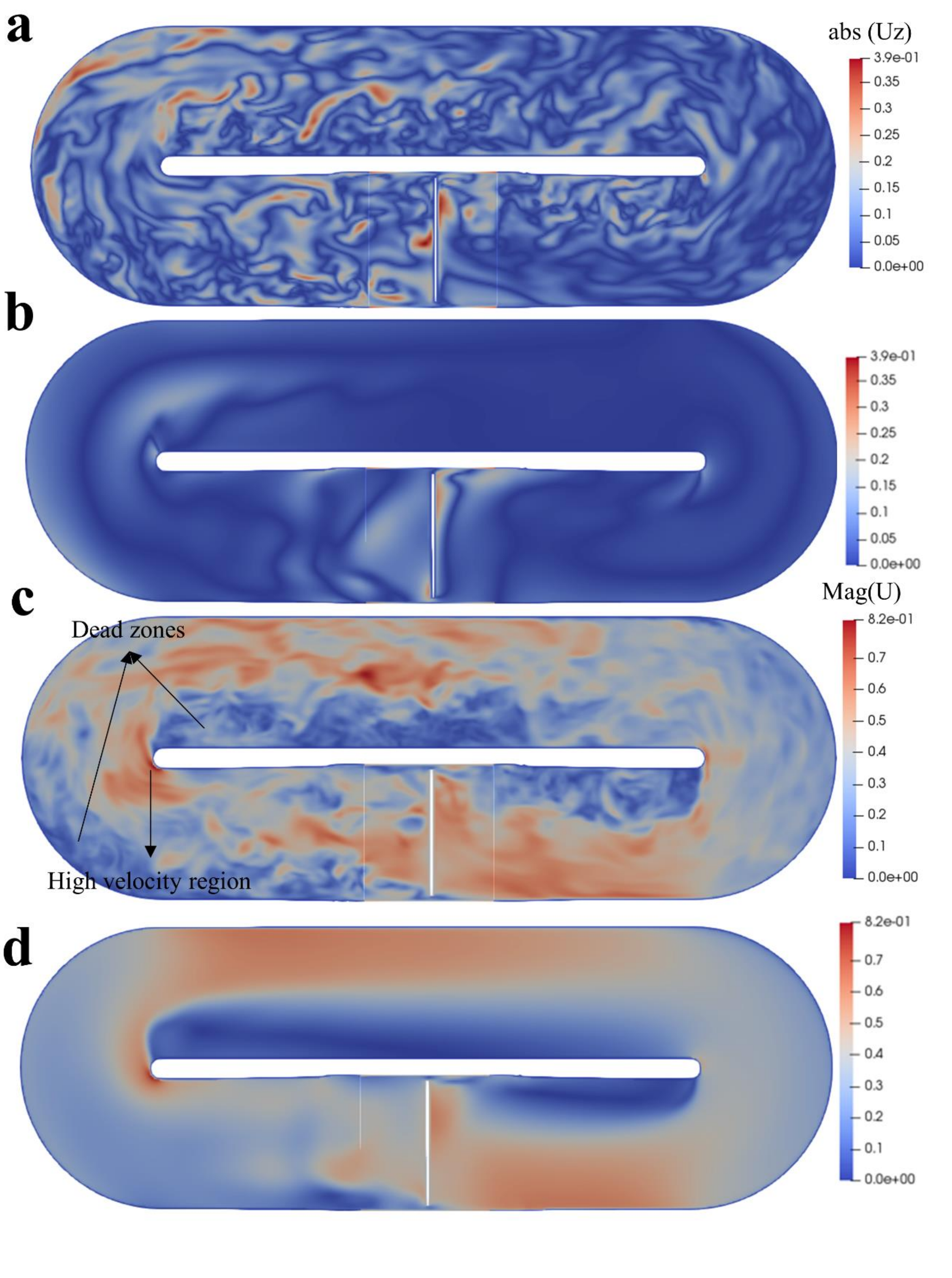

Figure. 2.6. Velocity contours at flow time = 100 s. (a) abs(u_z) at time = 100 s predicted by LES model. (b) abs(u_z) at time = 100 s predicted by the k-ε model. (c) mag($\boldsymbol{u}$) at time = 100 s predicted by LES model. (d) mag($\boldsymbol{u}$) at time = 100 s predicted by the k-ε model.

The swirling motion is a three-dimensional phenomenon, and it is beneficial to visualize it in a three-dimensional format. For this purpose, the Q-criterion iso-surface plots for Q = 20 predicted by the k-ε and LES models, color-coded by the absolute value of the vertical velocity component, are shown in Figures. 2.7a and 2.7b. Moreover, an iso-surface for the absolute value of the vertical velocity component equal to 0.1 m/s is shown in Figure. 2.7c. The Q-criterion quantifies the second invariant of the velocity gradient and is a powerful tool used to identify the presence of rotational motion. One major finding comes from comparing Figures 2.7b and 2.6c: the iso-surface plots for abs(u_z) and the Q-criterion display very similar patterns in general, and the region where the flow has high vertical velocity also has a high rotational motion. It may be concluded that the vertical motions, as well as the vertical mixing, are mainly induced by the swirling motions in the raceway pond.

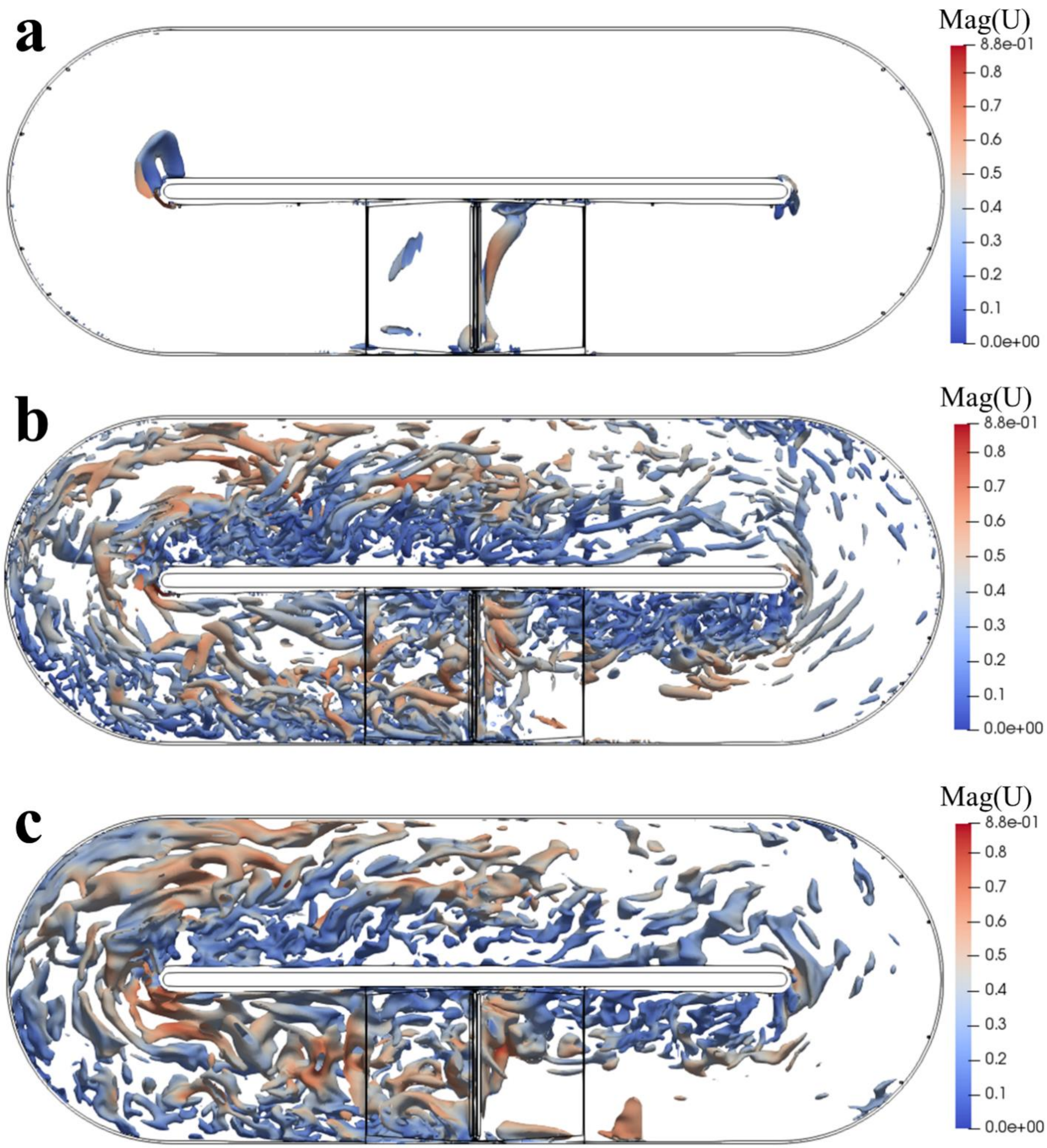

Figure. 2.7. Iso-surfaces at flow time = 100 s. (a) Iso-surface Q-criterion = 20, k-ε model. (b) Iso-surface Q-criterion = 20, LES model. (c) Iso-surface abs(u_z) = 0.1, LES model.

Swirling motions predicted by the LES model are strong downstream of the paddle wheel, in the first bend, as well as various small, disconnected regions in the dead zones after the divider. It is believed that a considerable amount of swirling motion is generated when fluid passes around the bends. This conclusion is more obvious when examining the Q-criterion contour downstream of the second bend, as illustrated by Figure. 2.7b. The swirling motion is weak at the center of the second bend due to the dissipation of the kinetic energy and begins to show up again downstream of the divider. These findings suggest that the geometry of the hairpin bends can intensively induce the swirling motion downstream the bends, which can significantly contribute to the vertical mixing performance of the pond. Secondary flow due to centripetal forces could be the potential mechanism to induce swirling motions when fluid flows across a hairpin bend. It can also be found that the axis of the swirling motion is horizontal and perpendicular to the main flow near the paddle wheel region. While the swirling motion is transported downstream, their axes are rotated to be in the same direction as the main flow. Furthermore, the dead zone is not a continuous region as suggested by the k-ε model in Figure. 2.6d; in contrast, it is a region containing both low-velocity elements and portions with swirling motion and recirculation.

On the other hand, from the comparison of the velocity magnitude contours as well as the Q-criterion iso-surface between the LES and k-ε models, it may be deduced that k-ε provides a relatively worse prediction in which limited swirling regions can only be found near the paddlewheel and at the tip of the divider. Given that understanding that the vertical motions are one of the main reasons for a detailed computational investigation of a raceway pond, the k-ε model would not be a suitable turbulence model to investigate the vertical mixing in raceway pond systems.

2.3.4. Time-varying hydrodynamic characteristics

As it has been demonstrated that the k-ε model under predicts swirling and vertical motion and fails to resolve the swirling motions in a raceway pond, attention is now focused on analyzing the results predicted using the LES model. By visualizing the LES results over a 72 s period, it is found that the swirling motion is transported by the primary flow as well. Therefore, it is important to investigate the time-varying hydrodynamic characteristics of the raceway pond rather than examining the flow field at specific time points. The CFD outputs such as velocity, pressure, and volume fraction α of the flow are extracted from 100 s to 172 s at an interval of 0.15 s to analyze the system behavior over a reasonably long period of time under fully developed conditions. The instantaneous volume fraction of the liquid that has high vertical velocity, i.e., abs(u_z) > 0.1 m/s, and low motion (dead zones) as a function of time are plotted in Figure. 2.8. It is observed that during the operation of the raceway pond, only a small fraction of the liquid has a high vertical velocity at any given time, with an average volume fraction of 15% with the highest 17.6% and the lowest 11% of all the liquid phase experience high vertical mixing motion. On the other hand, the volume percentage of the dead zone averages around 14% and ranges from 13% to 15.5%. The results reveal that the raceway pond investigated is a highly dynamic system. As the swirling motion is generated by the paddle wheel and the geometry of the hairpin bend, transported by the primary flow, and dissipated due to viscous effects, the volume of high vertical velocity regions was changing at a degree of 6.6% of the total liquid volume. Similar to the swirling motion, the volume of the dead zone changes with time as well, but to a significantly lower degree, with only about 2.5% from the maximum to minimum. One explanation for the low range of the volume of the dead zone was that the fluid flows slowly in the dead zones, and therefore, the fluid's kinetic energy is low in those regions. As a result, there is not much driving force for the volume of the dead zones to change significantly.

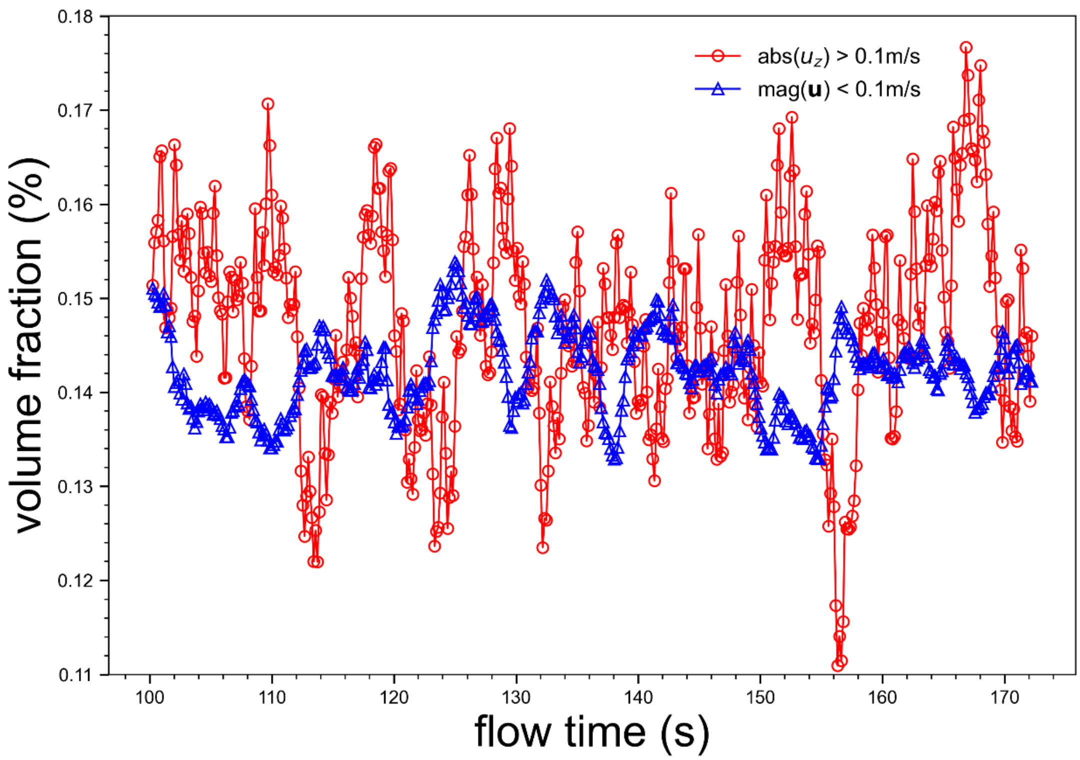

Figure. 2.8. Volume percentage of dead zones and high vertical velocity regions.

After it has been demonstrated the temporal behavior of how the swirling motions are generated and propagated by the motion of the fluid, it would be interesting to investigate the spatial distribution of the swirling motion as well as the dead zones. Figure. 2.9 shows the regions for which the vertical velocity magnitude was larger than 0.1 m/s (Figure. 2.9a) as well as the corresponding dead zones (Figure. 2.9b), for more than 20% over the 72 s period. Comparing Figure. 2.9a with Figure. 2.7b, it may be seen that over an extended sampling time, the regions with high vertical velocity shown in Figure. 2.9a are much larger in volume than at a single instant of time. The region of high vertical mixing occupied about 29.1% of the total liquid volume that including almost all the liquid in the first hairpin bend and the first half of the second straight section. The reason behind this phenomenon is that the fluid gains turbulent kinetic energy and the swirling motion remains strong after the first hairpin bend with the current geometry and operating conditions. The fluid develops a wake effect when it passes the divider, where high recirculation motion and swirling motion exists. The swirling motions, as well as the vortices, are then transported by the fluid flow and propagate and eventually dissipate. Their locations vary dynamically with time but almost all the volume near the first hairpin bend has a probability of stronger vertical motion at any given time. As a result, almost all the liquid volume near the first hairpin bend has a vertical velocity magnitude greater than 0.1 m/s for more than 20% of the time. The high vertical velocity regions disappear along the second straight section and appear again downstream the divider (Figure. 2.9a), indicating that vortices are generated due to flow separation downstream the divider.

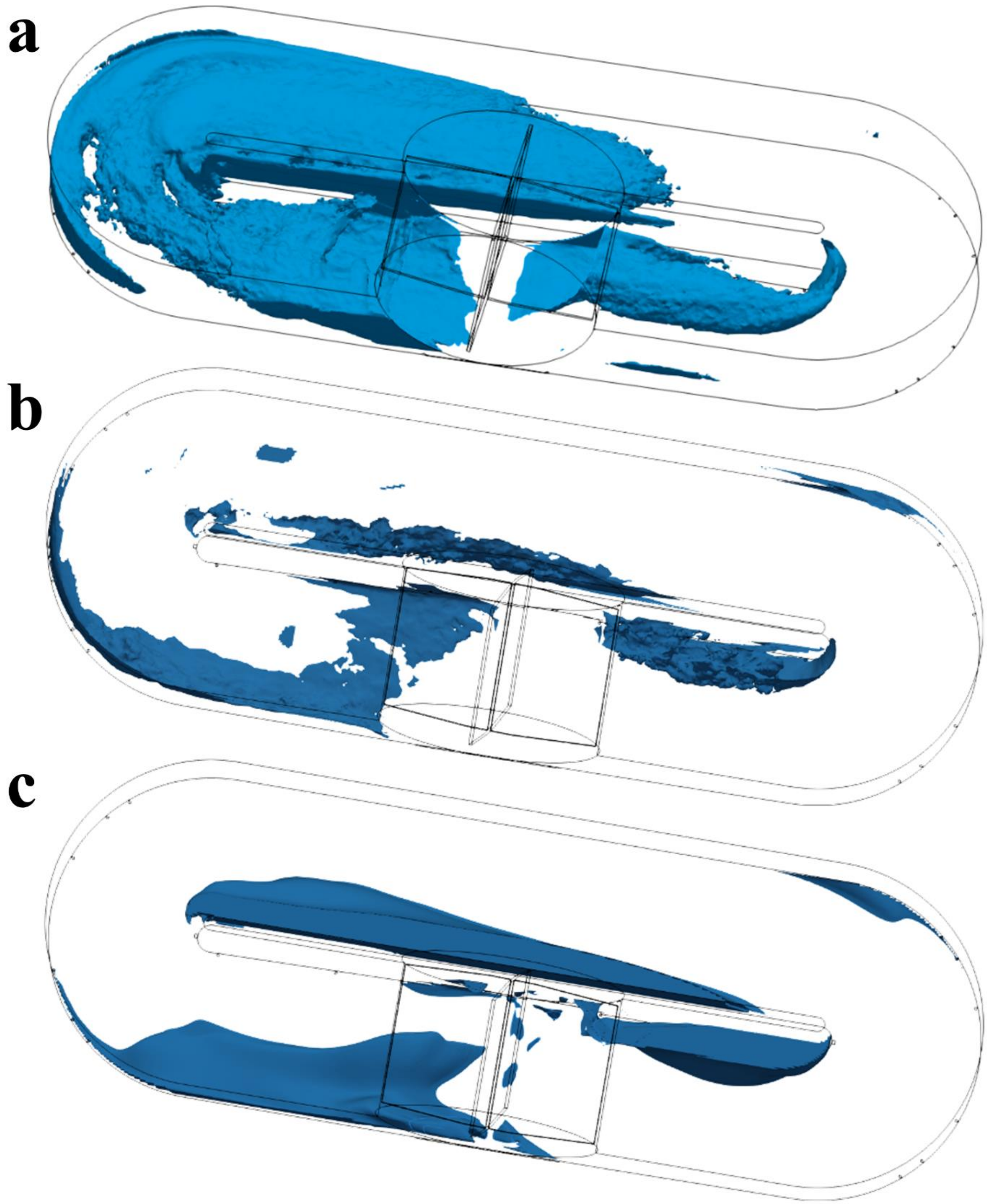

Figure. 2.9. Regions in raceway ponds where (a) abs(u_z) > 0.1 m/s for more than 20% of flow time. (b) mag($\boldsymbol{u}$) < 0.1 m/s for more than 20% of flow time predicted by LES model. (c) mag($\boldsymbol{u}$) < 0.1 m/s predicted by the k-ε model.

Dead zones are believed to have negative effects on the production rate because harmful chemicals might accumulate in those regions due to poor mixing. The velocity magnitude is low there for most of the time, and strong recirculation motion exists so that the harmful chemicals and algae are accumulated. Figure. 2.9b represents the regions where the predicted velocity magnitude is smaller than 0.1 m/s for more than 20% of the sampling time. Unlike the k-ε model, the LES model predicts that the velocity magnitude of all the liquid volume is larger than 0.1 m/s at some time point during the examined 72 seconds. The 20% was chosen because, at this percentage, the dead zones LES model predicted would have similar spatial distribution as the dead zones predicted by the k-ε model (Figure. 2.9c). It may be seen that those low-velocity regions are located near the entrance of the first bend, the inner region of the second straight section, and downstream of the divider at the second bend. The reason why there is a low velocity region downstream of the paddle wheel is because as the fluid is driven by the paddle wheel it encounters the wall of the first 180° bend. While the fluid is forced to change its direction, it forms a negative pressure gradient at the bottom near the first bend which slows the fluid and creates a low velocity region. This phenomenon is weaker near the second bend. On the other hand, the low-velocity region for more than 50% of the sampling time predicted by the k-ε model has a wider and larger volume (Figure. 2.9c). Since the k-ε model under predicts the strength of the vertical motion, it is not surprising that it over predicts the volume of the dead zone. As shown in Figure. 2.9b and Figure. 2.7b, there is considerably strong swirling motion in the wake zone downstream of the divider tip, which should improve the mass transfer and dissipation of harmful chemicals. Therefore, it appears that the recirculation motion should be responsible for the insufficient mass transfer since there is a certain time that some high-velocity motion can be found downstream of the divider, where is usually predicted as a dead zone. Comparing Figure.

2.9a with 2.9b, we could find that the dead zones in the wake zones are mostly distributed near the bottom, and the region near the surface had a high potential to have strong vertical motions (Figure. 2.9a).

2.3.5. Particle tracking

Since accurate flow fields are essential to acquire realistic cell trajectories and as the k-ε model is shown to under predict the vertical motion because of its tendency to smooth out velocity fields, the LES model is used as the turbulence model to solve the velocity fields used by the DPM model.

In order to provide a clear and concise visualization of cell trajectories, only 200 of the 10,216 particles are represented in Figure. 2.10 with the views from different angles (Figures. 2.10a, 2.10c, 2.10d, 2.10e). From these figures, the mixing characteristics can be determined by visualizing the particles' trajectories. From Figure. 2.10c, different characteristics of particles trajectories can be seen upstream and downstream the paddle where particles have smooth trajectories upstream the paddle wheel. Once the particles enter the paddle wheel region, their trajectories immediately become chaotic, suggesting that the paddle wheel produces an intense turbulent flow that has a positive impact on vertical mixing. Figure. 2.10a illustrates the trajectories of the second straight section in a horizontal view. Compared with Figure. 2.10c, a significant difference can be observed in that the trajectories of Figure. 2.10a are significantly smoother than the left part of Figure. 2.10c where fluid gains kinetic energy downstream of the paddle wheel. This difference indicates that the microalgae may not experience many L/D transitions in the second straight section compared with the first straight section where the paddle is located. Furthermore, the particles' trajectories become smoother downstream of the second straight section, which could be the consequence of the dissipation of the kinetic energy. However, the trajectories become chaotic again once the particles enter the second hairpin bend region, which suggests that the vertical mixing is enhanced by the hairpin bend geometry. Figures. 2.10d and 2.10e represent the trajectories at the first hairpin bend and the second hairpin bend. Comparing Figure. 2.10d with Figure. 2.10e, it can be observed that the trajectories of Figure. 2.10d are more likely to have vertical position changes than particles in a straight section, suggesting that the special shape of the hairpin bend can increase the vertical motion of microalgae. Furthermore, Figure. 2.10e represents the trajectories of particles in the second hairpin bend. It is found that compared with the first hairpin bend (which is shown in Figure. 2.10d), the probability for a particle to change its vertical position significantly is smaller, suggesting that the vertical kinetic energy of the fluid is smaller due to viscous dissipation and the long past effect of the paddle wheel. However, the probability for vertical motion is still larger than in the straight sections.

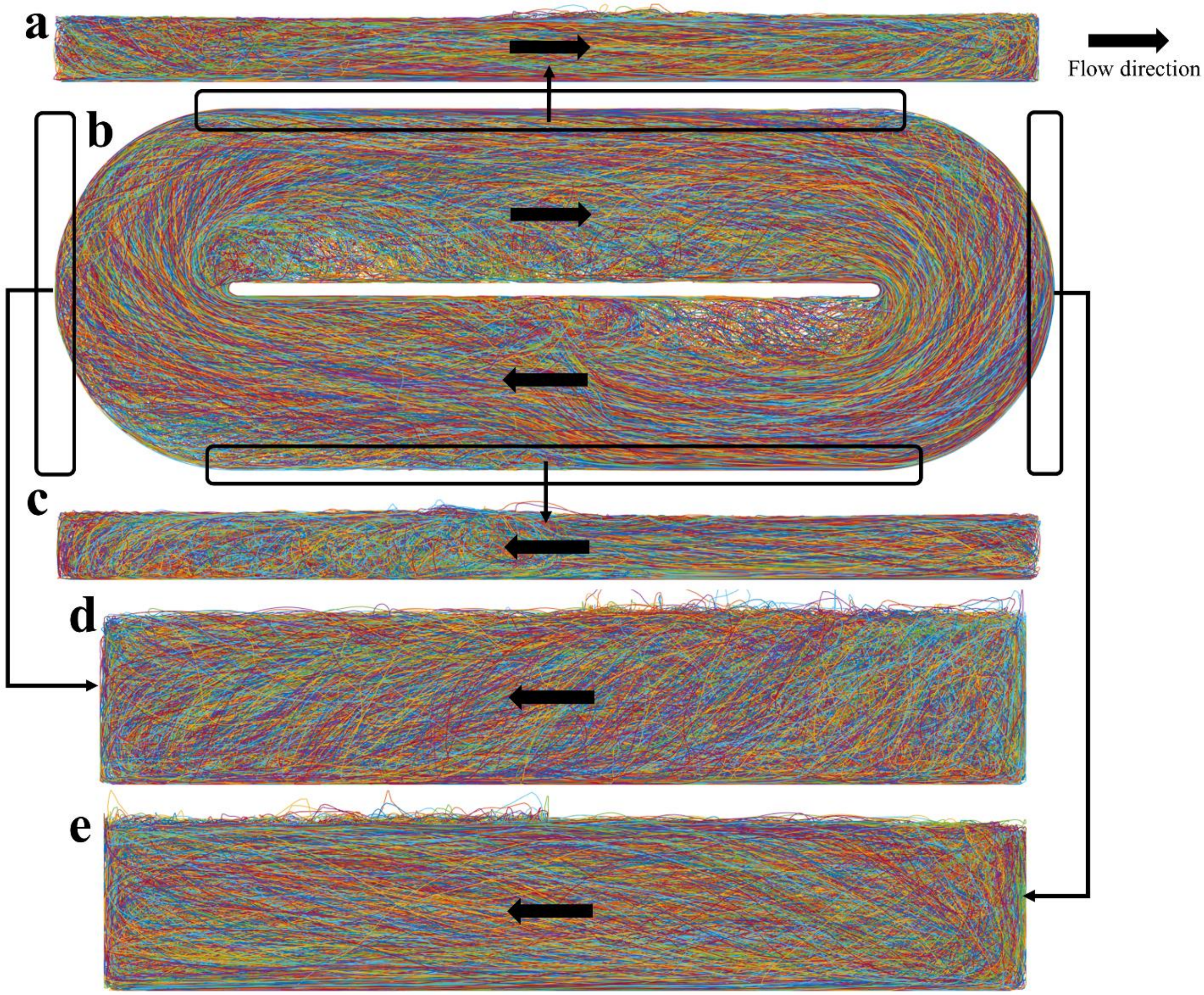

Figure. 2.10. Trajectories of 200 sample particles over 1111s. (a) Horizontal view of the second straight section. (b) Top view of the pond. (c) Horizontal view of the first straight section. (d) Horizontal view of the first hairpin bend. (e) Horizontal view of the second hairpin bend.

In order to study the light history of the particles, the depth history of all tracked particles are recorded, and the light intensity each particle experiences through the tracked time is calculated using the Beer-Lambert law:

$$I = \frac{I_{max}}{e^{AD}} \tag{2.19}$$

where I_{max} is the light intensity at the interface which is set to 2000 μmol photons m^{-2} s^{-1}, and A is the absorption coefficient which is set to 40 m^{-1} to reflect a dense cell culture. To illustrate this process, the depth, and the calculated light intensity history of one particle are plotted in Figure. 2.11.

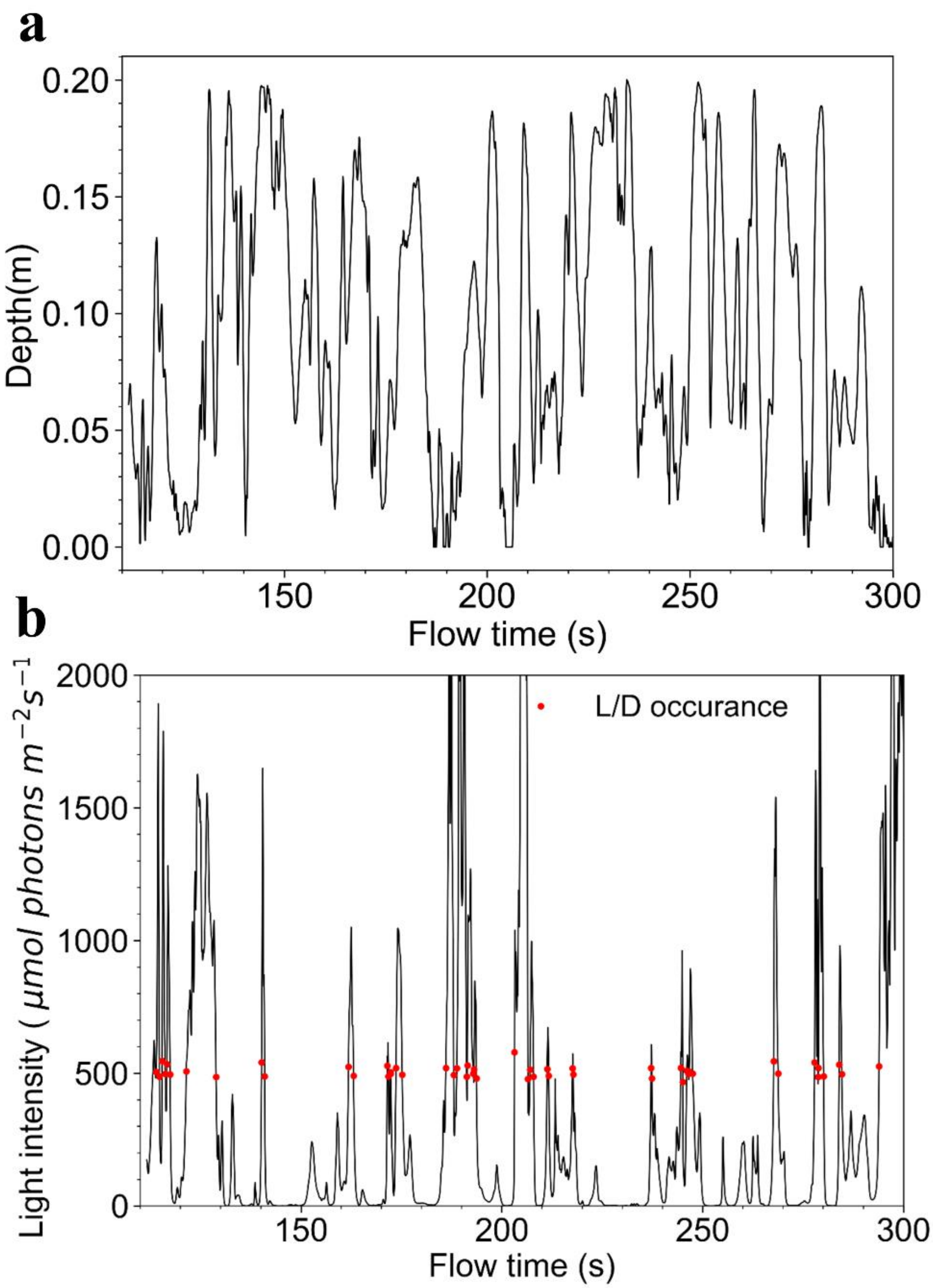

Figure. 2.11. Light intensity history converted from the vertical depth. (a) The depth measured from the gas-liquid interface of one selected particle (b) Light intensity history calculated from the depth of one selected particle

The light zone and the dark zones are assumed to be separated at the light intensity 500 μmol photons m^{-2} s^{-1}, and the transitions between the light zone and the dark zone are denoted by the red dots shown in Figure. 2.11b. Compared to Figure. 2.11a, the cells are experiencing significant depth changes when they are entering or leaving the light zone and dark zone. To understand the spatial distribution of the location that transition between the light zone and dark zone occurs, the same procedure is performed for all the tracked particles in the raceway pond and the instances of the L/D transitions is mapped to a horizontal plane whose probability is plotted and colorized in Figure. 2.12. As presented in Figure. 2.12, the cells have a larger probability of having L/D transitions near the paddle wheel region, first hairpin bend, and a large volume of the inner region of the second straight section. The region with the lowest probability to have L/D transitions includes the outer region of the second straight section and second hairpin bend. Nevertheless, there are regions of the second hairpin bend where the probability for microalgae cells to have L/D transitions are higher than other regions in the second bend. Those regions including the outer part of the second bend and the inner region near the divider downstream of the second bend. Compare Figure. 2.12 with Figure. 2.7, it can be observed that the regions where cells will have a larger probability are overlapped the region with the swirling motion predicted by the Q-criterion = 20 (Figure. 2.7b). Therefore, the conclusion can be drawn that the swirling motion thanks to the paddle wheel and the secondary flow by the hairpin bends is the primary source for inducing the vertical mixing, and the microalgae will have a larger probability at those regions where swirling motion is predicted.

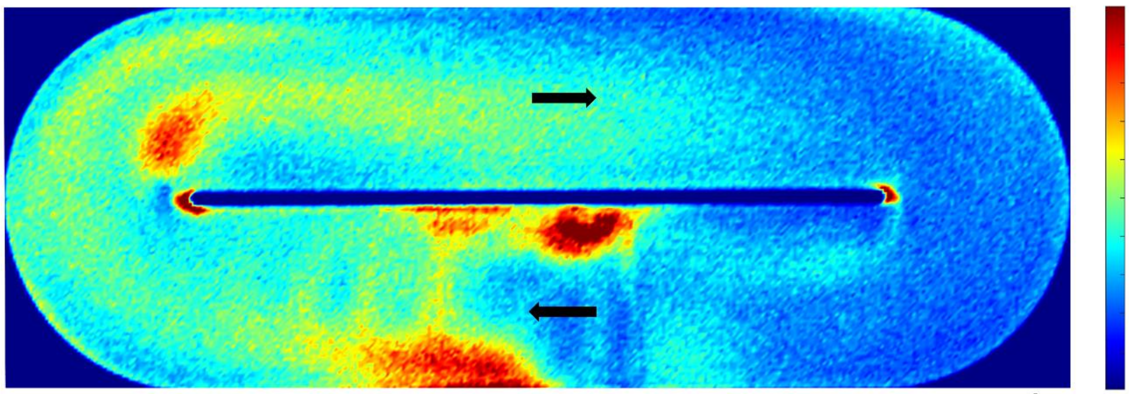

Figure. 2.12. Probability of L/D transitions on a horizontal plane.

2.3.6. Mixing performance of a raceway pond

To obtain a more fundamental understanding of the mixing performance in a raceway pond, the fluid domain is divided into 3 categories as illustrated in Figures. 2.13a and 2.13b: i) Dead zones, which are defined as the regions where the total velocity magnitude is lower than a threshold value, and 0.1 m/s is used here. It is reported that dead zones would cause cell stratification, toxic chemicals accumulation, increased energy dissipation, and cause cell's physiological state to deteriorate, which negatively affects algae cell productivity [23, 40-42]. Therefore, one of the optimization targets is to reduce the volume of the dead zones. iii) Regions with high vertical velocity are defined as the volumes where the magnitude of the vertical velocity component is greater than the 0.1 m/s threshold. The volume of these regions defines the vertical mixing performance of a raceway pond as the microalgae would have a strong vertical motion in these regions, mitigating the stratification effect and enhancing the light/dark effects. We want to increase the volume of these regions to enhance the vertical mixing performance and, therefore, to increase the biomass production rate in a raceway pond. ii) The remaining regions not meeting the criteria of regions (i) or (iii). The fluid in region (ii) will have a high speed but mostly flow parallel to the bottom and sides and show a primary flow resulting from the motion of the paddlewheel. Energy is continuously provided to maintain the fluid momentum in those regions without contributing to the vertical motion of the liquid and therefore the microalgae cells. The energy dissipates to sound and heat due to the viscous effect and is thus wasted. The volume of those regions needed to be minimized, and the way to minimize it is to increase the volume of the region (iii) while simultaneously decreasing the volume of the region (i).

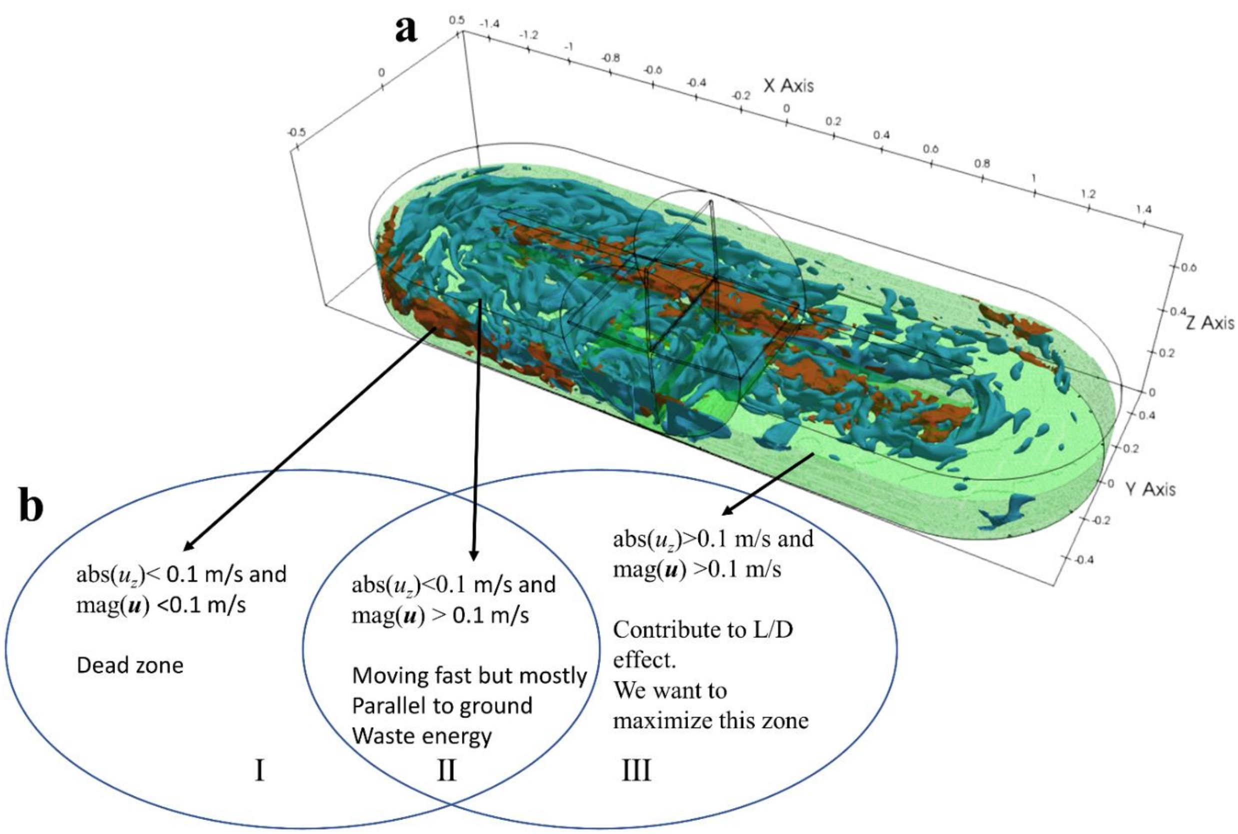

Figure. 2.13. (a) The raceway pond can be categorized into 3 regions. (b) Criterion of the 3 regions.

2.4. Conclusion

In this study, CFD simulations using the LES and k-ε turbulence models have been employed to simulate a mesoscale raceway pond with a water depth of 0.2 m. Laboratory studies conducted with a custom-made pygmy flow meter are used to validate the CFD simulations. It is found that the measured velocity data and the simulation results are in good agreement with one another, and the time-averaged geometry of a dead zone in a selected vertical cross-section is well predicted by simulations using the LES model. The computational results are visualized and indicate the following:

1) The k-ε model fails to identify, or at least under predicts, the extent of swirling motion and therefore the vertical motions downstream of the bends and the divider, contrary to what is seen by comparing the vertical velocity contours as well as the Q-criterion iso-surface plots and the LES model results. Although the k-ε model accurately captures the mean flow field along the primary flow direction, the vertical velocity component is significantly under-predicted because the k-ε model transiently time-averaged the velocity components. Consequently, LES has proven to be an essential tool for obtaining a high-fidelity flow field and is favored as the turbulence model to investigate the transient structures of the vortices and the mixing performance of raceway ponds considering numerous research focusing on these fields were conducted using the k-e model.

2) Swirling motions due to the paddle wheel and the geometry of the hairpin bend have both been identified as playing major roles in enhancing vertical mixing performance in the raceway pond. The time-dependent characteristics of the swirling motion, as well as the instantaneous fraction of the pond undergoing this motion have been investigated. It is found that the raceway pond is a highly dynamic system, and the swirling motions are generated,

transported, and dissipated downstream of their sources. Although an extensive amount of the pond including downstream of the paddle wheel, near the two 180° bends, and the wake regions downstream of the bends all have the potential to experience swirling motion, the instantaneous fraction of the liquid volume with swirl was low. Furthermore, by analyzing the microalgae cells' trajectories, it is found that the cells will have a higher probability of experiencing L/D transitions at the locations where swirling motions are predicted to occur. Passive strategies should be investigated in order to enhance the swirling motion in a greater fraction of the liquid volume.

3) The dead zone is not a continuous region as suggested by the k-ε model. In contrast, it is a highly time-dependent region containing lower vertical velocity sections and higher velocity sections. Regions of swirling motion can occur at the wake zone downstream of the bends. Furthermore, strong recirculation motion exists in discrete volumes within the dead zones, which is believed to cause the stagnation of the cell culture and the accumulation of chemicals, and therefore, have a negative impact on the pond mixing. An internal baffle to break the recirculation motion in the dead zones might be helpful for preventing toxic chemical accumulations.

4) To better characterize the raceway pond dynamics, its domain has been divided into 3 regions: i) low-velocity regions where the velocity magnitude is below 0.1 m/s, which are referred to as the dead zones; ii) the regions where the velocity magnitude is larger than 0.1 m/s, but the magnitude of the vertical component is less than 0.1 m/s. In these regions, the fluid is moving fast, however, it is mostly traveling horizontally. Microalgae will not experience much vertical redistribution in these two regions and the input kinetic energy introduced by the paddle wheel is dissipated by viscous effects without contributing to vertical mixing and thus, is wasted in those regions. iii) High vertical velocity zone where the vertical velocity magnitude is larger

than 0.1 m/s and the overall velocity magnitude is, therefore, greater than 0.1 m/s. These regions are expected to contribute to increased biomass yield because the flow tends to be stirred vertically in those regions where the vertical mixing performance of the raceway pond is improved, and the frequency of algae cells experienced between the light region and dark region is enhanced. It is important to point out that we want to maximize the volume of region iii) while minimizing the volume of the region i) to improve the algal biomass yield rate. The spatial distribution of these three regions is resolved accurately by LES simulations. Introducing internal structures such as baffles near the second bend and the end of the second straight section should further enhance the formation of vortices and increase vertical mixing.

5) A systematic way to quantify the vertical mixing performance of a raceway pond system has been developed. It is convenient and effective to use the average volume percentage of the high vertical velocity region and dead zone to characterize a raceway pond's vertical mixing efficiency, and it provides a way to compare across different raceway ponds. For this mesoscale pond, it is found that although approximately 40% of the liquid domain can experience vertical motion larger than 0.1 m/s for more than 20% of the time, only 15% of the domain will experience high vertical velocity at any given time. Flow manipulation or flow baffles will be required to increase the volume percentage of vertical mixing and should be placed strategically near the second straight section.

2.5 References

[1] Y. Chisti, "Biodiesel from microalgae beats bioethanol," *Trends Biotechnol.*, vol. 26, no. 3, pp. 126–131, Mar. 2008, doi: 10.1016/j.tibtech.2007.12.002.

[2] É. C. Francisco, D. B. Neves, E. Jacob-Lopes, and T. Franco, "Microalgae as feedstock for biodiesel production: Carbon dioxide sequestration, lipid production and biofuel quality," 2010, doi: 10.1002/JCTB.2338.

[3] P. Schenk *et al.*, "Second Generation Biofuels: High-Efficiency Microalgae for Biodiesel Production," *BioEnergy Res.*, 2008, doi: 10.1007/s12155-008-9008-8.

[4] J. B. K. Park, R. J. Craggs, and A. N. Shilton, "Wastewater treatment high rate algal ponds for biofuel production," *Bioresour. Technol.*, vol. 102, no. 1, pp. 35–42, Jan. 2011, doi: 10.1016/j.biortech.2010.06.158.

[5] A. Hosikian, S. Lim, R. Halim, and M. K. Danquah, "Chlorophyll Extraction from Microalgae: A Review on the Process Engineering Aspects," *Int. J. Chem. Eng.*, vol. 2010, p. e391632, Jun. 2010, doi: 10.1155/2010/391632.

[6] M. Janssen, J. Tramper, L. R. Mur, and R. H. Wijffels, "Enclosed outdoor photobioreactors: light regime, photosynthetic efficiency, scale-up, and future prospects," *Biotechnol. Bioeng.*, vol. 81, no. 2, pp. 193–210, Jan. 2003, doi: 10.1002/bit.10468.

[7] A. Richmond, "Principles for attaining maximal microalgal productivity in photobioreactors: an overview," p. 5.

[8] K. L. Terry, "Photosynthesis in modulated light: quantitative dependence of photosynthetic enhancement on flashing rate," *Biotechnol. Bioeng.*, vol. 28, no. 7, pp. 988–995, Jul. 1986, doi: 10.1002/bit.260280709.

[9] B. Kok, "Photosynthesis in flashing light," *Biochim. Biophys. Acta*, vol. 21, no. 2, pp. 245–258, Aug. 1956, doi: 10.1016/0006-3002(56)90004-X.

[10] J. U. Grobbelaar, L. Nedbal, and V. Tichý, "Influence of high frequency light/dark fluctuations on photosynthetic characteristics of microalgae photoacclimated to different

light intensities and implications for mass algal cultivation," *J. Appl. Phycol.*, vol. 8, no. 4, pp. 335–343, Jul. 1996, doi: 10.1007/BF02178576.

[11] J. C. Weissman, R. P. Goebel, and J. R. Benemann, "Photobioreactor design: Mixing, carbon utilization, and oxygen accumulation," *Biotechnol. Bioeng.*, vol. 31, no. 4, pp. 336–344, Mar. 1988, doi: 10.1002/bit.260310409.

[12] G. Haller, "An objective definition of a vortex," *J. Fluid Mech.*, vol. 525, pp. 1–26, Feb. 2005, doi: 10.1017/S0022112004002526.

[13] W.-S. Fu, Y. Lai, and C.-G. Li, "Estimation of turbulent natural convection in horizontal parallel plates by the Q criterion," 2013, doi: 10.1016/J.ICHEATMASSTRANSFER.2013.04.001.

[14] Gao, Zhuwei, Juan Wang, Jiangyun Wang, Yu Mao, and Yaodong Wei. "Analysis of the effect of vortex on the flow field of a cylindrical cyclone separator." Separation and Purification Technology 211 (2019): 438-447.

[15] J. Zhan, Y. Li, W. Wai, and W.-Q. Hu, "Comparison between the Q criterion and Rortex in the application of an in-stream structure," *Phys. Fluids*, vol. 31, Dec. 2019, doi: 10.1063/1.5124245.

[16] M. Lesieur, *Turbulence in Fluids: Stochastic and Numerical Modelling*, 2nd ed. Springer Netherlands, 1990. doi: 10.1007/978-94-009-0533-7.

[17] M. T. Landahl and E. Mollo-Christensen, *Turbulence and Random Processes in Fluid Mechanics*, 2nd ed. Cambridge: Cambridge University Press, 1992. doi: 10.1017/9781139174008.

[18] P. Moin and K. Mahesh, "DIRECT NUMERICAL SIMULATION: A Tool in Turbulence Research," *Annu. Rev. Fluid Mech.*, vol. 30, no. 1, pp. 539–578, 1998, doi:

10.1146/annurev.fluid.30.1.539.

[19] S. M. Hosseini, R. Vinuesa, P. Schlatter, A. Hanifi, and D. S. Henningson, “Direct numerical simulation of the flow around a wing section at moderate Reynolds number,” *Int. J. Heat Fluid Flow*, vol. 61, pp. 117–128, Oct. 2016, doi: 10.1016/j.ijheatfluidflow.2016.02.001.

[20] K. Mahesh, G. Constantinescu, and P. Moin, “A numerical method for large-eddy simulation in complex geometries,” *J. Comput. Phys.*, vol. 197, no. 1, pp. 215–240, Jun. 2004, doi: 10.1016/j.jcp.2003.11.031.

[21] K. Liffman, D. A. Paterson, P. Liovic, and P. Bandopadhayay, “Comparing the energy efficiency of different high rate algal raceway pond designs using computational fluid dynamics,” *Chem. Eng. Res. Des.*, vol. 91, no. 2, pp. 221–226, Feb. 2013, doi: 10.1016/j.cherd.2012.08.007.

[22] A. H. Godfrey, R. E. Spall, and B. D. Wood, “Computational Fluid Dynamics Analysis of Vertical Mixing in Algae Biofuel Raceways Through the Addition of Delta Wings at Angle-of-Incidence,” Jul. 2013, pp. 1259–1266. doi: 10.1115/FEDSM2012-72126.

[23] R. Hreiz, B. Sialve, J. Morchain, R. Escudié, J.-P. Steyer, and P. Guiraud, “Experimental and numerical investigation of hydrodynamics in raceway reactors used for algaculture,” *Chem. Eng. J.*, vol. 250, pp. 230–239, Aug. 2014, doi: 10.1016/j.cej.2014.03.027.

[24] M. Prussi *et al.*, “Experimental and numerical investigations of mixing in raceway ponds for algae cultivation,” *Biomass Bioenergy*, vol. 67, pp. 390–400, Aug. 2014, doi: 10.1016/j.biombioe.2014.05.024.

[25] R. Pandey and M. Premalatha, “Design and analysis of flow velocity distribution inside a raceway pond using computational fluid dynamics,” *Bioprocess Biosyst. Eng.*, vol. 40, pp. 1–12, Mar. 2017, doi: 10.1007/s00449-016-1712-8.

[26] J. Huang *et al.*, “Investigation on the performance of raceway ponds with internal structures by the means of CFD simulations and experiments,” *Algal Res.*, vol. 10, pp. 64–71, Jul. 2015, doi: 10.1016/j.algal.2015.04.012.

[27] B. Xu, P. Li, and P. Waller, “Optimization of the Flow Field of a Novel ARID Raceway (ARID-HV) for Algal Production,” presented at the ASME 2013 7th International Conference on Energy Sustainability collocated with the ASME 2013 Heat Transfer Summer Conference and the ASME 2013 11th International Conference on Fuel Cell Science, Engineering and Technology, Dec. 2013. doi: 10.1115/ES2013-18003.

[28] S. Park and Y. Li, “Integration of biological kinetics and computational fluid dynamics to model the growth of Nannochloropsis salina in an open channel raceway,” *Biotechnol. Bioeng.*, vol. 112, no. 5, pp. 923–933, May 2015, doi: 10.1002/bit.25509.

[29] D. Chiaramonti *et al.*, “Review of energy balance in raceway ponds for microalgae cultivation: Re-thinking a traditional system is possible,” *Appl. Energy*, vol. 102, pp. 101–111, Feb. 2013, doi: 10.1016/j.apenergy.2012.07.040.

[30] M. Zijlema, A. Segal, and P. Wesseling, “Finite volume computation of 2D incompressible turbulent flows in general co-ordinates on staggered grids,” *Int. J. Numer. Methods Fluids*, vol. 20, pp. 621–640, Apr. 1995, doi: 10.1002/fld.1650200703.

[31] J. Smagorinsky, “GENERAL CIRCULATION EXPERIMENTS WITH THE PRIMITIVE EQUATIONS: I. THE BASIC EXPERIMENT,” *Mon. Weather Rev.*, vol. 91, no. 3, pp. 99–164, Mar. 1963, doi: 10.1175/1520-0493(1963)091<0099:GCEWTP>2.3.CO;2.

[32] H. Bockhorn *et al.*, “Numerical Simulation of Turbulent Flows in Complex Geometries Using the Coherent Vortex Simulation Approach Based on Orthonormal Wavelet Decomposition,” in *Numerical Simulation of Turbulent Flows and Noise Generation:*

Results of the DFG/CNRS Research Groups FOR 507 and FOR 508, C. Brun, D. Juvé, M. Manhart, and C.-D. Munz, Eds. Berlin, Heidelberg: Springer, 2009, pp. 175–200. doi: 10.1007/978-3-540-89956-3_8.

[33] F. Zeng, J. Huang, C. Meng, F. Zhu, J. Chen, and Y. Li, "Investigation on novel raceway pond with inclined paddle wheels through simulation and microalgae culture experiments," *Bioprocess Biosyst. Eng.*, vol. 39, no. 1, pp. 169–180, Jan. 2016, doi: 10.1007/s00449-015-1501-9.

[34] R. J. Craggs, R. J. Davies-Colley, C. C. Tanner, and J. P. Sukias, "Advanced pond system: performance with high rate ponds of different depths and areas," *Water Sci. Technol. J. Int. Assoc. Water Pollut. Res.*, vol. 48, no. 2, pp. 259–267, 2003.

[35] J. L. Mendoza *et al.*, "Fluid-dynamic characterization of real-scale raceway reactors for microalgae production," *Biomass Bioenergy*, vol. 54, pp. 267–275, Jul. 2013, doi: 10.1016/j.biombioe.2013.03.017.

[36] M. Zhao, H. Tan, and B. Zhang, "A High-Resolution Characteristics-Based Implicit Dual Time-Stepping VOF Method for Free Surface Flow Simulation on Unstructured Grids," *J. Comput. Phys.*, vol. 183, pp. 233–273, Nov. 2002, doi: 10.1006/jcph.2002.7196.

[37] F. Ducros, N. Franck, and T. Poinsot, "Wall-Adapting Local Eddy-Viscosity Models for Simulations in Complex Geometries," *Numer. Methods Fluid Dyn. VI*, Jan. 1998.

[38] S. A. Morsi and A. Alexander, "An investigation of particle trajectories in two-phase flow systems," 1972, doi: 10.1017/S0022112072001806.

[39] H. Amini *et al.*, "An integrated growth kinetics and computational fluid dynamics model for the analysis of algal productivity in open raceway ponds," *Comput. Electron. Agric.*, vol. 145, pp. 363–372, Feb. 2018, doi: 10.1016/j.compag.2018.01.010.

[40] E. W. Becker, *Microalgae: Biotechnology and Microbiology*. Cambridge University Press, 1994.

[41] C. Meng, J. Huang, C. Ye, W. Cheng, J. Chen, and Y. Li, “Comparing the performances of circular ponds with different impellers by CFD simulation and microalgae culture experiments,” *Bioprocess Biosyst. Eng.*, vol. 38, no. 7, pp. 1347–1363, Jul. 2015, doi: 10.1007/s00449-015-1376-9.

[42] H. Ali, T. A. Cheema, and C. W. Park, “Effect of Paddle-Wheel Pulsating Velocity on the Hydrodynamic Performance of High-Rate Algal Ponds,” *J. Energy Eng.*, vol. 141, no. 4, p. 04014039, Dec. 2015, doi: 10.1061/(ASCE)EY.1943-7897.0000219.

Chapter 3: Dimensional analysis of strength and persistence of swirling motion in raceway pond systems coupled with computational fluid dynamics

3.1. Introduction

Due to ever-increasing energy demands, carbon dioxide emissions, and climate change threats, the need for alternative sustainable energy resources to replace fossil fuels is of high importance [1]. Microalgae-based biofuels have drawn much attention as a substitute fuel source to fossil fuels [2]. The advantages of using microalgae as the feedstock for biofuels include high growth rate, high lipid content, ease of cultivation, and uptake of atmospheric carbon dioxide [3-6]. Raceway pond systems are one of the most widely used open bioreactors for microalgae cultivation. Compared to enclosed bioreactor configurations, raceway pond systems are inexpensive to set up, require lower costs to operate, and are straightforward to scale up [7]. A typical raceway pond consists of a closed-loop channel usually in an oval shape. The oval is divided into two long, straight, parallel sections by a divider placed in the middle. The two straight sections are connected by two 180° hairpin-shaped bends. One or more paddle wheels are used to drive and mix the liquid media, which are essential for achieving a high yield rate as the liquid motion 1) ensures uniform light exposure for the cells and prevents stratification; 2) creates a homogenous distribution of nutrients and inhibits undesirable chemicals from concentrating; and 3) prevents thermal stratification [8]. During daytime, the light is continuously supplied by the sun, but as the culture density increases, the light cannot penetrate as effectively as for a lower culture density due to the cell shading effect. Furthermore, as liquid and cells are driven by the paddle wheel, their vertical positions are changing dynamically, and the light intensity they are exposed to varies between light and dark. This flashing light effect has been reported to promote the cells' growth rate when microalgae alternate between the light zones and dark zones with a higher light/dark (L/D) frequency [9-12]. As a result, the paddle wheel's agitation improves the vertical mixing, which contributes to increased production yield by enhancing the L/D effect.

Secondary flow phenomena such as those in a raceway pond occur when the fluid has sufficient inertia that a relatively abrupt change in flow direction disrupts path lines due to centripetal forces. In a system with a large enough bend in the geometry, the secondary flows are referred to as Dean vortices based on the analytical solution for laminar flow first obtained by WR Dean [13-14]. In those studies, the theoretical solution of the fluid motion was derived using a perturbation method in cylindrical coordinates. Similar behavior can be observed downstream when the fluid flows through a curved open channel. Vaghefi et al. analyzed the flow field in a 180° open channel as measured by an Acoustic Doppler Velocimeter and reported that two clockwise vortices were observed [15]. In another study, existences of spiral vortices were reported in and downstream of a sharp meander bend [16]. Secondary flow phenomena have also been observed in pipes, conduits, and open channels [17-22]. The Dean number (De) is a dimensionless group that arises from the governing differential momentum equations as the ratio of centripetal and viscous forces and can be used to describe the secondary flow's strength:

$$De = Re\sqrt{\frac{D_h}{2R}} \tag{3.1}$$

where R is the radius of the bend, Re is the Reynolds number, given by

$$Re = \frac{UD_h}{\nu} \tag{3.2}$$

where U is the average channel velocity, ν is the kinematic viscosity, and D_h is the hydraulic diameter. For an open channel with a rectangular cross section:

$$D_h = \frac{4wh}{w+2h} \tag{3.3}$$

where w is the width of the channel and h is the height, which is equal to the water depth for a raceway pond. Therefore, the strength of secondary flows is strongly dependent on the cross-sectional dimensions and radius of curvature of the bend.

For raceway pond systems, the shape ratio (SR) can be used as a geometrical parameter representing the straight section and is defined as

$$SR = \frac{w}{h} \tag{3.4}$$

where a large SR represents a wide, shallow open channel, and a small SR represents a narrow and tall channel. For commercial-scale raceway ponds, the length of the straight sections can be as long as 300 m, corresponding to an SR over 1000 [23]. For long enough straight sections, it is known that vertical mixing and secondary swirling motion generated by the paddle wheel will dissipate before flow reaches the hairpin bends. Hence, the geometry of the 180° hairpin bend has a considerable effect in contributing to the generation of secondary flow and swirling motion which has a positive impact on vertical mixing and the L/D effect.

For most raceway ponds, the radius of the hairpin bend is very close to the width of the straight sections, as a higher land usage efficiency can be achieved, and a reduced contact surface can be ensured, which helps to reduce viscous dissipation and head loss. Therefore, it is hypothesized that the strength, as well as the persistence length of the swirling motions only depends on the SR of the pond and the rotational speed of the paddle wheel. It is critical to be able to predict the strength and persistence length of the swirling motions in order to assess the mixing performance of a raceway pond without resorting to costly computational fluid dynamics (CFD) simulations, which can be prohibitively expensive for an industrial-scale raceway pond. Additionally, the prediction of the persistence will be helpful to guide the placement of baffles and other interior structures that passively promote vertical mixing. CFD has been used to successfully simulate the flow field and liquid motion in raceway pond systems by solving the Navier-Stokes equations and continuity equation using the finite volume method [24-29]. However, to model turbulent flow, each variable, such as velocity and pressure, must be decomposed into a mean component and a fluctuating component. As more unknown variables are introduced, a closure problem arises, and turbulence models are required to close the equations by modeling the Reynolds stress term. The k-ε model has been widely used to predict flow dynamics in raceway pond systems [29-35]. The k-ε model is coupled by two transported variables, one is the turbulent kinetic energy (k) and the other is the turbulent dissipation rate (ε). As one of the Reynolds-averaged Navier-Stokes (RANS) family, the k-ε model solves the mean turbulent flow field by modeling the fluctuating portion [36].

However, since the primary flow direction in a raceway pond is horizontal, the fluid motion in the vertical direction is smoothed out in a time-averaging step performed within the k-ε model. The way to address this shortcoming is to move away from a RANS model and instead apply a turbulence model known as large eddy simulation (LES). This model has been shown to efficiently resolve the swirling motions and vortices for incompressible fluid flows in curved bends and T-junctions [37-38]. Unlike the k-ε model, the LES model resolves large eddies directly by solving the full Navier-Stokes equations and capturing small eddies using sub-grid stress models. As a result, the smallest eddies that can be resolved using the LES model are directly related to the size of the mesh, and the temporal characteristics of swirling motions can be resolved with a fine mesh when the LES model is used.

In this study, raceway ponds with 7 *SR* values and 8 paddle wheel speeds per *SR* geometry are simulated using CFD with LES as the turbulence model. Those 56 cases range from small-scale ponds to pilot-scale raceway ponds over a wide range of operating conditions. The strength and persistence length of the swirling motions generated by the hairpin bends have been extracted from the results and analyzed. A critical vertical velocity is proposed here to describe the strength of the swirling motion, and the results demonstrate that the critical vertical velocity is proportional to the averaged velocity magnitude downstream of the bends. Furthermore, the ratio between the critical vertical velocity and the averaged velocity magnitude in the bends depends directly on the geometric design of the pond characterized by the dimensionless group ($D_h/2R$) appearing in the Dean number. This relationship is identified and fitted into a rational model, which will allow practitioners to predict the strength and spatial distribution of high vertical velocity regions without the need for additional CFD simulations.

3.2. Material and methods

3.2.1 The Geometry and operating conditions of the mesoscale raceway pond

The dimensions and the operating conditions as well as the *SR*, *Re*, *De*, and surface area of the raceway ponds simulated with 7 *SR* are given in Table 3.1, and the definition for the dimensional parameters are shown in Figure. 3.1. The tip velocity of the paddle wheel is selected as the characteristic velocity used to calculate *Re* and *De*. After carrying out multiple simulations, it was found that a more appropriate choice for the characteristic velocity is the average velocity magnitude in the hairpin bend, but this quantity is not possible to predict prior to the CFD simulations. The *SR* ranges from 0.5 to 7.05 and for each pond *De* ranges from 16,140 to 242,120. The pond surface areas range from 0.52 m^2 (*SR* = 0.5) to 25 m^2 (*SR* = 7.05), and the liquid depths are maintained near 0.2 m, which is a common cultivation depth, except for the case with the *SR* = 0.5 where the liquid depth is set to 0.28 m. Otherwise, the pond with *SR* = 0.5 would be too small and the paddle wheel tip velocity would be unrealistically large to achieve *De* = 242,120, which has little practical significance. The dimensions are adopted from the raceway ponds listed by the Microbio Engineering (RW0.5 to RW22). A four-blade paddle wheel is placed at the center of the first straight section.

Table. 3.1 The dimensions and the operating conditions of the 56 modeled raceway ponds such as the *SR*, *Re*, *De*, and surface area.

case	L(m)	W(m)	H(m)	SR	RPM	U_{tip}	Re	De	Surface area (m^2)
1a	1.8	0.14	0.28	0.5	2.05	0.074	18679	16141	0.4
1b	1.8	0.14	0.28	0.5	4.1	0.148	37359	21282	0.4
1c	1.8	0.14	0.28	0.5	8.21	0.297	74718	64564	0.4
1d	1.8	0.14	0.28	0.5	12.32	0.45	112078	96846	0.4
1e	1.8	0.14	0.28	0.5	16.43	0.594	149437	129128	0.4
1f	1.8	0.14	0.28	0.5	20.54	0.742	186796	161410	0.4
1g	1.8	0.14	0.28	0.5	24.65	0.89	224156	193692	0.4
1h	1.8	0.14	0.28	0.5	30.81	1.113	280195	242116	0.4
2a	1.9	0.18	0.18	1	2.13	0.077	20838	16141	0.7
2b	1.9	0.18	0.18	1	4.27	0.154	41676	21282	0.7

2c	1.9	0.18	0.18	1	8.55	0.309	83352	64564	0.7
2d	1.9	0.18	0.18	1	12.83	0.463	125028	96846	0.7
2e	1.9	0.18	0.18	1	17.11	0.618	166704	129128	0.7
2f	1.9	0.18	0.18	1	21.38	0.772	208380	161410	0.7
2g	1.9	0.18	0.18	1	25.66	0.927	250056	193692	0.7
2h	1.9	0.18	0.18	1	32.08	1.159	312570	242116	0.7
3a	2.54	0.25	0.2	1.25	1.71	0.061	21383	16141	1.3
3b	2.54	0.25	0.2	1.25	3.42	0.123	42766	21282	1.3
3c	2.54	0.25	0.2	1.25	6.84	0.247	85532	64564	1.3
3d	2.54	0.25	0.2	1.25	10.27	0.371	128298	96846	1.3
3e	2.54	0.25	0.2	1.25	13.69	0.494	171065	129128	1.3
3f	2.54	0.25	0.2	1.25	17.19	0.618	213831	161410	1.3
3g	2.54	0.25	0.2	1.25	20.54	0.742	256597	193692	1.3
3h	2.54	0.25	0.2	1.25	25.67	0.927	320746	242116	1.3
4a	2.74	0.35	0.2	1.67	1.45	0.052	22470	16141	1.9
4b	2.74	0.35	0.2	1.67	2.9	0.104	44941	21282	1.9
4c	2.74	0.35	0.2	1.67	5.8	0.209	89883	64564	1.9
4d	2.74	0.35	0.2	1.67	8.7	0.314	134825	96846	1.9
4e	2.74	0.35	0.2	1.67	11.6	0.419	179767	129128	1.9
4f	2.74	0.35	0.2	1.67	14.49	0.523	224708	161410	1.9
4g	2.74	0.35	0.2	1.67	17.39	0.628	269650	193692	1.9
4h	2.74	0.35	0.2	1.67	21.74	0.785	337063	242116	1.9
5a	4	0.51	0.2	2.55	1.36	0.049	24818	16141	4

5b	4	0.51	0.2	2.55	2.72	0.098	49637	21282	4
5c	4	0.51	0.2	2.55	5.45	0.197	99274	64564	4
5d	4	0.51	0.2	2.55	8.18	0.295	148909	96846	4
5e	4	0.51	0.2	2.55	10.91	0.394	198548	129128	4
5f	4	0.51	0.2	2.55	13.63	0.492	248185	161410	4
5g	4	0.51	0.2	2.55	16.36	0.591	197822	193692	4
5h	4	0.51	0.2	2.55	20.45	0.738	377278	242116	4
6a	6.04	1	0.2	5	1.31	0.047	30497	16141	11.4
6b	6.04	1	0.2	5	2.62	0.095	60995	21282	11.4
6c	6.04	1	0.2	5	5.25	0.19	121990	64564	11.4
6d	6.04	1	0.2	5	7.89	0.285	182986	96846	11.4
6e	6.04	1	0.2	5	10.52	0.38	243981	129128	11.4
6f	6.04	1	0.2	5	13.14	0.475	304976	161410	11.4
6g	6.04	1	0.2	5	15.78	0.57	365972	193692	11.4
6h	6.04	1	0.2	5	19.72	0.712	457465	242116	11.4
7a	9	1.48	0.2	7.05	1.26	0.047	34562	16141	25.1
7b	9	1.48	0.2	7.05	2.53	0.094	69124	21282	25.1
7c	9	1.48	0.2	7.05	5.05	0.188	138248	64564	25.1
7d	9	1.48	0.2	7.05	7.58	0.282	207372	96846	25.1
7e	9	1.48	0.2	7.05	10.11	0.376	276496	129128	25.1
7f	9	1.48	0.2	7.05	12.64	0.47	345620	161410	25.1
7g	9	1.48	0.2	7.05	15.17	0.564	414744	193692	25.1
7h	9	1.48	0.2	7.05	18.96	0.705	518430	242116	25.1

3.2.2 Mesh generation and solver

The computational grid is constructed using the ANSYS meshing utility and then translated to the openFoam format with the openFoam's utility "Fluent3DMeshToFoam" [39]. To simulate the rotation of the paddle wheel, the fluid domain is divided into a static and a rotational domain. The arbitrary coupled mesh interface (ACMI) boundary condition connects these two domains [40]. In preliminary studies, it was discovered that simulations with a hexahedral mesh achieved greater numerical stability and efficiency. To maintain accuracy and to resolve the smallest eddies, simulations with an average mesh size of up to 14,563,000 cells are conducted.

The solver used is a minor modification of openFoam's "interFoam" function where a residual evaluation is performed at the end of each pressure-implicit with splitting of operators (PISO) iteration, and the inner pressure corrector loop is configured to terminate when the residual reaches the desired value [39]. Additionally, a velocity sweep was included to remove excessively high velocities following each outer pressure correction iteration to improve the stability of the simulations. The simulations are conducted on a high-performance computer at the National Renewable Energy Laboratory equipped with dual Intel Xeon Gold Skylake 6154 processors (3.0 GHz, 18-core). For each of the 56 instances, an average of 21920 core-hours were utilized to collect flow time history data.

3.2.3 Boundary conditions and scheme

The boundary conditions are shown in Figure. 3.1b. Apart from the interface between the rotating and static domains, which is defined as an ACMI boundary condition, the top surface of the rotatory domain is set as an atmosphere boundary condition. Other pond boundaries, such as the pond's wall, divider, and bottom, are configured as no-slip wall boundaries. The size of the time step is time-variant in relation to the Courant number, which is limited to 20 and the time step size is limited to 0.01 s. To achieve an improved accuracy, the second-order Crank-Nicolson scheme is used [41]. The least-squares scheme is used as the gradient scheme and is reported to have a higher order of accuracy compared with the Green-Gauss scheme on unstructured meshes [42]. The Gauss cubic corrected method was utilized to calculate Laplacian terms.

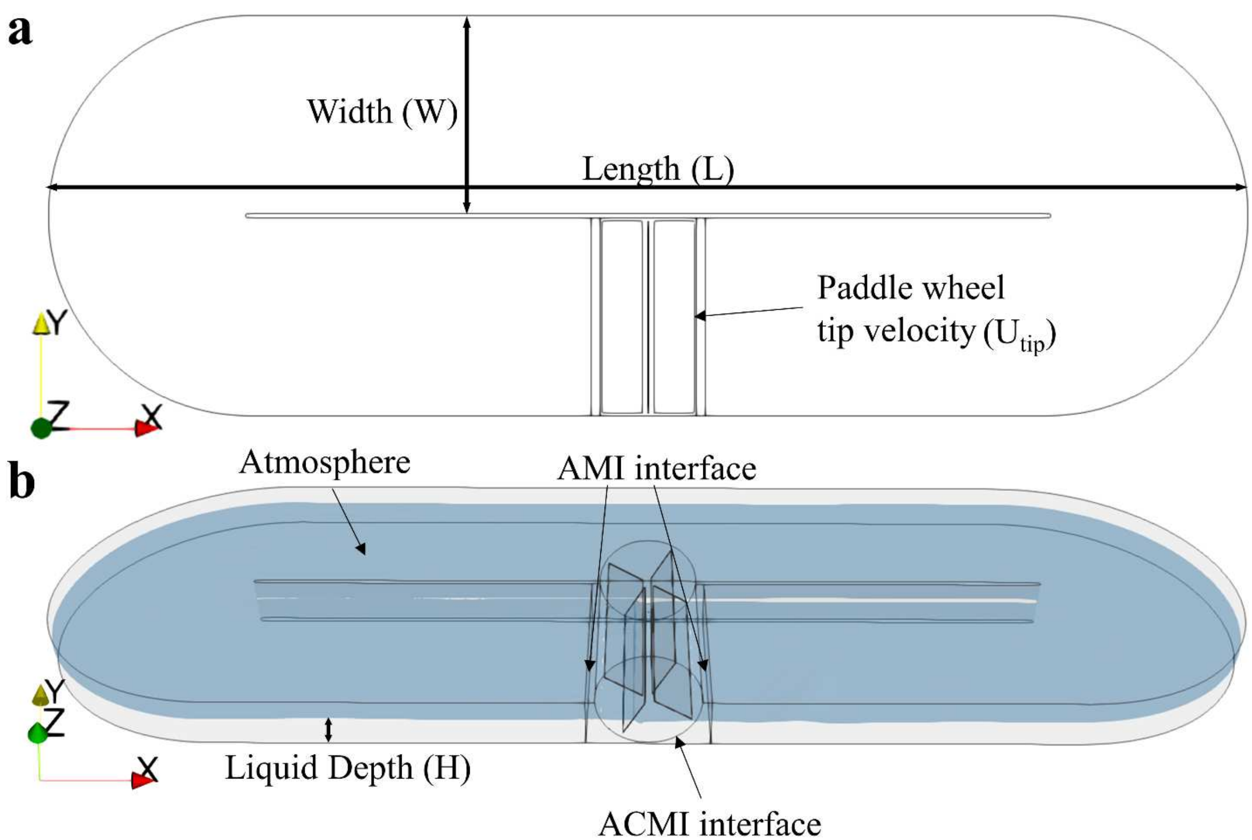

Figure. 3.1. Schematic diagram of the raceway pond (a) Top view of a raceway pond with definitions of geometry parameters. (b) Boundary condition setup for the simulation.

3.2.4 Volume of fluid (VOF) model

The pond is modeled as multiphase flow, and the volume of fluid (VOF) model is used to accurately track the interface between the gas and liquid and solve the flow field of both phases. Each microalgae cell's motion is assumed to have a negligible impact on liquid motion as well as fluid properties. The VOF model denotes each phase using a scalar function, the volume fraction α [43]. In our case: $\alpha = 0$ if the mesh cell is in the gas phase; $\alpha = 1$ if the mesh cell is in the liquid phase; and an α value between 0 and 1 denotes that the mesh cell is at the interface. Density and viscosity are calculated as:

$$\rho = \rho_g \alpha_g + \rho_l \alpha_l \tag{3.5}$$

$$\mu = \mu_g \alpha_g + \mu_l \alpha_l \tag{3.6}$$

where μ is the viscosity, α is the volume fraction, ρ is the density, and subscripts *g* and *l* denote the gas and liquid phases, respectively.

With the assumption that the fluids modeled in raceway pond systems are incompressible, immiscible, and isothermal, the continuity equation and the momentum equation are solved by the VOF model as:

$$\nabla \cdot \boldsymbol{u} = 0 \tag{3.7}$$

$$\frac{\partial}{\partial t}(\alpha_k \rho_k \boldsymbol{u}_k) = -\nabla \cdot \left((\alpha_k \rho_k \boldsymbol{u}_k \boldsymbol{u}_k)\right) - \alpha_k \nabla p - \nabla \cdot (\alpha_k \overline{\boldsymbol{\tau}_{\boldsymbol{k}}}) + \alpha_k \rho_k \boldsymbol{g} + \boldsymbol{F} \tag{3.8}$$

where p is the pressure, $\overline{\boldsymbol{\tau}}$ is the stress tensor, $\boldsymbol{g}$ is the gravity vector, $\boldsymbol{F}$ is the source term, and subscript *k* denotes this equation is for the kth phase. The transport equation for the volume of fluid scalar α_k for the kth phase is:

$$\frac{\partial \alpha_k}{\partial t} + \nabla \cdot (\alpha_k \boldsymbol{u}_k) + \nabla \cdot (\alpha_k (1 - \alpha_k) \boldsymbol{u}_r) = 0 \tag{3.9}$$

where the third term is for artificial compression and $_r$ is the relative velocity suitable for interface compressing [44-45]. This artificial compression term is used to sharpen the interface and is only active in the interface region, because of the $\alpha_k(1 - \alpha_k)$ term [46-47]. The relative velocity is defined as

$$\boldsymbol{u}_r = C_\alpha \left|\frac{\phi}{|S_f|}\right| \boldsymbol{n}_f \tag{3.10}$$

where C_α is the adjustable compression factor, ϕ is the velocity flux, $|S_f|$ is the cell surface area, and $\boldsymbol{n}_f$ is the surface normal vector. It is suggested that C_α is set between 0 and 4, where 0 corresponds to no compression, 1 corresponds to conservative compression and $1 \leq C_\alpha \leq 4$ corresponds to enhanced compression [48-49]. C_α is set to 1 as suggested by literature to model practical flow scenarios [49].

In order to use a relatively larger time step size but still ensure accuracy, a semi-implicit multi-dimensional limiter for explicit solution (MULES) method is used to solve Equations (8) and (9). This method ensures boundedness and stability when a larger time step size is used. The MULES method is used to solve the α_k equation and update the interface before the PISO interactions at each time step.

3.2.5 Turbulence model

The k-ε turbulence model, as one of the RANS family that is derived from time-averaging the Navier-Stocks equation, imposes a high risk for the loss of the vertical velocity information. Therefore, the LES model is used as the turbulence model. The sub-grid scale model used in the LES model is a one equation Smagorinsky-type eddy viscosity model developed by Yoshizawa [50].

3.2.6 Flow field validation

The cases with SR = 2.55 are validated with ANSYS Fluent and experimental data collected with a custom-made pygmy flow meter that is calibrated using FlowExplorer laser doppler anemometry (LDA) manufactured by DENMARK in the Armfield model S6MkII glass-sided tilting flume.

3.2.7 Determining the persistence length

3.3.7.1 Use persistence length to characterize the mixing performance and the strength of the swirling motion

The persistence length L_p is defined as the length measured from the tip of the bend to the location where the magnitude of the vertical velocity no longer continuously exceeds some vertical velocity magnitude $u_{z,\mathrm{cri}}$ over a specified minimum fraction of the channel width. Compared with using the Q-criteria or other vortex identification methods to define persistence length, using $u_{z,\mathrm{cri}}$ is more computationally convenient as it does not require calculating the gradient of the velocity field, and it is directly related to the most relevant variables associated with vertical mixing and the L/D frequency. For example, if the liquid depth is 0.2 m, a $u_{z,\mathrm{cri}}$ of 0.2 m/s indicates an L/D frequency of 1 Hz.

The vertical mixing characteristics of a raceway pond system can be determined in two ways: 1. Fix the L_p relative to the bend radius R, (L_p = 4R is considered in this study) and determine the corresponding $u_{z,\mathrm{cri}}$, where a larger value of $u_{z,\mathrm{cri}}$ indicates a better-mixed scenario. The method to find $u_{z,\mathrm{cri}}$ for L_p = 4R is given in section 2.8.2. 2. define a $u_{z,\mathrm{cri}}$, and use it to determine L_p for all the cases with different SR values and paddle wheel RPMs. In that case a larger value of L_p indicates a better-mixed scenario. The method to calculate L_p for a given $u_{z,\mathrm{cri}}$ is presented in section 2.8.3. In section 3.3.2, it is demonstrated that the predicted L_p for both methods are comparable.

3.2.7.2. Determining $u_{z,\mathrm{cri}}$ with $L_p = 4R$

A trial-and-error method is used to determine the critical velocity that leads to $L_p = 4R$. More precisely, the midpoint technique was utilized, which begins by defining a high critical velocity threshold value that results in $L_p < 4R$ and a low value that results in $L_p > 4R$ (0 m/s was used). The L_p was calculated with $u_{z,\mathrm{cri}}$ using the method in section 2.8.3. If the calculated $L_\mathrm{p} < 4R$, the middle point of the lower section is evaluated, and so on until the difference between the high and low thresholds is less than the predetermined error, which in this study is set at 0.00025. This, however, does not guarantee that the predicted persistence length is exactly four times the radius. For instance, as demonstrated in Figure. 3.2, an example scenario for SR=2.55, RPM= 2.73 is shown for which the persistence is calculated to be 4.28R when the critical velocity is set to =0.04028 m/s and 3.10R when the critical velocity is set to 0.04040 m/s. A small increase of $u_{z,\mathrm{cri}}$ can result in a significant increase in L_p. Nonetheless, the critical velocity calculated in this manner will be the one for which the corresponding persistence length is closest to 4R.2.8.3 Determining L_p for a given $u_{z,\mathrm{cri}}$.

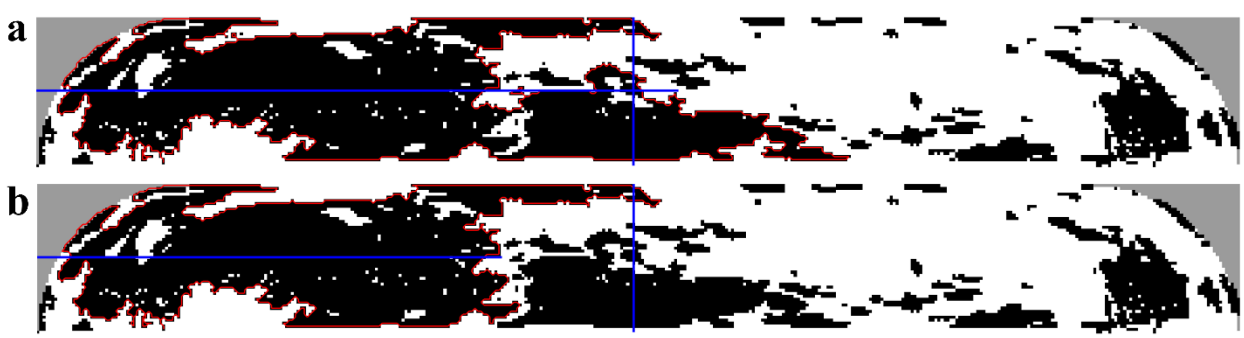

Figure. 3.2. Diagram showing that in the case where SR = 0.5, RPM = 2.1, a small change of $u_{z,cri}$ and consequently a preserved region near the lower center of the figures is disconnected can result in a significant change of L_p. However, the resulted $u_{z,cri}$ is within the predetermined error

margin. The connected region is marked by a red line, L_p is denoted by a blue horizontal line, and the location of $4R$ is marked by a vertical blue line. (a) $L_p = 4.28R$ when $u_{z,cri} = 0.04028$ m/s. (b) $L_p = 3.10R$ when $u_{z,cri} = 0.04040$ m/s.

To determine the L_p of the swirling motion in a raceway pond using a specific $u_{z,\mathrm{cri}}$, a total of 75 velocity fields (taken from a 15 s span with 0.2 s interval) for each case are analyzed in Matlab. The air portion of the velocity field is filtered, and the vertical component of the remaining liquid portion velocity field is compared with $u_{z,\mathrm{cri}}$. If the vertical component of the velocity field at a certain region is larger than the critical velocity, these regions are preserved while other regions are filtered out. As the spatial distribution of the swirling motions in a horizontal plane is of more interest rather than in the vertical direction, those liquid regions where the vertical velocity component is larger than the critical velocity are then projected to a 2-dimensional horizontal plane. The same procedure is performed for the total 75 velocity fields for each case and the preserved liquid region where abs(u_z) > $u_{z,\mathrm{cri}}$ are overlapped with each other. The generated result represents the spatial distribution of the swirling motion in the 2-D horizontal space. As demonstrated in Figure. 3.3, the preserved region at t =100.0 s with SR = 2.55 is plotted in Figure. 3.3a, and the preserved region at t = 100.2 s is plotted in Figure. 3.3b. The preserved region of all the velocity fields is then projected into a horizontal plane, resulting in a large, connected region (Figure. 3.3c).

The largest connected region (bounded by the red line) is then identified, and the persistence length is measured from the tip of the bend and the point that the largest connected region occupies more than 40% of the width at that point. The criterion is defined in such a way as in some cases, the connected region has a thin tail that will affect the calculation of the persistence length. At the region of these "thin tails", the fluid has a chance to experience vertical motion, but the strength is so low that it does not occupy enough space and including these regions will result in overestimates of L_p (Figure. 3.3d). Therefore, those regions are excluded from the persistence length calculations.

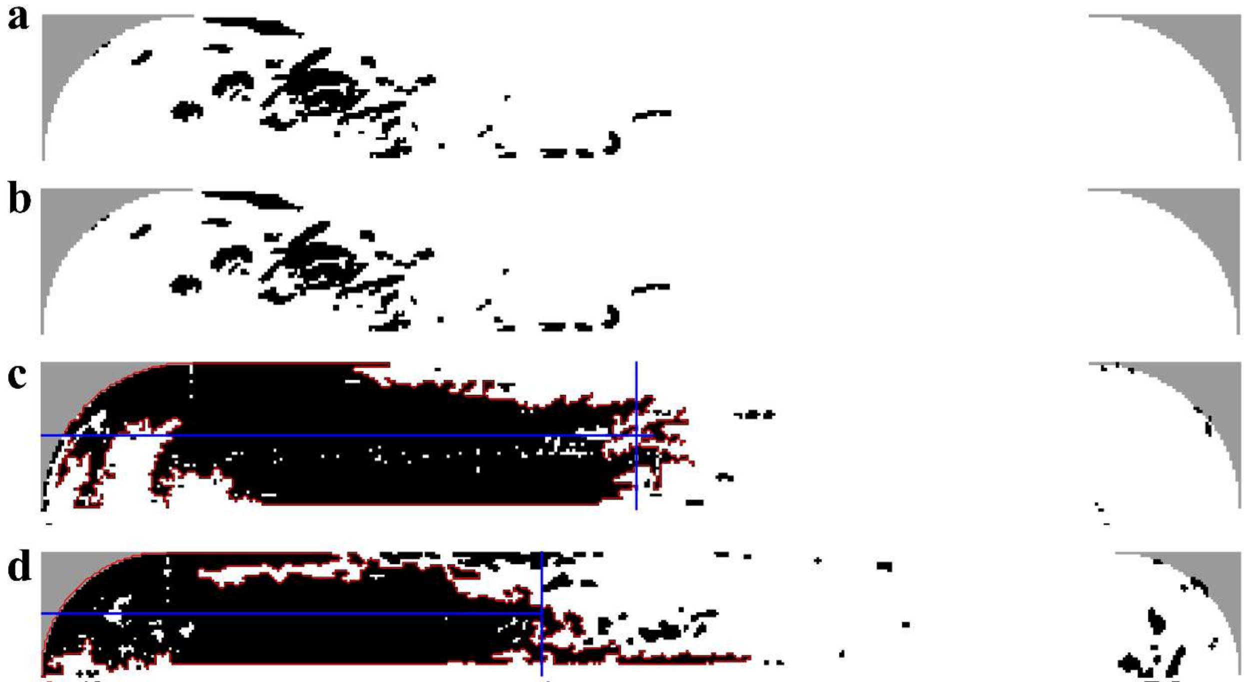

Figure. 3.3. Diagram demonstrating an example where SR = 2.55, RPM = 13.6 to calculate L_p for a given $u_{z,cri}$. The connected region is marked by a red line, L_p is denoted by a blue horizontal line, and the location of $4R$ is marked by a vertical blue line. (a) Liquid region where abs(u_z) > $u_{z,cri}$ is projected to a horizontal plane at t = 100.0 s; (b) Liquid region where abs(u_z) > $u_{z,cri}$ is projected to a horizontal plane at t =100.2 s; (c) The liquid region where abs(u_z) > $u_{z,cri}$ for all the velocity fields are overlapped, resulting in a large, connected region that represents the region where swirling motion can occur; (d) Case where SR = 1.25, RPM = 13.7 shows a "thin tail" that will influence the calculation of L_p, and the "thin tail" is excluded when calculating L_p.

3.3. Results and Discussion

3.3.1 Flow field validation

To validate the results predicted by openFoam, the time-averaged velocity profile is extracted at the cross-section measured 0.68 m from the tip of the bend of a meso-scale raceway pond and compared with the simulation results carried out by ANSYS Fluent as well as the time-averaged velocity profile measured by a custom-made pygmy flow meter. The results are shown in Figure. 3.4.

The dead zone is generated downstream of the first hairpin bend in the vertical cross-section, as represented by a low velocity region in Figure. 3.4. It is suggested by comparing the three contour plots that the boundary of the dead zone is well captured by the simulations using ANSYS Fluent and openFoam with openFoam slightly overestimating the size of the dead zone. Furthermore, both simulation results suggest the presence of a high-velocity zone near the bottom of the cross-section, and the magnitude of the velocity is predicted around 0.63 m/s by both CFD packages. To summarize, the velocity fields generated by ANSYS Fluent and openFoam match with the experimental data.

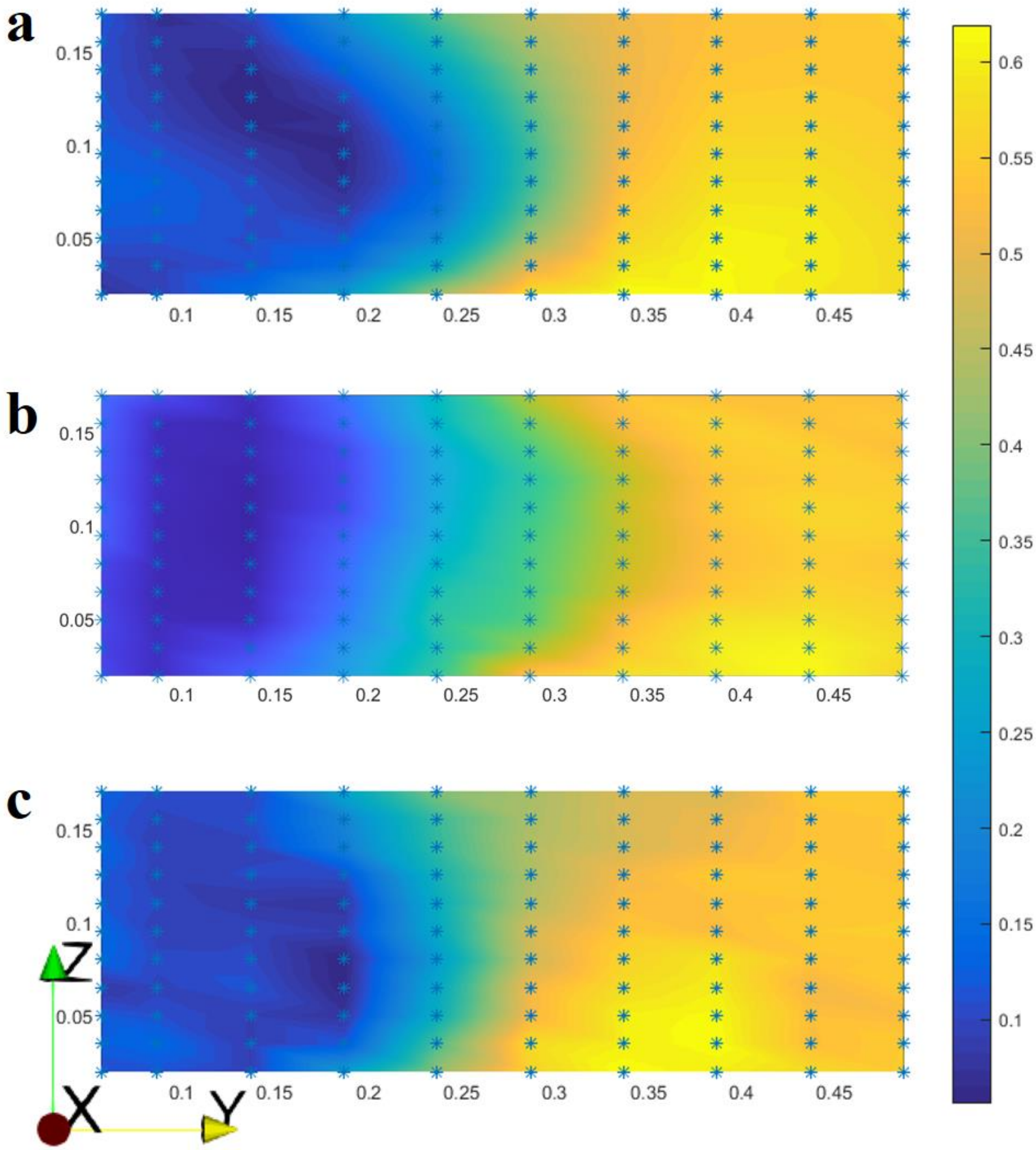

Figure. 3.4. Comparison of the time averaged x-component of the velocity in the vertical cross section 0.68 m downstream of the first bend tip in a meso-scale raceway pond. *SR* = 2.55 RPM = 13.6 Raceway length is *L*= 3.13 m (a) prediction by LES model with ANSYS Fluent. (b) prediction by LES model with openFoam. (c) experimental measurements.

3.3.2 Swirling motion

Centripetal force is a significant contributor to the secondary flow swirling motions. As fluid flows through bends in the open channels, the high velocity regions are shifted away from the surface and toward the outer bend. The region in a raceway pond with SR = 2.55 where mag($\boldsymbol{u}$) is greater than 0.35 m/s is depicted in Figure. 3.5. The high-velocity zones can be found downstream of the paddle wheel, close to the surface. As the liquid flows around the hairpin bends, the high-velocity zones at the surface upstream of the bends move to the channel's outer region, where they are visible at any depth. This motion forces the liquid downward in the bends' outer sections. On the other hand, the liquid must move upwards from the bottom of the inner bends so that the mass is conserved. As the locations of the high-velocity region shift while fluid flows across the bend, a counter-clockwise rotational motion (viewed in the main flow direction) is generated as illustrated in Figure. 3.6a.

In addition to the centripetal force, the negative pressure gradient and the corresponding boundary layer separations also help generate the swirling motion. Upstream of the hairpin bends, as fluid flows toward the wall of the pond, there exists a strong negative pressure gradient applied at the wall of the hairpin bends. As a result, the velocity vectors along with a sampling line probe from a cross-section 0.05 m measured from the bottom of the pond show that the fluid slows down and flows backward near the outer channel, indicating the boundary layer is separated (Figure. 3.5b). Similar to the outer bend, the boundary layer is separated downstream of the divider's edge where the presence of the divider works as an obstacle, and the wake is generated downstream the divider. The boundary layer separations form recirculation zones with vortices, enhancing the flow's instability, and therefore, have a positive impact on generating the swirling motions.

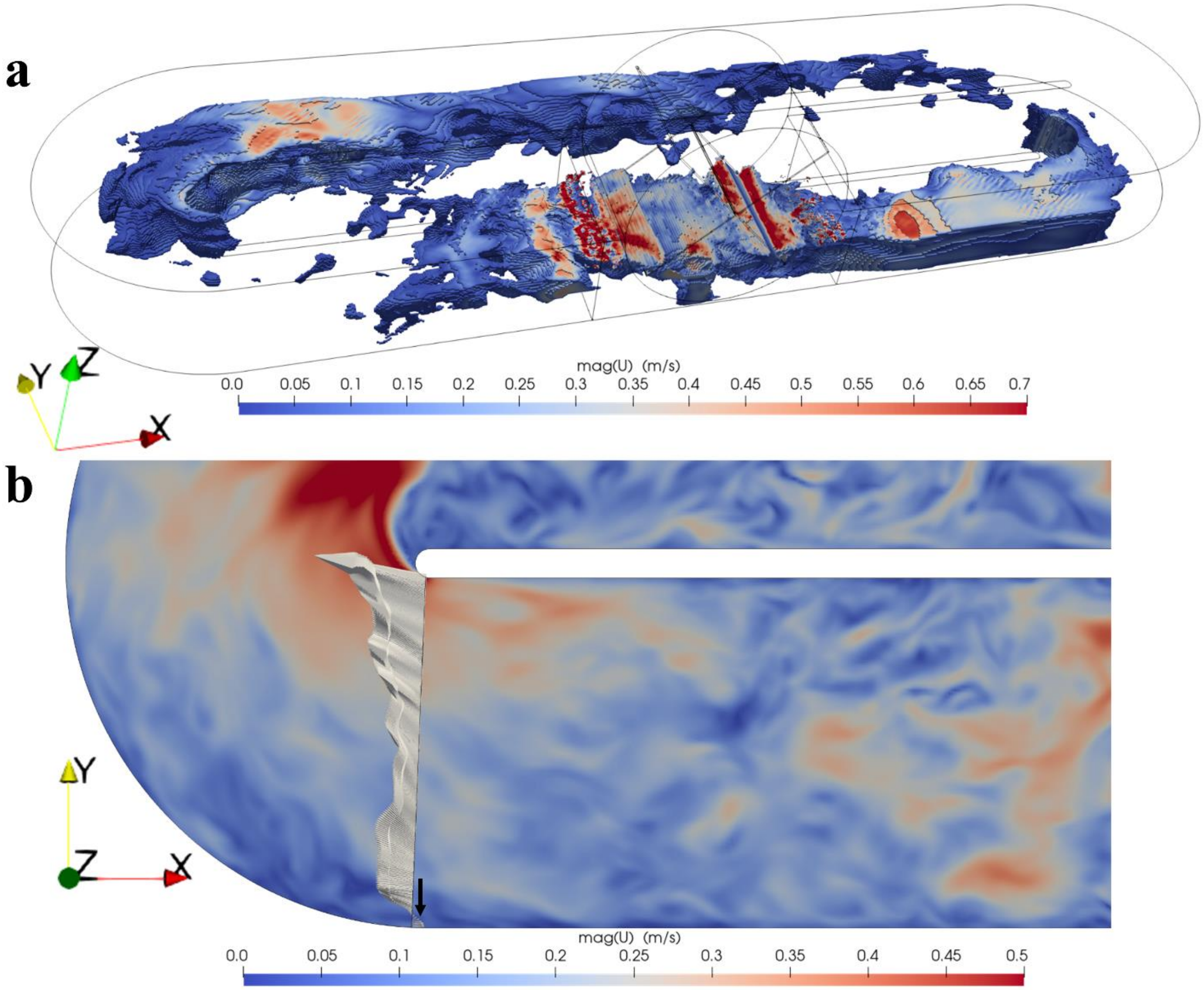

Figure. 3.5. Illustration of secondary flow phenomena and boundary layer separation. (a) Demonstration that high velocity magnitude region (mag($\boldsymbol{u}$) > 0.35 m/s) shifted from near to surface to the outer region of the channel downstream the hairpin bends due to centripetal forces. (b) Contours of mag($\boldsymbol{u}$) at z = 0.05 m and the velocity vectors along with a line probe indicates that boundary layer separation occurs at the entrance of the hairpin bend.

3.3.3 Spatial pattern of the swirling motions

One major finding of this study is that it is found a different number of occurrences of swirling motion exhibits for different *SR* of the ponds. For *SR* ≈ 1, one occurrence of swirling motion can be found downstream of the divider, as can be seen in Figure. 3.6a. Since the cross-section of the channel is close to a square, one occurrence of swirling motion is generated more frequently than multiple occurrences. For a larger pond where the *SR* > 1, multiple occurrences of swirling motion can be found downstream of the bends. For instance, Figure. 3.6b presents the velocity vectors with large abs(u_z) for *SR* = 7.05 where several instances can be found, one near the inner bend, one near the outer bend, and some in the middle of the channel. For an *SR* value much larger than 1 the channel cross-section is a thin rectangle, and it is more unlikely to form a single continuous vortex, but rather multiple discrete vortices.

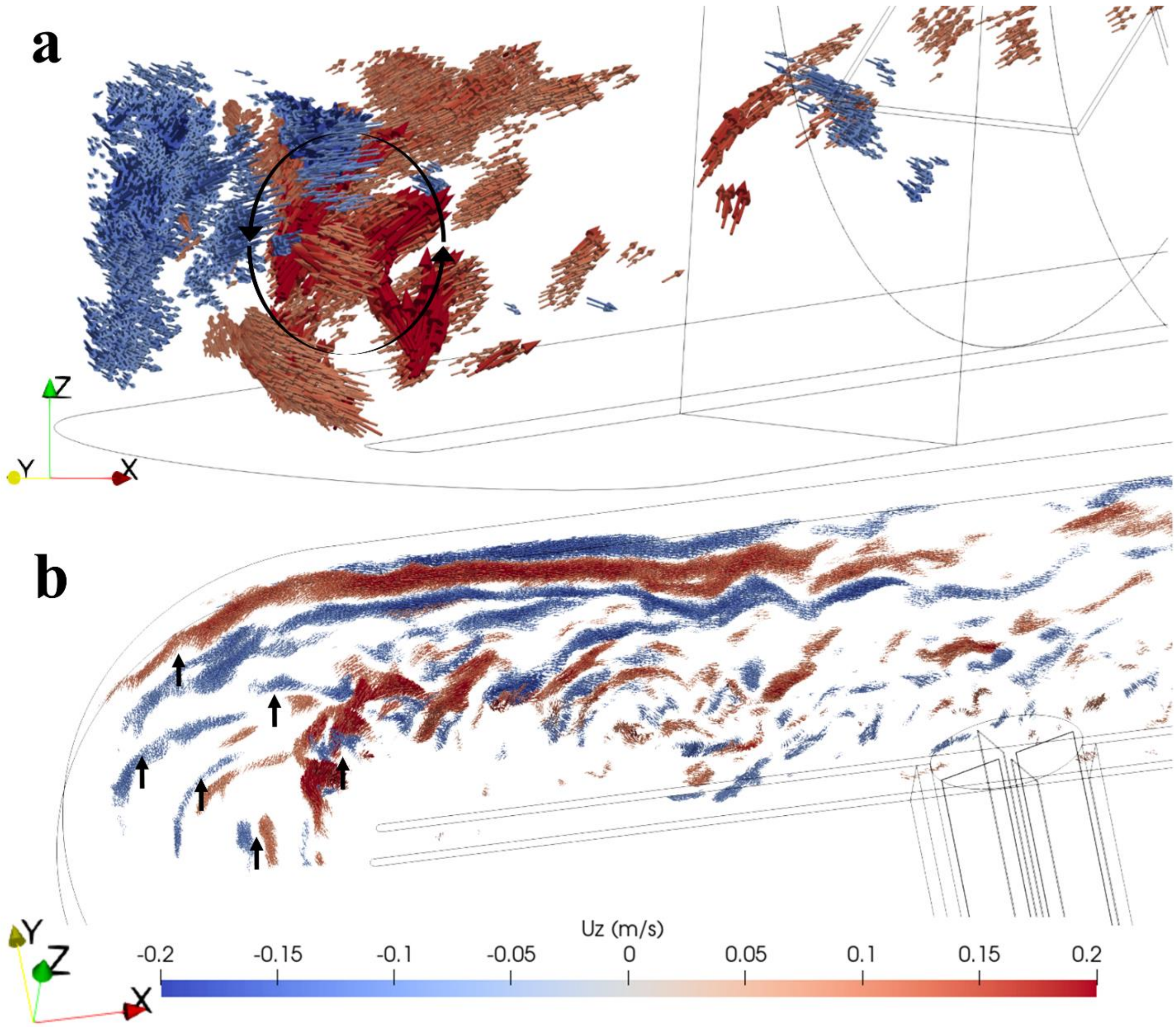

Figure. 3.6. different instances of swirling can be found for different *SR*. (a) the velocity field in the first hairpin band indicates one occurrence of clockwise swirling motion in the pond with *SR* = 1, RPM = 17; (b) the velocity field in the first hairpin band indicates multiple occurrences

of swirling motion present in the pond when $SR = 7.05$, RPM = 12.6.

Figure. 3.7 shows the velocity fields case in the vertical cross-sections at 90°, 135°, and 180° of the first bend for an $SR = 7.05$ raceway pond so that the fluid flows into the page. Interestingly, most vortices are counterclockwise, which can be found from the inner to the middle of the bend. However, one occurrence of a strong clockwise vortex can be found in the outer bend regions. Examining all the cases with different SR and RPM values, it is found that this result is true for most of the cases whose $SR > 1$. Since the persistence of swirling motion is the primary focus of this work, the reason for the existence of this clockwise vortex is not investigated further.

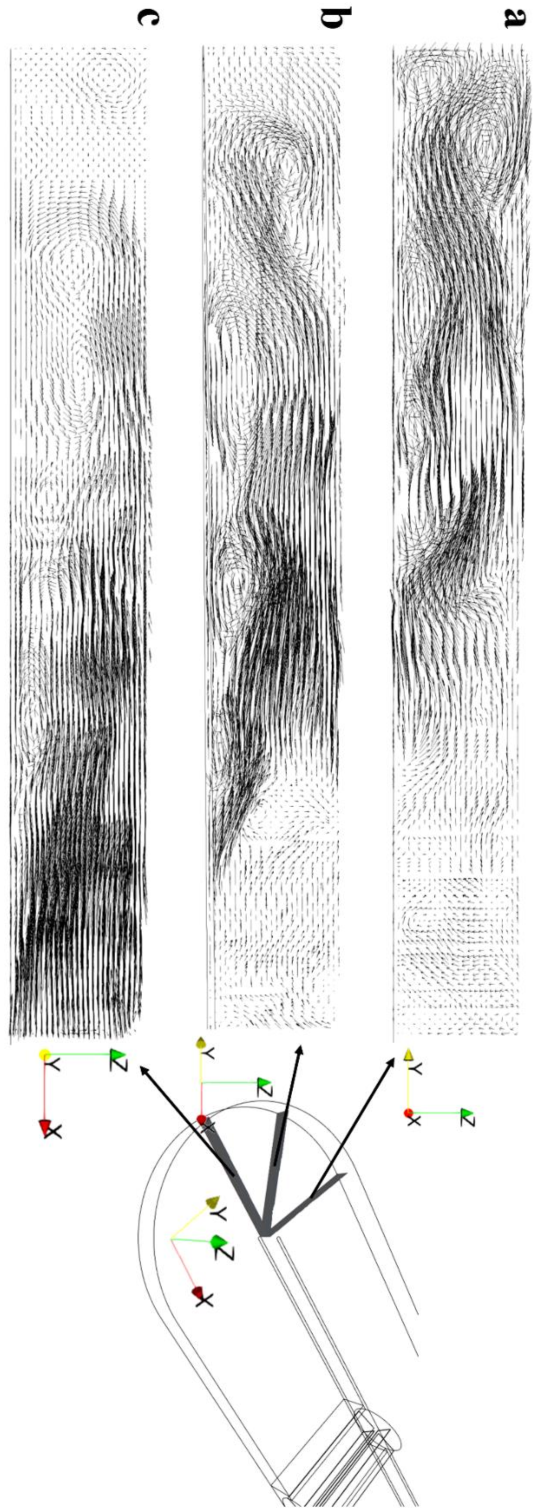

Figure. 3.7. Velocity fields in vertical cross-sections in the first hairpin band indicate the presence of multiple occurrences of swirling motion in the pond when *SR* = 7.05, RPM = 12.6. (a) vertical cross-section located at 90° in the first bend. (b) vertical cross-section located at 135° in the first bend. (c) vertical cross-section located at 180° in the first bend.

3.3.4 Persistence length of the swirling motion

The swirling motions are generated and enhanced by the centripetal force and boundary layer separation. Along with the straight sections, swirling motions are expected to promote vertical mixing in raceway ponds, increasing mass transfer and the L/D effect, and reducing cell stratification and chemical accumulation in dead zones. The swirling motions are the only motion that introduces vertical mixing in a raceway pond other than the rolling motions immediately downstream of the paddle wheel. These dampen and disappear after a relatively short distance. Investigation of the strength of the swirl generated by the 180° bends is critical to quantify the vertical mixing behavior and efficiency in a raceway pond. Due to the dissipation of kinetic energy, the effects of viscosity, and friction, the strength of swirling motions will attenuate with distance downstream of the bend in the straight section.

To understand how the swirling motion is propagated and determine how far it can persist, a total of 56 simulations of raceway ponds with 7 *SR* values are carried out for about 115 s for each case. Those cases are set up in such a way that the water depth is always close to 0.2 m, except for the extreme case with $SR = 0.5$, where a water depth of 0.28 m is used. $SR = 1$ corresponds to the RW0.5 mini raceway pond manufactured by MicroBio Engineering, and the largest raceway pond simulated with $SR = 7.05$ is close to their RW22 configuration. A raceway pond with $SR < 1$ is seldom used in practice but is investigated in this study to highlight secondary flow phenomena and vertical mixing in an extreme case.

Although swirl is a three-dimensional motion, the focus here is on vertical mixing; as such, the strength of the swirling motion is quantitatively characterized by the magnitude of the vertical velocity component abs(u_z) at each point in the liquid's computational domain. Once the liquid regions with low abs(u_z) values are filtered and removed by the algorithm, the remaining results clearly show the boundary and the shape of the region of swirling motion responsible for the most efficient vertical mixing. Therefore, $u_{z,\mathrm{cri}}$ is used to filter the velocity fields rather than using other more complex vortex detecting criteria such as the Q criteria and the λ2 criteria.

3.4.4.1 Characterize swirling motion based on $u_{z,\mathrm{cri}}$ corresponding to $L_p = 4R$

The $u_{z,\mathrm{cri}}$ which corresponds to $L_p = 4R$ is used to quantify the mixing performance and the strength of the swirling motion. The reason why $L_p = 4R$ is chosen as the criterion is provided later in this section. The approach to identify the critical velocity in this way is given in section 3.2.7.2. Figure. 3.8 displays the averaged velocity magnitude at the vertical cross-section where $x = 2R$ measured from the tip of the first bend, denoted as $\overline{U}_{2R}$. As the results of the continuity equation and the flow is incompressible and therefore divergence-free, the cross-sectional flow rate is the same across the channel. However, because of the effect of the paddle wheel, there exists a head loss all along the looped channel where the liquid depth is higher downstream the paddle than upstream of the paddle wheel. As the fluid encounters the first hairpin bend, the liquid depth is further raised, refed as superelevation in the literature [51-52]. Consequently, $\overline{U}_{2R}$ is used to represent the averaged velocity in the bend because the change of the liquid depth is considerably smaller than in the bend and the value is very close to the averaged velocity magnitude in the bend measured from 0 to 180 degrees of the bend. It is also found the averaged velocity magnitude in the bend plays a critical role in calculating the dimensionless group that characterizes $u_{z,\mathrm{cri}}$. Further, it is simple to measure $\overline{U}_{2R}$ rather than the averaged velocity in the bends. It can be observed from Figure. 3.8a that at lower paddle wheel tip velocity ranges ($0 \leq U_{tip} \leq 0.35$ m/s and $16140 < De < 96850$), $\overline{U}_{2R}$ increases linearly with U_{tip}. However, when U_{tip} is further increased, $\overline{U}_{2R}$ continues to increase but does not maintain the same linear relationship.

Instead, $\overline{U}_{2R}$ becomes sub-linear with U_{tip}. The ratio holds near a constant at a low U_{tip} region and then decreases at high U_{tip} region ranges, which is more obvious for the cases with lower *SR* as U_{tip} is larger for the same *De* value. This behavior has been observed by a previous investigation [53]. In that study, a pilot-scale 500 m^2 raceway pond 80 m long and 3 m wide was driven by a flat 8-bladed wheel and the velocity 5 m downstream of the paddle wheel was measured with the paddle wheel RPM from 3 to 10 for 0.3 m and 0.25 m liquid depths. It was discovered for both cases that the downstream velocity increased initially in response to paddle wheel RPM increase of up to 5 RPM, but thereafter increased slower in response to subsequent RPM increases. Additionally, it was reported that the efficiency of the paddle wheel, as measured by the ratio of acquired hydraulic power to input shaft power, dropped monotonically as the paddle wheel RPM increased. The decreased efficiency with paddle wheel RPM increase can be the result of several factors. First, the slip factor k_s is defined as the ratio of the contact fluid velocity and the blade:

$$\boldsymbol{u}_{fluid} = (1 - k_s)\boldsymbol{u}_{balde} \tag{3.11}$$

A linear relationship was reported by Hendricks (2005) between k_s with paddle wheel RPM as [54]

$$k_s = 0.074 + 0.007\times\text{RPM} \tag{3.12}$$

Eq. (12) indicates that when blade velocity rises, the slip factor increases, resulting in a decrease in efficiency as less blade momentum is converted to water momentum. There is a backflow beneath and around the paddle wheels due to the gap between the paddle wheel and the side and bottom walls. This backflow is exacerbated as the RPM of the paddle wheel increases, reducing net flow and therefore decreasing efficiency. Furthermore, by analyzing the CFD data, it is observed that more fluid is lifted by the paddle wheel and less fluid is pushed by it, which contributes to the decrease for efficiency. Additionally, analysis of the CFD data reveals that the paddle wheel lifts more fluid, and less fluid is pushed by it, contributing to the loss in efficiency. U_{tip} was used to compute *De* and calculate the RPM for each case, as the averaged velocity in the bends was unknown prior to performing the CFD simulations. However, the averaged velocity in the bends is more appropriate to be used to define *Re* in the bends and consequently, *De* for the secondary flow as the magnitude of the fluid velocity may be less than the U_{tip} due to head loss, the friction of the wall, and the slipping coefficient. Therefore, $\overline{U}_{2R}$, which is close to the averaged velocity in the bend, is a more appropriate choice as the characteristic velocity used to define *Re* and *De*.

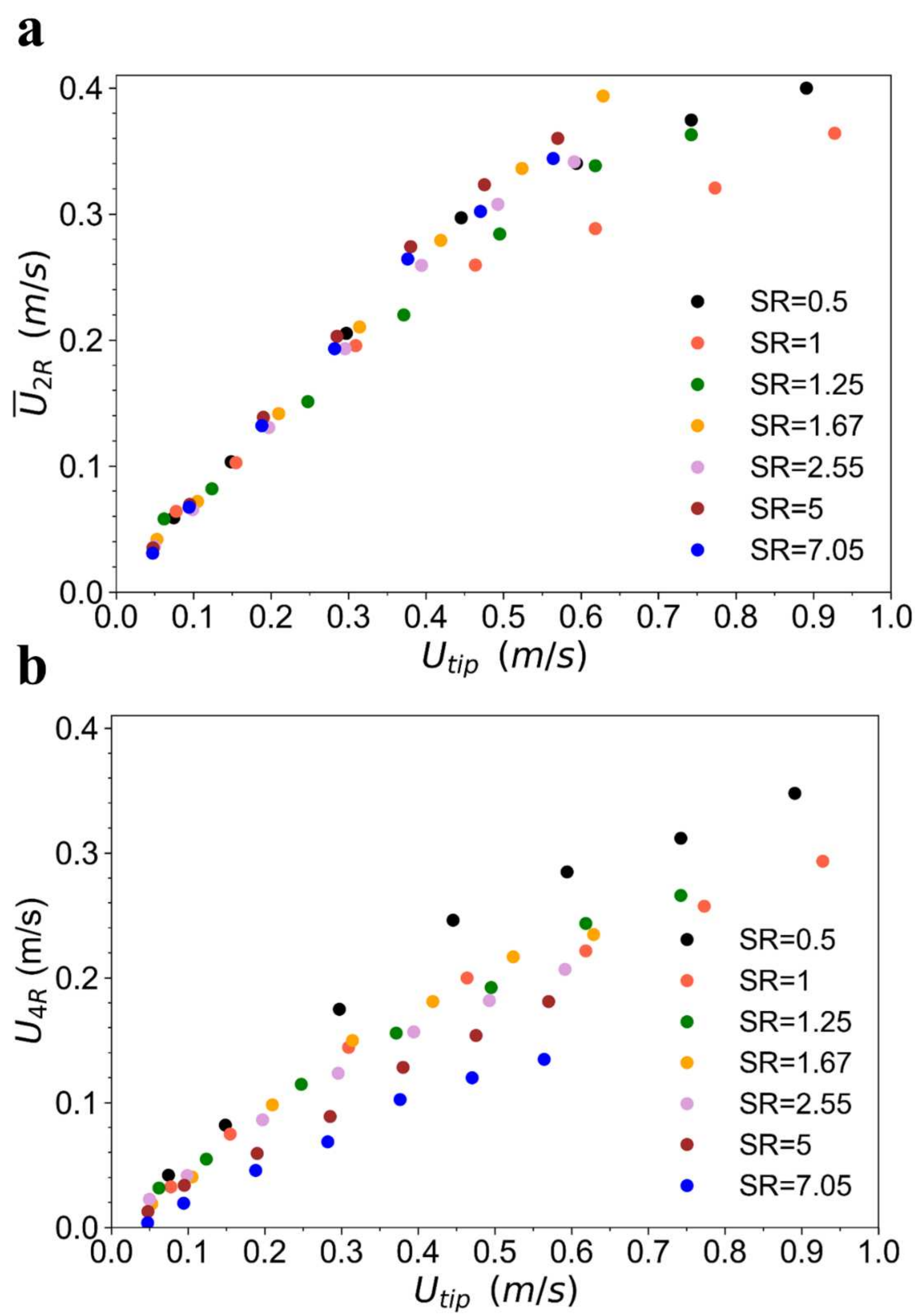

Figure. 3.8. $\overline{U}_{2R}$ and U_{4R} versus U_{tip} (a) averaged velocity magnitude in the vertical cross-section where $x = 2R$ measured from the tip of the first bend $\overline{U}_{2R}$ response to the paddle wheel tip velocity U_{tip}. (b) $u_{z,cri}$ corresponding to $L_p = 4R$ (U_{4R}) versus the paddle wheel tip velocity U_{tip}.

Figure. 3.8b shows U_{4R}, which is the $u_{z,\mathrm{cri}}$ corresponding to $L_p = 4R$, versus U_{tip}. Similar to the behavior of $\overline{U}_{2R}$, U_{4R} increases linearly at lower U_{tip}, and becomes sub-linear at higher U_{tip} values, which indicates that U_{4R} is better correlated with $\overline{U}_{2R}$ than U_{tip}. Given this observation, U_{tip} should increase linearly with $\overline{U}_{2R}$ at all tip velocities. Figure. 3.9a shows the value of U_{4R} with respect to $\overline{U}_{2R}$ for all the bend geometries. It can be observed that a linear correlation can be identified for all the ranges of $\overline{U}_{2R}$. Furthermore, the slopes of the correlation curves indicates that a raceway pond design with lower SR will have a higher slope where the SR = 0.5 case has the largest slope of 0.833 and the SR = 7.05 case has the lowest slope value of 0.385. This observation implies that increasing paddle wheel RPM results in a reduced increase in swirling motion strength for a pond with a higher SR compared with a lower SR. The largest root mean square error (RMSE) is 0.013 for SR = 2 and the lowest RMSE is 0.0034 for SR = 0.2. The low RMSE values suggest that U_{4R} has a strong linear dependence on $\overline{U}_{2R}$. Therefore, this leads to one of the critical findings that the strength of the generated swirling motion is linearly proportional to the averaged velocity magnitude in the bend under normal operating conditions ($16410 < De < 164140$).

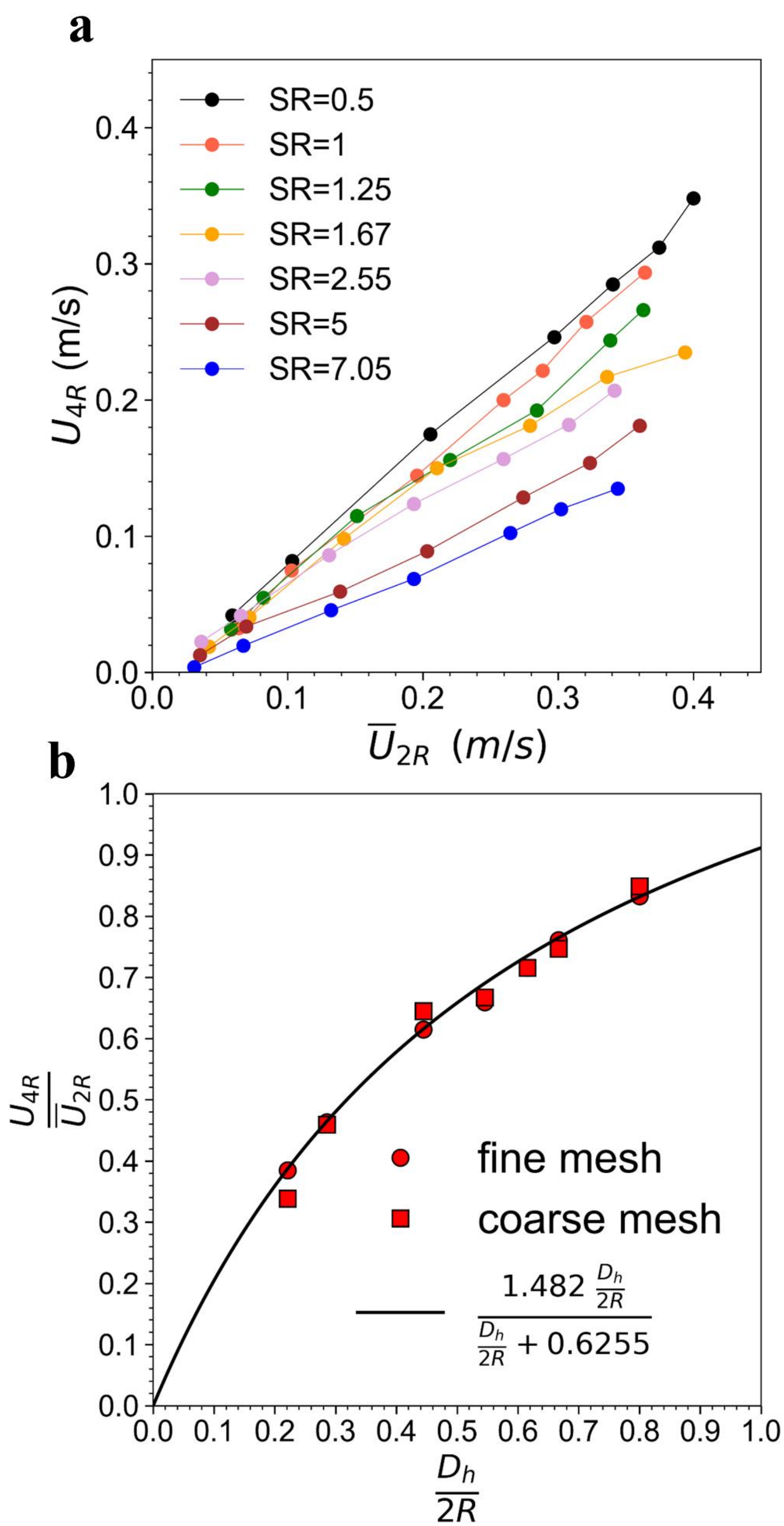

Figure. 3.9. A rational function can be used to predict U_{4R}. (a) U_{4R} versus averaged velocity magnitude at the vertical cross-section where $x = 2R$ measured from the tip of the first bend $\overline{U}_{2R}$ (b) $U_{4R}/\overline{U}_{2R}$ versus $D_h/2R$.

As $\overline{U}_{2R}$ is the characteristic velocity that determines *Re*, dimensional analysis indicates that the dimensionless variable $U_{4R}/\overline{U}_{2R}$ should correlate a dimensionless group associated with *De*. Because *Re* is already associated with $\overline{U}_{2R}$, it is reasonable to evaluate the remaining term inside *De*, that is, $D_h / 2R$.

Moreover, $D_h / 2R$ is the geometric parameter that contains the shape information of the raceway pond since $D_h / 2R$ only depends on *SR* with $w \approx R$. To predict the strength of swirling motions for a specific raceway pond, the relationship between $U_{4R}/\overline{U}_{2R}$ and $D_h / 2R$ is investigated. It is essential to confirm that the hydrodynamic characteristics of the swirling motion, especially U_{4R} and $\overline{U}_{2R}$ do not have a significant dependency on the mesh size. Therefore, a mesh independent study is performed where coarse meshes were used for all the cases. The mesh cell numbers range from 1,039,000 to 2,417,000 with the average of 1,561,000. The slope of $U_{4R}/\overline{U}_{2R}$ vs $D_h / 2R$ calculated from the fine meshes and coarse meshes are plotted in Figure. 3.9b. It is found that the relationship between these dimensionless numbers can be curve fitted using a rational function:

$$\frac{U_{4R}}{\overline{U}_{2R}} = \frac{p_1 \dfrac{D_h}{2R}}{\dfrac{D_h}{2R} + q_1} \tag{3.13}$$

The parameters are calculated using the curve fitting toolbox provided by Matlab 2019 in which the values of $p_1 = 1.527$ and $q_1 = 0.6834$ are determined. The R-square is calculated as 0.9959 with an RMSE of 0.01142, indicating that the curve fits the relationship exceptionally well. The rational function is chosen for various reasons. First, when *SR* goes to infinity, $D_h/2R$ goes to zero. At this condition, the radius of the pond goes to infinity, representing the extreme case when the width of the straight section goes to infinity and the liquid depth goes to zero. As the fluid domain is so thin that the fluid will mainly flow horizontally with extraordinarily weak vertical motions. Therefore, the ratio of the critical velocity and the mean velocity magnitude goes to zero. One of the advantages of a rational function is that it goes through the point (0,0) as well. However, when the *SR* is close to 0 represents the extreme case where the liquid depth goes to infinity, and the width of the channel goes to zero. With this geometric design, the value $D_h / 2R$ is close to 1. Therefore, the ratio between the critical velocity / mean velocity magnitude should be inclined to a certain value when $D_h / 2R$ approaches to one, however, the rational function chosen does not have this property. Nonetheless, the *SR* of a raceway pond is rarely smaller than 1 and the raceway pond geometry with an extremely low *SR* does not have practical usage and is beyond the scope of this work. Therefore, the rational function chosen is good enough to be used in raceway ponds for algal cultivation purposes with *SR* larger than 0.5.

At this point, two dimensionless groups of variables and a method are developed to predict the strength of the swirling motion in raceway pond systems. First, the value of $D_h / 2R$ is calculated and the averaged velocity at $x = 2R$ is either measured or calculated from CFD simulations. The second step is to calculate U_{4R}, which is the critical vertical velocity corresponding to a persistence length of 4*R* using Eq. (13).

3.4.4.2 Characterize swirling motion by L_p based on $u_{z,\mathrm{cri}}$.

Other methods to quantify the strength of the swirling motions include (1) defining a constant critical velocity threshold $u_{z,\mathrm{cri}}$ for abs(u_z) and determining the persistence length associated with this critical velocity; (2) defining critical velocities based on the operating conditions such as *De*, *Re*, and pond size. It's necessary to take *Re* into account when defining

$u_{z,\text{cri}}$ because it contains the characteristic velocity of the flow, which in turn is based on the paddle wheel tip speed. Thus, method (1) has significant disadvantages. If the same critical velocity is chosen for all the cases, difficulty arises where the L_p becomes close to zero if $u_{z,\text{cri}}$ is set too high and L_p tends to fill the straight section if $u_{z,\text{cri}}$ is set too low. Additionally, filtering regions with abs(u_z) < $u_{z,\text{cri}}$ fails to identify the boundary of the region of swirling motion when the critical velocity is set too high. As a result, no appropriate single value of $u_{z,\text{cri}}$ exists that is applicable to all the different pond sizes and paddle wheel speeds. Thus, distinct $u_{z,\text{cri}}$ values must be determined for each situation involving a specific geometric design and operating conditions.

In this study, it was found that the persistence length for a given geometry and paddle speed depends significantly on the choice of $u_{z,\text{cri}}$. With a larger value of $u_{z,\text{cri}}$, less volume of the liquid phase where abs($\underline{u}_z$) > $u_{z,\text{cri}}$ will be preserved after filtering the region where abs(u_z) < $u_{z,\text{cri}}$, and therefore, the persistence length will be shorter and vice versa. The choice was made to determine $u_{z,\text{cri}}$ by monitoring the velocity field of the liquid in the pond for 15 s and is set to be the top 3% of the magnitude of the vertical velocity components throughout the bend (from 90° to 180°). This 3% value is chosen because it recapitulates well the shape and boundaries of the swirling motion as visualized in the CFD simulation and varying the percentage value to 4% does not change the boundary significantly, demonstrated in Figure. 3.10. Figure. 3.10a represents the abs(u_z) contour at the z = 0.1 m horizontal plane. The strength of the swirling motion is determined by the magnitude of abs(u_z). Figure. 3.10b shows the region when $u_{z,\text{cri}}$ is set to be the top 3% of the magnitude of the vertical velocity component (red) and 4% (blue). Varying the $u_{z,\text{cri}}$ criteria from 3% to 4% does not have a significant impact on the volume of the preserved region, i.e., the region associated with swirl.

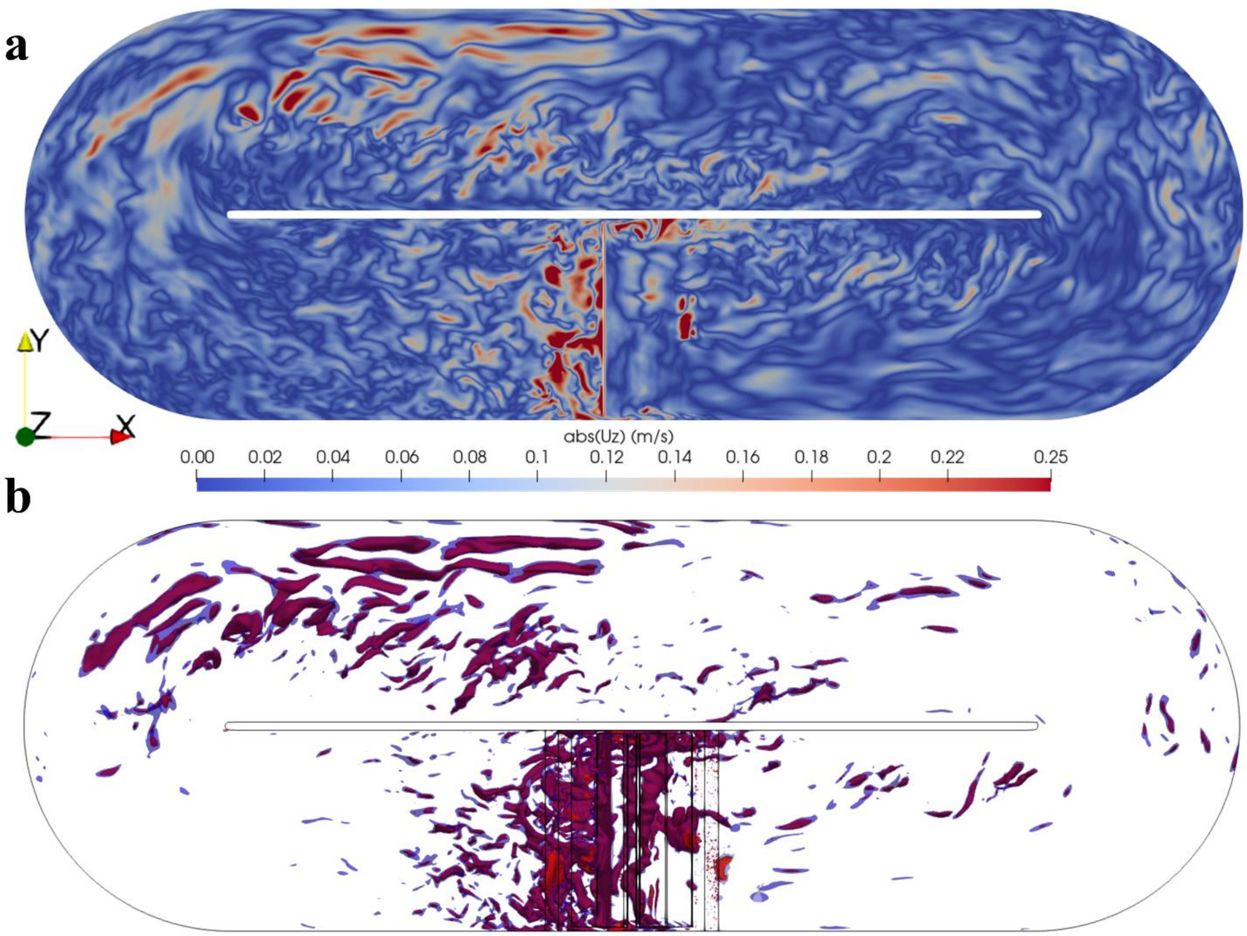

Figure. 3.10. Illustration of top 3% vertical velocity in the 90° to 180° region of the first hairpin bend can be used as $u_{z,\mathrm{cri}}$. (a) abs(u_z) contours at the z = 0.1 m horizontal plane in a raceway pond with SR = 7.05, RPM = 12.6. (b) iso-surfaces of $u_{z,\mathrm{cri}}$ = top 3% (red) and 4% (blue) of the magnitude of the abs(u_z) predicted in the 90° to 180° region of the first hairpin bend.

Once the top 3% of the vertical velocity component in the bend is chosen to calculate $u_{z,\mathrm{cri}}$, the L_p is given in Figure. 3.11. It can be observed that for the same SR, the $u_{z,\mathrm{cri}}$ values increase with paddle wheel RPM. However, the results do not reflect strong correlations between the $u_{z,\mathrm{cri}}$ and SR for the same De across the pond sizes. On the other hand, the dependence of the persistence distance on De as well as SR is not easy to determine either, which indicates that the criterion for choosing critical velocity as the top 3% of the vertical velocity component might not be the best approach. Nonetheless, Figure. 3.11 indicates that the $3R \leq L_p \leq 5R$ for the majority of cases when using the top 3% of the vertical velocity component as the criterion.

Additionally, the straight section of the *SR* = 7.05 design is approximately 4.1 times the width. Therefore, the method introduced in the previous section where U_{4R} was used as the indicator for the strength of the swirling motion was used. However, it is believed that a similar rational relationship can be established for $u_{z,\mathrm{cri}}$ corresponding with $L_p > 4R$.

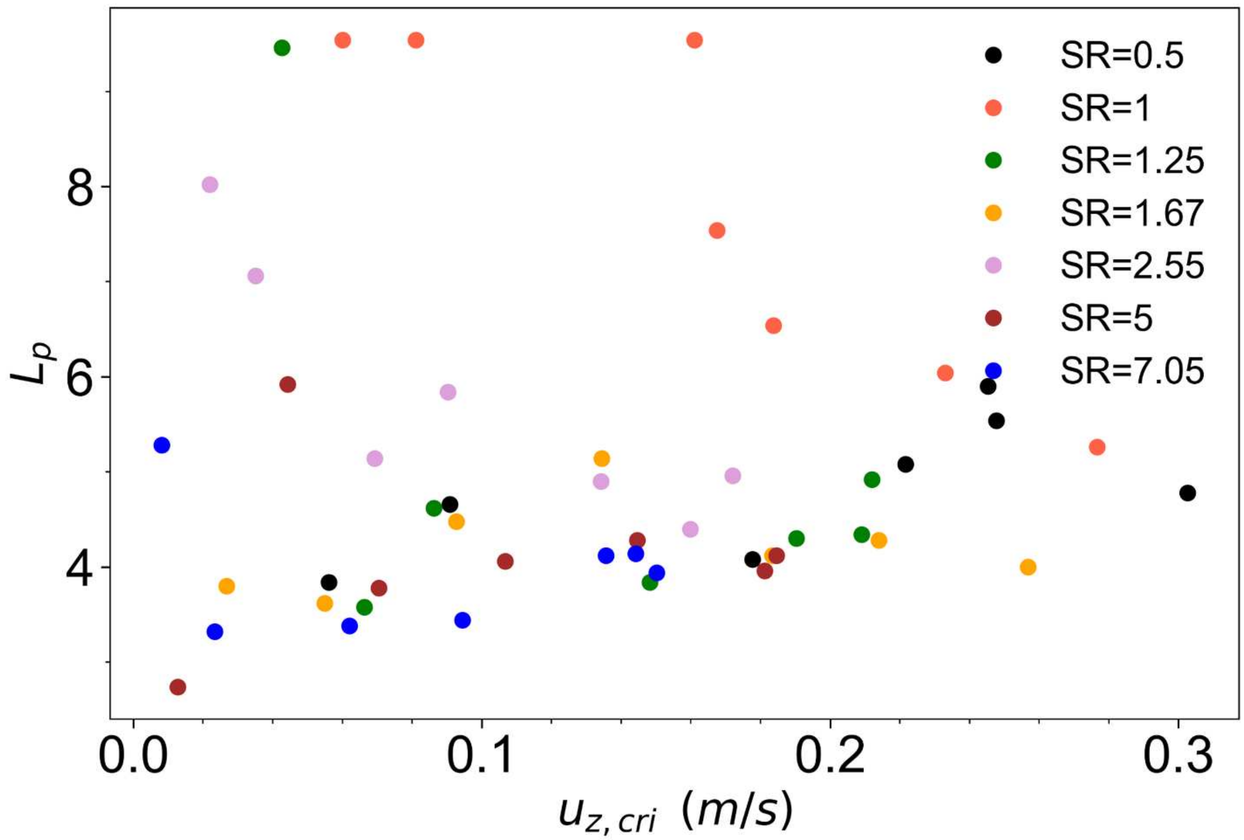

Figure. 3.11. Predicted L_p using $u_{z,\mathrm{cri}}$ = top 3% of the magnitude of the abs(u_z) predicted in the 90° to 180° region of the first hairpin bend.

3.4. Conclusion

In this study, a total of 56 cases with 7 geometric raceway pond designs and 8 paddle wheel rotation rates are carried out and the findings are:

1. Numerical simulations are carried out using an open source CFD package openFoam6.0. The results of the baseline raceway pond using openFoam is compared with the results using ANSYS Fluent, which has been validated with experimental data. It is found that

openFoam is a good tool to accurately simulate the raceway pond.

2. The swirling motion is generated as the high velocity region of the fluid shifts from the surface to the outer bend due to centripetal force caused by the geometry of the hairpin bends. A secondary reason is that there exist negative pressure gradients which cause the boundary layer separation. These driving forces for swirling motion indicate that baffles or other passive devices near the bend may further enhance boundary layer separation and increase the strength of the swirling motion.

3. For a *SR* close to 1, one instance of swirling is observed, while for a larger pond with a smaller *SR* (close to 0), multiple instances of swirling motion are found in the hairpin bend and propagate down the straight section.

4. A method to identify a critical velocity indicator of swirl is proposed. It is the value associated with the persistence of continuous vertical motion over a length four times the radius of the 180° bend. Further, it is found that there exists a linear relationship under normal operating conditions between the critical velocity parameter and the mean velocity near the bend region. This result is consistent with the linear dependence of *De* on *Re*.

5. The slope of critical velocity versus mean velocity is calculated to represent the relationship between the slops and the dimensionless group ($D_h / 2R$) is determined as a rational function. This will be helpful to determine the critical velocity for any raceway ponds under normal operating conditions without requiring an expensive simulation or numerous measurements.

3.5 References

[1] C. S. Jones and S. P. Mayfield, "Algae biofuels: versatility for the future of bioenergy,"

Curr. Opin. Biotechnol., vol. 23, no. 3, pp. 346–351, Jun. 2012, doi: 10.1016/j.copbio.2011.10.013.

[2] Y. Ghasemi, S. Rasoul-Amini, A. T. Naseri, N. Montazeri-Najafabady, M. A. Mobasher, and F. Dabbagh, "Microalgae biofuel potentials (Review)," *Appl. Biochem. Microbiol.*, vol. 48, no. 2, pp. 126–144, Mar. 2012, doi: 10.1134/S0003683812020068.

[3] Y. Chisti, "Biodiesel from microalgae beats bioethanol," *Trends Biotechnol.*, vol. 26, no. 3, pp. 126–131, Mar. 2008, doi: 10.1016/j.tibtech.2007.12.002.

[4] H. M. Amaro, Â. C. Macedo, and F. X. Malcata, "Microalgae: An alternative as sustainable source of biofuels?," *Energy*, vol. 44, no. 1, pp. 158–166, Aug. 2012, doi: 10.1016/j.energy.2012.05.006.

[5] Y. Chisti, "Biodiesel from microalgae," *Biotechnol. Adv.*, vol. 25, no. 3, pp. 294–306, May 2007, doi: 10.1016/j.biotechadv.2007.02.001.

[6] R. Davis, A. Aden, and P. T. Pienkos, "Clarens, AF, Resurreccion, EP, White, MA, & Colosi, LM (2010). Environmental Life Cycle Comparison of Algae to Other Bioenergy Feedstocks. Environmental Science & Technology, 44 (5), 1813-1819. doi: 10.1021/es902838n," *Use Algae Landfill Leachate Treat. Syst.*, vol. 44, no. 5, p. 7, 2017.

[7] S. Basu, A. S. Roy, K. Mohanty, and A. K. Ghoshal, "CO2 biofixation and carbonic anhydrase activity in Scenedesmus obliquus SA1 cultivated in large scale open system," *Bioresour. Technol.*, vol. 164, pp. 323–330, Jul. 2014, doi: 10.1016/j.biortech.2014.05.017.

[8] E. W. Becker, *Microalgae: Biotechnology and Microbiology*. Cambridge University Press, 1994.

[9] J. U. Grobbelaar, L. Nedbal, and V. Tichý, "Influence of high frequency light/dark fluctuations on photosynthetic characteristics of microalgae photoacclimated to different

light intensities and implications for mass algal cultivation," *J. Appl. Phycol.*, vol. 8, no. 4, pp. 335–343, Jul. 1996, doi: 10.1007/BF02178576.

[10] M. Janssen *et al.*, "Efficiency of light utilization of Chlamydomonas reinhardtii under medium-duration light/dark cycles," *J. Biotechnol.*, vol. 78, no. 2, pp. 123–137, Mar. 2000, doi: 10.1016/S0168-1656(99)00233-3.

[11] J. C. Merchuk, M. Ronen, S. Giris, and S. (Malis) Arad, "Light/dark cycles in the growth of the red microalga Porphyridium sp.," *Biotechnol. Bioeng.*, vol. 59, no. 6, pp. 705–713, 1998, doi: 10.1002/(SICI)1097-0290(19980920)59:6<705::AID-BIT7>3.0.CO;2-J.

[12] S. Xue, Z. Su, and W. Cong, "Growth of Spirulina platensis enhanced under intermittent illumination," *J. Biotechnol.*, vol. 151, no. 3, pp. 271–277, Feb. 2011, doi: 10.1016/j.jbiotec.2010.12.012.

[13] W. R. Dean, "LXXII. The stream-line motion of fluid in a curved pipe (Second paper)," *Lond. Edinb. Dublin Philos. Mag. J. Sci.*, vol. 5, no. 30, pp. 673–695, Apr. 1928, doi: 10.1080/14786440408564513.

[14] W. R. Dean, "XVI.Note on the motion of fluid in a curved pipe," *Lond. Edinb. Dublin Philos. Mag. J. Sci.*, vol. 4, no. 20, pp. 208–223, Jul. 1927, doi: 10.1080/14786440708564324.

[15] M. Vaghefi, M. Akbari, and A. R. Fiouz, "An experimental study of mean and turbulent flow in a 180 degree sharp open channel bend: Secondary flow and bed shear stress," *KSCE J. Civ. Eng.*, vol. 20, no. 4, pp. 1582–1593, May 2016, doi: 10.1007/s12205-015-1560-0.

[16] K. Blanckaert, "Hydrodynamic processes in sharp meander bends and their morphological implications," *J. Geophys. Res. Earth Surf.*, vol. 116, no. F1, 2011, doi: 10.1029/2010JF001806.

[17] S. N. BARUA, “ON SECONDARY FLOW IN STATIONARY CURVED PIPES,” *Q. J. Mech. Appl. Math.*, vol. 16, no. 1, pp. 61–77, Feb. 1963, doi: 10.1093/qjmam/16.1.61.

[18] R. W. Detra, “The secondary flow in curved pipes,” ETH Zurich, 1953. doi: 10.3929/ETHZ-A-000091196.

[19] R. Gerard, “Secondary Flow in Noncircular Conduits,” *J. Hydraul. Div.*, vol. 104, no. 5, pp. 755–773, May 1978, doi: 10.1061/JYCEAJ.0004999.

[20] M. Murakami, Y. Shimizu, and H. Shiragami, “Studies on Fluid Flow in Three-Dimensional Bend Conduits,” 1969, doi: 10.1299/JSME1958.12.1369.

[21] M. Falcon, “Secondary Flow in Curved Open Channels,” *Annu. Rev. Fluid Mech.*, vol. 16, no. 1, pp. 179–193, 1984, doi: 10.1146/annurev.fl.16.010184.001143.

[22] H. Kikkawa, A. Kitagawa, and S. Ikeda, “Flow and Bed Topography in Curved Open Channels,” *J. Hydraul. Div.*, vol. 102, no. 9, pp. 1327–1342, Sep. 1976, doi: 10.1061/JYCEAJ.0004615.

[23] S. Yadala and S. Cremaschi, “A Dynamic Optimization Model for Designing Open-Channel Raceway Ponds for Batch Production of Algal Biomass,” *Processes*, vol. 4, no. 2, Art. no. 2, Jun. 2016, doi: 10.3390/pr4020010.

[24] S. S. Sawant, H. P. Khadamkar, C. S. Mathpati, R. Pandit, and A. M. Lali, “Computational and experimental studies of high depth algal raceway pond photo-bioreactor,” *Renew. Energy*, vol. 118, pp. 152–159, Apr. 2018, doi: 10.1016/j.renene.2017.11.015.

[25] Z. Yang, J. Cheng, Q. Ye, J. Liu, J. Zhou, and K. Cen, “Decrease in light/dark cycle of microalgal cells with computational fluid dynamics simulation to improve microalgal growth in a raceway pond,” *Bioresour. Technol.*, vol. 220, pp. 352–359, Nov. 2016, doi: 10.1016/j.biortech.2016.08.094.

[26] T. Pirasaci, A. Manisali, I. Dogaris, G. Philippidis, and A. Sunol, “Hydrodynamic design of an enclosed Horizontal BioReactor (HBR) for algae cultivation,” *Algal Res.*, vol. 28, pp. 57–65, Dec. 2017, doi: 10.1016/j.algal.2017.10.009.

[27] K. Liffman, D. A. Paterson, P. Liovic, and P. Bandopadhayay, “Comparing the energy efficiency of different high rate algal raceway pond designs using computational fluid dynamics,” *Chem. Eng. Res. Des.*, vol. 91, no. 2, pp. 221–226, Feb. 2013, doi: 10.1016/j.cherd.2012.08.007.

[28] R. Peralta Muniz Moreira, A. Cabrera Reina, P. Soriano Molina, J. A. Sánchez Pérez, and G. Li Puma, “Computational fluid dynamics (CFD) modeling of removal of contaminants of emerging concern in solar photo-Fenton raceway pond reactors,” *Chem. Eng. J.*, vol. 413, p. 127392, Jun. 2021, doi: 10.1016/j.cej.2020.127392.

[29] C. Inostroza, A. Solimeno, J. García, J. M. Fernández-Sevilla, and F. G. Acién, “Improvement of real-scale raceway bioreactors for microalgae production using Computational Fluid Dynamics (CFD),” *Algal Res.*, vol. 54, p. 102207, Apr. 2021, doi: 10.1016/j.algal.2021.102207.

[30] H. Ali, T. A. Cheema, and C. W. Park, “Effect of Paddle-Wheel Pulsating Velocity on the Hydrodynamic Performance of High-Rate Algal Ponds,” *J. Energy Eng.*, vol. 141, no. 4, p. 04014039, Dec. 2015, doi: 10.1061/(ASCE)EY.1943-7897.0000219.

[31] J. Huang *et al.*, “Investigation on the performance of raceway ponds with internal structures by the means of CFD simulations and experiments,” *Algal Res.*, vol. 10, pp. 64–71, Jul. 2015, doi: 10.1016/j.algal.2015.04.012.

[32] H. Amini *et al.*, “Numerical and experimental investigation of hydrodynamics and light transfer in open raceway ponds at various algal cell concentrations and medium depths,”

Chem. Eng. Sci., vol. 156, pp. 11–23, Dec. 2016, doi: 10.1016/j.ces.2016.09.003.

[33] J. Cheng, W. Guo, C. Cai, Q. Ye, and J. Zhou, “Alternatively permutated conic baffles generate vortex flow field to improve microalgal productivity in a raceway pond,” *Bioresour. Technol.*, vol. 249, Oct. 2017, doi: 10.1016/j.biortech.2017.10.031.

[34] P. Ranganathan, J. C. Amal, S. Savithri, and A. Haridas, “Experimental and modelling of Arthrospira platensis cultivation in open raceway ponds,” *Bioresour. Technol.*, vol. 242, pp. 197–205, Oct. 2017, doi: 10.1016/j.biortech.2017.03.150.

[35] S. Park and Y. Li, “Integration of biological kinetics and computational fluid dynamics to model the growth of Nannochloropsis salina in an open channel raceway,” *Biotechnol. Bioeng.*, vol. 112, no. 5, pp. 923–933, May 2015, doi: 10.1002/bit.25509.

[36] H. Tennekes and J. L. Lumley, *A First Course in Turbulence*. MIT Press, 2018.

[37] S. Kashyap, C. D. Rennie, R. Townsend, G. Constantinescu, and T. E. Tokyay, “Flow around submerged groynes in a sharp bend using a 3D LES model,” p. 9.

[38] R. Tunstall, D. Laurence, R. Prosser, and A. Skillen, “Large eddy simulation of a T-Junction with upstream elbow: The role of Dean vortices in thermal fatigue,” 2016, doi: 10.1016/J.APPLTHERMALENG.2016.07.011.

[39] H. G. Weller, G. Tabor, H. Jasak, and C. Fureby, “A tensorial approach to computational continuum mechanics using object-oriented techniques,” *Comput. Phys.*, vol. 12, no. 6, pp. 620–631, Nov. 1998, doi: 10.1063/1.168744.

[40] H. Jasak, “Dynamic Mesh Handling in OpenFOAM,” in *47th AIAA Aerospace Sciences Meeting including The New Horizons Forum and Aerospace Exposition*, American Institute of Aeronautics and Astronautics. doi: 10.2514/6.2009-341.

[41] J. Crank and P. Nicolson, “A practical method for numerical evaluation of solutions of

partial differential equations of the heat-conduction type," *Math. Proc. Camb. Philos. Soc.*, vol. 43, no. 1, pp. 50–67, Jan. 1947, doi: 10.1017/S0305004100023197.

[42] A. Syrakos, S. Varchanis, Y. Dimakopoulos, A. Goulas, and J. Tsamopoulos, "A critical analysis of some popular methods for the discretisation of the gradient operator in finite volume methods," *Phys. Fluids*, vol. 29, no. 12, p. 127103, Dec. 2017, doi: 10.1063/1.4997682.

[43] C. W. Hirt and B. D. Nichols, "Volume of fluid (VOF) method for the dynamics of free boundaries," *J. Comput. Phys.*, vol. 39, no. 1, pp. 201–225, Jan. 1981, doi: 10.1016/0021-9991(81)90145-5.

[44] K. J. Vachaparambil and K. E. Einarsrud, "Comparison of Surface Tension Models for the Volume of Fluid Method," *Processes*, vol. 7, no. 8, Art. no. 8, Aug. 2019, doi: 10.3390/pr7080542.

[45] H. Hemida, "OpenFOAM tutorial: Free surface tutorial using interFoam and rasInterFoam," p. 31.

[46] H. Rusche, "Computational fluid dynamics of dispersed two-phase flows at high phase fractions," Ph.D., Imperial College London (University of London), 2003. Accessed: Oct. 02, 2021. [Online]. Available: http://hdl.handle.net/10044/1/8110

[47] P. Cifani, W. R. Michalek, G. J. M. Priems, J. G. M. Kuerten, C. W. M. van der Geld, and B. J. Geurts, "A comparison between the surface compression method and an interface reconstruction method for the VOF approach," *Comput. Fluids*, vol. 136, pp. 421–435, Sep. 2016, doi: 10.1016/j.compfluid.2016.06.026.

[48] E. Berberović, N. P. van Hinsberg, S. Jakirlić, I. V. Roisman, and C. Tropea, "Drop impact onto a liquid layer of finite thickness: Dynamics of the cavity evolution," *Phys.*

Rev. E, vol. 79, no. 3, p. 036306, Mar. 2009, doi: 10.1103/PhysRevE.79.036306.

[49] S. Deshpande, L. Anumolu, and M. Trujillo, "Evaluating the performance of the two-phase flow solver interFoam," *Comput. Sci. Discov.*, vol. 5, Nov. 2012, doi: 10.1088/1749-4699/5/1/014016.

[50] A. Yoshizawa, "Statistical theory for compressible turbulent shear flows, with the application to subgrid modeling," *Phys. Fluids*, vol. 29, no. 7, pp. 2152–2164, Jul. 1986, doi: 10.1063/1.865552.

[51] K. Blanckaert, Ed., "Secondary currents measured in sharp open-channel bends," *River Flow 2002 5th Int. Conf Hydroinformatics*, 2002.

[52] K. Blanckaert and W. H. Graf, "Mean Flow and Turbulence in Open-Channel Bend," *J. Hydraul. Eng.*, vol. 127, no. 10, pp. 835–847, Oct. 2001, doi: 10.1061/(ASCE)0733-9429(2001)127:10(835).

[53] E. Musgrove, "Investigating the performance of paddlewheels used in microalgae raceways for the production of biomass," phd, University of Southampton, 2017. Accessed: Oct. 02, 2021. [Online]. Available: https://eprints.soton.ac.uk/420751/

[54] D. W. Hendricks, *Water Treatment Unit Processes: Physical and Chemical*. CRC Press, 2018.

Chapter 4 Investigation of the light environment in a raceway pond using particle tracking

4.1. Introduction

Open raceway ponds are paddle wheel driven outdoor bioreactors that have been widely used to cultivate microalgae [1-5]. However, compared to lab-scale enclosed bioreactors, the production rates in raceway ponds are usually lower [6-7]. The limiting factors causing this discrepancy include the culture media recipe, microalgae species, mixing performance, pH, temperature, and light environment. Among those factors, the light availability and light/dark (L/D) effect are reported to dominate the microalgae growth rate [8]. The intensity of light drops dramatically with distance from the air-liquid interface, especially in the case of high-density culture media. The cells close to the interface are exposed to a high light intensity such that photoinhibition can potentially occur, and the cells located further from the interface experience low enough light exposure that photolimitation occurs.

The L/D effect is reported to enhance photosynthesis when cells are cycling between the light and dark zones with a suitable frequency [9-10]. Therefore, the microalgae cells' trajectories have a significant impact on the light environment experienced by the cells and hence, the biomass productivity. The cells' motion is almost completely controlled by the liquid velocity field and the vertical mixing behavior of the raceway pond system.

Computational fluid dynamics (CFD) has been widely used to resolve cells' trajectories where microalgae cells are modeled as a discrete phase governed by equations of motion, and their trajectories are integrated of the acceleration rates created by pressure, gravity, drag, lift, and added mass in an Euler–Lagrange scheme [11-14]. Compared to traditional experimental techniques involving acoustic- or laser-based measurement techniques, CFD simulations are significantly less expensive in terms of capital and manpower. Particles can be tracked in a deterministic manner using a steady-state velocity field predicted by CFD simulations by which particles are injected and subsequently tracked. The drawbacks of this steady-state tracking method are that particles can be trapped in a recirculation zone or concentrated at a location where the velocity field is not divergence-free due to numerical error. Both situations are not physically realistic. Conversely, transient particle tracking solves the particles' trajectories coupled with the velocity fields that are updated at each time step. More realistic trajectories can be predicted using transient particle tracking, although this method requires much more computational expense since the Navier-Stokes equations must be solved at each time step.

The current study demonstrates a new method to efficiently perform particle tracking in raceway ponds. The particle trajectories are then converted to the light intensity where the main parameter, light peak to light (L/L) peak interval, is analyzed statistically. Closely related to the L/D frequency, the probability density function (PDF) of L/L intervals can be fit to a lognormal distribution. Moreover, a correlation between the PDF of the L/L interval and abs(u_z) is established. The spatial distributions of L/D transitions are analyzed by varying the size of the raceway ponds and the RPM of the paddle wheel.

4.2. Material and methods

4.2.1. The geometry of the mesoscale raceway pond and numerical tool

The geometry, paddle wheel RPM, pond surface area, and water depth are provided in

Table. 4.1. The velocity fields are predicted using the methods covered in section 3.2.2. To validate that pre-calculated velocity fields can be reliably used for particle tracking and comparable particle tracking results can be expected, a meso-scale raceway pond with shape ratio *SR* = 2.55, RPM = 13.6 was simulated for 1200 s and coupled with transient particle tracking. The *SR* is defined as the ratio of the width of the straight section to the liquid depth.

Table. 4.1 The dimensions and the operating conditions of the raceway ponds for particle tracking such as the length (L), width (W), liquid depth (H), *SR* and surface area.

case	L(m)	W(m)	H(m)	SR	Surface area (m^2)	RPM
1a	1.9	0.18	0.18	1	0.7	4.27
1b	1.9	0.18	0.18	1	0.7	8.55
1c	1.9	0.18	0.18	1	0.7	12.83
1d	1.9	0.18	0.18	1	0.7	17.11
1e	1.9	0.18	0.18	1	0.7	21.38
1f	1.9	0.18	0.18	1	0.7	25.66
2a	2.54	0.25	0.2	1.25	1.3	3.42
2b	2.54	0.25	0.2	1.25	1.3	6.84
2c	2.54	0.25	0.2	1.25	1.3	10.27
2d	2.54	0.25	0.2	1.25	1.3	13.69
2e	2.54	0.25	0.2	1.25	1.3	17.19
2f	2.54	0.25	0.2	1.25	1.3	20.54

3a	2.74	0.35	0.2	1.67	1.9	2.9
3b	2.74	0.35	0.2	1.67	1.9	5.8
3c	2.74	0.35	0.2	1.67	1.9	8.7
3d	2.74	0.35	0.2	1.67	1.9	11.6
3e	2.74	0.35	0.2	1.67	1.9	14.49
3f	2.74	0.35	0.2	1.67	1.9	17.39
4a	4	0.51	0.2	2.55	4	2.72
4b	4	0.51	0.2	2.55	4	5.45
4c	4	0.51	0.2	2.55	4	8.18
4d	4	0.51	0.2	2.55	4	10.91
4e	4	0.51	0.2	2.55	4	13.63
4f	4	0.51	0.2	2.55	4	16.36
5a	6.04	1	0.2	5	11.4	2.62
5b	6.04	1	0.2	5	11.4	5.25
5c	6.04	1	0.2	5	11.4	7.89
5d	6.04	1	0.2	5	11.4	10.52
5e	6.04	1	0.2	5	11.4	13.14
5f	6.04	1	0.2	5	11.4	15.78
6a	9	1.48	0.2	7.05	25.1	2.53
6b	9	1.48	0.2	7.05	25.1	5.05
6c	9	1.48	0.2	7.05	25.1	7.58
6d	9	1.48	0.2	7.05	25.1	10.11
6e	9	1.48	0.2	7.05	25.1	12.64

6f	9	1.48	0.2	7.05	25.1	15.17

4.2.2. Particle tracking

Microalgae cells movements are tracked throughout the computational domain using a Lagrangian particle tracking method. Each microalgae cell is treated as a sphere and is assumed to have no effect on the liquid motion. The movements and positions of tracked particles are solved by the equation of motion:

$$\frac{d\boldsymbol{u}_p}{dt} = F_D\left(\boldsymbol{u}_l - \boldsymbol{u}_p\right) + \frac{\boldsymbol{g}(\rho_p - \rho)}{\rho_p} + \boldsymbol{F} \tag{4.1}$$

where $\boldsymbol{u}_p$ is a particle's velocity vector, $F_D\left(\boldsymbol{u}_l - \boldsymbol{u}_p\right)$ is the acceleration term due to the drag force, $\boldsymbol{u}$ is velocity vector for the fluid, ρ_p is the particle density, and $\boldsymbol{F}$ is the additional force induced acceleration term. The drag force coefficient F_D is calculated as

$$F_D = C_D \frac{\pi D_p^2}{8 m_p} \rho_l \left|\boldsymbol{u}_l - \boldsymbol{u}_p\right| \tag{4.2}$$

where D_p is the particle diameter and is set as 2 μm, ρ_l is the liquid phase density, $\boldsymbol{u}_l$ is the liquid velocity, $\boldsymbol{u}_p$ is the particle velocity, and m_p is the particle mass. The microalgae cells are treated as spheres, and the drag coefficient is estimated using the model developed by Schiller et al. (1935) [15]:

$$C_D = \begin{cases} \frac{24}{Re_p}\left(1 + 0.15\, Re_p^{0.687}\right) & Re_p \le 1000 \\ 0.44 & Re_p \ge 1000 \end{cases} \tag{4.3}$$

The pre-calculated velocity fields are predicted using the procedures described from section 3.2.2 to section 3.2.5. Because the effect of the paddle wheel and its rotational motion on the fluid velocity is already included in the pre-calculated velocity fields, it is no longer necessary to simulate the details of the paddle wheel and its rotation for particle tracking purposes. To further reduce the computational complexity and expense, stationary meshes are generated without the paddle wheel represented, and the height of the stationary mesh is significantly reduced with a large portion of the gas phase removed as particles that mimic the microalgae cells are bounded by the interface. The velocity fields for the stationary meshes are mapped from the pre-calculated velocity fields using an interpolation method. The pre-calculated velocity field and the mapping process are illustrated in Figure. 4.1. Although the walls of the raceway pond are treated as no-slip boundary conditions, the velocity fields of the inner layer cell are extrapolated to the boundaries and represented in the visualization software paraView 5.8.1. It can be observed that identical velocity fields are generated by mapping the velocity fields from Figure. 4.1a to Figure. 4.1b. However, the fluid domain is greatly reduced, and the requirement to represent the paddle wheel using dynamic mesh methods is avoided, the wall clock time for particle tracking simulations is significantly reduced.

a

b

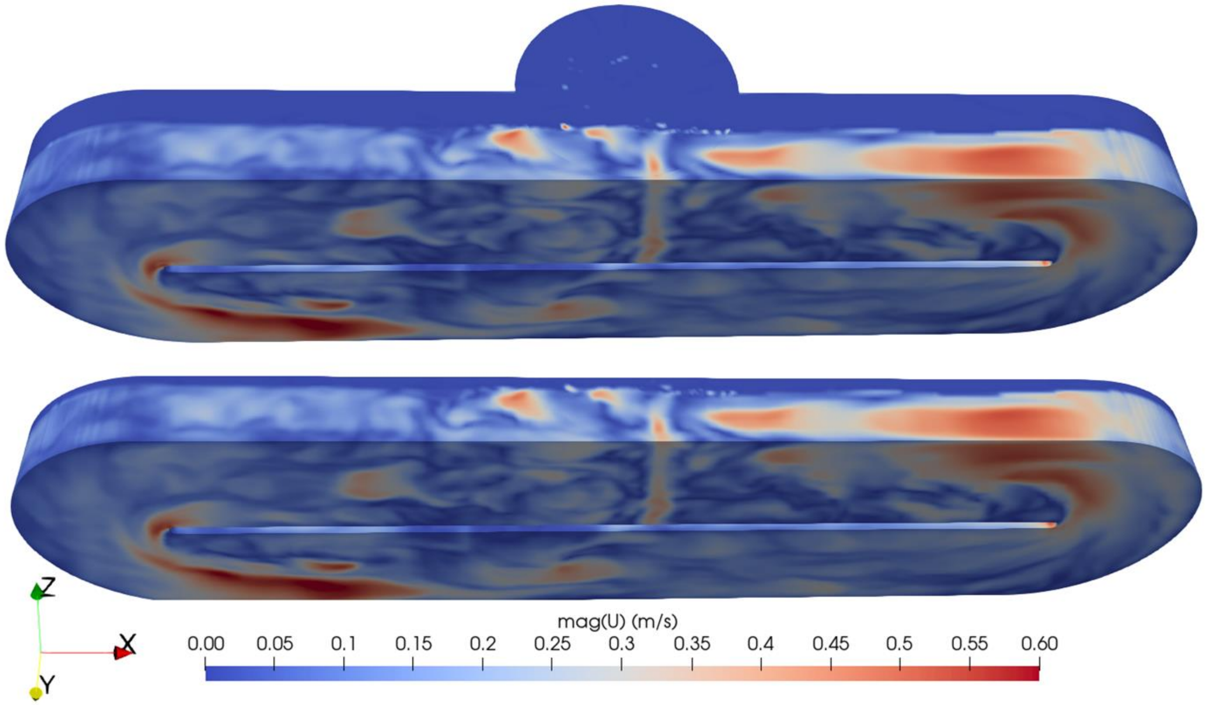

Figure. 4.1. Demonstration that pre-calculated velocity field is mapped to a stationary mesh for fast particle tracking. (a) pre-calculated velocity field on the full raceway pond mesh. (b) mapped velocity field on a simplified mesh for particle tracking where the paddle wheel and a large portion of the gas phase are omitted.

4.2.3 Convert particle trajectories to light history

The light intensity decays with distance into the microalgae media and can be modeled by the Lambert-Beer law, given as

$$A = log_{10}\left(\frac{P}{P_0}\right) = \varepsilon cd \tag{4.4}$$

where A is the absorbance, P_0 is the light intensity at the air-liquid interface, ε is the molar absorption coefficient, c is the biomass density, and d is the path length of the light in the absorbing medium [16]. Figure. 4.2a demonstrates the vertical position of a single particle for the first 100 s. The light intensity decay constant εc is set to 17 m^{-1} to represent the conditions in a dense culture media, and the light zone and the dark zone is determined by the light intensity 100 μmol photons $m^{-2}s^{-1}$. The light intensity is converted from the depth calculated from the vertical position as shown in Figure. 4.2b, where the light zone is denoted by light green, and the dark region is dark grey. The peak of the light duration is detected and the peaks with prominence less than 80 μmol photons $m^{-2}s^{-1}$ are removed to exclude the situation where particles are oscillating back and forth near the light/dark threshold. The light/light (L/L) intervals are calculated as the time span between two neighbor light peaks denoted as red dots in Figure. 4.2b. The L/L interval has a close relationship with the L/D frequency as the L/D frequency can be calculated as 2/(L/L interval)).

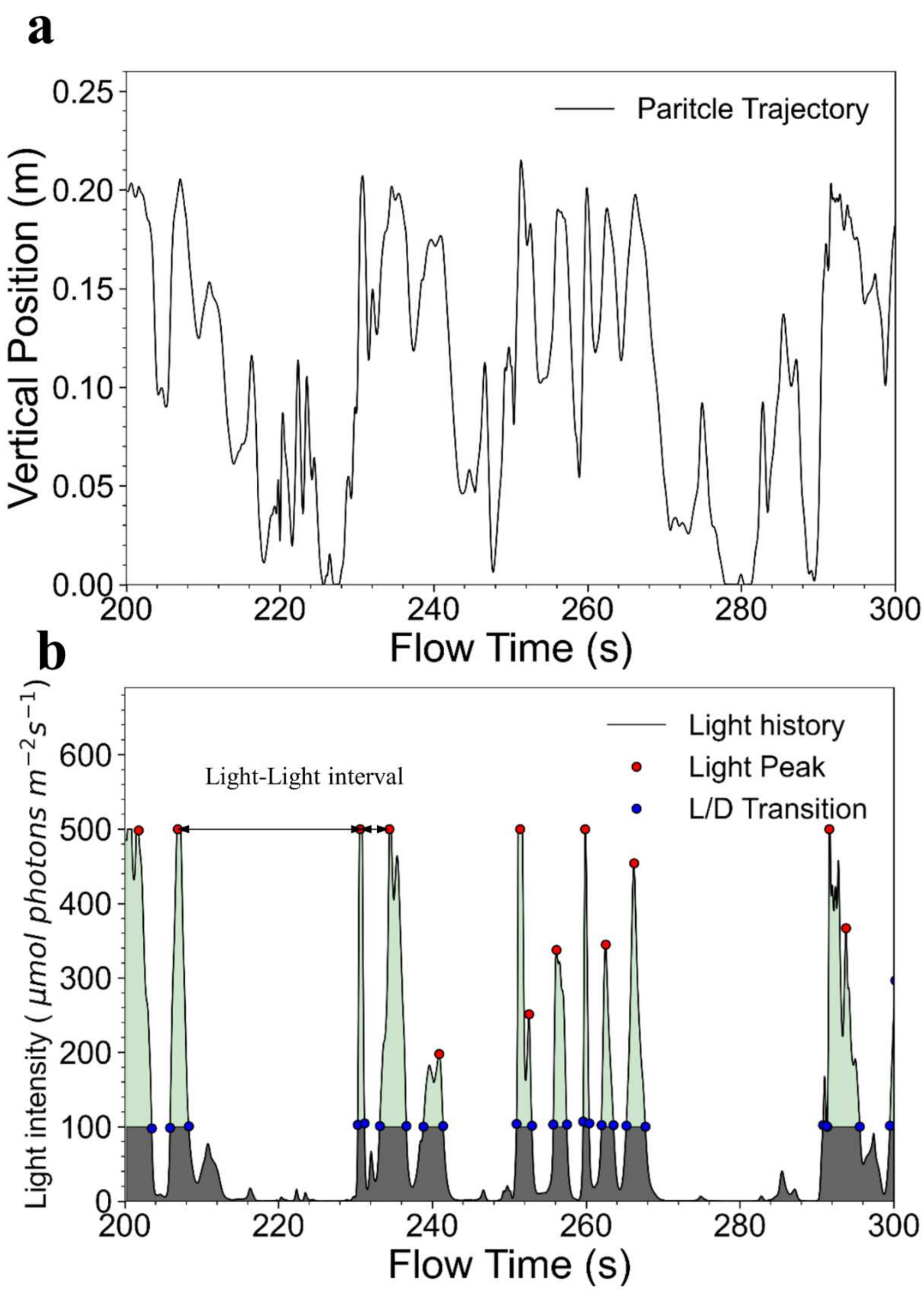

Figure. 4.2. Illustration of light intensity history converted from a particle's depth. (a) vertical position of a representative microalgae cell for the first 100 s of tracking time. (b) Light intensity history converted from the vertical location of the particle's trajectory. The light zone is marked with bright green, the dark zone is marked with dark grey. The peak of each light session is detected and marked with red dots. The Light/Dark transition is denoted by blue dots.

4.3. Results and discussion

4.3.1 Using pre-calculated velocity fields as the input for transient particle tracking

The vertical direction is of most interest since the vertical position of cells directly determines the amount of light the microalgae receive. For this reason, u_z is monitored throughout the pond over a period of 30 s at 0.2 s intervals. Figure. 4.3 depicts the contours of abs(u_z) at the horizontal mid-plane in the liquid (z = 0.1 m). The height of 0.1 m was chosen because abs(u_z) is predicted to be low near the bottom surface due to the no-slip boundary condition and similarly, positioning the horizontal plane too close to the gas-liquid interface produces similarly ambiguous results, since the liquid is prevented from passing through the interface.

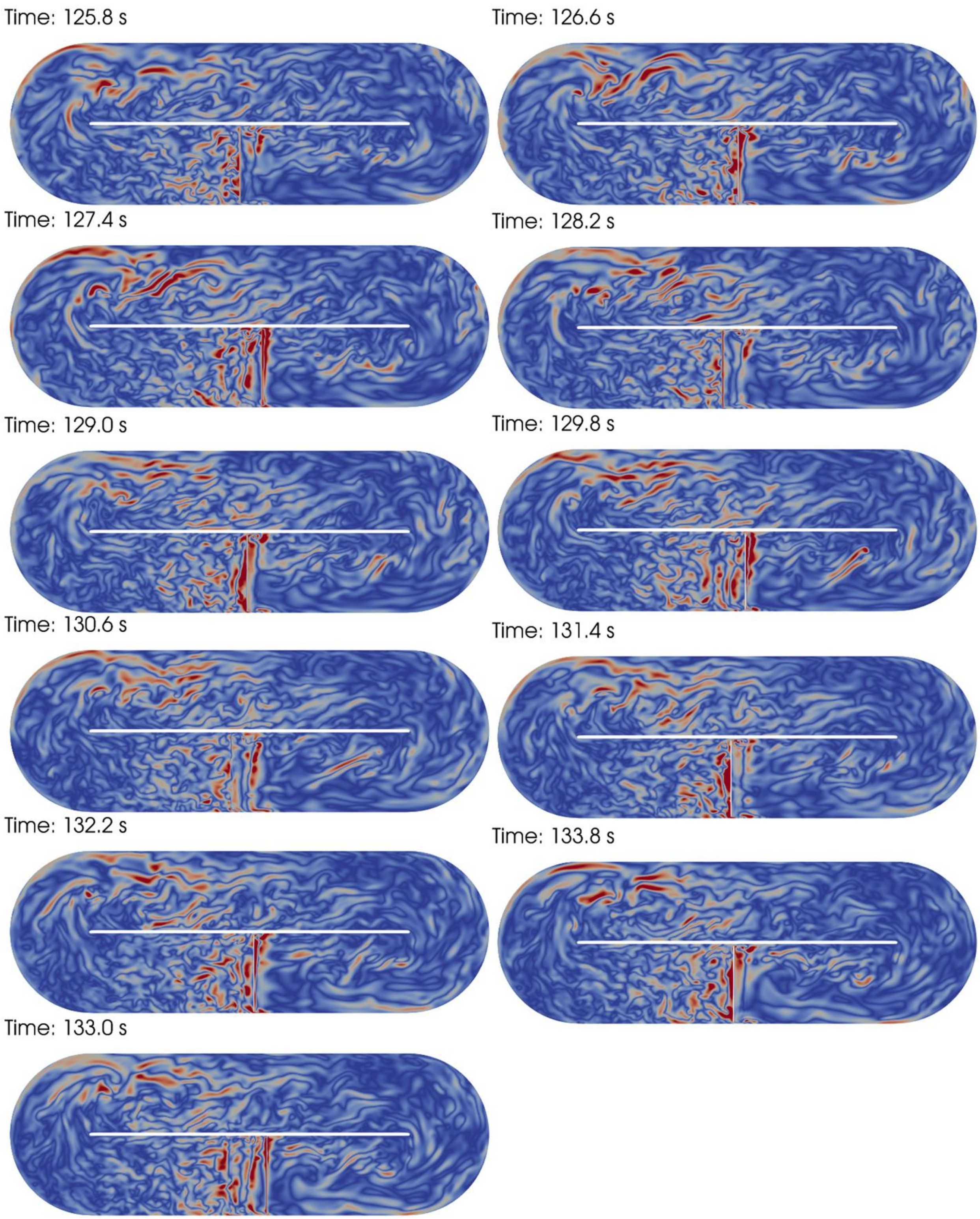

Figure. 4.3. abs(u_z) contours at the horizontal cross section at z = 0.1 m.

As shown in Figure. 4.3, the vertical velocity profile exhibits a very similar spatial pattern at various time point where the high vertical motion regions include the paddle wheel region and the region downstream of the two hairpin-bends. Moreover, the vertical velocity contours indicate that when swirling motion is generated, transported downstream and dissipated, new swirling motion will be generated, therefore, the vertical velocity exhibits strong periodic patterns. As a result, the pre-calculated velocity fields can be used periodically as the input for transient particle tracking to capture the main flow characteristics for a raceway pond system. For this purpose, the openFoam solver "icoUncoupledKinematicParcelFoam" is modified to store the pre-calculated velocity field data in memory and distribute at each time step, considerably reducing computational expense and hard drive input/output rates [17].

Because of the way the modified solver is implemented, the number of particles injected on the total liquid volume and more particles can be tracked as pond size increases. At 200 s, when the flow is fully developed, 5,000 particles per cubic meter are injected and tracked for 800 s using pre-calculated velocity data covering a 30 s period at 0.1 s intervals. This results in an averaged number of 14,000 particles per pond based on the size of modeled raceway ponds. The number density of 5,000 particles per cubic meter is chosen because it provides a good balance between tracking time and the total number of tracked particles. The particle tracking time step size is specified to be the same as the interval between the pre-calculated velocity fields. Probability density functions (PDFs) are employed to evaluate the distribution of the intervals between two neighbor light events using the method introduced by section 4.2.3. To ensure that the velocity fields collected over a 30 s period as 0.1 s intervals accurately capture the velocity variation in the raceway ponds so that negligible velocity field information is lost, the PDF of L/L intervals is compared with the PDF where the full-time flow fields are simulated for the scenario where SR = 2.55 and RPM = 13.6 as illustrated in Figure. 4.4a, the two L/L interval PDFs from both simulations overlap considerably well. Although the PDF predicted by resolving all the velocity fields has a lower probability density at the lower interval regions, the position of the peak (where the PDF has a local maximum value) are quite close where the peak location predicted by the pre-calculated velocity fields is 0.78 s and the peak location computed by resolving all the velocity fields is 0.94 s. Therefore, it can be concluded that that the 30 s of velocity fields at 0.1 s intervals contains the majority of the velocity information necessary to accurately predict particle trajectories. Additionally, computational costs are reduced 50-fold compared with the simulation that requires 1,840 core-hours when coupled with the PISO algorithm to predict the velocity field at all the time steps versus 38 core-hours when using pre-calculated velocity fields. Therefore, long-time particle trajectories can be determined at an affordable computational cost.

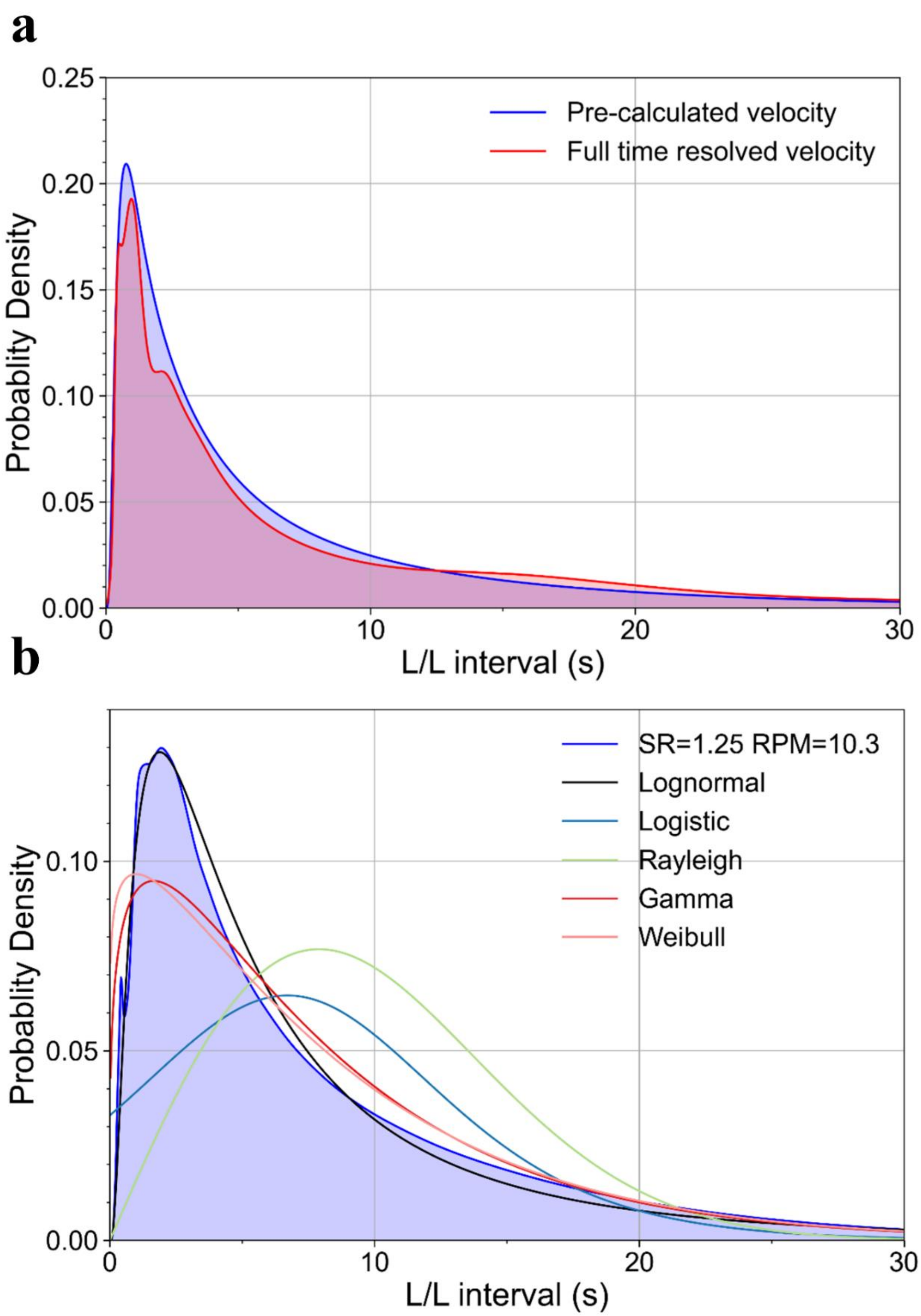

Figure. 4.4. Probability density function of L/L intervals can be fitted in lognormal distribution. (a) probability density function of L/L intervals with SR = 2.55 and RPM = 13.6 using pre-

calculated velocity fields (blue) and velocity field predicted by simultaneously solving the Navier-Stocks equations (red). (b) probability density function of L/L intervals with *SR* = 2.55 and RPM = 13.6 fit with common probability functions.

An example PDF of L/L intervals for a raceway pond with *SR* = 1.25 and RPM = 10.3 is plotted in Figure. 4.4b along with the PDF fit to several common distributions, including lognormal, logistic, Rayleigh, Gamma, and Weibull distributions. Among these distribution functions, the lognormal distribution best matches the PDF of L/L intervals as it accurately captures the shape of the PDF and the position of the peak. All other distribution functions either under-predict the probability density in the 5 s to 10 s range or failed to predict the correct peak location. To validate that the PDF of L/L intervals follows a lognormal distribution for raceway ponds with different *SR* values and operating conditions, i.e., paddle wheel RPM, the PDFs of all the simulated cases have been fit to a lognormal distribution, with the best fit and the worst fit cases displayed in Figure. 4.5. The lognormal distribution best fits the case with *SR* = 5 and RPM = 2.6 with a RMSR of 2.22×10^{-6}. The worst fitted case was *SR* = 2.55 and RPM = 16.4 where the PDF is more tightly distributed near the peak. However, the lognormal distribution can still fit the general shape of the PDF and capture the location of the peak.

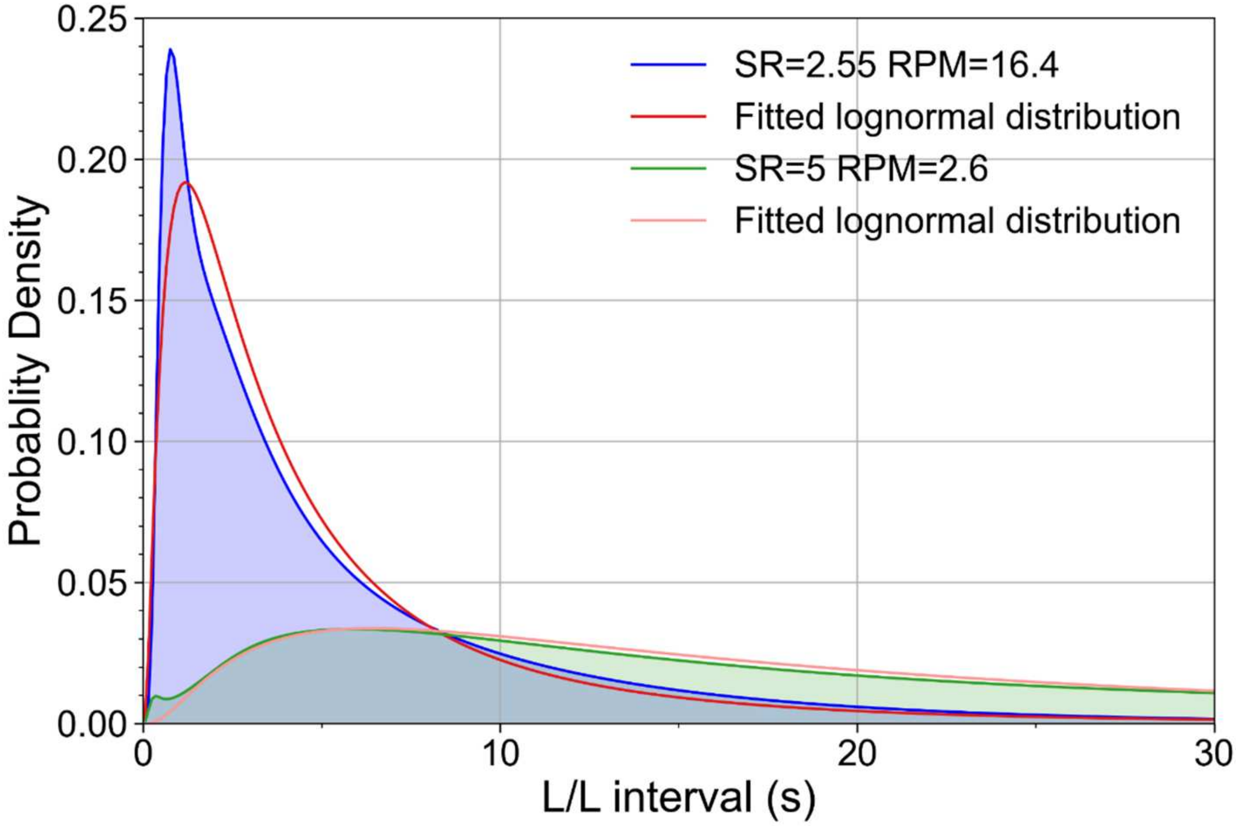

Figure. 4.5. The worst fit case (*SR* = 2.55 and RPM = 16.4) and best fit case (*SR*= 5 and RPM = 2.6) of L/L interval probability density function fitted by lognormal distribution.

As illustrated in Figure. 4.6, the L/L interval corresponds to the PDF peak for *SR* = 2.55 decreases as RPM is increased. This result implies that the time interval between two light-light exposures will be reduced, resulting in an increase in the L/D frequency. Additionally, the standard deviation of the PDF is reduced, indicating that not only the averaged L/D increases, but that the L/D frequency cells encountered are more concentrated at a lower level.

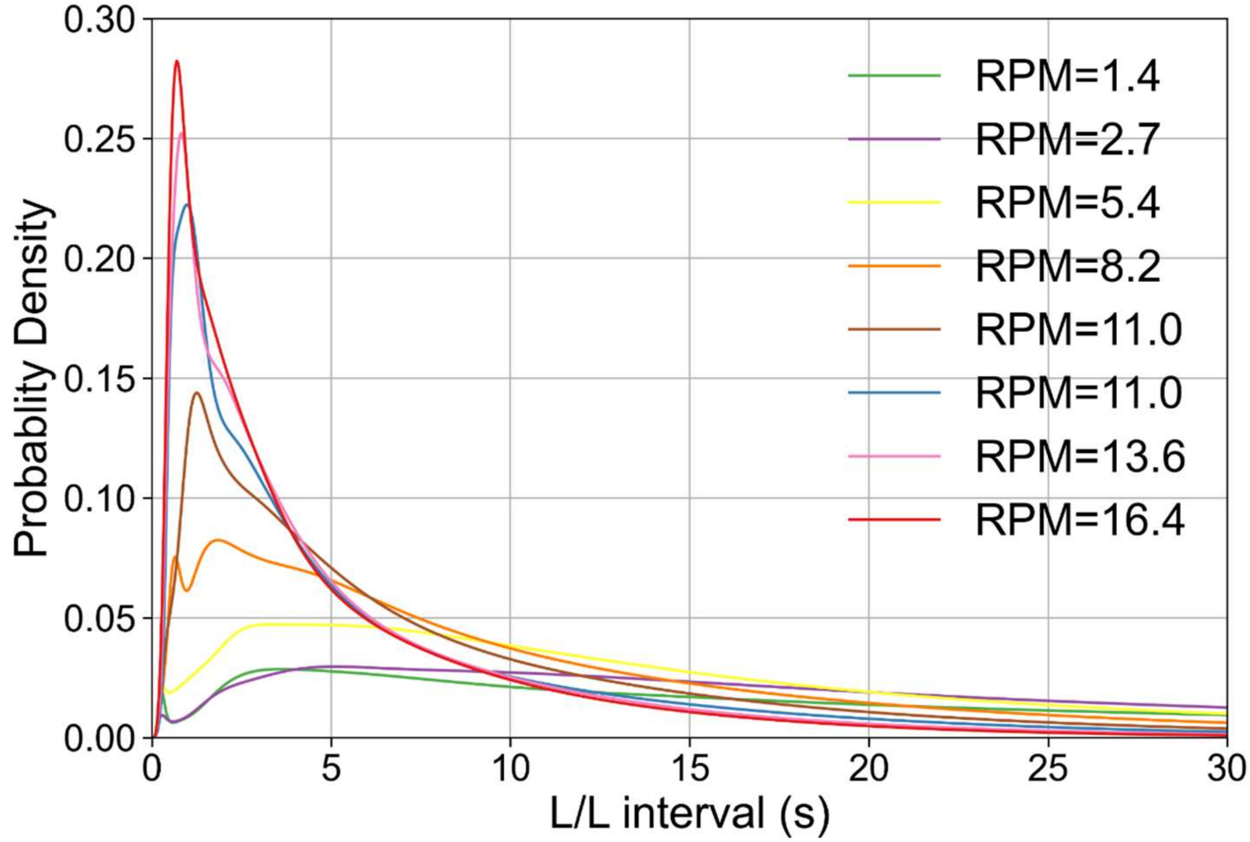

Figure. 4.6. L/L interval probability density for the case *SR*=2.55 where the paddle wheel RPM is varying.

Increasing the RPM of the paddle has significant impacts on the liquid velocity field, not only the magnitude of the velocity, but also the vertical velocity component u_z. To quantitatively analyze this effect, Figure. 4.7a depicts the PDF of the vertical velocity u_z in the pond for SR = 5 as RPM is increased. The PDFs have kinks at $u_z = 0$ m/s, and it appears the probability density decreases exponentially as abs(u_z) deviates from 0 m/s, suggesting that the PDF of abs(u_z) can be potentially fit with an exponential distribution. Since an exponential distribution can only be applied to non-negative data values, the PDF of abs(u_z) is displayed in Figure. 4.7b. For the same raceway pond, increasing the paddle wheel RPM increases the likelihood of the pond having a larger magnitude of abs(u_z). As a result, the PDF has a wider tail that covers a larger range of abs(u_z) values, decreasing the probability density of abs(u_z) = 0 m/s.

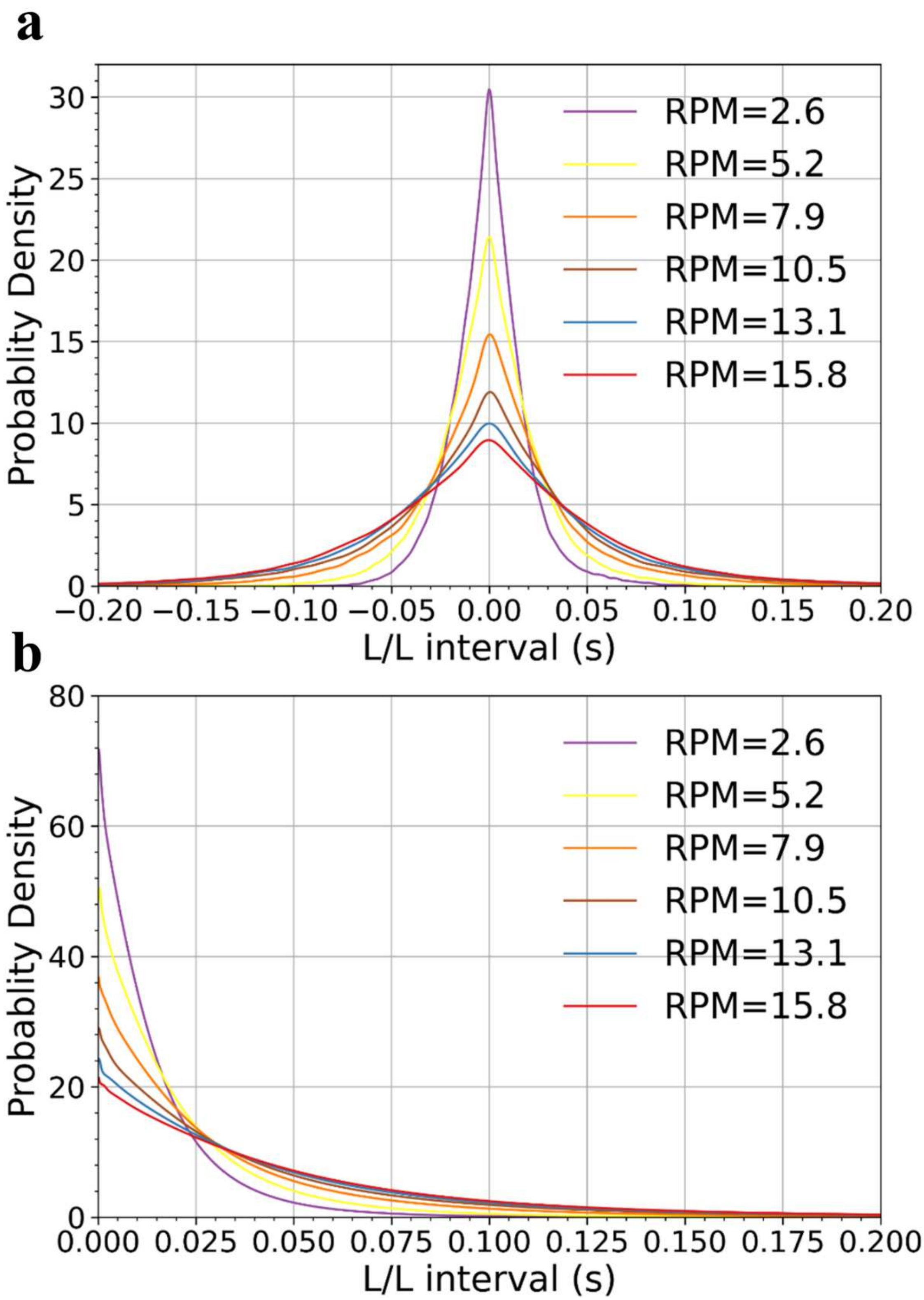

Figure. 4.7. PDF of u_z and abs(u_z). (a) probability density of u_z for the case SR = 5. (b) probability density of abs(u_z) for the case SR = 5.

Quantile-Quantile (Q-Q) analyses are performed to test the goodness of fit with an exponential distribution, and the results are shown in Figure. 4.8. If the PDF of abs(u_z) follows an exponential distribution, the points on the Q-Q plot will lie approximately on a straight line where the slope and intercept of the line are determined by the parameters of the exponential distribution. Among the 36 cases, the scenario with SR = 7.05 and RPM = 1.26 has the best fit, while the scenario with SR = 1.67 and RPM = 14.49 has the worst fit. Even in the worst-case scenario, the exponential distribution closely approximates the PDF of abs(u_z) as the quantile closely follows the exponential distribution quantiles.

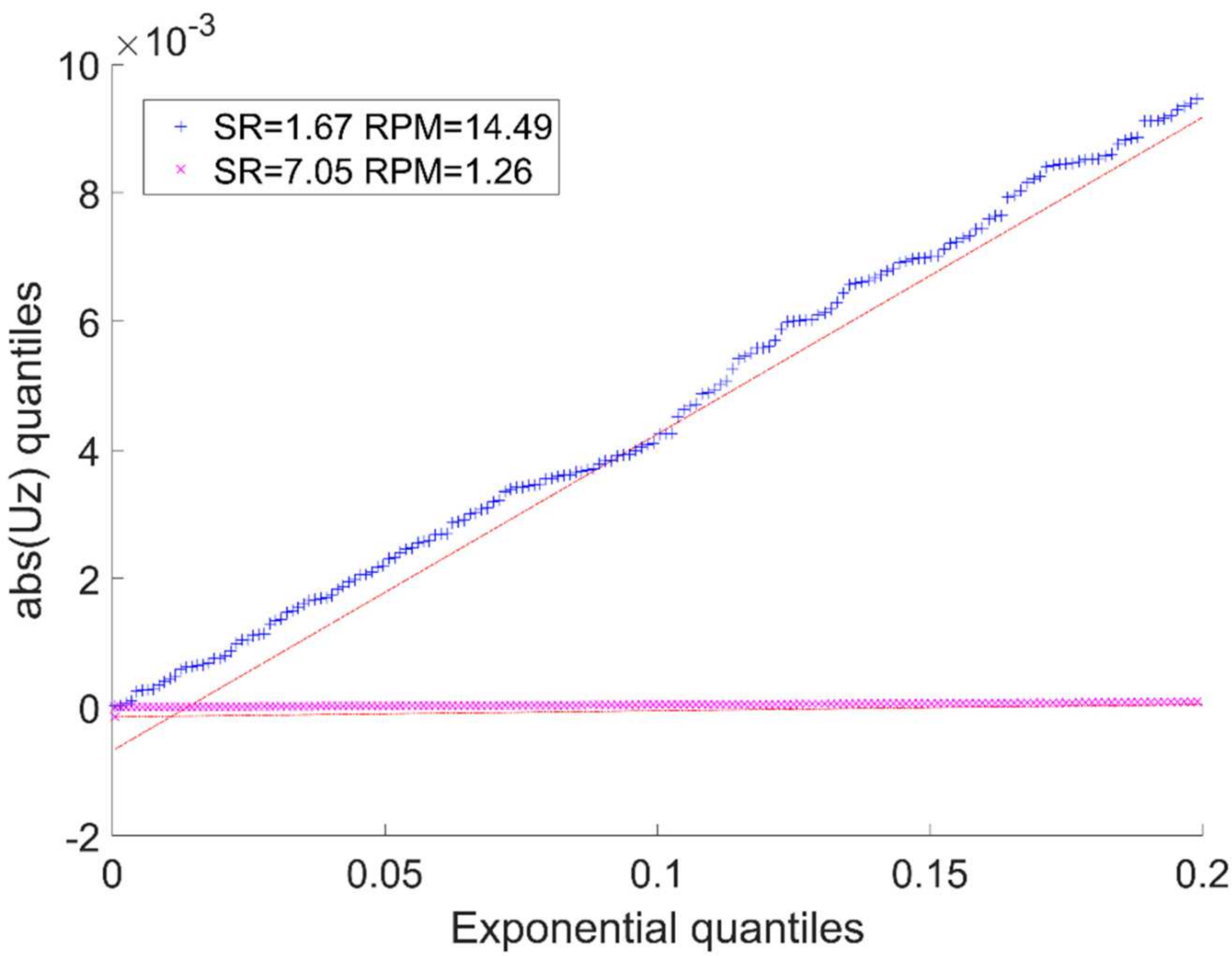

Figure. 4.8. Quantile-Quantile plot for abs(u_z) observed (y-axis) versus expected exponential distribution (x-axis) for the best fit case (SR = 7.05, RPM = 1.26), and for the worst fit case (SR = 1.67, RPM = 14.49).

In comparison with Figure. 4.7b and Figure. 4.6, it is observed that as the paddle wheel RPM increases, the probability density of abs(u_z) = 0 is reduced and the L/L interval corresponding to the peak in Figure. 4.6 also moves closer to 0. Therefore, a correlation is believed to exist between the PDF of abs(u_z) and the pdf of L/L intervals. To determine the correlation between these two variables, the exponential distribution is fit by the theoretical equation

$$f(x,\lambda) = \begin{cases} \lambda e^{-\lambda x} & x \geq 0 \\ 0 & x < 0 \end{cases} \tag{4.5}$$

The L/L interval at the PDF peak versus the exponential distribution parameter λ is depicted in Figure. 4.9. A point with a small value of λ indicates the scenario with a wider abs(u_z) span and a higher paddle wheel RPM. Consequently, the paddle wheel RPMs for the data in Figure. 4.9 decrease from left to right. According to the design of the studies, the paddle wheel RPM decreases at the same rate, and a steeper slope at the lower λ region implies that increasing the RPM by the same percentage results in a greater improvement in terms of L/L intervals and L/D frequency. As shown in Figure. 4.9, the raceway pond with *SR* = 1.67 exhibits the largest slope, and the pond with *SR* = 7.05 has the smallest slope. The slopes of the curves, however, do not exhibit a substantial correlation with the pond design parameter *SR*.

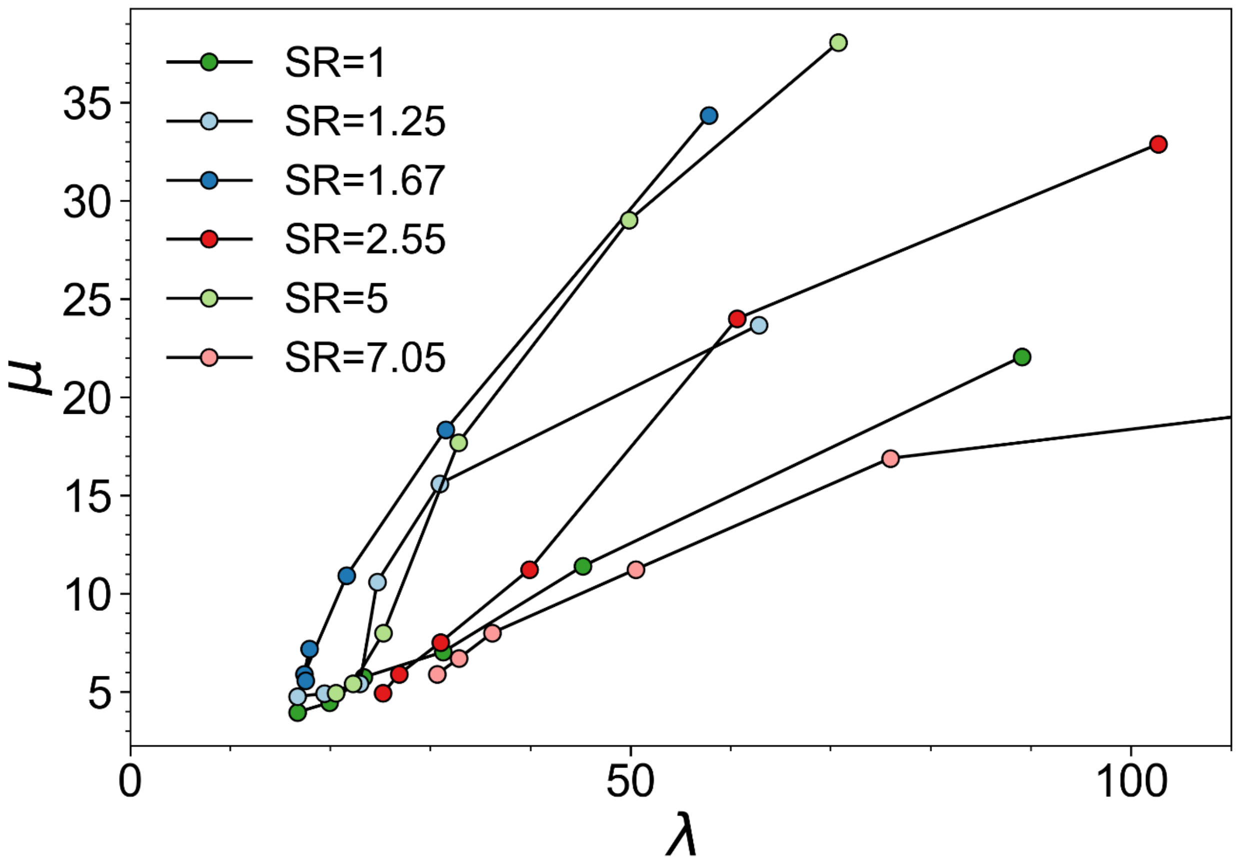

Figure. 4.9. The L/L interval corresponding to the probability density peak vs exponential distribution parameter λ.

The smallest L/L interval was achieved with *SR* = 1 and RPM = 25.7 with a value of 3.97 s, which corresponds to an L/D frequency of 0.50 Hz. For the largest pond modeled in this chapter, *SR* = 7.05, the L/L interval is 5.90 s under the operating condition that corresponds to the same Dean number, which translates to an L/D frequency of 0.33 Hz. Since it has been reported that the optimal L/D frequency from microalgae cultivation ranges from 1 Hz to 10 Hz, the results reveal the reason why a lower production rate is obtained for a bigger pond [18-19].

4.3.2. Spatial distribution of L/D transition probability

To investigate the spatial distribution of the probability that an L/D transition will take place, the occurrences of L/D transitions are counted for each mesh cell and normalized by the mesh cell's volume and the total number of tracked particles. Figure. 4.10 displays the probability contours for the raceway pond with SR = 2.55 and surface area 4.0 m^2. As can be seen, the high probability zones cover the region near the paddle wheel, notably downstream of the paddle wheel, where the liquid is lifted with considerable strong vertical velocities.

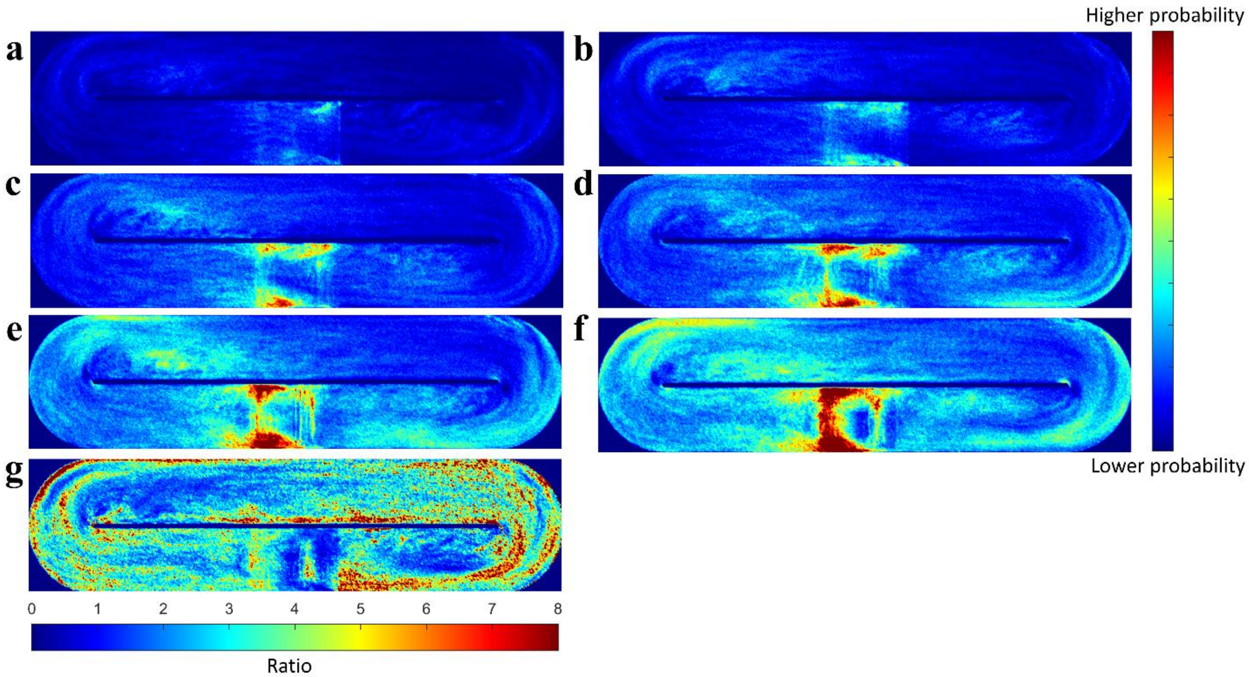

Figure. 4.10. Normalized spatial probability distribution of L/D transition for the case where SR = 2.55. (a) RPM = 2.7. (b) RPM = 5.4. (c) RPM = 8.2. (d) RPM = 10.9. (e) RPM = 13.6. (f) RPM = 16.4. (g) The ratio of the normalized spatial probability distribution between RPM = 16.4 (f) and RPM = 5.4 (b).

For lower RPM values, the probability of L/D transitions decreases rapidly downstream of the paddle wheel region. The high probability region reappears at the 45° location in the bends and persists for a considerable distance downstream of the bends. The zone with a high probability of L/D transition has a larger volume than the region downstream of the paddle wheel, indicating that the swirling motion caused by the hairpin bend contributes more to the enhancement of the L/D effect than the paddle wheel does. The ratio of the probability for the case RPM = 16.3 and RPM = 5.5 is depicted in Figure. 4.10g. The ratio denotes the spatial increase in the probability of the L/D transition in response to the same RPM increase. It can be observed that increasing the paddle wheel RPM 3-fold increases the probability of an L/D transition by more than 7-fold in certain regions. These regions are consistent with the region of high probability identified previously. At the same time, it is found that increasing the paddle wheel's RPM has a relatively small impact on the probability of L/D transitions near the paddle wheel, which can be attributed to the knowledge that the fluid motion near the paddle wheel is turbulent even at low RPM, and that increasing the RPM does not result in a significantly increased probability of L/D transitions near the paddle wheel region.

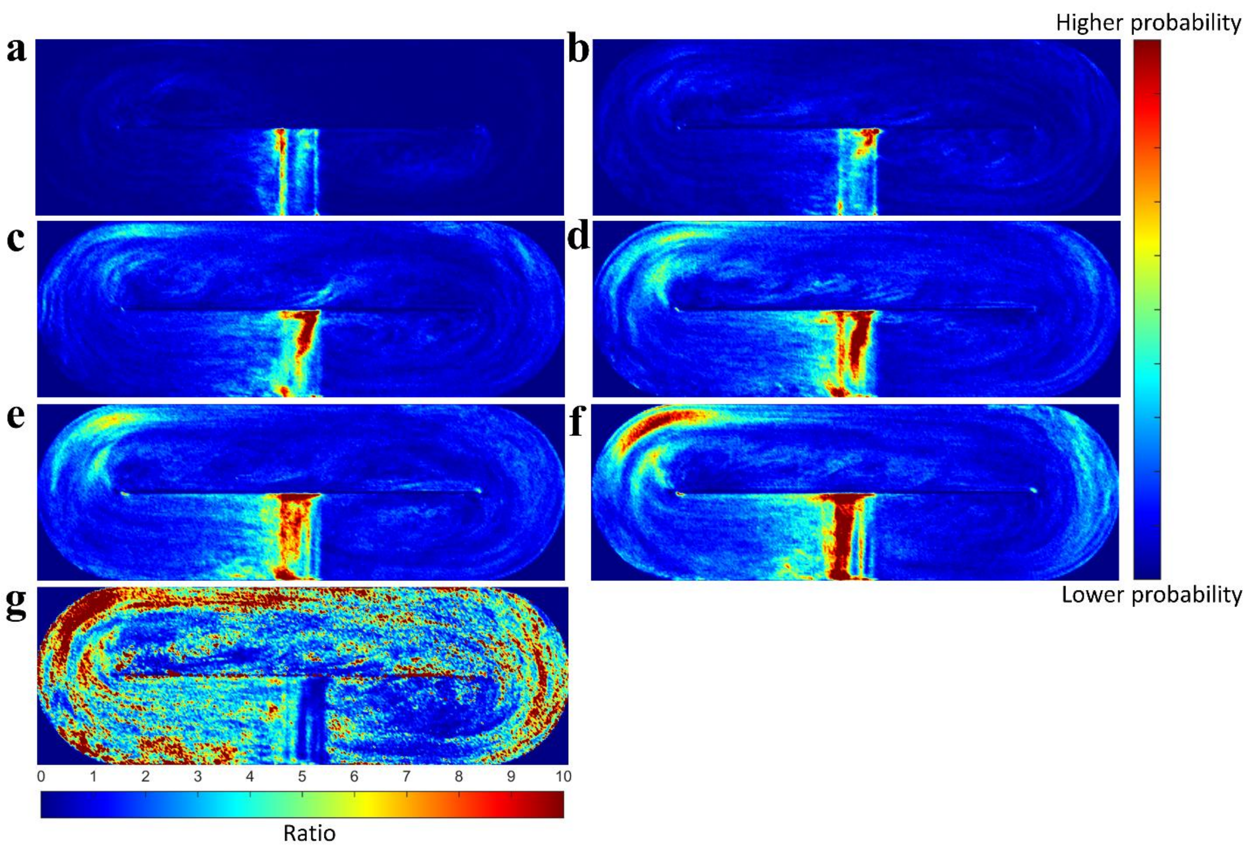

Figure. 4.11. Normalized spatial probability distribution of L/D transition for the case where *SR*=7.05. (a) RPM = 2.5. (b) RPM = 5.1. (c) RPM = 7.6. (d) RPM = 10.1. (e) RPM = 12.6. (f) RPM = 15.2. (g) The ratio of the normalized spatial probability distribution between RPM = 12.5 (f) with RPM = 5.1 (b).

Figure. 4.11 displays the spatial distribution of L/L transition probabilities for a larger pond (SR = 7.05, surface area 25.1 m^2). Similar characteristics can be observed such as the high probability regions include the downstream of the paddle wheel and hairpin bends. The results are normalized by the number of tracked particles and the area of the mesh cell, therefore, the probability represented in Figure. 4.10 can be compared with the one in Figure. 4.11 as both represent the probability L/D transitions occurring per unit pond area. Comparing Figure. 4.10 with Figure. 4.11, it can be observed that the overall probability is reduced as the pond's size increases. One explanation is that as the driving force of the liquid motion, the paddle wheel can only induce vertical mixing for a limited downstream distance. Similarly, the swirling motion generated by the hairpin bends will disperse eventually due to viscous dissipation. As a result, when the size of the pond is increased, and especially the length of the straight section is increased, the volume fraction with a higher abs(u_z) magnitude is reduced. As the direct impact of this, the probability density of abs(u_z) will be more concentrated near abs(u_z) = 0 m/s, and the microalgae cells in the pond will have a lower probability of experiencing rapid L/D transitions and high vertical motions when agitated in the larger pond, concluded by the correlation established in section 3.1.

4.4. Conclusion

Transient particle tracking is accomplished by utilizing pre-calculated velocity fields predicted by the open source CFD software openFoam6. It is found that velocity fields covering a 30 s span with 0.1 s intervals accurately represent the vertical flow characteristics in a raceway pond, and that particle trajectories can be accurately integrated using a custom-developed solver, as evidenced by the fact that the PDF of L/L intervals produced this way is comparable to simulations with full-time velocity data.

A lognormal distribution can be used to model the PDF of L/L intervals, while an exponential distribution can be used to fit the pdf of abs(u_z). Increased RPM for a raceway pond has the effect of expanding the width of the abs(u_z) PDF, and therefore a larger volume fraction of the raceway pond will have a stronger vertical motion. It is indicated that increasing the width of the abs(u_z) PDF correlates significantly with reducing the L/L interval time associated with the peak point as well as lowering the standard deviation of the L/L interval PDF. Both factors contribute to an increase in the mean L/D frequency which means that microalgae will have an increased probability to experience more rapid L/D transitions.

It is found that increasing the paddle wheel RPM significantly increases the probability of an L/D transition in regions where the probability of an L/D transition is already substantial. The exception is within the paddle wheel region, liquid the fluid is already turbulent and increasing the paddle wheel RPM does not result in a nearly as large rise in the probability of L/D transition as it does in other regions. The overall probability of experiencing L/D transition is reduced for larger ponds operated with an RPM that matches *De* for a smaller one. An explanation is that for a larger pond, increasing the paddle wheel RPM does not increase the abs(u_z) in the pond wise as effectively as for a smaller size pond, therefore, the L/D frequencies are not improved as significantly as for a smaller sized pond.

4.5 References

[1] V. Ashokkumar, E. Agila, Z. Salam, M. Ponraj, M. F. M. Din, and F. N. Ani, “A study on large scale cultivation of Microcystis aeruginosa under open raceway pond at semi-continuous mode for biodiesel production,” *Bioresour. Technol.*, vol. 172, pp. 186–193,

Nov. 2014, doi: 10.1016/j.biortech.2014.08.100.

[2] K. H. Ryu, J. Y. Lee, S. Heo, and J. H. Lee, “Improved Microalgae Production by Using a Heat Supplied Open Raceway Pond,” *Ind. Eng. Chem. Res.*, vol. 58, no. 21, pp. 9099–9108, May 2019, doi: 10.1021/acs.iecr.9b00986.

[3] R. R. Narala *et al.*, “Comparison of Microalgae Cultivation in Photobioreactor, Open Raceway Pond, and a Two-Stage Hybrid System,” *Front. Energy Res.*, vol. 4, p. 29, 2016, doi: 10.3389/fenrg.2016.00029.

[4] S. Dahmani, D. Zerrouki, L. Ramanna, I. Rawat, and F. Bux, “Cultivation of Chlorella pyrenoidosa in outdoor open raceway pond using domestic wastewater as medium in arid desert region,” *Bioresour. Technol.*, vol. 219, pp. 749–752, Nov. 2016, doi: 10.1016/j.biortech.2016.08.019.

[5] “In situ carbon supplementation in large-scale cultivations of Spirulina platensis in open raceway pond | SpringerLink.” https://link.springer.com/article/10.1007/s12257-011-0319-9 (accessed Oct. 05, 2021).

[6] T. Granata, “Dependency of Microalgal Production on Biomass and the Relationship to Yield and Bioreactor Scale-up for Biofuels: a Statistical Analysis of 60+ Years of Algal Bioreactor Data,” *BioEnergy Res.*, vol. 10, no. 1, pp. 267–287, Mar. 2017, doi: 10.1007/s12155-016-9787-2.

[7] “Microalgae as biodiesel & biomass feedstocks: Review & analysis of the biochemistry, energetics & economics - Energy & Environmental Science (RSC Publishing) DOI:10.1039/B924978H.” https://pubs.rsc.org/en/content/articlehtml/2010/ee/b924978h (accessed Oct. 05, 2021).

[8] M. Janssen, J. Tramper, L. R. Mur, and R. H. Wijffels, “Enclosed outdoor photobioreactors:

light regime, photosynthetic efficiency, scale-up, and future prospects," *Biotechnol. Bioeng.*, vol. 81, no. 2, pp. 193–210, Jan. 2003, doi: 10.1002/bit.10468.

[9] E. A. Laws, K. L. Terry, J. Wickman, and M. S. Chalup, "A simple algal production system designed to utilize the flashing light effect," *Biotechnol. Bioeng.*, vol. 25, no. 10, pp. 2319–2335, 1983, doi: 10.1002/bit.260251004.

[10] C. Vejrazka, M. Janssen, G. Benvenuti, M. Streefland, and R. H. Wijffels, "Photosynthetic efficiency and oxygen evolution of Chlamydomonas reinhardtii under continuous and flashing light," *Appl. Microbiol. Biotechnol.*, vol. 97, no. 4, pp. 1523–1532, Feb. 2013, doi: 10.1007/s00253-012-4390-8.

[11] P. Fernández del Olmo, F. G. Acién, and J. M. Fernández-Sevilla, "Analysis of productivity in raceway photobioreactor using computational fluid dynamics particle tracking coupled to a dynamic photosynthesis model," *Bioresour. Technol.*, vol. 334, p. 125226, Aug. 2021, doi: 10.1016/j.biortech.2021.125226.

[12] "Evaluation of a Photobioreactor Performance Grafting Microalgal Growth Model and Particle Tracking Technique Using CFD." https://doi.org/10.13031/trans.57.10339 (accessed Oct. 05, 2021).

[13] P. Ghadimi, H. Nowruzi, M. Yousefifard, and M. A. Feizi Chekab, "A CFD study on spray characteristics of heavy fuel oil-based microalgae biodiesel blends under ultra-high injection pressures," *Meccanica*, vol. 52, no. 1, pp. 153–170, Jan. 2017, doi: 10.1007/s11012-016-0410-6.

[14] Z. Chen, X. Zhang, Z. Jiang, X. Chen, H. He, and X. Zhang, "Light/dark cycle of microalgae cells in raceway ponds: Effects of paddlewheel rotational speeds and baffles installation," *Bioresour. Technol.*, vol. 219, pp. 387–391, Nov. 2016, doi:

10.1016/j.biortech.2016.07.108.

[15] L. SCHILLER, “A Drag Coefficient Correlation,” *Zeit Ver Dtsch. Ing*, vol. 77, pp. 318–320, 1933.

[16] D. F. Swinehart, “The Beer-Lambert Law,” *J. Chem. Educ.*, vol. 39, no. 7, p. 333, Jul. 1962, doi: 10.1021/ed039p333.

[17] H. G. Weller, G. Tabor, H. Jasak, and C. Fureby, “A tensorial approach to computational continuum mechanics using object-oriented techniques,” *Comput. Phys.*, vol. 12, no. 6, pp. 620–631, Nov. 1998, doi: 10.1063/1.168744.

[18] S. Xue, Z. Su, and W. Cong, “Growth of Spirulina platensis enhanced under intermittent illumination,” *J. Biotechnol.*, vol. 151, no. 3, pp. 271–277, Feb. 2011, doi: 10.1016/j.jbiotec.2010.12.012.

[19] “Full article: Flashing light enhancement of photosynthesis and growth occurs when photochemistry and photoprotection are balanced in Dunaliella salina.” https://www.tandfonline.com/doi/full/10.1080/09670262.2015.1069404 (accessed Oct. 05, 2021).

Chapter 5 Application of passive vortex generators to enhance vertical mixing in an open raceway pond

5.1. Introduction

Due to the depletion of fossil fuels, biofuel production has been drawn significant attention as a substitute for fossil fuels. Microalgae utilize solar energy and absorb CO_2 to generate mid-products such as lipids, which can be converted to biofuels. As a result, microalgae-based biofuel is a promising substitute for fossil fuel as it has an extremely fast growth rate, can make use of nutrients from wastewater, yields high lipid carbohydrate content, does not compete with food crops for arable land, can produce high-value by-product chemicals and reduce global warming [1-2].

Microalgae can be cultivated in closed photobioreactors such as tubular or flat panel reactors or outdoor open reactors [3-5]. Raceway ponds are one of the most popular and preferable outdoor cultivation facilities as they are simple to construct and scale up, require small capital investment, are easy to maintain, and require low energy inputs to operate [6-8]. The ponds consist of an oval-shaped channel with a divider placed in the center of the straight sections. One or multiple paddle wheels are installed to drive the flow around the track. Subject to the liquid motion, the vertical positions of microalgae cells are constantly changing, and the light each cell receives is consequently changing dynamically. It has been reported that microalgae have the potential to yield an improved production rate when the cells are exposed to light sources that frequently change between light and dark, which is known as the light/dark (L/D) effect [9-11]. Other than enhancing the L/D effect, vertical mixing also prevents cell stacking and biofilm formation, improves mass transfer, reduces thermal stratification, and avoids oxygen accumulation [12-14].

Computational fluid dynamics (CFD) simulations have been widely utilized to design and study flows in photobioreactors (PBRs) and open raceway pond systems by solving the Navier-Stokes equations with suitable turbulence models [15-18]. CFD can be used as an effective design tool, accurately describing flow field details prior to construction and experimentation, hence saving significant time and cost. Multiple studies have been conducted to improve the mixing performance of raceway ponds. Voleti (2012) has investigated the effect of installing delta wings in open raceway pond systems [19]. The flow field and turbulence were measured by Acoustic Doppler Velocimetry and Particle Image Velocimetry methods. It was reported that multiple longitudinal streamwise vortices were generated downstream of a delta wing placed in the straight section and were sustained for a distance of up to 3 m. The vertical mixing enhancement was demonstrated by computing and comparing the vertical mixing index of the raceway with and without a delta wing. A novel mixing baffle for open raceway ponds has been proposed by Yang et al. [1]. A 24% decrease of the L/D cycle period and a 22% increase of the biomass yield were achieved by placing up-down chute baffles in a raceway pond. Zhang et al. have reported on the influence of the flow field of a raceway pond with flow deflectors and wing baffles [21]. CFD simulations and particle tracking demonstrated that, with the addition of wing baffles, swirling flow was generated, and averaged L/D cycle period was significantly shortened. Additionally, it has been reported that with the wing baffles in place, the dead zone volume decreased by 60.42%, and the biomass yield increased by 30.11%. However, the rotational motion generated by chute baffles and wing baffles has axes perpendicular to the direction of the primary flow. One hypothesis is that if swirling motions can be generated in such a way that the axis is longitudinal and parallel to the primary flow direction, as are the swirling motions generated by bend geometries, the swirling motions will persist for a longer distance.

In this work, a novel design of a vortex generator is presented that can efficiently convert horizontal fluid motion into three-dimensional swirling motion. CFD simulations are carried out with vortex generators placed in the second straight section where the natural vertical motion is predicted to be quite low. The vortex generators are studied in a straight channel as well to eliminate the effect of the downstream hairpin bend. An algorithm to determine the persistence length of the generated swirling motion with a given critical velocity is developed. The placement strategy, the optimal diameter D_{opt} for a given liquid depth, as well as the optimal length L_{opt} for a 0.18 m diameter vortex generator in a 0.2 m deep pond is determined by analysis of CFD simulation results.

5.2. Material and methods

5.2.1 The Geometry of the vortex generator and the raceway ponds

The vortex generator is composed of a cylindrical outer surface and a propeller-like internal structure, as shown in Figure. 5.1a. The internal structure consists of 5 propeller-shaped blades which are connected to an axle located in the center of the generator. Based on a nominal pond depth of 0.20 m, the internal diameter of the vortex generator is set to 0.16 m, and the thickness of the outer cylinder shell is 0.01 m, such that the outer diameter for all the vortex generators studied is 0.18 m. The blades are designed to be parallel to the main flow for 0.033 m at the generator inlet, and then curve gradually to prevent the flow from abruptly changing direction, which might create an excessive wake zone downstream of the blades and deteriorate the ability to generate vortices. The pitch of the vortex blades is given in Figure. 5.2.

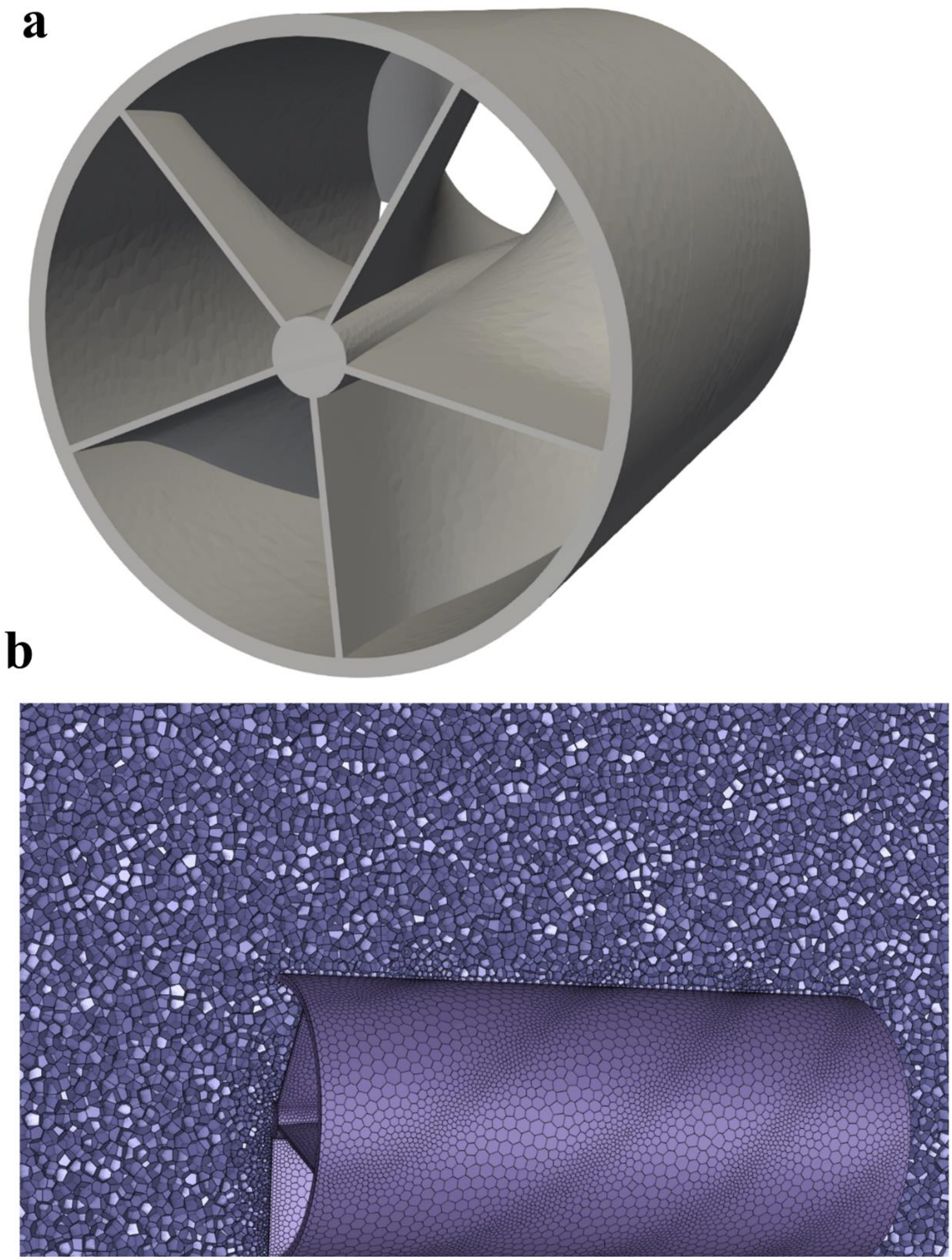

Figure. 5.1. Geometric design of the vortex generator and the corresponding mesh. (a) Geometric design of the vortex generator. (b) A vertical plane showing the mesh of the vortex generator zone generated by ANSYS mosaic meshing algorithm.

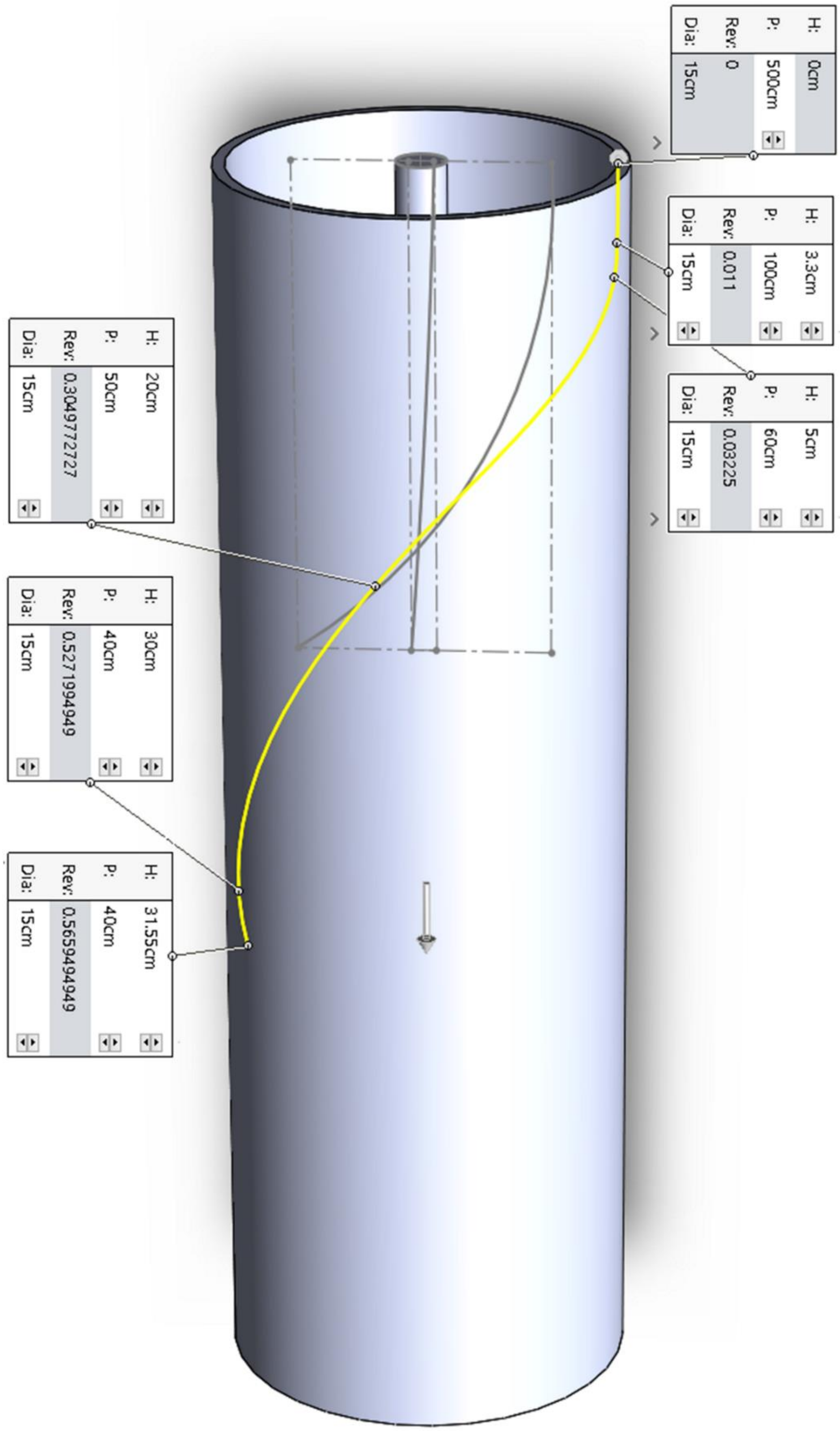

Figure. 5.2. SOLIDWORKS schematic diagram of the vortex generator with the blades' pitch parameters. H: height; P: pitch; Rev: revolution; Dia: diameter.

The vortex generator is extruded to different lengths (0.1, 0.15, 0.2, 0.25, 0.3, and 0.4 m) using the same pitch of the blades in order to identify the L_{opt} that creates the strongest vortices that persist the longest distance. The vortex generators are placed in a long raceway pond as well as in a straight channel. The tested raceway pond is designed to be long enough so that most of the swirling motion generated by the 180° bend upstream of the generator will dissipate before the flow reaches the generators. In this way, the performance of the generators can be fully quantified in a region where flow is largely horizontal. After analyzing the performance of the generators in unidirectional and counter-directional blade configurations to determine the best orientation, the vortex generators with the six lengths are positioned in a straight channel without the hairpin bends present to eliminate the swirling motion generated by the hairpin bends, quantify the maximum persistence length in the straight section, and simultaneously minimize computational costs. The straight section of the raceway pond modeled here measures 6 m in length and 1 m in width. The thickness of the divider in the raceway is set to 0.04 m. The paddle wheel is located in the middle of the first straight section, and the vortex generators are placed near the center of the second straight section. The separate straight channel is 9 m long measured from the inlet to the outlet and 0.48 m wide, that is, the width of a straight section in the raceway pond. The paddle is positioned 1 m downstream of the inlet, and the vortex generators are placed 3.0 to 3.4 m downstream of the inlet, depending on generator length. The water depth is set to be 0.2 m for all cases.

5.2.2 Mesh generation, solver, and numerical setup

The numerical solution method is a small modification to the solver "interFoam" under the framework openFoam 6.0.0 [22]. The residual evaluation is included at the conclusion of each inner pressure correction loop with splitting of operators (PISO) iteration, and the inner pressure corrector loop is configured to terminate when the residual approaches the target residual to improve performance while maintaining stability. The simulations are carried out on a high-performance computer at the National Renewable Energy Laboratory equipped with dual Intel Xeon Gold Skylake 6154 processors (3.0 GHz, 18 cores). An average of 6912 core-hours were used to collect flow time history data for each of the cases.

The computational grid is generated using the ANSYS meshing utility and then converted to the openFoam format. To simulate the rotational motion of the paddle wheel, the fluid domain is meshed separately as a static domain and a rotational domain. The interface between these two domains is coupled by an arbitrary coupled mesh interface (ACMI) boundary condition [23]. To ensure accuracy and resolve eddies of all scales, fine meshes with an average mesh size of 4,333,000 cells are employed for the simulations.

Due to the intricate geometric design of the vortex generator and the presence of sharp angles, creating the mesh with tetrahedral or hexahedral mesh cells will result in an excessively large cell number and loss of geometric features, reducing simulation accuracy and stability To overcome this, the vortex generator domain is isolated from the liquid domain and connected to the liquid domain via the AMI interface [23]. The vortex generator domain is meshed with polyhedral elements using the Fluent mosaic meshing algorithm, and all geometric characteristics are captured with a high mesh quality with an averaged non-orthogonality of 1.8462. Figure. 5.1b shows the generated mesh for the vortex generator domain on a horizontal plane.

5.2.3 Boundary condition and scheme

Figure. 5.3 illustrates the boundary conditions for the raceway pond and a straight channel with a vortex generator installed. Other than for the interface between the paddle wheel and pond regions, the top surface is configured as an ACMI boundary condition; the interface between the paddle wheel and pond regions is set as an atmosphere boundary condition. Other pond boundaries, such as the pond's wall, divider, and bottom, are specified to have no-slip wall boundary restrictions. Because the pond region and the vortex generator region are meshed differently, those two regions are connected by an AMI interface. For the straight channel simulation, the inlet and the outlet are paired with an AMI interface (Figure. 5.3b). The size of the time step is time-variant based on the Courant number, which is limited to 20 and the maximum time step size is limited to 0.01 s.

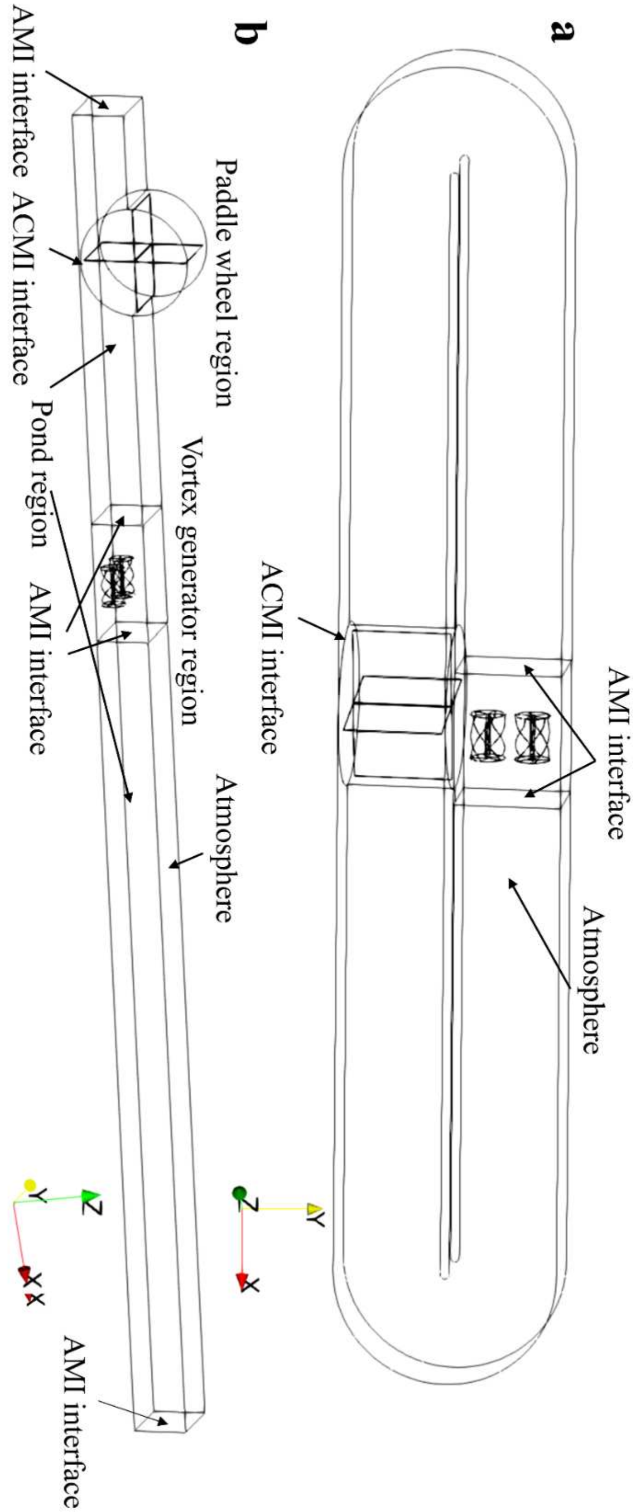

Figure. 5.3. Boundary condition setup for raceway pond simulation and straight channel simulation. (a) Boundary condition setup of the raceway pond simulation. (b) Boundary condition setup of the straight channel simulation.

5.2.4 Volume of fluid (VOF) model

The detail of the VOF model used in raceway pond simulations as well as straight channel simulations are given in section 3.2.4.

5.2.5 Turbulence model

The large eddy simulation (LES) model is utilized as the turbulence model in order to get high-fidelity velocity fields for the analysis of the vortices' transient structures. The LES model employs a one-equation Smagorinsky-type eddy viscosity model created by Yoshizawa [24].

5.2.6 Determine persistence length using a critical vertical velocity

To determine the persistence length of the swirling motion downstream of the vortex generators in the straight section (Figure. 5.3b), as well as the swirling motion generated by the paddle wheel in a raceway pond (Figure. 5.3a), once the flow is fully developed, the flow fields over a total of 15 s, sampled at 0.2 s intervals are visualized and analyzed in Matlab. Numerical filtration is performed on the air phase of the flow fields to eliminate those, and the liquid velocity fields are filtered using a critical vertical velocity $u_{z,\mathrm{cri}}$. Regions where the vertical component of the liquid velocity are greater than $u_{z,\mathrm{cri}}$ are retained, while other regions are removed. The retained regions are then overlapped and projected to a horizontal plane for all the velocity fields as the spatial distribution of the swirling motion in the horizontal plane is of most interest. The connected regions downstream the vortex generator and the paddle wheel (bounded by the red line) are identified by a custom Matlab code, and the persistence length is measured from the outlet of the vortex generators (denoted by a vertical blue line) to the point where the connected regions occupy at least 30% of the channel width at that location.

5.3. Results and discussion

5.3.1 Flow field of a raceway pond with the vortex generators

Figure. 5.4a illustrates the contours of abs(u_z) in the horizontal plane midway between interface and bottom when there are no vortex generators present. It can be observed that high vertical velocity zones are formed downstream of the paddle wheel because of its motion, and downstream of the hairpin bends due to the secondary flow phenomena resulting from Dean flow. However, abs(u_z) is low compared to these high vertical velocity regions near the middle and the end portion of the second straight section as the swirling motion generated by the secondary flow dissipates. As shown in Figure. 5.4b, vortex generators are positioned in a counterclockwise configuration at the center of the second straight section, and the abs(u_z) in the horizontal mid-plane is used to find regions of high vertical velocity and swirling motion at a flow time of 100 s. The swirling motion is weak upstream of the vortex generator entrances due to viscous dissipation. When fluid flows out a generator's exit, the swirling motion re-establishes and propagates downstream. It can be observed that the vortex generators successfully created two instances of swirling movements that propagated all the way to the second hairpin bend (the abs($\underline{u_z}$) contour demonstrates four high vertical velocity traces). Figure. 5.4d illustrates the velocity magnitude contours in the horizontal mid-plane. It can be observed that the velocity magnitude of the flow downstream of the vortex generators is not impaired, indicating that adding the vortex generators in the straight channel does not increase the flow resistance significantly, and it does not increase the power consumption significantly.

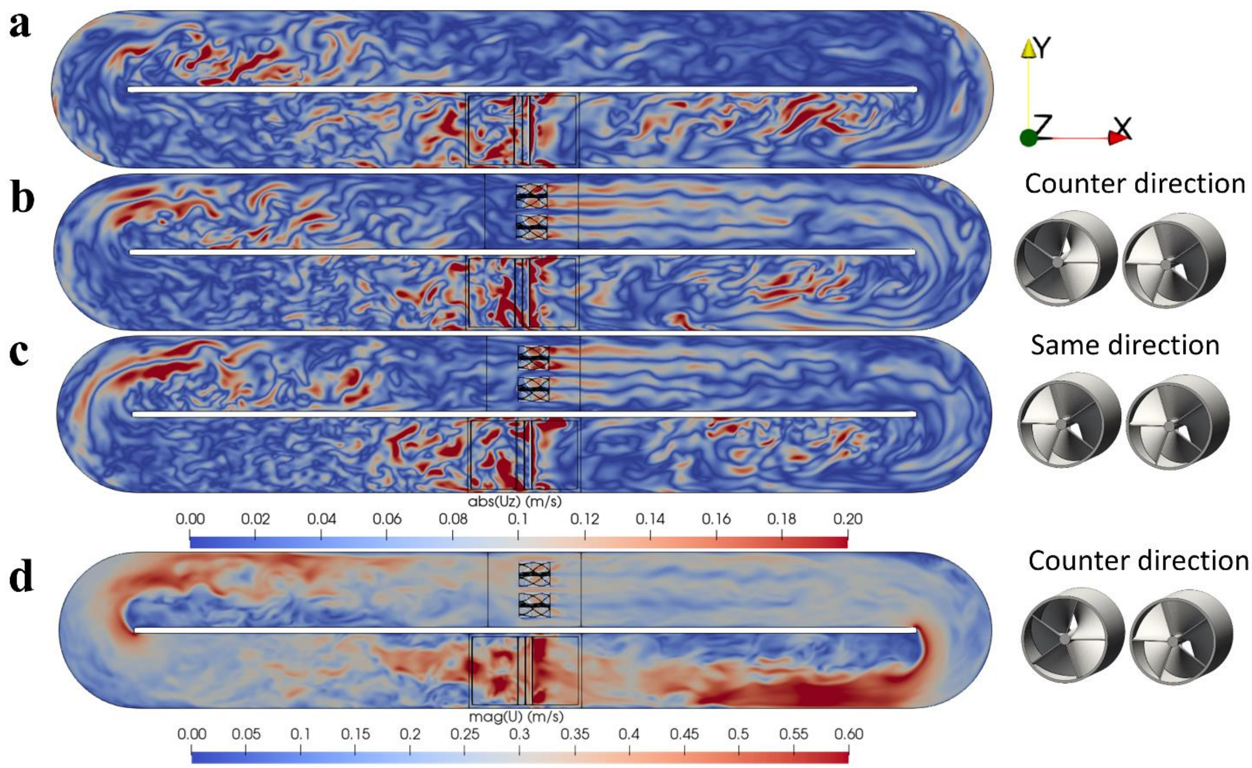

Figure. 5.4. The abs(u_z) contours at z = 0.1 m. (a) abs(u_z) contour at the horizontal plane at z = 0.1 m, flow time t = 100 s without vortex generators placed. (b) abs(u_z) contour at the horizontal plane at z = 0.1 m, flow time t = 100 s when the vortex generators are placed in the counter directions. (c) abs(u_z) contours at the horizontal plane at z = 0.1 m, flow time t = 100 s when the vortex generators are placed in the same direction. (d) mag($\boldsymbol{u}$) contours at the horizontal plane at z = 0.1 m, flow time t = 100 s when the vortex generators are placed in counter directions.

5.3.2 Vortex generator deployment strategy

Since the five blades inside the vortex generator are curved in the same direction and the width of a raceway pond is invariably larger than the diameter of the generator, the generators must be situated in parallel and can be oriented in the same direction or counter directional. Figure. 5.4b shows the abs(u_z) contours in the horizontal mid-plane when two vortex generators are placed in a counter direction. Compared to the unidirectional configuration (Figure. 5.4c), the swirling motion generated in the counter configuration occupies a larger volume and propagates for a longer distance. One explanation is that when multiple vortex generators are placed counter to one another, the downstream fluid flows in the same direction at the center of two neighbor generators. To illustrate this, Figure. 5.5a displays the velocity fields in 3 vertical planes downstream of the vortex generators when they are oriented in a counter configuration, which is highlighted by the rotational direction of the internal blades. As the blades are curved clockwise in the right vortex generator and count clockwise in the left vortex, the swirling motion generated downstream of the vortex generators are oriented in the same direction as the blades. With the right swirling motion oriented clockwise and the left one oriented counterclockwise, the fluid in the center flows upward. On the contrary, when adjacent generators are placed with blades oriented in the same direction, the fluid between them will flow in opposite directions, with one flowing upward next to the other flowing downward, so that their momentum cancels to some extent, and as a result, the swirling motion cannot propagate as far as in the counter orientation due to this dampening effect.

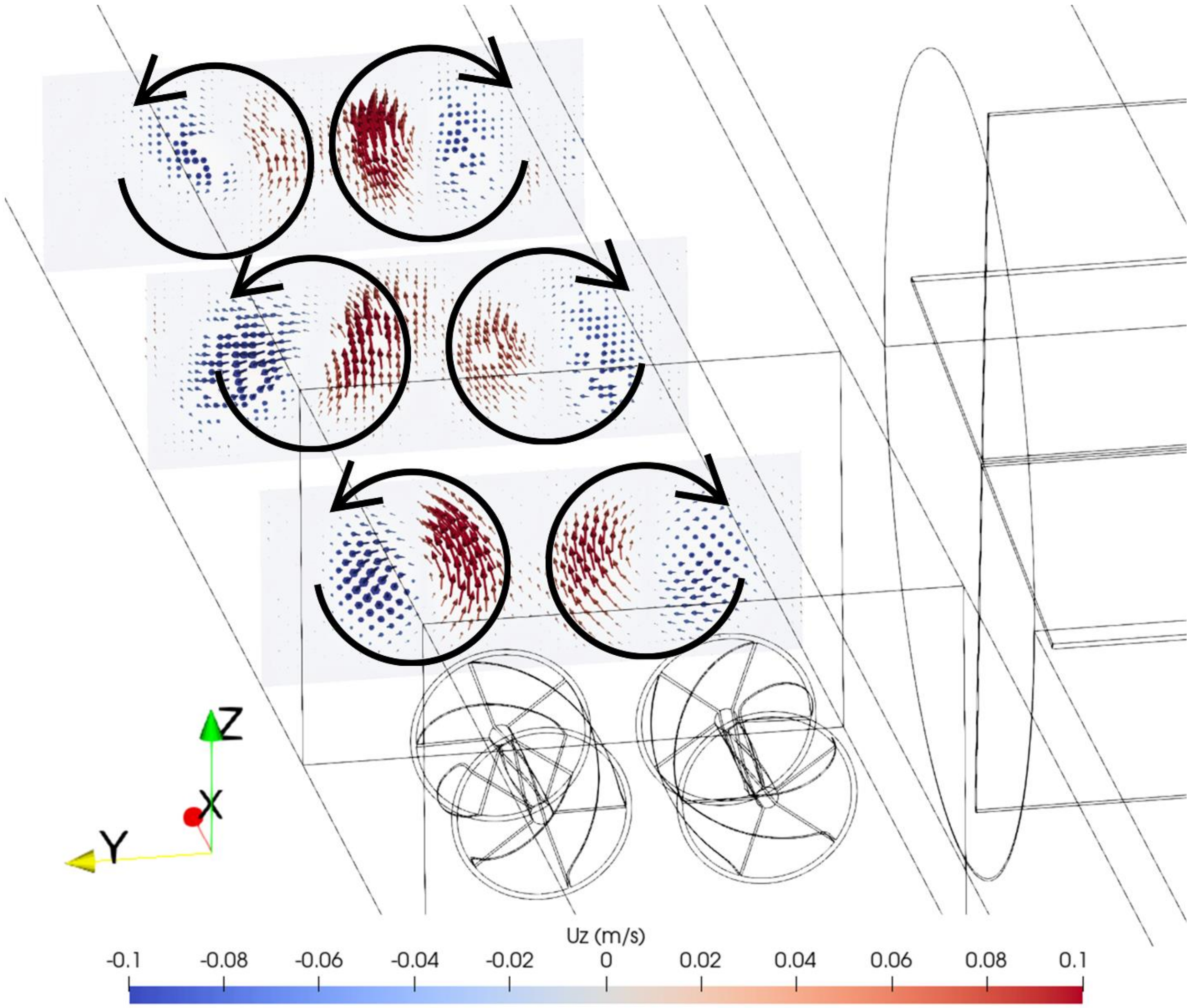

Figure. 5.5. Velocity fields on 3 vertical cross sections downstream the pair of vortex generators that is placed in the counter configuration. The velocity vectors are colored by the magnitude of u_z.

5.3.3 Determine the optimal diameter of the vortex generator.

It is hypothesized that there exists an optimal generator diameter relative to the water depth of the raceway pond. If the diameter of the generator exceeds the liquid depth of the pond, a portion of the generator will protrude through the air-liquid interface, preventing the liquid from turning completely inside the generator. When the diameter of the generator is significantly smaller than the water depth, it is hypothesized that the swirling motion generated will have a reduced strength and dissipate faster.

To address these hypotheses and determine the optimal diameter for a vortex generator, three water depths were simulated (0.1, 0.15, and 0.25 m), rather than changing the diameter of the generators and placing them in a constant water depth. As it was determined in Section 5.3.2 that placing the vortex generators in a counter configuration results in a stronger swirling motion with a longer persistence length, the vortex generators are configured this way to investigate the optimal diameter in this part of the study. Figure. 5.6a displays the contours of abs(u_z) in the horizontal mid-plane (z = 0.05 m) for a water depth of 0.1 m. When the water depth is set to 0.1 m, the generators are unable to produce a significant swirling motion, with 44% of the generator body protruding through the air-water interface. However, vortices can still be observed downstream of the vortex generators, albeit at a much weaker strength than the swirling motion depicted in Figure. 5.4b.

When the water depth is set to 0.15 m, slightly less than the diameter of the vortex generator, the resulting abs(u_z) contours in the horizontal mid-plane (z = 0.075 m) can be seen in Figure. 5.6b. It reveals that the swirling motion generated is sufficiently strong to be observed in the abs(u_z) contours and is significantly stronger than the case with the 0.1 m water depth. Although the liquid cannot make a full turn inside the generators due to the section of the generators protruding through the liquid-gas interface, significant swirling motions can be observed downstream of the generators.

For the 0.25 m water depth, Figure. 5.6c displays the abs(u_z) contours at the horizontal mid-plane (z = 0.125 m). The swirling motion downstream of the generators has a comparable strength as in the 0.15 m water depth case.

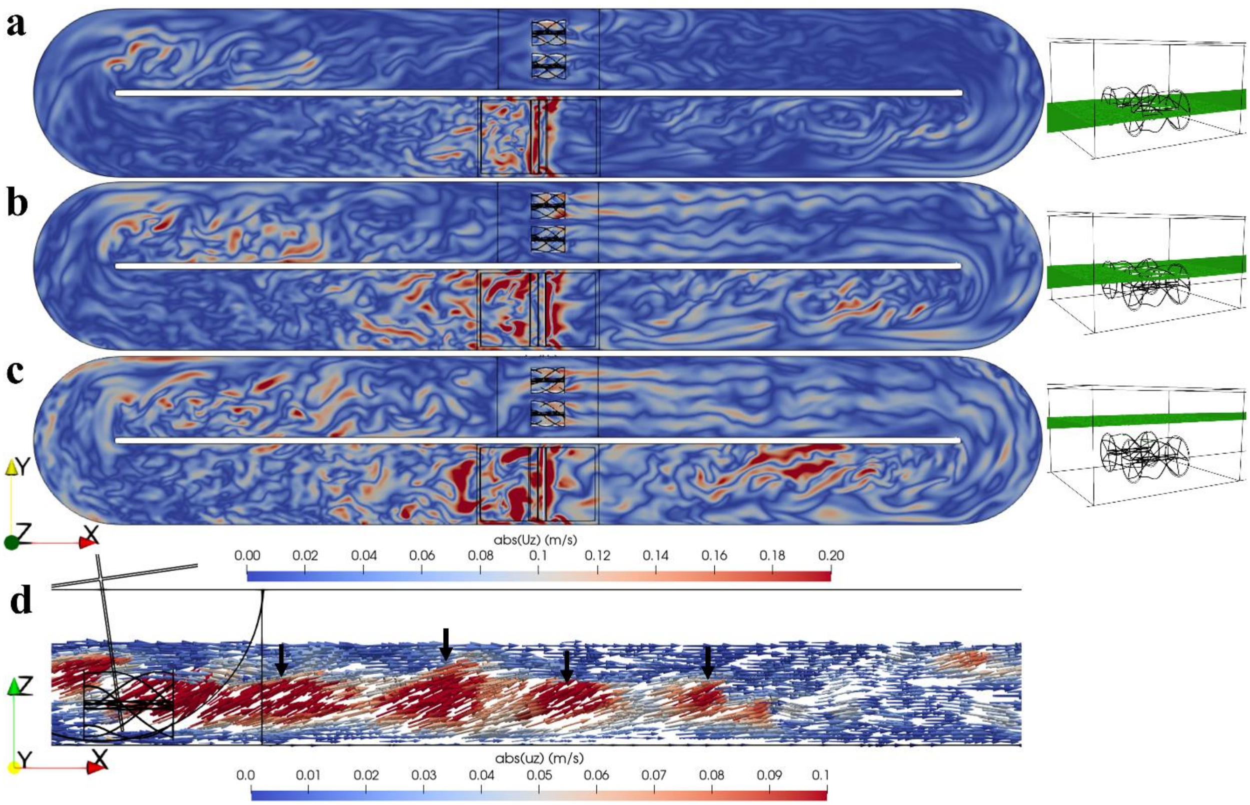

Figure. 5.6. abs(u_z) contour at the horizontal plane at z = 0.1 m, flow time t = 100 s where the vortex generators are placed in counter directions. (a) Diameter of the vortex generator is 0.18 m, water depth is 0.1 m. (b) Diameter of the vortex generator is 0.18 m, water depth is 0.15 m (c) Diameter of the vortex generator is 0.18 m, water depth is 0.25 m. (d) velocity field of a vertical cross section downstream of the vortex generators and colored by abs(u_z).

In none of these cases does the generated swirling motion persist as far as the 0.2 m water depth scenario seen in Figure. 5.4b. As there is considerable liquid flowing above the vortex generators when liquid depth is 0.25 m, that region is primarily flowing horizontally and has the potential to interfere with the swirling motion downstream of the generators. This potential interference is demonstrated in Figure. 5.6d where the velocity field of a vertical cross section is plotted and colored by abs(u_z). It can be observed that there is considerable liquid above the swirling motion that flows horizontally from the left to the right of the section, and the positions where the high vertical velocity region contacts with the horizontal flow are marked with black arrows. It is logical to assume that when those two flows are in contact, their momentum will be exchanged, and as the result, the swirling motion is negatively impacted, and the persistence length is reduced in comparison to the 0.2 m water depth case (Figure. 5.4b).

By studying the abs(u_z) contours in the horizontal plane located at the center of the liquid region at various operating water depths, there is the somewhat straightforward conclusion that the diameter of the vortex generators should be equal to or slightly smaller than the operating water depth. If the diameter of the generator is greater than the water depth, the liquid cannot make complete rotations inside the generators, and the angular momentum cannot be sustained for a long distance downstream of the generators. When the generator diameter is significantly less than the liquid depth (more than 3 cm smaller), the fluid flow above the generators may interfere with the swirling motion generated downstream of the generators and have a negative impact on the persistence length of the generated swirling motion. It is important to note that there is some leeway in the relationship between generator diameter and water depth. The generator can protrude 15% above the interface or lie 25% below the interface and still produce a significant swirling flow that persists for long distances.

5.3.4 Determine the optimal length

To determine the optimal length L_{opt}, vortex generators with the lengths of 0.1, 0.15, 0.2, 0.25, 0.3, and 0.4 m with the same blade pitch are positioned in a straight channel where flow is driven by a paddle wheel. The diameters of all the vortex generators are 0.18 m, and the water depth is 0.2 m.

A straight channel is utilized to eliminate the secondary flow effect created by the bends, and the straight channel's inlet and outlet are coupled to AMI boundary conditions to impose periodic boundary conditions where the same flow field information will be distributed. Thus, the swirling motion caused by the hairpin is avoided, and the swirling motion caused by vortex generators of various designs can be isolated and compared at a reduced computational cost.

The performance of the vortex generators can be characterized by the volume fraction of liquid containing the high vertical velocity regions downstream of the generators, with a larger occupied volume and a longer persistence length indicating better performance. As illustrated in Figures. 5.4a, 5.4b, and 5.4c, the high vertical velocity zones occupy the majority of the space across the channel width in all circumstances. Thus, rather than calculating the volume of liquid occupied by the high vertical velocity regions, the persistence length of these regions is utilized to quantify the vortex generators' performance. Section 2.6 covers the procedure for calculating the persistence length for various critical vertical velocity magnitudes, and the persistence length is measured from the outlet of the vortex generators.

The persistence lengths for the six different lengths are presented in Figure. 5.6, with the outlet of each vortex generator marked by a vertical blue line and the computed persistence length denoted by a horizontal blue line. It can be observed that when the critical vertical velocity magnitude increases, the persistence length for all the cases decreases, which is reasonable as a more liquid region is filtered out when a larger critical vertical velocity is used, resulting in a shorter persistence length.

When 0.12 m/s is used as the critical vertical velocity, the persistence length decreases from 3.90 m to 3.73 m when the vortex generator length increases from 0.1 m to 0.15 m and then continues to increase up to a generator length of 0.3 m. A significant persistence length decrease can be observed when the length of the vortex generator increased from 0.3 m to 0.4 m. When the length is between 0.1 m and 0.3 m, the fluid spends more time inside the generators and gains more angular momentum and therefore, results in a longer persistence length. However, when the length is further increased above 0.3 m, it is believed that the resistance force that fluid experienced due to the internal propeller blades is increased to the point that the performance of the 0.4 m long vortex generator deteriorates. Similar results can be observed when the critical vertical velocities are set to 0.16 and 0.18 m/s.

The longest persistence lengths of 2.25 m and 1.67 m are obtained when the generators are 0.3 m in length, which can be explained by the extra angular momentum gained by the fluid with a longer generator length. Thus, when the critical vertical velocity is between 0.16 and 0.18 m/s, the optimal length is 0.3 m.

When the generator's length is increased above 0.3 m, the persistence length decreases, and the ability to generate whirling motion deteriorates. When the critical vertical velocity is set to 0.18 m/s, the retained high velocity region is the core of the swirling motion where the rotational speed is high and occupies a considerably smaller volume compared to the case with a lower critical vertical velocity such as 0.12 m/s (Figures. 5.7a and 5.7c). However, the volume of high vertical velocity regions within the vortex generators is comparable, indicating that the fluid gains significant angular momentum almost as soon as it enters the generator inlets. When the length of the generator is increased from 0.1 m to 0.15 m, the resulting persistence length is decreased. One possible explanation for this is that the shorter length in the 0.1 m length scenario imposes a less resistance force for the fluid and therefore, a longer persistence length can be achieved. Regardless, observation was consistent regardless of the specifics of how persistence length is calculated.

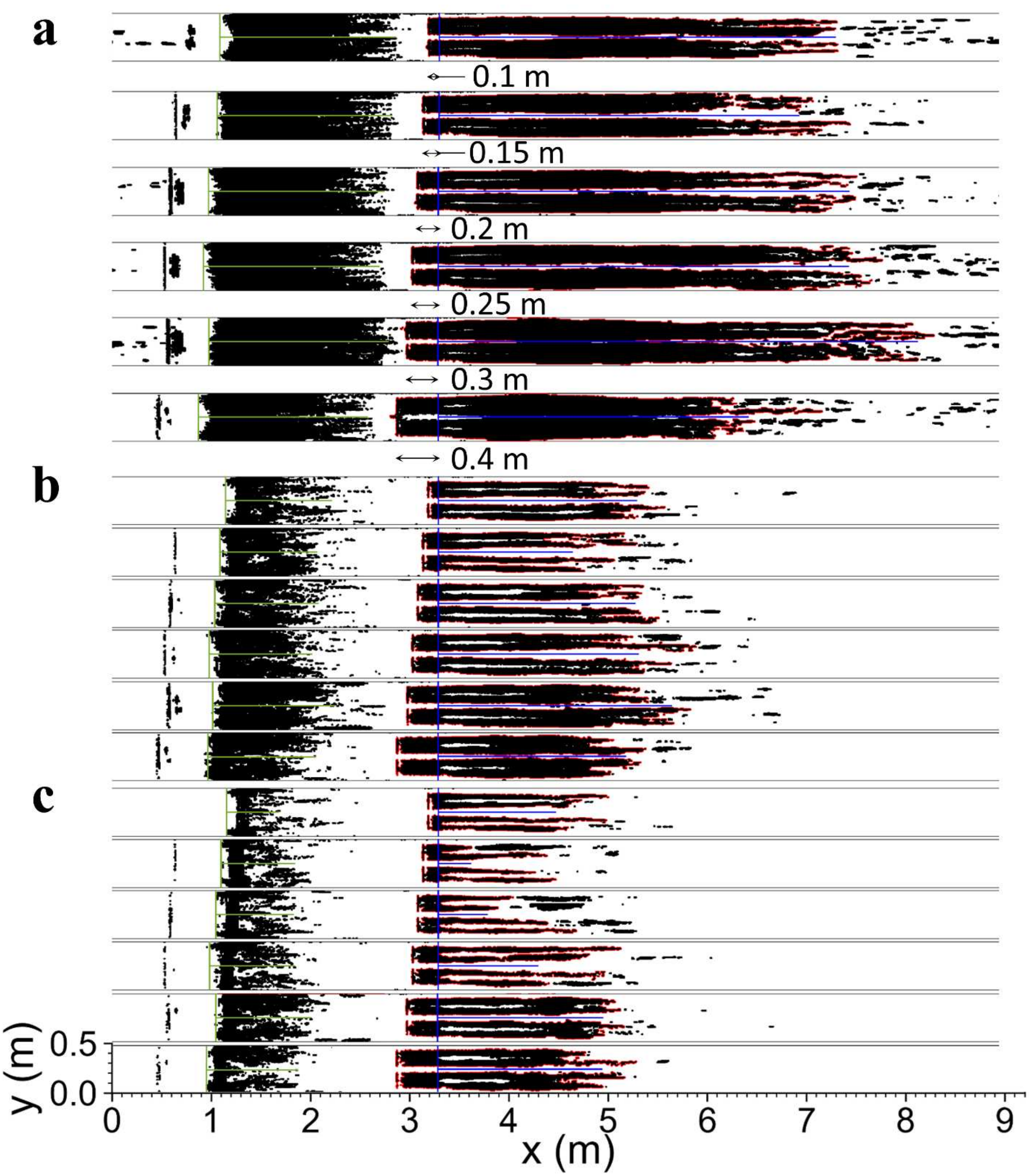

Figure. 5.7. High vertical velocity regions and persistence length of swirling motion generated by the paddle wheel (horizontal green line) and swirling motion generated by vortex generators (horizontal blue line). (a) $u_{z,cri}$ =0.12 m/s. (b) Critical vertical velocity=0.16 m/s. (c) $u_{z,cri}$ =0.18 m/s.

To summarize, when the swirling motion persistence length is considered at three different values of critical vertical velocity, the L_{opt} is determined to be 0.3 m. At this length/diameter ratio, the generated swirling motion occupies the largest volume downstream of the generator (shown in Figures. 5.7a and 5.7b), with the core of the swirling motion persisting the longest distance (Figure. 5.7c).

However, when the material cost is taken into consideration, the 0.1 m long vortex generator achieves an impressive degree of swirling motion where the averaged persistence length is 81.8% of the best case when $u_{z,\mathrm{cri}}$ = 0.18 m/s and the persistence length is only 25.8% lower than the 30 cm generator when 0.12 m/s is chosen as the critical vertical velocity. When a higher critical vertical velocity is used, the persistence length of the 0.1 m system still shows a long persistence length close to the 0.30 m long design. For ponds with extremely long straight sections, it may be more cost effective to install multiple instances of the 0.1 m generators.

5.3.5 Swirling motion morphology

A significant finding from this work is that the vertical motion induced by the paddle wheel's rotational motion cannot propagate over a significant distance, as illustrated in Figures. 5.4 and 5.7. The region of high vertical velocity observed using three distinct critical vertical velocities reveals that the swirling motion generated by the paddle wheel has a substantially shorter persistence length than the swirling motion downstream of the vortex generators (Figure. 5.8). When $u_{z,\mathrm{cri}}$ = 0.12 m/s is used, the persistence length of the swirling motion generated by the paddle wheel is estimated to be 1.75 m, whereas the swirling motion generated by the 0.1 m long vortex generator can travel up to 3.90 m. This is also the case when a critical vertical velocity of 0.18 m/s is employed. The swirling motion generated by the paddle wheel is limited to 0.77 m, while the 0.1 m long vortex generator induces swirling motion that can propagate as far as 1.28 m. As the length a commercial raceway pond, such as the RW101 raceway pond design developed by MicroBio Engineering Inc., can easily reach to 33.8 m, the vertical mixing induced by the paddle wheel is limited and the swirling motion generated by the paddle wheel can only persist for a short distance compared with the length of the straight section. This inadequacy can be explained by the morphology of the swirling motion. Figure. 5.9 represents the iso-surface for a Q criterion of 5. When the swirling motion is generated by the rotational motion of the paddle wheel, the rotational axis of the motion is perpendicular to the direction of the main flow.

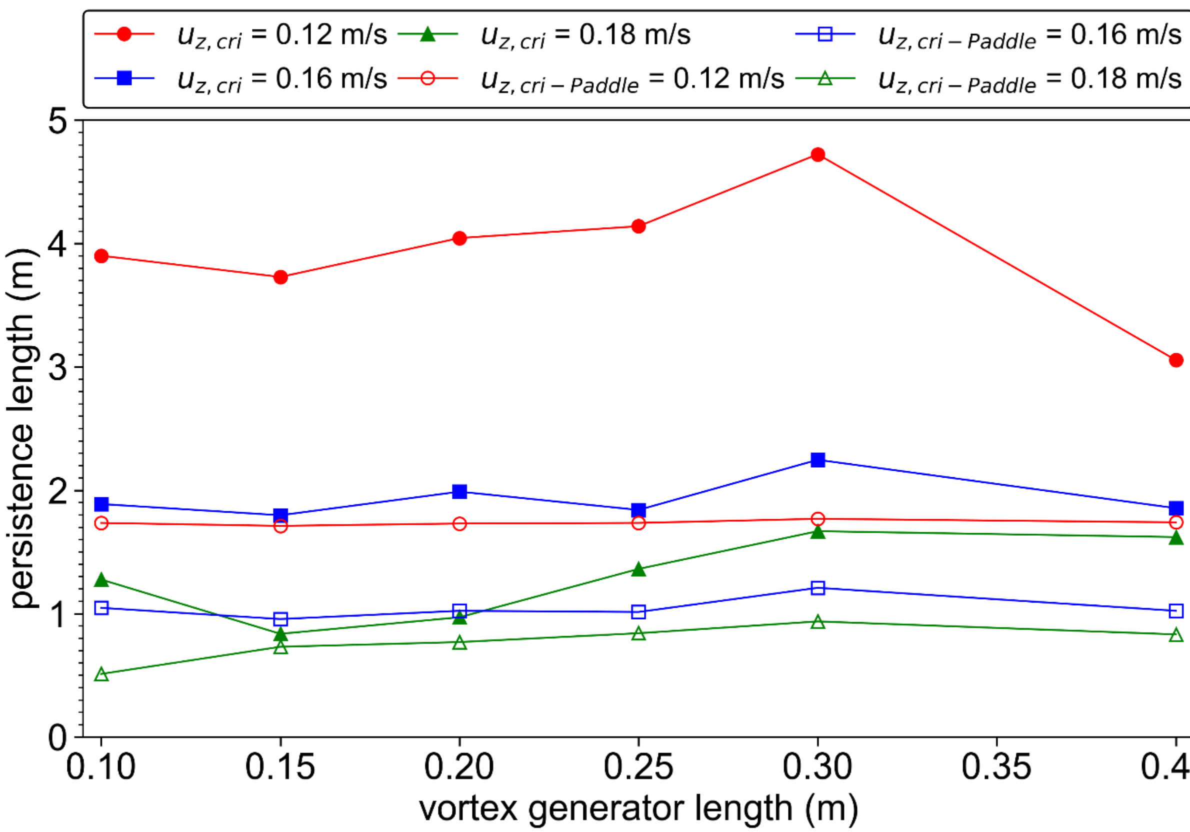

Figure. 5.8. Persistence length of the swirling motion generated by the vortex generators and the paddle wheel.

Since the fluid velocity field is not uniform across the channel width, the swirling motion transported downstream of the paddle wheel breaks up to smaller vortices, and their axes are turned to the direction of the main flow, which is illustrated in Figure. 5.8. On the contrary, the rotational axis of the swirling motion generated by the secondary flow downstream the hairpin bend as well as those downstream the vortex generators are parallel to the direction of the primary flow. The results of the straight channel simulation (Figure. 5.9), as well as the one with the raceway pond geometry (Figures. 5.4a and 5.4c) suggest that the swirling motion does not dissipate as quickly when the axis of rotational motion is parallel to the main flow direction, and therefore, can persist for a longer distance. Since the swirling motion induced by the vortex generators has a similar morphology with the one generated by the secondary flow at the bend, it is believed that the swirling motion generated by the hairpin bend also benefits from this mechanism.

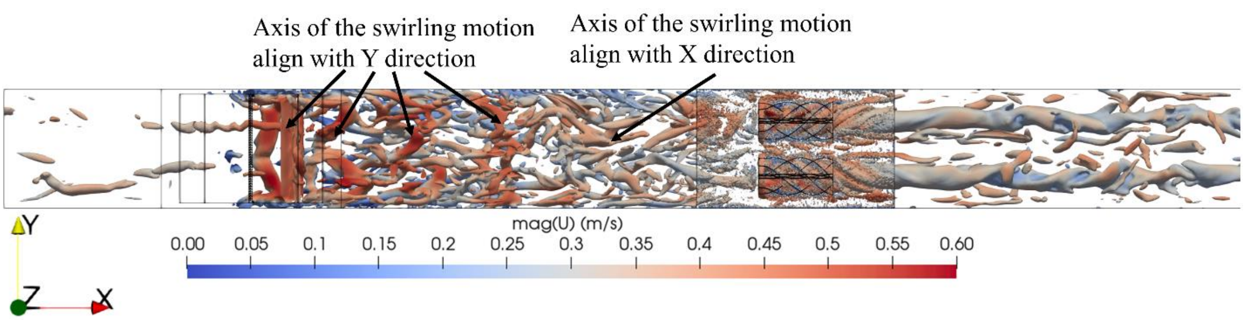

Figure. 5.9. Iso-surfaces Q-criterion = 5 at flow time = 100 s where 0.3 m long vortex generators are placed in counter directions in a straight channel.

5.4. Conclusion

In this study, the novel design and characterization of a vortex generator with inclined internal baffles is presented. Its ability to enhance vertical motion by generating vortices downstream of the generator is evaluated and quantified using CFD simulations in which the vortex generator is located in the second straight section of a raceway, as well as in a straight channel with a paddle wheel. The CFD results indicate the following:

1. It is predicted that there is a significant enhancement of vertical mixing downstream of the vortex generator.

2. To obtain optimal vertical mixing and persistence length, the vortex generators should be placed in a counter configuration such the fluid motion will be symmetrical between two adjacent generators, and the vertical motion is enhanced as a result.

3. The generator's diameter should be slightly smaller than the intended water depth. For example, for a 20 cm depth pond, the optimal diameter appears to be around 18 cm. If the generator's diameter is significantly larger than the water depth, the fluid cannot make complete turns inside the vortex generator, and the swirling motion cannot persist reasonably far. Leaving excessive space above the vortex generator is also considered sub-optimal since the horizontal flow above tends to dampen the generated swirling motion.

4. The optimal length is determined to be around 0.3 m for a 0.18m-diameter vortex generator. However, it is found that a vortex generator with a length of 0.1 m can still generate significant secondary motion such that the persistence length will be only 18.2% less than the optimal scenario and may be desirable when material costs are taken into account.

5. The paddle wheel has been thought to have a significant impact on the mixing performance in raceway pond systems. However, the results of the straight channel simulations suggest that the swirling motion generated by a paddle wheel cannot persist over a distance comparable with the swirling motion generated by the current vortex generator design. Since the swirling motion induced by the paddle wheel has a rotational axis that is perpendicular to the direction of the main flow, the eddies are broken up into smaller, weaker vortices. Therefore, one strategy identified in this study is to induce swirling motion with a rotational axis parallel to the main flow direction in order to obtain optimal vertical mixing enhancement and persistence.

5.5 References

[1] J. E. Keffer and G. T. Kleinheinz, "Use of Chlorella vulgaris for CO2 mitigation in a photobioreactor," *J. Ind. Microbiol. Biotechnol.*, vol. 29, no. 5, pp. 275–280, Nov. 2002, doi: 10.1038/sj.jim.7000313.

[2] A. P. Carvalho, S. O. Silva, J. M. Baptista, and F. X. Malcata, "Light requirements in microalgal photobioreactors: an overview of biophotonic aspects," *Appl. Microbiol. Biotechnol.*, vol. 89, no. 5, pp. 1275–1288, Mar. 2011, doi: 10.1007/s00253-010-3047-8.

[3] "A matter of detail: Assessing the true potential of microalgal biofuels - Klein-Marcuschamer - 2013 - Biotechnology and Bioengineering - Wiley Online Library." https://onlinelibrary.wiley.com/doi/full/10.1002/bit.24967 (accessed Oct. 04, 2021).

[4] C. Posten, "Design principles of photo-bioreactors for cultivation of microalgae," *Eng. Life Sci.*, vol. 9, pp. 165–177, Jun. 2009, doi: 10.1002/elsc.200900003.

[5] F. G. Acién *et al.*, "1 - Photobioreactors for the production of microalgae," in *Microalgae-Based Biofuels and Bioproducts*, C. Gonzalez-Fernandez and R. Muñoz, Eds. Woodhead Publishing, 2017, pp. 1–44. doi: 10.1016/B978-0-08-101023-5.00001-7.

[6] C. Jiménez, B. R. Cossío, D. Labella, and F. Xavier Niell, "The Feasibility of industrial production of Spirulina (Arthrospira) in Southern Spain," *Aquaculture*, vol. 217, no. 1, pp. 179–190, Mar. 2003, doi: 10.1016/S0044-8486(02)00118-7.

[7] L. Rodolfi et al., "Microalgae for Oil: Strain Selection, Induction of Lipid Synthesis and Outdoor Mass Cultivation in a Low-Cost Photobioreactor," Biotechnol. Bioeng., vol. 102, pp. 100–12, Jan. 2009, doi: 10.1002/bit.22033.

[8] O. Jorquera, A. Kiperstok, E. A. Sales, M. Embiruçu, and M. L. Ghirardi, "Comparative energy life-cycle analyses of microalgal biomass production in open ponds and

photobioreactors," *Bioresour. Technol.*, vol. 101, no. 4, pp. 1406–1413, Feb. 2010, doi: 10.1016/j.biortech.2009.09.038.

[9] S. Abu-Ghosh, D. Fixler, Z. Dubinsky, and D. Iluz, "Flashing light in microalgae biotechnology," *Bioresour. Technol.*, vol. 203, pp. 357–363, Mar. 2016, doi: 10.1016/j.biortech.2015.12.057.

[10] Z. Chen, X. Zhang, Z. Jiang, X. Chen, H. He, and X. Zhang, "Light/dark cycle of microalgae cells in raceway ponds: Effects of paddlewheel rotational speeds and baffles installation," *Bioresour. Technol.*, vol. 219, pp. 387–391, Nov. 2016, doi: 10.1016/j.biortech.2016.07.108.

[11] K. Lee and C.-G. Lee, "Effect of light/dark cycles on wastewater treatments by microalgae," *Biotechnol. Bioprocess Eng.*, vol. 6, no. 3, pp. 194–199, Jun. 2001, doi: 10.1007/BF02932550.

[12] G. Persoone, J. Morales, H. Verlet, and N. De Pauw, "Air-lift pumps and the effect of mixing on algal growth," 2000. Accessed: Oct. 04, 2021. [Online]. Available: http://www.vliz.be/imisdocs/publications/128033.pdf

[13] A. Richmond, "Biological Principles of Mass Cultivation of Photoautotrophic Microalgae," in *Handbook of Microalgal Culture*, John Wiley & Sons, Ltd, 2013, pp. 169–204. doi: 10.1002/9781118567166.ch11.

[14] "Large-Scale Production of Algal Biomass: Raceway Ponds | SpringerLink." https://link.springer.com/chapter/10.1007/978-3-319-12334-9_2 (accessed Oct. 04, 2021).

[15] J. P. Bitog *et al.*, "Application of computational fluid dynamics for modeling and designing photobioreactors for microalgae production: A review," *Comput. Electron. Agric.*, vol. 76, no. 2, pp. 131–147, May 2011, doi: 10.1016/j.compag.2011.01.015.

[16] J. C. M. Pires, M. C. M. Alvim-Ferraz, and F. G. Martins, "Photobioreactor design for microalgae production through computational fluid dynamics: A review," *Renew. Sustain. Energy Rev.*, vol. 79, pp. 248–254, Nov. 2017, doi: 10.1016/j.rser.2017.05.064.

[17] F. Krujatz *et al.*, "Light-field-characterization in a continuous hydrogen-producing photobioreactor by optical simulation and computational fluid dynamics," *Biotechnol. Bioeng.*, vol. 112, no. 12, pp. 2439–2449, Dec. 2015, doi: 10.1002/bit.25667.

[18] L. Wang, Y. Tao, and X. Mao, "A novel flat plate algal bioreactor with horizontal baffles: Structural optimization and cultivation performance," *Bioresour. Technol.*, vol. 164, pp. 20–27, Jul. 2014, doi: 10.1016/j.biortech.2014.04.100.

[19] R. S. Voleti, "Experimental Studies of Vertical Mixing in an Open Channel Raceway for Algae Biofuel Production," p. 124.

[20] F. Zeng, J. Huang, C. Meng, F. Zhu, J. Chen, and Y. Li, "Investigation on novel raceway pond with inclined paddle wheels through simulation and microalgae culture experiments," *Bioprocess Biosyst. Eng.*, vol. 39, no. 1, pp. 169–180, Jan. 2016, doi: 10.1007/s00449-015-1501-9.

[21] Q. Zhang, S. Xue, C. Yan, X. Wu, S. Wen, and W. Cong, "Installation of flow deflectors and wing baffles to reduce dead zone and enhance flashing light effect in an open raceway pond," *Bioresour. Technol.*, vol. 198, pp. 150–156, Dec. 2015, doi: 10.1016/j.biortech.2015.08.144.

[22] H. G. Weller, G. Tabor, H. Jasak, and C. Fureby, "A tensorial approach to computational continuum mechanics using object-oriented techniques," *Comput. Phys.*, vol. 12, no. 6, pp. 620–631, Nov. 1998, doi: 10.1063/1.168744.

[23] H. Jasak, "OpenFOAM: Open source CFD in research and industry," *Int. J. Nav. Archit.*

Ocean Eng., vol. 1, no. 2, pp. 89–94, Dec. 2009, doi: 10.2478/IJNAOE-2013-0011.

[24] A. Yoshizawa, "Statistical theory for compressible turbulent shear flows, with the application to subgrid modeling," *Phys. Fluids*, vol. 29, no. 7, pp. 2152–2164, Jul. 1986, doi: 10.1063/1.865552.

Chapter 6 Conclusion and future work

6.1 Conclusion

Raceway ponds are frequently utilized as open, outdoor photobioreactors for microalgae cultivation. However, the unit production rate and biomass density achieved in raceway ponds are considerably lower than those reported in lab-scale closed photobioreactors. Significant research has been conducted utilizing CFD modeling approaches to optimize vertical mixing and mass transfer in raceway ponds. The k-ε and LES models have been investigated extensively as possible turbulence models. Since the k-ε model is derived from Reynolds-averaged Navier–Stokes equations by time-averaging the equations of motion for fluid flow, deploying k-ε as the turbulence model has the potential to lose information regarding vertical motion because the vertical fluid motion is secondary to the primary flow in the horizontal direction. In Chapter 2, a meso-scale raceway pond is modeled using the k-ε and LES turbulence models. The predicted flow field is tested experimentally using a custom-built pygmy flow meter. The LES model predicted strong swirling motions around the paddle wheel and downstream of the hairpin bends. The k-ε model, on the other hand, fails to capture the degree of swirling motion, which is supported by examination and comparison of the u_z contours, and the Q-criterion iso-surface predicted by the k-ε and LES models. On the contrary, the LES model has been shown to be critical in capturing small eddies and swirling motion, which will have a substantial impact on future studies of vertical mixing in raceway ponds. For this reason, the LES model is deployed as the turbulence model for the studies presented in chapters 3, 4, and 5. Additionally, the vertical mixing performance is quantified using a systematic method developed in this work, and it is found that, for the meso-scale raceway pond, swirling motion is predicted to occur in approximately 40% of the liquid volume, but only 15% of the liquid volume experiences vertical velocities greater than 0.1 m/s on an average basis.

The knowledge gained from the results suggests that it makes sense to divide the raceway pond into 3 regions: i) low-velocity regions, which are referred to as the dead zones; ii) horizontally moving regions where high velocities are expected but u_z is low; iii) high vertical velocity regions that contribute to enhancing the L/D effect and vertical mixing. The threshold for distinguishing high and low vertical velocity regions was chosen to be u_z = 0.1 m/s. The knowledge gained from Chapter 2 becomes the motivation of the studies in Chapter 3 and Chapter 5 where the spatial distribution of region iii) is predicted in chapter 3 and a vortex generator is designed to convert region ii) into region iii) in chapter 5.

The naturally occurring swirling motion induced in the raceway ponds by the secondary flow generated downstream of the hairpin bends is highlighted as a significant factor in improving the raceway pond's vertical mixing performance. To determine the distance over which swirling motion can persist, 56 examples with 7 shape ratios and 8 paddle wheel RPMs that cover a wide range of *Re* and *De* are simulated in chapter 3 using the open-source CFD tool openFoam and validated with the experimental data from chapter 2. In chapter 3 it is found that the spatial pattern of generated swirling motion varies depending on the shape ratio (straight section width to liquid depth) of the raceway pond. When the shape ratio is near 1, one instance of swirling motion is likely to be observed downstream of the hairpin bend. However, when the shape ratio is greater than 1, numerous instances of swirling motion are predicted. Additionally, a systematic approach for determining the persistence length of the swirling motion is developed. A dimensional analysis study shows that the dimensionless groups $U_{4R}/\overline{U}_{2R}$ and $D_h/2R$ can be correlated with a rational function:

$$\frac{U_{4R}}{\overline{U}_{2R}} = \frac{p_1 \frac{D_h}{2R}}{\frac{D_h}{2R} + q_1}$$

This empirical equation can be used to predict the critical velocity in a large-scale raceway pond design under a wide range of operating circumstances prior to construction or conducting costly numerical simulations.

In chapter 4, transient particle tracking is performed to determine the microalgae cells' trajectories using the pre-calculated velocity data predicted by openFoam in chapter 2. It is discovered that a significant computational expense can be avoided by using pre-calculated velocity data while still capturing accurate microalgae trajectories. The probability density of the primary parameter light to light intervals is compared to the predicted particle trajectories using full-time velocity fields, and it is found that a comparable result is obtained. The probability density function of L/L intervals is fit well by lognormal distributions, and the probability density function of abs(u_z) is shown to be fit by exponential distributions. The impact of increasing the paddle wheel RPM on the velocity fields and light environment is determined as widening the abs(u_z) PDF and reducing the standard deviation of L/L intervals while reducing the L/L interval that corresponds to the PDF peak. Additionally, Chapter 4 investigates the spatial probability distribution of L/D transitions. The zone with a higher probability of L/D transitions overlaps with the swirling motion, demonstrating that the swirling motion contributes significantly to reducing the L/L intervals and therefore increasing the L/D frequency. When the paddle wheel RPM is increased, the locations with a high probability of an L/D transition is further increased. The exception is the zone near and downstream of the paddle wheel where small improvement is observed with increased paddle wheel RPM. In comparison to a small-size raceway pond (SR = 2.55, surface area = 4.0 m^2), a large-scale raceway pond (SR = 7.05, surface area = 25.1 m^2) has a lower overall spatial probability of L/D transition. One rationale is that increasing the paddle wheel RPM in a larger pond does not increase the abs(u_z) in the pond as effectively as it does in a smaller pond, and hence the L/D frequencies are not improved as significantly as they are in a smaller pond.

In chapters 2 and 3 it is demonstrated that an effective and efficient method for increasing vertical mixing and L/D frequency is to install passive vortex enhancing devices that are capable of converting horizontal flow motion to vertically rotational motion. Chapter 5 presents a novel design of a vortex generator to demonstrate this effect. By modeling the flow field with and without the vortex generator in the second straight section of a raceway pond, it is found significant vertical mixing is produced downstream of the vortex generator. To achieve the best results, it is recommended that the vortex generators be placed in a counter configuration; the optimal diameter of the vortex generator should be slightly smaller than the liquid depth, and the optimal length for the 0.18 m diameter vortex generator is determined to be around 0.3 m. Furthermore, comparing the persistence length downstream of the paddle wheel and vortex generator under various $u_{z,\mathrm{cri}}$, it is found that the swirling motion generated downstream of the paddle wheel does not persist as long as compared to the swirling motion observed downstream of the vortex generator. An explanation is that swirling motion with its rotational axis parallel to the main flow direction can persist for a longer distance than the rolling motion whose axis is perpendicular to the main flow direction.

6.2 Future work

In chapter 2, the time-averaged velocity fields of the simulation results are compared with experimental measurements in one vertical cross section. To fully validate the simulation results, a particle image velocimetry of a raceway pond constructed with transparent material is suggested. In chapter 3, a systematic way to predict the U_{4R} is established. Extending the method to explore the constants of the rational function to predict the critical velocity for longer persistence length is promising. In chapter 4, integrating the light history to a varying-intensity light array for microalgae cultivation in open ponds will provide insight into the impact of the light environment on microalgae growth. In chapter 5, the optimal length for the 0.18 m diameter vortex generator is determined. It would be promising to determine the optimal length for vortex generators with different diameters and validate the flow field with experimental measurements with vortex generators built and installed in the raceway ponds.

Appendix A

The effect of the body wake and operator motion on the containment of nanometer-scale airborne substances using a conventional fume hood and specially designed enclosing hood: A comparison using computational fluid dynamics

Introduction

It is desirable when working with nanometer-scale airborne materials, including engineered nanomaterials whose agglomerated sizes are within a few hundred nanometers, to employ effective exposure controls and proper work practices so that exposure and subsequent adverse effects on process performance are minimized and a safe and healthy work environment is maintained [1, 2]. Airborne substances smaller than one micrometer in size would mostly follow airflow pattern and flow in the airstream [3]. This property emphasizes the importance of understanding the airflow dynamics to further manage the control measures to toxic airborne substances such as nanometer-sized particles [4, 5]. Chemical fume hoods are being utilized as primary controls for worker exposure to airborne substances including nanometer-scale materials due to their overall availability and history of effective contaminant [6]. However, traditional designs for laboratory fume hoods create airflow patterns that form recirculation regions inside the hood. In addition, airflow around the worker creates a negative pressure region downstream of the worker that may provide a mechanism for transporting contaminants out of the hood and into the breathing zone of the worker [7]. This study utilized computational fluid dynamics (CFD) to assess the impacts of the presence of the worker body and the motion of the arms on the containment effectiveness of a traditional constant air volume (CAV) fume hood and a ventilated enclosure that is designed for handling nanomaterials.

The use of visualization techniques has proved critical in gaining a better understanding of the flow patterns which affect overall hood performance [8-11]. Several researchers have identified the existence of an airflow pattern inside the hood that carries contaminants released above the work surface into a large recirculation zone located behind the sash [10, 12-18]. This recirculation region acts to trap contaminants and is potentially a problematic area for leakage of contaminants generated inside the hood. In addition, boundary layer separation produces a wake region, characterized by eddies or vortices that entrain air into a reverse-flow region near the body [19-23]. This near-wake region may serve to transport contaminants from the fume hood into the breathing zone of the person standing in front of the hood.

Kim and Flynn (1991) showed that a recirculation region forms downstream of a worker in a free stream (as air flows from the back of the worker) with a length proportional to the mannequin's shoulder width [21]. Their research also indicated that a vertical flow field was present downstream near the worker where the mean flow field would serve to transport contaminants from the waist level or higher into the breathing zone. Further research by Kim and Flynn (1991) confirmed that this recirculation region could transport contaminants released downstream of the worker into the breathing zone [22]. Welling et al.(2000) evaluated a range of conditions related to potential exposure of a mannequin in free stream including body heat, arm motion, variations in air velocity and body orientation [24]. This research observed lower breathing zone concentrations for a mannequin at lower free stream velocities than at higher velocities; and the effect of arm motion was likened to a fan that disrupted airflows and resulted in increased contaminant dispersion upward. Upstream disruptions that interfere with near-wake eddy formation and maintenance have also been explored as a contaminant control measure [25].

Other researchers have also identified significant fume hood leaks when the operator moved their arms in and out of the hood, a common practice used to move objects and equipment in and out of the hood or upon completion of work [26, 27].

In an experimental study, the presence of a mannequin was shown to interact with the regions of airflow separation near the bottom and sides of the hood to increase the size of the recirculation region near the doorsill and side poles than without the mannequin [28]. The presence of the mannequin increased the intensity and size of the separation and recirculation zones around the middle and lower levels of the hood opening. These effects resulted in fume hood leaks at the middle and lower levels hood opening being more likely than without the mannequin. A meta-analysis of 43 published experimental fume hood containment studies was conducted to identify the important elements that affect the performance of a laboratory fume hood [29]. This analysis showed that the presence of a mannequin/human subject in front of the hood caused the greatest risk of containment failure among all factors evaluated, resulting in a 199% higher risk of hood failure than when no mannequin was present.

The impacts of the body on fume hood containment have also been evaluated using CFD. CFD is a useful tool and has been used in several previous studies to evaluate the impact of hood design on containment performance [13-16, 30, 31]. These studies have led to a better understanding of how design factors affect performance and have improved hood containment. Hu et al. used 2-D CFD models to look at several different design configurations including the inclusion of a sash handle, the effect of interior baffles and a louvered bypass on hood airflow characteristics [13, 14]. They found that the design and placement of the sash handle has important consequences on the likelihood of contaminant leakage around the bottom of the sash. This effect is due to the impact of turbulence caused by the handle which causes contaminants caught in the large recirculation region behind the hood sash to leak out of the hood. Nicholson et al. (2000) developed a 3-D model which included a rear baffle and an aerodynamic lipfoil (located at the base of the fume hood opening) [15]. The simulations showed that removing the rear baffle eliminated the flow across the hood floor, increased the size of the vortex behind the sash and created a large stagnant zone at the back of the work surface. With full aerodynamic features (baffle and lipfoil), the face velocity across the opening was uniform and containment performance was dramatically improved. Because of these and other studies, most of these features are commonly found on chemical fume hoods today. Kumula et al. (1996) evaluated the effect on exposure of the recirculation region downstream of the worker using both experimental and CFD methods [32]. Experimental results showed that the mean recirculation region length did not greatly depend on free stream velocity and appeared to be 1.5 times the mannequin's width. A clockwise upward recirculation region existed above the mannequin hip level which provided transport to the breathing zone consistent with the findings from other researchers. Braconnier and Bonthoux (2010) evaluated a type II microbiological safety cabinet (BSC) (called a cytotoxic safety cabinet) using a 3-D CFD model [30]. The BSC differs from a standard fume hood in that there is an exhaust slot along the front of the hood at the base and a continuous down flow inside the hood which is recirculated from the overall exhaust flow following high efficiency particulate air (HEPA) filtration. A blockage representing an operator in front of the hood caused a small wake in front of the mannequin. In addition, there was a reduction in the inward air velocity at mid opening heights; but it did not cause air to flow out of the hood. Further, a simplified arm geometry (without a body) similar to one used for BSC containment testing was evaluated and found not to have a significant effect on containment [30]. No fume hood CFD studies found in the published literature have evaluated the impact of user motion on containment effectiveness.

Nano hoods specifically designed for nanomaterials have been manufactured based on low turbulence balance enclosures which were initially developed for the weighing of pharmaceutical powders. Bench-mounted weighing enclosures are commonly used for the manipulation of small amounts of material. These fume hood-like local exhaust ventilation devices typically operate at airflows lower than those in traditional fume hoods and use airfoils at enclosure sills to reduce turbulence and potential for leakage. New lower flow hoods are being marketed and used for the manipulation of nanomaterials. The use of lower inlet airflows may reduce the impact of turbulence and the body wake on the potential for fume hood leakage. However, there is little information on their performance.

This study used numerical methods to evaluate the impact of the body wake on containment performance of a CAV and the nano hood. Previous experimental studies presented hood leakages with nanomaterials handled inside the hood [33, 34]. We performed experiments in the current study to validate the CFD models and to provide a basis for evaluating the impact of the human body on fume hood containment performance. Thus, the effects of arm motion into and out of the hood was simulated using CFD in this study to assess how one of the common actions of an operator/user may affect containment.

Methods Description of Hoods and Equipment Setup

The "nano" ventilated enclosing hood evaluated was the A1 Safetech ST1 (Dusseldorf, Germany) potent powder weighing enclosure (hereafter referred to as the nano hood). The exhaust of the hood is routed through an attached fan and HEPA filtration unit with air recirculated into the room. The HEPA fan/filter unit provides the important function for the removal of powders and filtration of air prior to recirculating the air to the workplace. The HEPA fan/filter unit (33 cm in width × 33 cm in depth × 50 cm in height) was co-located to the right of the hood face. This hood located in a university lab was 7.32 m in width by 4.85 m in depth with a ceiling height of 2.75 m. The hood was located on a bench top with shelving located above the hood along with an assortment of lab equipment (see Figure. S1a). More details on these hoods as well as the laboratory spaces are discussed in a previous study by Dunn et al. [33].

The traditional fume hood evaluated in this study was the Safety-Flow Laboratory Fume Hood, Model 93-509Q (Fisher Scientific, Pittsburgh, PA). This type of fume hood is known as a constant air volume hood which maintains a uniform volumetric exhaust flow (hereafter referred to as the CAV hood). The hood was located on a bench top adjacent to an atomic absorption spectrophotometer and lab sink. The hood dimensions are 62 cm (height) × 130 cm (width) × 68 cm (depth). This hood was located in a university lab, 7.3 m wide by 5.8 m deep and with a ceiling height of 2.8 m (see Figure. S1b). The hood was exhausted out of the room through a facility exhaust system.

The mannequin used for the experiments was the upper body of a standard mannequin mounted on a wooden platform as shown in Figure. S1a. This mannequin had a shoulder width of 42 cm with a shoulder height of 140 cm and a total height of 164 cm above the floor. The mannequin head dimensions were 16 cm from back of head to nose tip and 16 cm across the head (from ear to ear). The body of the mannequin was placed at a distance of 5 cm from the inlet airfoil of the nano hood. When using the CAV hood, the body of the mannequin was placed directly against the inlet airfoil with the nose distance to the sash of approximately 10 cm. The distance between the mannequin and the CAV hood sash was set by the ASHRAE test method

(ASHRAE 1995). For the nano hood, it was set based on the physical limitations for positioning the mannequin close to the hood opening. The difference in geometry between these two hoods does not allow for the distance to be consistent.

Figure. S1. Mannequin and Hood Setup for Experiments. a) nano hood. b) CAV hood

Numerical Model Details

Airflow and contaminant dispersion simulations were conducted using ANSYS/Fluent version 16.1.0, a commercially available CFD code (Ansys, Canonsburg, PA). The hood and surrounding details were modeled to account for the impact of furniture and lab equipment on airflow patterns. The mannequin was simulated in the CFD model as a block structure with the following dimensions: head: 16 cm × 16 cm × 32 cm; legs: 12 cm × 12 cm; arms: 8 cm × 8 cm; shoulder width: 43 cm; shoulder height: 142 cm; body depth: 20 cm, and; torso length: 70 cm. For the base model case, the arms were positioned at the side of the torso consistent with the experimental conditions. When simulating arm motion, the arms were placed inside the hood.

The furniture and lab equipment were modeled as well to account for the impact of obstacles on the flow field. Hexahedron-dominated meshes were created for low element distortion and skewness. The hood and the room were meshed separately and then merged in ANSYS/Fluent and the contact face of the two mesh was modeled as interface where two regions were mapped. The meshes were more densely packed inside the hood in the vicinity of important geometrical features such as hood inlet, airfoils, and baffle plates for both the CAV and nano hoods. The meshes were coarser outside of the hood and further away from the hood face where flow features were less likely to impact flow patterns inside the hood.

In addition, the grid convergence was evaluated by the development of several grids and the inspection of the solution at key parameters. Grid convergence was assessed on grids ranging from 213,089 cells for CAV Hood to 277,757 cells for nano hood for the coarse grid; further ranging from 3,770,115 cells for CAV Hood to 4,007,074 cells for nano hood for the fine grid. The grids were refined by increasing the number of cells in areas of interest including at the hood wall boundaries and surrounding the body form.

A gas tracer source of sulfur hexafluoride (SF_6) was positioned inside the hoods for all simulations to evaluate the dispersion pattern of contaminant gas released inside the hood and the containment for both hood designs. A small cylindrical tracer gas source with a mass flow of 0.26 ml/min of SF_6 (species mass fraction of 0.13%) was used for the nano hood simulations, while a mass flow of 0.79 ml/min (species mass fraction of 0.40%) was used for the CAV hood. The wall across from the hood face was modeled as a pressure outlet, being set to zero gauge pressure (one atmosphere); flow through pressure boundaries was determined through the CFD solution process. The exhaust boundary condition was established by measuring total hood exhaust flow and imposing this volumetric flow on the exhaust duct as a velocity inlet. The hood exhaust boundary condition was the only source of air movement specified a priori. A summary of key boundary conditions is shown in Table. S1.

Table S1. Boundary conditions used in the simulations

	CAV Hood	Nano Hood
Averaged Mesh cells	5296094	3150528
Exhaust velocity	7.13 m/s Turbulent Intensity=10%, Hydraulic Diameter=0.275m	7.11 m/s Turbulent Intensity=10%, Hydraulic Diameter=0.1m
Room Inlet	Gauge Total Pressure=0 pa Turbulent Intensity=10% Turbulent Viscosity Ratio=10	Gauge Total Pressure=0 pa Turbulent Intensity=10% Turbulent Viscosity Ratio=10

SF_6	Diffuser velocity=2.0417e-5 Turbulent Intensity=10% Turbulent Viscosity Ratio=10	Diffuser velocity =2.0417e-5 Turbulent Intensity=10% Turbulent Viscosity Ratio=10

All simulations discussed in this paper were single phase, steady state, isothermal, and incompressible. A second order upwind spatial discretization scheme was used for model parameters including momentum, turbulent energy and dissipation and a third-order MUSCL discretization scheme was used for species transportation. The least squares cell-based discretization scheme was used for gradient terms and the enhanced wall treatment method was used to accurately capture the flow field near the wall boundaries. The solution process was iterated until the normalized residuals for each conservation equation were less than 10^{-3} for all parameters including velocity components, turbulent kinetic energy and dissipation, pressure and species.

The realizable k-ε turbulence closure model was used as

$$\frac{\partial}{\partial t}(\rho k) + \frac{\partial}{\partial x_j}(\rho k u_j) = \frac{\partial}{\partial x_j}\left[\left(\mu + \frac{\mu_t}{\sigma_k}\right)\frac{\partial k}{\partial x_j}\right] + \mu_t S^2 - \rho\varepsilon \tag{1}$$

$$\frac{\partial}{\partial t}(\rho \varepsilon) + \frac{\partial}{\partial x_j}(\rho \varepsilon u_j) = \frac{\partial}{\partial x_j}\left[\left(\mu + \frac{\mu_t}{\sigma_\varepsilon}\right)\frac{\partial \varepsilon}{\partial x_j}\right] + \rho C_1 S\varepsilon - \rho C_2 \frac{\varepsilon^2}{k+\sqrt{\nu\varepsilon}} \tag{2}$$

where k is turbulent kinetic energy, ε is the turbulence dissipation rate, t is the time variable, ρ is the density of the fluid, u_j is the mean component of the velocity in the direction x_j, and

$$C_1 = \max\,[0.43, \frac{\eta}{\eta+5}] \tag{3}$$

$$\eta = S\frac{k}{\varepsilon} \tag{4}$$

$$S = \sqrt{2S_{ij}S_{ij}} \tag{5}$$

where S_{ij} is the mean strain-rate tensor and is defined as

$$S_{ij} = \frac{1}{2}\left(\frac{\partial u_i}{\partial x_j} + \frac{\partial u_j}{\partial x_i}\right) \tag{6}$$

The default values of the constants for this turbulence model were applied ($C_2 = 1.9$, $\sigma_k = 1.0$, $\sigma_e = 1.2$).

Lagrangian particle tracking was used to provide a better understanding of the transport mechanisms which may lead to operator exposure. The Lagrangian particle tracking predicts the trajectories of the particles by solving the equation of motion:

$$\frac{d\boldsymbol{u}_p}{dt} = F_D\left(\boldsymbol{u} - \boldsymbol{u}_p\right) + \frac{\boldsymbol{g}(\rho_p - \rho)}{\rho_p} + \boldsymbol{F} \tag{7}$$

where F_D is the drag force coefficient, $\boldsymbol{u}_p$ is the velocity vector for particles, $\boldsymbol{u}$ is the fluid velocity vector, ρ is the fluid density, $\rho_p$is the particle density, and $\boldsymbol{F}$ is the acceleration term due to additional forces. The drag force coefficient F_D is defined as

$$F_D = \frac{18\mu}{\rho_p d_p^2}\frac{C_D Re}{24} \tag{8}$$

where $d_p$is the particle diameter, μ is the molecular viscosity of the fluid, and Re is the relative Reynolds number. The shape of particles is approximated as spherical and thus the spherical drag law was applied to calculate C_D.

The Fluent Discrete Phase Model (DPM) served to calculate the paths of nanometer-sized (50 nm) particles to provide insight on factors that affect exposure, both in the traditional fume hood and in the Nano hood. To accurately predict particle trajectories under the influence of turbulent flow, Fluent uses a stochastic tracking model [35]. This model allows for a more detailed look at the potential impact of flow patterns on particle dispersion and leaks from the hoods. For these models, the impact of Brownian motion has been calculated and included in the simulations. To assess the impact of operator motion during CFD simulations, the arms were positioned inside of the cabinet near the contaminant source.

The action of pulling arms from the cabinet was simulated using the moving wall boundary condition on the arm boundaries. This condition is implemented in the steady state model by a moving wall boundary condition on cells that define the arm surfaces, which then imparts the velocity to the adjacent air flow, via the no-slip condition. The impact of the motion was evaluated by releasing 50 nm diameter particles from a 10 cm diameter sphere whose center was located inside and 15 cm from the face of each hood. The diameter of 50 nm was chosen based on the medium size of the spherical nanoparticles with defined diameter of 100 nm or smaller. These simulations were conducted using the DPM with the release spheres located in 3 different positions: 1) at the center of the hood; 2) 10 cm from the left side of the hood and 3) 10 cm from the right side of the hood. These simulations were conducted with arm removal velocities of 0.5, 1.25, and 2.5 m/s. The fate of the particles was evaluated to assess the number of particles escaping the influence of the hood. A grouping of 56,590 particles was released from the sphere to evaluate containment performance.

Experimental Validation of Hood Face Velocity

Experimental data were collected to allow for CFD model validation. Airflow measurements were taken to characterize the inlet air flow profile at the face of the fume hoods. A traverse of the hood face with a hot wire anemometer was conducted to evaluate the spatial and temporal variation in air velocities entering the hood. The air velocity measurements were collected using a TSI model 8360 thermal anemometer (Shoreview, MN) with a range of 0.15 to 50 m/s, an accuracy of 3% of reading or 0.02 m/s and a response time of 200 milliseconds (ms) (to 63% of final value). These measurements were conducted both with and without a mannequin in place and with the hood free of clutter and internal obstructions. For the enclosing nano hood, the velocity profile was measured at the mid-plane of the hood face—at a distance of 8.5 cm from the hood base. For the CAV hood, two velocity profiles were conducted at the sash design height of 45 cm. This hood face traverse was conducted at 33% of the sash opening height which was 15 cm above the hood base.

Results and Analyses

Model verification and validation

The models were validated by comparing numerical predictions to experimental results, including comparison of both the hood face velocities as shown in Figure. S2. For both hoods, the change in solution parameters was minimal with increasing cell number, and both solutions are shown in the comparison of experimental and CFD results in this section. To allow for comparison of results, the overall grid density and count were kept similar between different hood CFD models. The face velocities of the nano hood were taken at an exhaust airflow of 3.40 m^3/min and ranged from 0.34 to 0.37 m/s across the face of the hood without the mannequin and 0.25-0.44 m/s with the mannequin in place. With the mannequin in place, the midplane velocity dropped significantly in front of the mannequin in the stagnation region downstream of the body for both hoods as presented in Figure. S2a. The root mean square (RMS) differences between the experimental measurements and analytical predictions for the face velocities were approximately 11% for the nano hood without the mannequin and 24% for the nano hood with the mannequin in place.

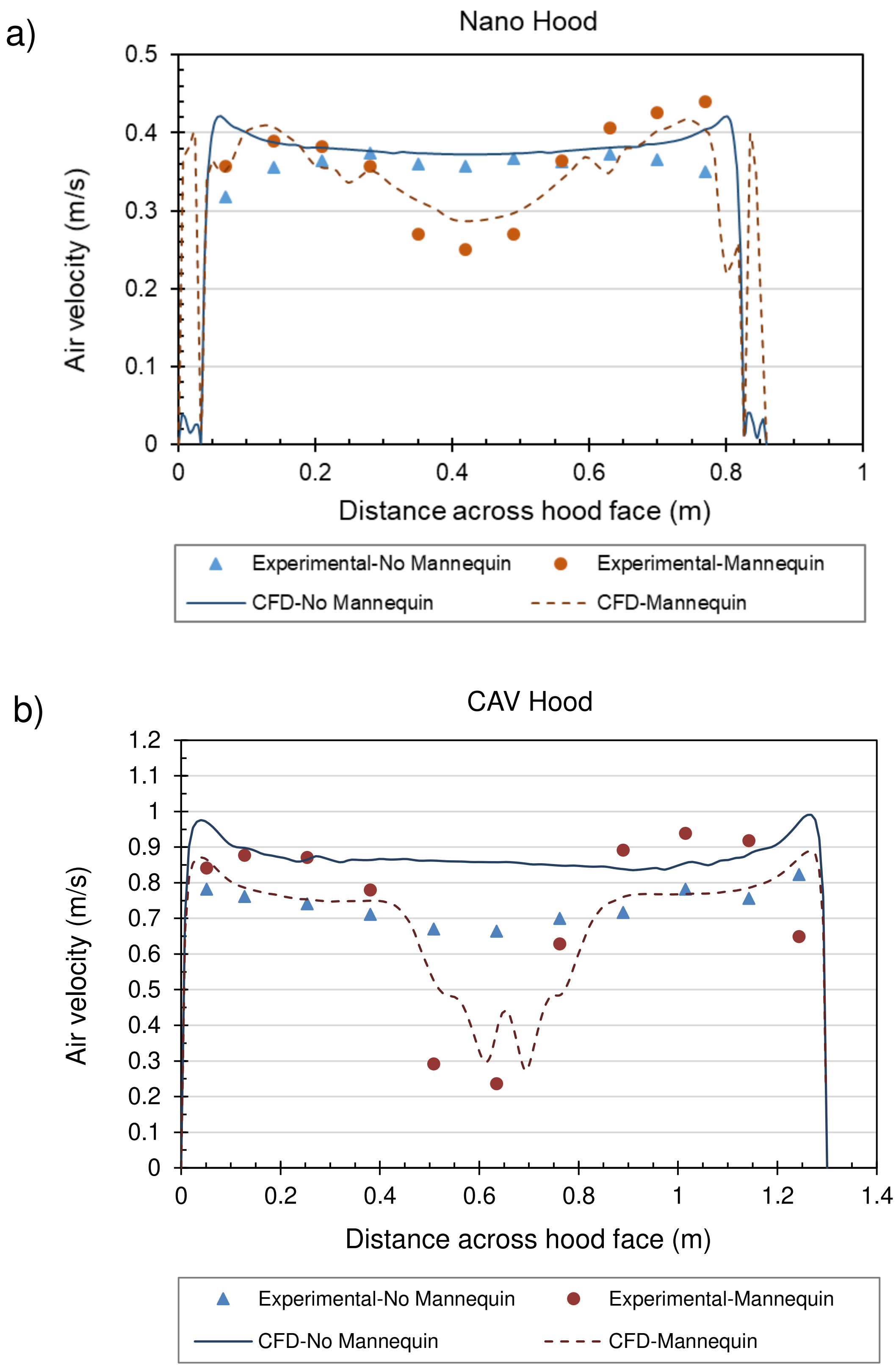

Figure. S2. Comparison of velocity profile with CFD predictions for the a) nano hood at midplane of the opening and b) the CAV hood at 33% of sash opening (15 cm).

For the CAV hood, the average face velocity at 33% of the sash height (15 cm) ranged in 0.66-0.82 m/s without the mannequin and 0.23-0.91 m/s with the mannequin in place as presented in Figure. S2b. The RMS differences between the experimental measurements and analytical predictions for the CAV hood face velocities were approximately 21% with no mannequin and 34% for the mannequin in place at 33% of sash opening. The results showed that the simulations agree with the experimental data reasonably well for both cases. The RMS error for the CAV case (with the mannequin) could be due to the chaotic and transient nature of the flow field in the wake region and the steady state time scheme was used. Similar to the nano hood, the velocity magnitude dropped significantly when the mannequin was present.

Hood interior airflow and particle dispersion patterns

The difference in the geometric design of both hoods resulted in different flow patterns inside the hoods. Both hoods exhibited large recirculation zones behind the sash as air accelerates into the hood opening and then slows down when reaching the much larger hood volume (Figures. S3a and S3c, tag number 1). The existence of a recirculation region behind the sash has been found in these types of hoods by other researchers using experimental and numerical methods. The nano hood also exhibited secondary recirculation zones related to the side post airfoils, as shown in Figure. S3b. These side airfoils, which were meant to reduce turbulence inside the nano hood, generate a recirculation zone along the sides of the hood. This result may be surprising given that the side airfoil is small and intrudes into the hood space only a few centimeters. However, as the air is brought into the hood, these small airfoils greatly impact the flow patterns near the sides of the nano hood. The CAV hood flow pattern shows a much smaller side recirculation pattern primarily due to the fact that the side airfoils end flush with the sides of the hood and did not intrude into the hood space (see Figure. S3d, tag number 2).

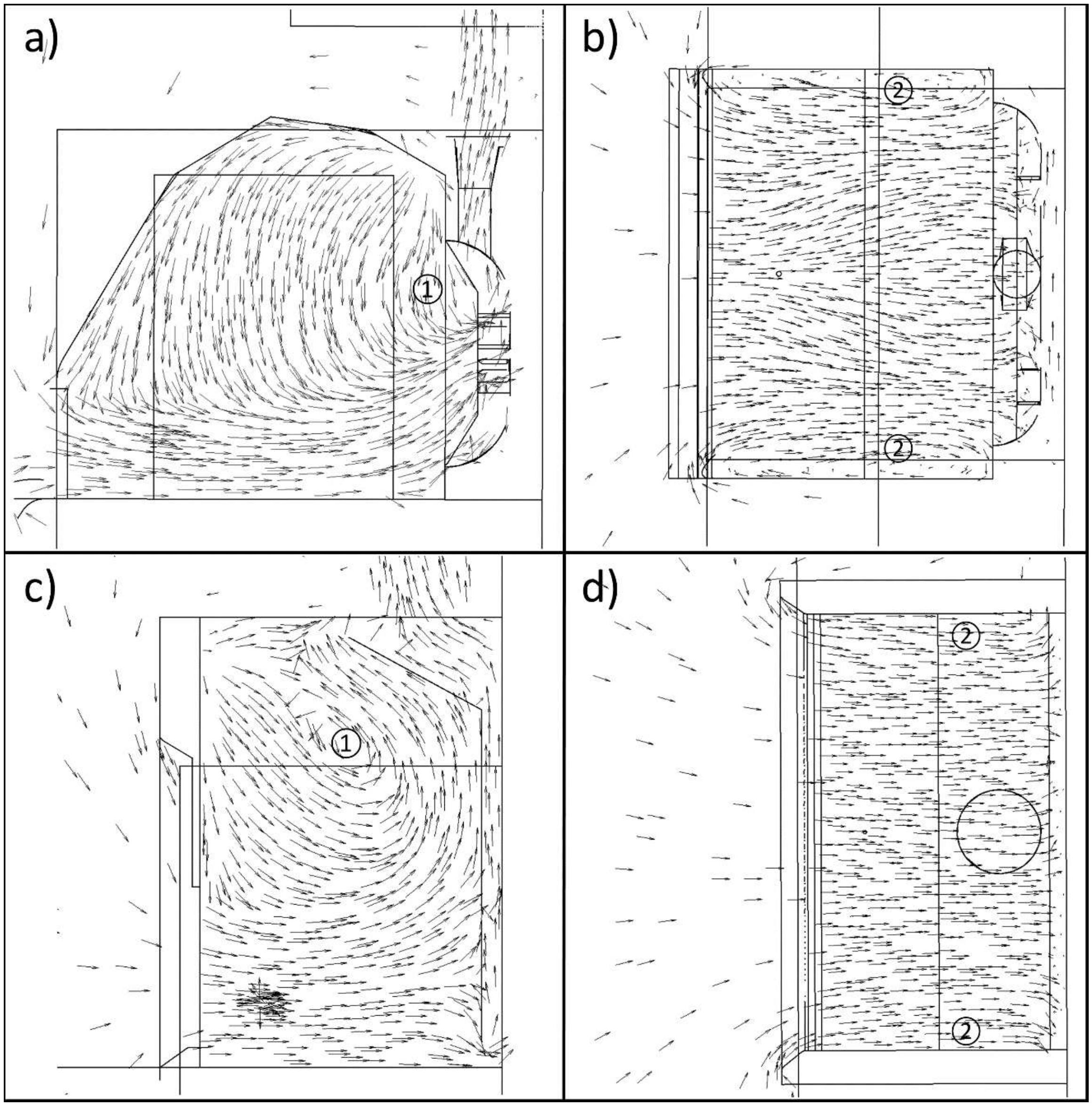

Figure. S3. Velocity at a) a vertical cross section of nano hood. b) a horizontal cross section of nano hood. c) a vertical cross section of CAV hood. d) a horizontal cross section of CAV hood.

To understand the performance of both designs on contaminant dispersion within the hood, a release of a tracer gas, SF_6, was simulated at the center of the hood and the predicted concentration contours at a vertical cross section are shown in Figure. S4 with and without a mannequin form in front of the hood. Figures. S4a and 4b show that the tracer gas gets caught up in the primary recirculation zone behind the nano hood sash but is reduced when the mannequin form is in front of the hood. However, Figures. S4c and 4d show that the inclusion of the mannequin body in front of the CAV hood dramatically disturbs the flow field and causes the tracer gas to move towards the hood face and increases the tracer concentration in the primary recirculation zone behind the hood sash. This airflow dynamic may increase the risk of contaminant escape in the CAV hood when attended by an operator. Further the concentration of the tracer in the upper part of the hood, near the bottom of the hood sash, provides an opportunity for leakage of contaminants to easily reach the operator's breathing zone (see Figures. S4 and S6).

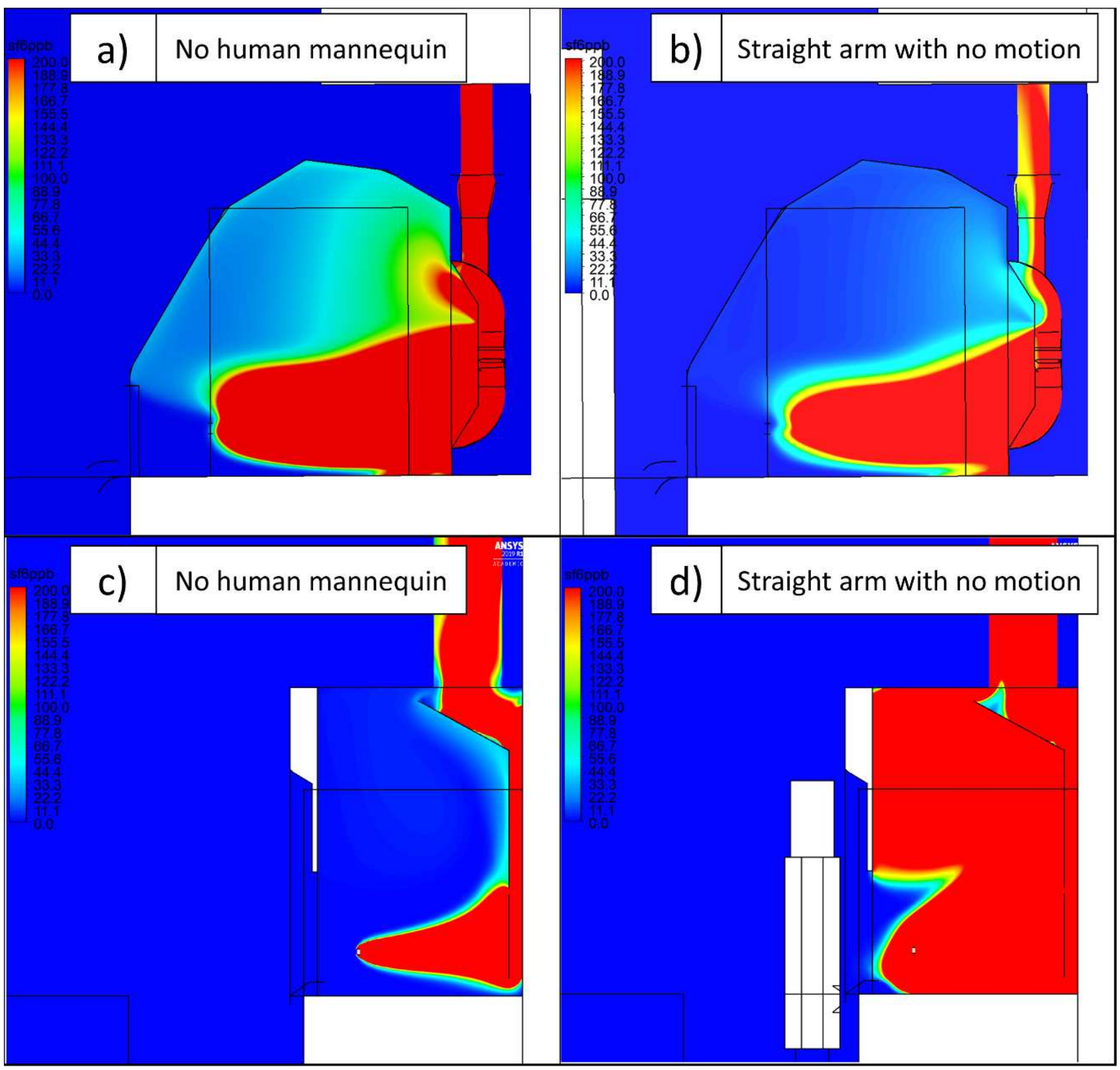

Figure. S4. SF_6 predicted concentration contours at a vertical cut plane with no human mannequin and with a straight-arm mannequin for a) nano hood without mannequin, b) nano hood with straight arm and no motion, c) CAV hood without mannequin, and d) CAV hood with straight arm and no motion.

Effects of arm motion on hood containment

Simulations with both tracer gas and nanoparticle releases were conducted to better understand the impact of the withdrawal of arms from the hood on contaminant dispersion patterns. Figure. S5 shows the impact of the highest withdrawal arm speed (2.5 m/s) on predicted tracer gas concentrations compared with no arm motion at a horizontal cut plane through the middle of the hood opening. The pulling arm motion does not seem to make a significant change in the dispersion patterns seen through this figure. However, the motion of the arm moving out of the hood shows that contaminant seems to be dragged out by the end of the arm (see figures. S5b and S5d) and tends to enlarge the overall shape of the high SF_6 concentration zones to a minor degree. This action may increase the potential for dragging out tracer gas out of the hood near the hood face.

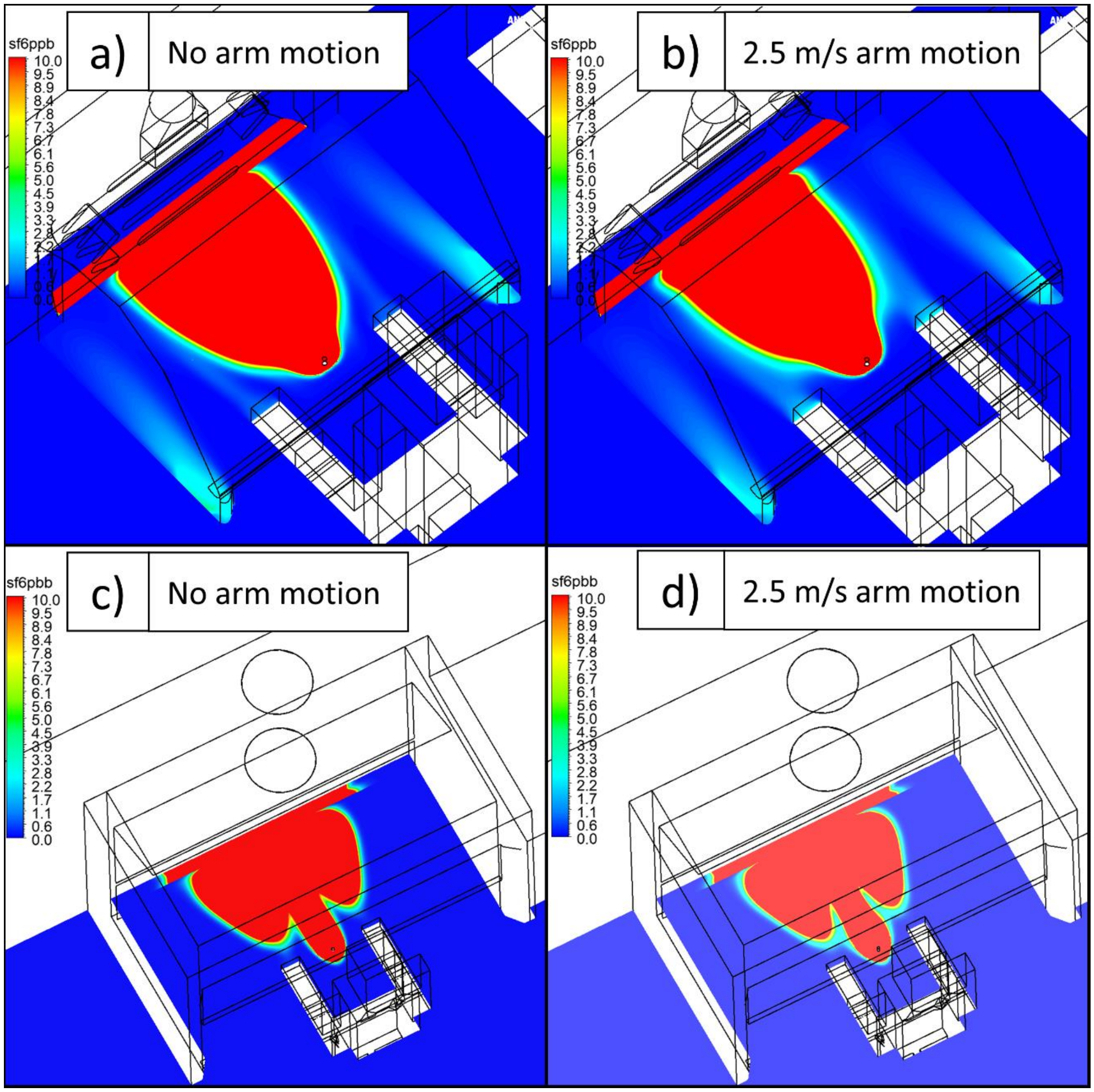

Figure. S5. SF_6 predicted concentration contours for the CAV hood with no arm motion and 2.5 m/s arm motion at a horizontal cut plane through both arms for a) nano hood and no arm motion, b) nano hood and 2.5 m/s arm motion, c) CAV hood and no arm motion, and d) CAV hood and 2.5 m/s arm motion.

Table. S2 contains a summary of the particle tracking results for a variety of simulation conditions, including varying source location (left, center, or right sphere location) and arm withdrawal speed (0, 0.5, 1.0, and 2.5 m/s). For all scenarios, more total particles were leaked from the CAV hood than the nano hood. Figures. S6a - S6d shows the particle tracks released from a source at the side and in the center of the both the nano and CAV hoods. A large portion of particles entered into the primary recirculation zone before they were eventually cleared in the nano hood. The speed of arm pulling motion did not show a significant impact on particle trajectories for the nano case. On the contrary, only a small portion of particles entered into the primary recirculation zone as most particles were sucked directly into the lower opening of the baffle in the CAV hood, shown in Figures. S6c and 6d. When the arm removal speed increased, some particles started to reach the hood face and show a tendency to leak from the hood (Figure. S6d and Table. S2). For the nano hood, only the highest arm removal rate resulted in loss of containment. These particles were predicted to escape the hood and move outward into the room. For the CAV hood, particles leaked at every condition even when there was no arm motion.

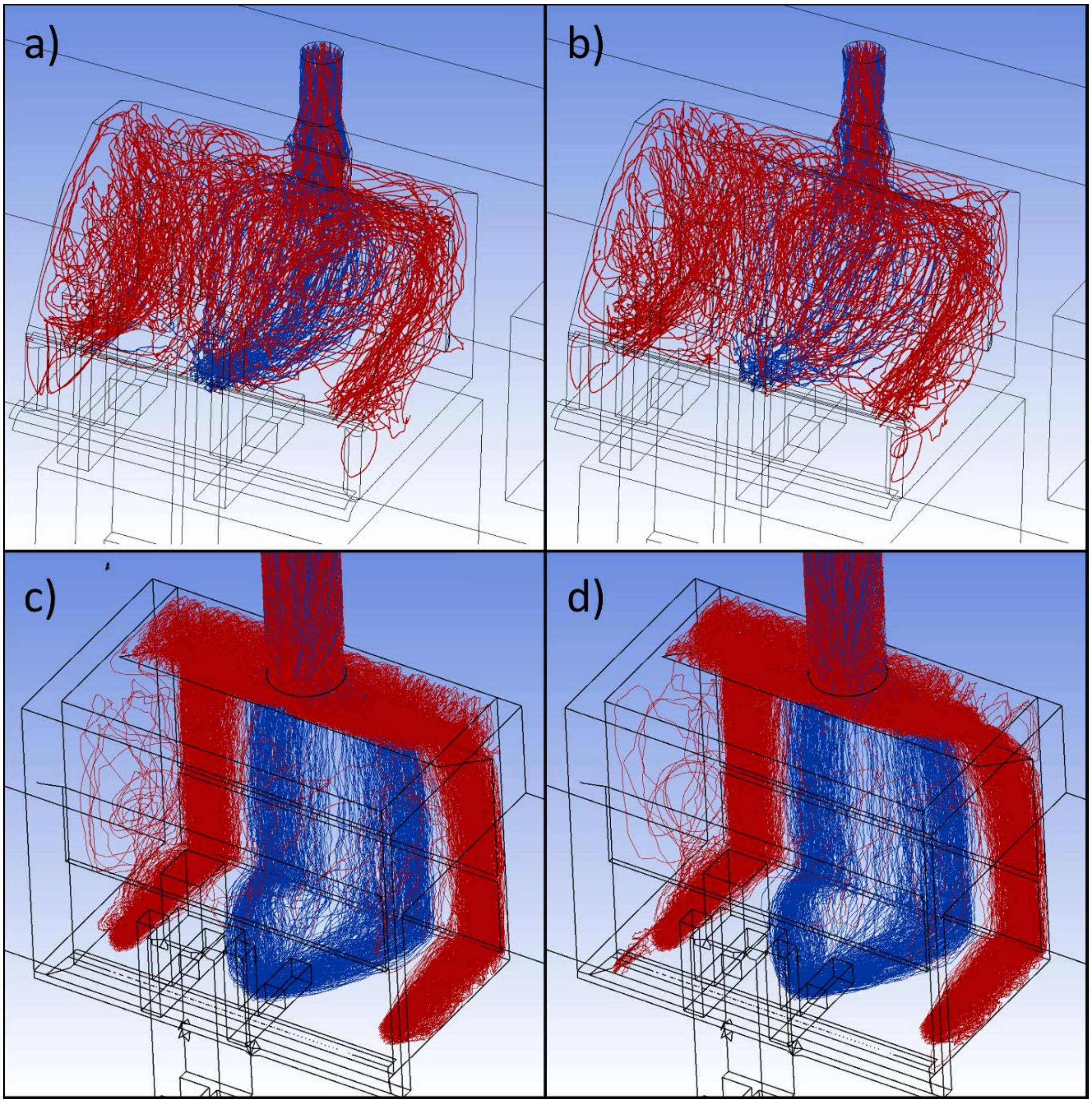

Figure. S6. Particle tracks for the source at center of hood with a) nano hood with no arm motion. b) nano hood with 2.5 m/s arm motion. c) CAV hood with no arm motion and d) CAV hood with 2.5 m/s arm motion.

The airflow dynamics inside the hood coupled with the mannequin in front of the hood and the motion of the arms from the hood impacts the containment performance of these hoods. Further where sources are located within the hood and their proximity to the primary and secondary recirculation regions affects the potential for leakage. When the particles are released in the center of the hood downstream of the body, they are more efficiently captured and exhausted from the hood. In general, with all simulations, particles become trapped in the recirculation zones resulting in some particles not being exhausted from the hood. Overall, both hoods leaked exhibited leakage of less than 1% based on these simulations (see Table. S2) however, the nano hood showed less particle leakage than the CAV hood. Based on these results, the best containment condition is for the source to be located at the center of the hood, especially for the nano hood, which suffers from the side recirculation zones. When the contaminant is released inside the hood at the center, the average flow path is for the contaminant to be picked up and efficiently removed by either hood. However, when the contaminant is located near the side of the hood, the flow patterns inside the nano hood increase the potential for leakage as the streamlines released from a source near the side do not leave the hood space directly but move back towards the hood opening (see Figure. S6).

Table. S2. Percentage (%) of 50 nm particles reaching hood face plane released under various simulation conditions including source location and arm withdrawal speeds for nano hood and traditional hood.

Arm Withdrawal Speed (m/s)	Nano Hood				Traditional (CAV) Hood			
	Source Location				Source Location			
	Left	Center	Right	Total	Left	Center	Right	Total
0	0.008	0	0	0.008	0.012	0	0.014	0.026
0.5	0.051	0	0	0.051	0.041	0	0.039	0.080
1.0	0.064	0	0	0.064	0.050	0	0.090	0.140
2.5	0.092	0	0.014	0.106	0.202	0.005	0.136	0.343

DISCUSSION

The current study evaluated a new fume hood being marketed for the containment of nanomaterials during handling compared to an existing conventional fume hood. One of the key findings was that the nano fume hood seemed to be less affected than the CAV hood by the presence of a body in front of the hood. However, the use of aerodynamic features like the side airfoils, which intruded into the hood volume, created a secondary recirculation zone. This secondary recirculation zone interacted with the primary recirculation region behind the sash to trap contaminants increasing the potential for leakage. In smaller hoods, such as the nano hood evaluated (hood width of 86 cm versus mannequin width of 43 cm), the impact of these effects might be magnified since the worker's arms will more likely interact with the side recirculation zones. However, the results also indicate a potential re-design that might lead to an improvement of performance. Moving the side airfoils outside of the volume so that they terminate at the hood side should reduce the size of the side recirculation zone although the optimum inlet angle should be investigated using CFD and confirmed using flow visualization methodologies. For the CAV hood, the mannequin represented a far smaller blockage to the opening area since the hood width was approximately 1.5 times as large as the smaller nano hood. These factors as well as the design of the side airfoils resulted in better airflow patterns along the hood side.

For both hoods, as air enters the hood opening and slows down, a large recirculation region is created behind the sash. The presence of this recirculation zone (behind the sash) has been seen in research findings on fume hoods by many researchers [10, 12-18]. Complex turbulent airflow patterns arose in areas where the incoming air met a wall boundary—along the sides of the hood, at the work surface and along the bottom of the sash [36]. When a transient disturbance impacts these regions of the hood, contaminants inside the hood can leak out of the hood into the work environment. These disturbances may be due to many common sources including the presence and motion of the worker, room ventilation, sash movement and the walk-by of workers within the room [7, 9, 12, 19, 26, 27, 29, 37-40]. Huang et al. developed an air curtain hood which sought to address these design issues by changing the overall flow patterns associated with the hood [41]. In that design, an air jet emanates from the sash and forms a barrier to the potential for leakage of contaminants inside the hood. An evaluation of that hood during nanomaterial handling activities showed good containment performance [42].

The presence of the mannequin did impact the airflow into the fume hood with a stagnation zone forming downstream of the mannequin. However, this factor was not sufficient to result in leakages for either hood. The impact of removing arms from the hood was evaluated with a Lagrangian particle tracking scheme. These simulations illustrated the effect of motion on the recirculation zones for both hoods which concentrate contaminants in the vortices behind the hood sash. For the nano hood, motion caused a much greater disturbance in the overall flow field inside the hood. This is likely due to the fact that the volumetric airflows are much lower for the nano hood than the CAV hood (nano hood: 2.83 m^3/min, CAV hood: 17.8 m^3/min). In addition, although the velocity at the face of both hoods were comparable for the simulation (nano hood: 0.36 m/s, CAV hood: 0.48 m/s), the air speeds decrease greatly once inside the nano hood as the air expands into the larger volume.

The procedure of removing the arm from the hood was demonstrated numerically through the steady state model. The flow pattern created by withdrawing the arms caused particles to be dragged out in the vicinity of the arm for the nano hood. This is consistent with fume hood experimental studies conducted by other researchers [27, 43]. The leakage only occurred at the highest arm speed simulated and one that is higher than those likely performed by workers. However, this movement is conducted by every user upon completion of tasks, and overall leakage could certainly be increased if the user is also pulling out an object, such as a beaker which would further disturb the flow field. The approach of using a moving wall boundary condition in a steady state framework is a reasonable initial approach that can be improved by using more recently available CFD techniques such as dynamic mesh methodologies.

With both the CAV and nano hood, the recirculation zones result in contaminants being transported to the front of the hood near the inlet boundary. As the particles get near the hood/room interface, the potential for leakage to occur increases due to user motion as well as outside disturbances, such as room air currents. These simulations did not include room air vents, which could have further disturbed the flow and resulted in leakage of particles from the hood. Other researchers have documented the negative impact of room air distribution on hood containment performance both experimentally and through numerical methods [27, 37, 38, 43].

Finally, the airflow patterns in the hood were transient in nature as evidenced by the predicted tracer gas concentration results. As the flow was unsteady, there were limitations with using steady state simulations. However, it was believed that the overall flow field features were well captured by the steady state model, and agreement with experimental measurements validated this approach.

Conclusions

The dearth of published studies on the implementation and effectiveness of engineering controls for nanometer-sized particles such as engineered nanoparticles provide an opportunity to assess exposure control approaches. Many users have adopted the laboratory fume hood as the primary exposure control given its ubiquitous nature and history as a standard control used in most research laboratories. Some newly developed fume hoods introduced in the past decade are being specifically targeted for application in the nanotechnology and advanced material markets. This study illustrated limitations in one such design; similar hoods by other manufacturers may exhibit similar limitations. In addition, CFD was used to evaluate the potential impact of worker arm motion on containment effectiveness. Results of the modeling effort point to some commonsense approaches to minimizing the likelihood of arm motion resulting in worker exposure. Specifically, the operator could wait a prescribed amount of time before withdrawing their arms to allow for the clearance of nanoparticles and do so at a lower speed, as an improved work practice to minimize leakage and potential for exposure.

This study along, with others conducted, showed limitations of some fume hood containment test methods. These approaches include the need to utilize a mannequin when conducting tracer gas tests and to evaluate common worker maneuvers, such as removing their arms from the hood. In addition, hood containment assessment methods should collect data near each hood wall boundary since these areas represented the regions where leakage was most likely to occur. More research is required to address the issues at these boundaries where leakage may occur to gain a better understanding of the interaction between hood containment and room airflows.

References

1. Bavasso I, Vilardi G, Stoller M, Chianese A, Di Palma L. Perspectives in nanotechnology based innovative applications for the environment. CHEMICAL ENGINEERING. 2016;47.
2. NIOSH. Approaches to Safe Nanotechnology: Managing the Health and Safety Concerns Associated with Engineered Nanomaterials. Cincinnati, OH: US Department of Health and Human Services, Public Health Service, Centers for Disease Control and Prevention, National Institute for Occupational Safety and Health, DHHS (NIOSH)

Publication No 2009-125. 2009.

3. Hinds WC. Aerosol technology - properties, behavior, and measurement of airborne particles. vol Book, Whole. New York: Wiley-Interscience; 1999.

4. Ong S, Tan Y, Chia P, Lee T, Ng O, Wong M, et al. Air, surface environmental, and personal protective equipment contamination by severe acute respiratory syndrome coronavirus 2 (SARS-CoV-2) from a symptomatic patient. JAMA. 2020;E1-E3. doi: 10.1001/jama.2020.3227.

5. Asadi S, Bouvier N, Wexler A, Ristenpart W. The coronavirus pandemic and aerosols: Does COVID-19 transmit via expiratory particles? Aerosol Science and Technology. 2020;54(6):635-8.

6. Ding Y, Kuhlbusch TA, Van Tongeren M, Jiménez AS, Tuinman I, Chen R, et al. Airborne engineered nanomaterials in the workplace—a review of release and worker exposure during nanomaterial production and handling processes. Journal of hazardous materials. 2017;322:17-28.

7. Flynn MR, Ljungqvist B. A review of wake effects on worker exposure. Ann Occup Hyg. 1995;39(2):211-21.

8. Tsai SJ. Potential inhalation exposure and containment efficiency when using hoods for handling nanoparticles. J Nanopart Res. 2013;15:1880. doi: 10.1007/s11051-013-1880-2.

9. Huang RF, Chen HD, Hung CH. Effects of walk-by and sash movement on contaminant leakage of air curtain-isolated fume hood. Ind Health. 2007;45(6):804-16.

10. Tseng L, Huang RF, Chen CC, Chang CP. Correlation between airflow patterns and performance of a laboratory fume hood. J Occup Environ Hyg. 2006;3:694-706.

11. Varley JO, Ghorashi B. The Effect of Turbulent Structures on Hood Design—A Review of CFD and Flow Visualization Studies. HVAC&R Research. 1997;3(3):291-308.

12. Ljungqvist B. Aerodynamic design of fume cupboards. Safety Health Pract. 1991(8):36-40.

13. Hu P, Ingham DB, Wen X. Effect of the location of the exhaust duct, an exterior obstruction and handle on the air flow inside and around a fume cupboard. Ann Occup Hyg. 1996;40(2):127-44.

14. Hu P, Ingham DB, Wen X. Effect of baffles and a louvered bypass on the airflow and the convective patterns of contaminant inside a fume hood. Am Ind Hyg Assoc J. 1998;59(5):303-12.

15. Nicholson GP, Clark RP, de Calcina-Goff ML. Computational fluid dynamics as a method for assessing fume cupboard performance. Ann Occup Hyg. 2000;44(3):203-17.

16. Lan NS, Viswanathan S. Numerical simulation of airflow around a variable volume/constant face velocity fume cupboard. AIHAJ. 2001;62(3):303-12.

17. Tseng LC, Huang RF, Chen CC. Significance of face velocity fluctuation in relation to laboratory fume hood performance. Ind Health. 2010;48(1):43-51. doi: JST.JSTAGE/indhealth/48.43 [pii].

18. Ivany RE, First MW, Diberardinis LJ. A new method for quantitative, in-use testing of laboratory fume hoods. American Industrial Hygiene Association Journal. 1989;50(5):275-80.

19. Flynn MR, Ljungqvist B. A review of wake effects on worker exposure. Ann Occup Hyg. 1995;39:211-21.

20. Kim TH, Flynn MR. The effect of contaminant source momentum on a worker's breathing zone concentration in a uniform freestream. Am Ind Hyg Assoc J. 1992;53(12):757-66.

21. Kim TH, Flynn MR. Airflow pattern around a worker in a uniform freestream. Am Ind Hyg Assoc J. 1991;52:287-96.

22. Kim TH, Flynn MR. Modeling a worker's exposure from a hand-held source in a uniform freestream. Am Ind Hyg Assoc J. 1991;52(11):458-63.

23. George DK, Flynn MR, Goodman R. The impact of boundary layer separation on local exhaust design and worker exposure. Applied Occupational and Environmental Hygiene. 1990;5(8):501-9.

24. Welling I, Andersson I-M, Rosen G, Räisänen J, Mielo T, Marttinen K, et al. Contaminant dispersion in the vicinity of a worker in a uniform velocity field. Ann Occup Hyg. 2000;44(3):219-25.

25. Bennett JS, Crouch KG, Shulman SA. Control of wake-induced exposure using an interrupted oscillating jet. Am Ind Hyg Assoc J. 2003;64(1):24-9. doi: Doi 10.1080/15428110308984779.

26. DiBerardinis LJ, First MW, Ivany RE. Field Results of an in-place, quantitative performance test for laboratory fume hoods. Appl Occup Environ Hyg. 1991;6(3):227-31.

27. Mosovsky JA. Sulfur hexafluoride tracer gas evaluations on hood exhaust reductions. Am Ind Hyg Assoc J. 1995;56(1):44-9.

28. Tseng LC, Huang RF, Chen CC, Chang CP. Aerodynamics and performance verifications of test methods for laboratory fume cupboards. Ann Occup Hyg. 2007;51(2):173-87. doi: 10.1093/annhyg/mel057.

29. Ahn K, Woskie S, DiBerardinis L, Ellenbecker M. A review of published quantitative experimental studies on factors affecting laboratory fume hood performance. J Occup

Environ Hyg. 2008;5(11):735-53. doi: 902305522 [pii] 10.1080/15459620802399989.

30. Braconnier R, Bonthoux F. Fluid dynamics of cytotoxic safety cabinets. Ann Occup Hyg. 2010;54 (2):236-46.

31. Lan NS, Viswanathan S. Numerical simulation of airflow around a variable volume/constant face velocity fume cupboard. Am Ind Hyg Assoc J. 2001;62(3):303-12.

32. Kulmala I, Saamanen A, Enbom S. The effect of contaminant source location on worker exposure in the near-wake region. Ann Occup Hyg. 1996;40(5):511-23. doi: Doi 10.1016/0003-4878(96)00003-8.

33. Dunn K, Tsai S, Woskie S, Bennett J, Garcia A, Ellenbecker M. Evaluation of Leakage from Fume Hoods Using Tracer Gas, Tracer Nanoparticles and Nanopowder Handling Test Methodologies. Journal of Occupational and Environmental Hygiene. 2014;11(10).

34. Tsai SJ, Ada E, Isaacs J, Ellenbecker MJ. Airborne nanoparticle exposures associated with the manual handling of nanoalumina and nanosilver in fume hoods. Journal of Nanoparticle Research. 2009;11(1):147-61. doi: 10.1007/s1 1051-008-9459-z.

35. ANSYS. ANSYS FLUENT 12.0 Theory Guide. 2009.

36. Tseng LC, Huang RF, Chen CC, Chang CP. Correlation between airflow patterns and performance of a laboratory fume hood. J Occup Environ Hyg. 2006;3:694-706.

37. Caplan KJ, Knutson GW. Influence of room air supply on laboratory hoods. Am Ind Hyg Assoc J. 1982;43(10):738-46.

38. Denev JA, Durst F, Mohr B. Room Ventilation and Its Influence on the Performance of Fume Cupboards: A Parametric Numerical Study. Ind Eng Chem Res. 1997;36:458-66.

39. Ljungqvist B. Ventilated benches and enclosures in laboratories. Safety Health Pract. 1992(10):41-4.

40. Flynn MR, Ahn K, Miller CT. Three-dimensional finite-element simulation of a turbulent push-pull ventilation system. Annals of Occupational Hygiene. 1995;39(5):573-89.

41. Huang RF, Wu YD, Chen HD, Chen CC, Chen CW, Chang CP, et al. Development and evaluation of an air-curtain fume cabinet with considerations of its aerodynamics. Ann Occup Hyg. 2007;51(2):189-206. doi: mel051 [pii]

10.1093/annhyg/mel051.

42. Tsai SJ, Huang RF, Ellenbecker MJ. Airborne nanoparticle exposures while using constant-flow, constant-velocity, and air-curtain-isolated fume hoods. Ann Occup Hyg. 2010;54(1):78-87.

43. DiBerardinis LJ, First MW, Ivany RE. Field Results of an in-place, quantitative perfromance test for laboratory fume hoods. Appl Occup Environ Hyg. 1991;6(3):227-31.